Ionization Kinetics of β-Substituted Radicals in Solution: A Nanosecond Laser Flash Photolysis Study

by

Sandy F. Lancelot

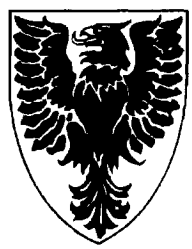

Submitted in partial fulfillment of the requirements
for the degree of Doctor of Philosophy

at

Dalhousie University
Halifax, Nova Scotia
December 2002

DALHOUSIE UNIVERSITY

FACULTY OF GRADUATE STUDIES

The undersigned hereby certify that they have read and recommend to the Faculty of Graduate Studies for acceptance a thesis entitled "Ionization Kinetics of ß-substituted Radicals in Solution: A Nanosecond Laser Flash Photolysis Study" by Sandy F. Lancelot in partial fulfilment for the degree of Doctor of Philosophy.

Dated: December 6, 2002

External Examiner: [redacted]

Research Supervisor: [redacted]

Examining Committee: [redacted]

DALHOUSIE UNIVERSITY

DATE: 6 December, 2002

AUTHOR: Sandy F. Lancelot

TITLE: Ionization Kinetics of β-Substituted Radicals in Solution: A Nanosecond Laser Flash Photolysis Study

DEPARTMENT OR SCHOOL: Department of Chemistry

DEGREE: Doctorate CONVOCATION: Summer YEAR: 2003

Permission is herewith granted to Dalhousie University to circulate and to have copied for non-commercial purposes, at its discretion, the above title upon the request of individuals or institutions.

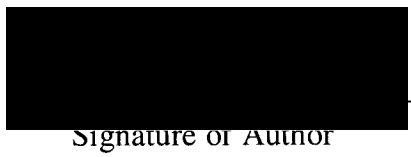

Signature of Author

Cette thèse est dédiée à Chris,

Maman, Papa, et Frédérick

'It takes a strong fish to swim against the current,
even a dead one can float with it.'
Unknown

TABLE OF CONTENTS

LIST OF FIGURES

Figure 3-52. Observed rate constants measured in (□) neat AcN, (●) 25% TFE/75% AcN, (○) 50% TFE/50% AcN, (■) 75% TFE/25% AcN, and (●) neat TFE, plotted as a function of perchloric acid concentration. Rate constants were measured from kinetic traces monitored at 590 nm after 266 nm laser irradiation of 3-(4-methoxyphenyl)-4-hydroxy-2-butanone **6(OMe)**.

Figure 3-53. First-order rate constant k_{het} calculated for the growth of the 4-methoxystyrene radical cation **8(OMe)** and plotted against % TFE in nitrogen-purged acetonitrile mixtures acidified with perchloric acid. Rate constants were determined from kinetic traces acquired at 590 nm after 266 nm laser photolysis of 3-(4-methoxyphenyl)-4-hydroxy-2-butanone **6(OMe)**.

Figure 3-54. Second-order acid-catalyzed rate constant (k_{cat}) for the growth of the 4-methoxystyrene radical cation **8(OMe)** plotted as a function of % TFE in nitrogen-purged acetonitrile mixtures acidified with perchloric acid. Rate constants were determined from kinetic traces acquired at 590 nm after 266 nm laser photolysis of 3-(4-methoxyphenyl)-4-hydroxy-2-butanone **6(OMe)**.

Figure 3-55. Acidity constant $K_{RH^{\bullet+}}$ calculated for the dissociation of the protonated β-hydroxy-4-methoxyphenethyl radical **7(OMe)** plotted as a function of % TFE in nitrogen-purged acetonitrile mixtures acidified with perchloric acid. Results were acquired from 266 nm laser photolysis of 3-(4-methoxyphenyl)-4-hydroxy-2-butanone **6(OMe)**.

Figure 3-56. Observed rate constants calculated for the growth of the 4-methoxystyrene radical cation **11(OMe)** in (□) neat AcN, (■) 25% TFE/75% AcN, (●) 50% TFE/50% AcN, (○) 75% TFE/25% AcN, and (●) neat TFE, and plotted as a function of perchloric acid concentration. Rate constants were measured from kinetic traces monitored at 590 nm after 266 nm laser irradiation of 2-(4-methoxyphenyl)-3-oxobutyl diethylphosphate **9(OMe)**.

Figure 3-57. First-order rate constants versus % TFE in acetonitrile acidified with perchloric acid. Data was collected following 266 nm laser irradiation of (●) 2-(4-methoxyphenyl)-3-oxobutyldiethylphosphate **9(OMe)** and (○) 3-(4-methoxyphenyl)-4-hydroxy-2-butanone **6(OMe)**.

LIST OF TABLES

ABSTRACT

β-Substituted radicals are transient species with a potential leaving group attached to the carbon adjacent to the unpaired electron. In nonpolar solutions, such intermediates exhibit familiar radical chemistry and react *via* radical-radical coupling and homolysis. However, when generated in polar media, β-substituted radicals undergo heterolytic cleavage of the β-group to form the corresponding olefin radical cation. This novel, open shell ionization mechanism has been implicated in a growing number of biochemical transformations, ranging from healthy enzyme mediated processes to the critical steps of radiation-induced DNA damage. Yet, in spite of its biological relevance, a survey of the literature unearths surprisingly little about the dynamics and kinetics of this β-heterolysis reaction that has been shown to occur unassisted, but that can be susceptible to acid catalysis.

This thesis presents the results of a mechanistic investigation into the ionization of β-mesylate, β-hydroxy, and β-diethylphosphate *para*-substituted phenethyl radicals in polar solvents such as HFIP, TFE and acetonitrile. The radicals of interest were generated upon nanosecond laser flash photolysis of the relevant precursor compound and detected by absorption spectroscopy. Time-resolved growth traces of the radical cation provides unambiguous evidence that the β-heterolysis mechanism is an energetically favorable reaction pathway for β-substituted radicals in nitrogen-saturated polar solvents. Rate constants calculated for the uncatalyzed ionization of the β-mesylate radicals are found to be fast, within the range of 10^6-10^7 s^{-1}. As anticipated, the β-hydroxy and β-diethylphosphate radicals required acid catalysis to undergo heterolysis. Typical bimolecular rate constants calculated for the acid-dependent ionization of these radicals are of the order of 10^8 M^{-1} s^{-1}.

The dynamics of the β-heterolysis mechanism were probed by varying the aromatic group on the radical and investigating how the electronic nature of the substituent influences the calculated rate constant for the ionization process. A linear correlation obtained between k_{het} and the σ^+ scale suggests the existence of some overlap between the SOMO and the cationic centre developing in the transition state. The sensitivity of the β-heterolysis reaction toward the ionizing ability of the solvent and the nucleofugality of the β-leaving group were also assessed with the use of the Y_X scale. Lastly, the results are compared to the more familiar S_N1 mechanism and in doing so, expose the extent to which the presence of an adjacent, unpaired electron alters the kinetics of the ionization process.

LIST OF ABBREVIATIONS AND SYMBOLS

ε	extinction coefficient
λ	wavelength
AcN	acetonitrile
AdoCbl	adenosylcobalamin
aq.	aqueous
DNA	deoxyribonucleic acid
EDG	electron donating group
ESR	electron spin resonance
g	grams
EWG	electron withdrawing group
E_a	activation energy
HFIP	1,1,1,3,3,3-hexafluoro-2-propanol
ISC	intersystem crossing
k	rate constant
kJ	kilojoule
LFP	laser flash photolysis
MeOH	methanol
ml	millilitre
ms	millisecond
nm	nanometer
NMR	nuclear magnetic resonance
ns	nanosecond
O.D.	optical density
ppm	parts per million
ps	picosecond
RDS	rate-determining step
TFE	2,2,2-trifluoroethanol
TMS	tetramethylsilane
UHP	ultra high purity
UV/Vis	ultraviolet/visible
$\Delta G^{\ddagger}$	free energy of activation
$\Delta H^{\ddagger}$	enthalpy of activation
ΔO.D.	change in optical density
$\Delta S^{\ddagger}$	entropy of activation
μs	microsecond
τ	lifetime

ACKNOWLEDGEMENTS

First and foremost, I wish to thank my supervisor Dr. Frances Cozens for welcoming me into her research group and in doing so, introducing me to the world of organic reactive intermediates. Her invaluable guidance in the last four years has been instrumental to both my research and teaching accomplishments. I also wish to express my gratitude for her friendship, understanding and encouragement that have helped me cope during the more dispirited moments of this Ph.D. I am equally indebted to Dr. Norman Schepp whom I sincerely thank for all his sound advice and for always keeping his door open.

I am also grateful to the members of my committee, Drs. Donald Arnold, James Pincock, and Jan Kwak, for valuable feedback during my preliminary exam and advice throughout this Ph.D. A special thank you also goes out to past and present members of the Cozens, Schepp and Pincock groups on who I could always count on for a sympathetic ear and some form of humorous distraction when experiments went pear shaped. Thanks for the support, the fun times, and friendship. Best of luck & take care.

On a more personal note, I wish to thank my terrific parents for not disowning me during my bouts of insanity and 'subtle' moodiness, and Frédérick for making me laugh when laughter seemed beyond the realms of possibility. Last but certainly not least, I thank Chris for writing that fateful letter way back in 1993 and for being a precious part of my life ever since. Thank you for being there, through thick and thin, as I've ploughed my way through the world of chemistry. For inspiring me, for your unwavering patience, encouragement and unconditional love, a million gazillion times thank you...

Royaumes-Unis, un *pois*. ☺

CHAPTER 1

β-SUBSTITUTED RADICALS AND THEIR IONIZATION IN SOLUTION

1.1 Introduction

Following the detection of gaseous free radicals in the early 1930s, close to a decade elapsed before the scientific community recognized that such reactive intermediates could also form in the course of a liquid phase reaction at room temperature. Since that time, seventy years of extensive research has led to the unearthing of a plethora of radicals existing in solution and exposed a vast repertoire of reactions available to them in this medium. Today, investigations into the structure, generation and reactions of free radicals in the liquid phase persist and the interest remains widespread. This can in part be attributed to the diverse relevance of radical chemistry to an increasing number of man-made phenomena as well as to the organic chemists who seek to harness, with increasing efficiency, the unique properties and high reactivity of radicals for synthetic strategies.

Arguably perhaps, the primary driving force behind much of the research into organic radical chemistry stems from the increasing pertinence of this subject matter to natural phenomena. For example, the existence of biological radicals has long been recognized but classically referred mainly to the flavin semiquinones and the

semiquinone forms of coenzyme Q, important molecules in natural redox processes. Modern research however has challenged these traditional views and is unraveling the far greater and somewhat unexpected role that radicals play in biological events.[1-5] In particular, β-substituted radicals **1**, transient species that have a potential leaving group attached to the carbon adjacent (β) to the radical centre, have been implicated in a myriad of biochemical transformations, *vide infra.*

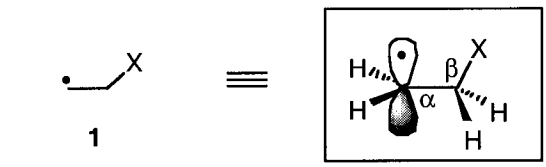

More specifically, the ionization of these radicals through heterolytic loss of the β-group to form an olefin radical cation **2**, referred to as the *β-heterolysis reaction*, Scheme 1-1, has been linked to a number of enzyme-mediated processes. Pertinent among these are the reactions catalyzed by diol dehydrase,[2,4,6-11] ethanolamine deaminase[3,12] and the ribonucleotide reductases.[2,4,13-17]

Scheme 1-1

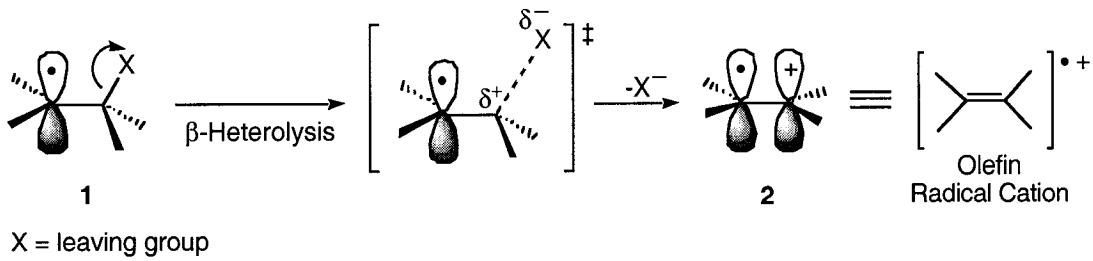

The first of these enzymes, diol dehydrase, is responsible for the conversion of glycols into aldehydes, eq. 1.1.

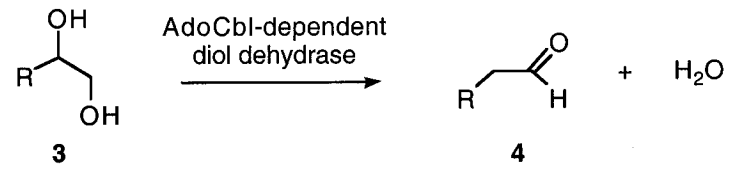

(1.1)

As indicated, diol dehydrase requires the assistance of vitamin B_{12} metallocofactor adenosylcobalamin (AdoCbl) to be biologically active. In the early stages of the mechanism, the substrate radical has been shown to be generated *via* hydrogen atom abstraction that is initiated by AdoCbl.[7,18] The subsequent steps leading to the aldehyde product **4** have been the focus of many enzyme studies; however chemical modeling has provided the greatest insight into the mechanistic details of this transformation. A reaction now known to mimic the rearrangement stages carried out by diol dehydrase is the hydroxyl radical initiated acid-catalyzed decomposition of ethylene glycol **5** to acetaldehyde **9**, Scheme 1-2.

Scheme 1-2

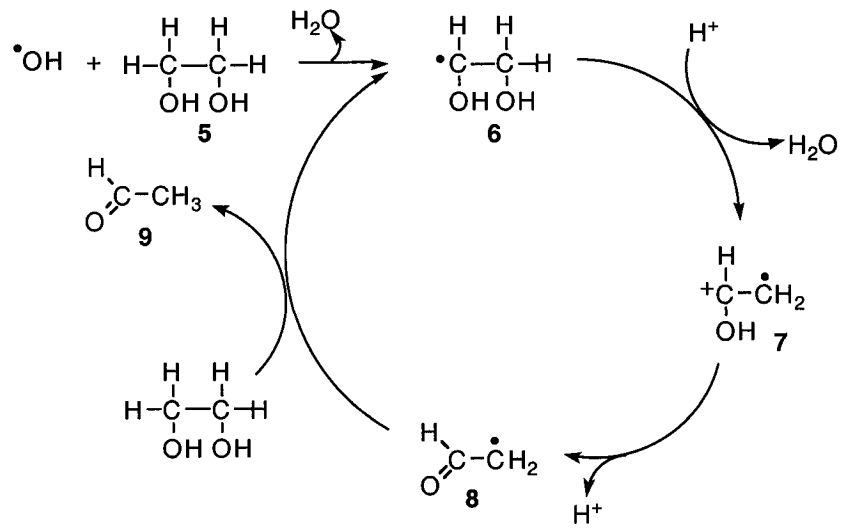

In the presence of hydroxyl radicals, ethylene glycol undergoes hydrogen abstraction to produce α,β-dihydroxyethyl radical **6**. Following protonation at the β-hydroxy group, heterolytic loss of water ensues to generate radical cation **7** that rapidly deprotonates to yield the acetaldehyde radical **8**. In the final step, radical **8** abstracts a hydrogen from another substrate molecule and the cycle is repeated. The reaction catalyzed by ethanolamine deaminase, also AdoCbl-dependent, is thought to proceed *via* a similar pathway, eq. 1.2.[19,20]

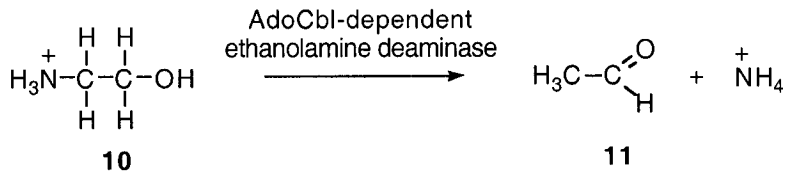

(1.2)

Sugar-based radicals involved in biochemical processes are also believed to be susceptible to the β-heterolysis reaction shown in Scheme 1-1. For instance, the conversion of ribonucleotides **12** to 2'-deoxyribonucleotides **13** is a critical step in DNA (2'-deoxyribonucleic acid) biosynthesis, eq. 1.3.

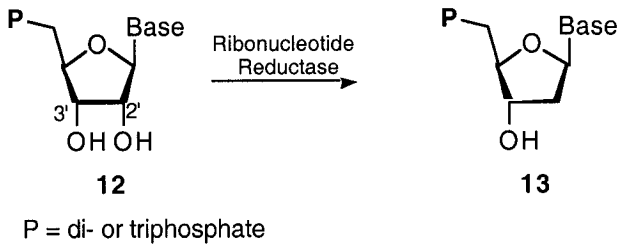

(1.3)

This important transformation, catalyzed by ribonucleotide reductases, is initiated by the generation of a C-3' nucleotide radical **14** through hydrogen abstraction, and leads to subsequent acid-catalyzed loss of the 2'-hydroxy group, Scheme 1-3. In the course of this reaction, radical cation **16** has been suggested as an intermediate that is subsequently reduced to give the deoxygenated nucleotide **13**. However, this proposed mechanism remains under scrutiny.[2,16,17,21]

Scheme 1-3

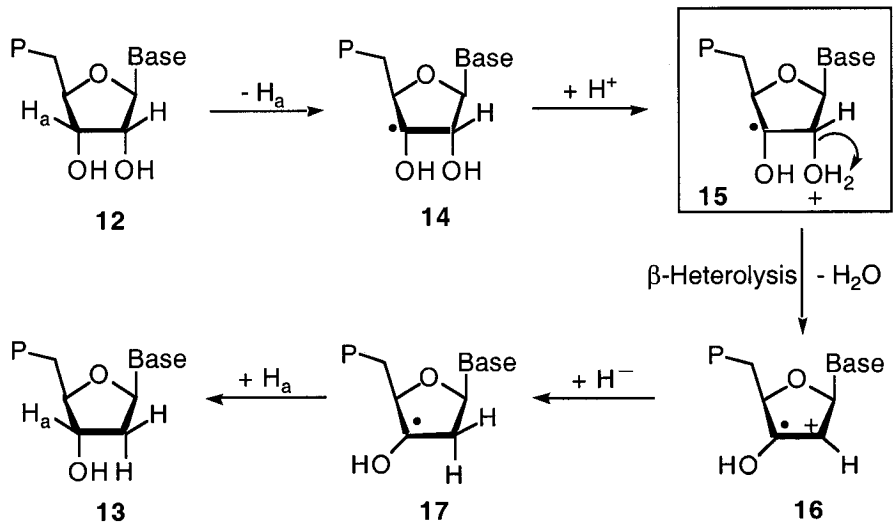

Despite its association to healthy biological events, the β-heterolysis reaction is more often noted for its involvement in the critical stages of radiation damage to DNA.[22] Years of research into the effects of ionizing radiation on aqueous solutions of nucleic acids and model carbohydrate systems provide firm evidence that the β-heterolysis reaction is implicated in the single- and double-stranded cleavage of DNA and RNA.[23-30] As can be expected, the potential consequences of such lesions are alarming as they include cell death, carcinogenesis, and mutagenesis.[23,31,32] Not surprisingly therefore, delineating the pathways of radiation-induced DNA cleavage has been the target of numerous investigations, driven by fundamental mechanistic interest as well as for possible advancements in tumor drug design such as bleomycins.[33,34]

When radicals are generated radiolytically or chemically within the nucleus of a cell, these powerful and indiscriminate oxidants are dangerously positioned in close proximity to nucleic acids. In some instances, damage ensues when they undertake hydrogen atom abstraction with double-stranded DNA. When hydrogen abstraction occurs at the C4'-position of the pentose sugar ring, **18**, the resulting 4'-deoxyribosyl radical has a propensity towards phosphate elimination at the β-position (C3') to the

radical centre, **19**, the culmination of which is scission of the nucleic acid strand, eq. 1.4.

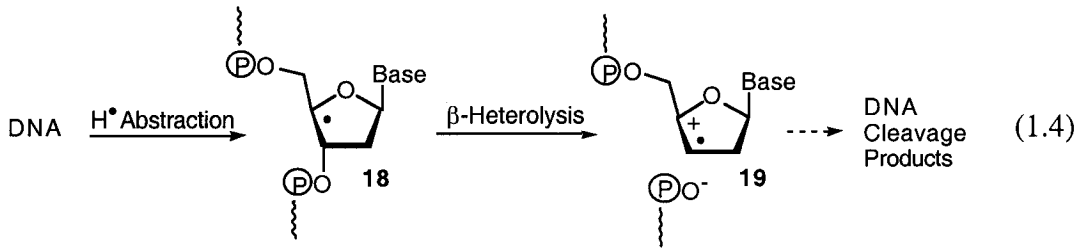

(1.4)

In light of its significance to the etiology and treatment of various diseases, the fragility of the sugar-phosphate backbone to such radiation-induced fragmentation has provided tremendous impetus for further study into the mechanistic details of the β-heterolysis reaction. A description of such studies is given in Section 1.3 below. As will be seen, there are some similarities between the factors that control β-heterolysis reactions of radicals and the key ionization step in S_N1 reactions. Since a considerably greater amount of fundamental information is available for S_N1 reactions, a brief summary of important factors that influence those kinds of reactions is given first in Section 1.2.

1.2 Nucleophilic Substitution Reactions

The reactivity of a solvated molecule toward nucleophilic substitution is dependent upon key factors such as substrate structure, leaving ability of the nucleofuge, solvent polarity, and nucleophilicity of the attacking species. In some instances, the presence of base or acid may play an important role in facilitating the heterolytic cleavage of the leaving group, in which case the reaction becomes catalyzed. Despite these variables, closed-shell aliphatic nucleophilic substitutions fall somewhere between two limiting mechanisms referred to as S_N1 and S_N2, first elucidated in 1933 by Hughes, Ingold and Patel.[35] We first begin with a brief review of these basic mechanistic principles associated with each limiting reaction pathway.

1.2.1 The Limiting S_N1 Mechanism

An S_N1 reaction (substitution, nucleophilic, unimolecular) is characterized by two successive steps, the first of which is rate-determining and involves the 'spontaneous' dissociation of the carbon-leaving group bond to generate a carbocation intermediate plus an anion, eq. 1.5. The substitution product is subsequently generated in a relatively rapid second step during which the nucleophile, with equal probability of approaching above or below the plane of the carbon atoms, attacks the carbocation to generate the final product, eq. 1.6. Consequently, the S_N1 mechanism is associated with scrambling of stereochemistry when the original site of substitution in the substrate molecule is chiral. The rate-determining step (RDS) of this mechanism involves only one molecule, the substrate, and is independent of the nucleophile concentration. Thus, an S_N1 reaction follows first-order kinetics and the rate law can be expressed as $\frac{d[P]}{dt} = k[CR_1R_2R_3X]$, where the rate of product formation is dependent on the first-order rate constant k for the dissociation step, eq. 1.5, and the concentration of the substrate only.

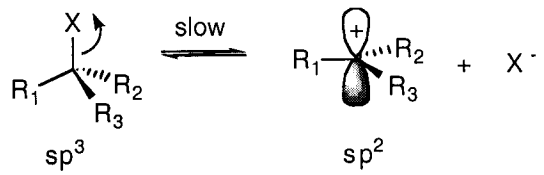

(1.5)

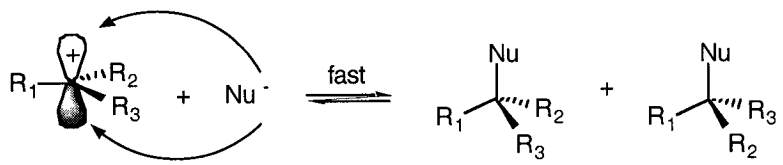

(1.6)

As the rate-determining step of the S_N1 mechanism involves the formation of a cationic centre, the structural features of the substrate play an important role. For instance, the degree of substitution of the substrate will largely dictate whether this unimolecular substitution mechanism will dominate over the S_N2 counterpart that is

reviewed below. The stability of a simple alkyl substituted carbocation is greatest when it is tertiary, and decreases as the number of alkyl linkages to the cationic centre decrease to form a secondary and primary carbocation. The lifetime of the cation will also be influenced by the presence of electron withdrawing groups (EWG) such as -F and $-CF_3$ that increase the energy the carbocation, while electron donating groups (EDG) such as alkoxy substituents stabilize the positive charge through resonance. An aryl group is of course another example where resonance delocalization of the positive charge favours the formation of (benzylic) carbocations via an S_N1 mechanism.

A reaction often used to exemplify the S_N1 mechanism is that of *tert*-butyl chloride in water. Figure 1-1 approximates the reaction's energy diagram and includes the configurations of the key transition states. The rate-determining step is represented by the highest activation barrier E_a and leads to the first transition state **a** in which the C—Cl bond has partially broken. Upon complete dissociation of the leaving group, a carbocation intermediate **b** is generated and is shown to exist in an energy well. A second but smaller activation barrier must subsequently be overcome by the system as nucleophilic addition takes place. The transition state for this step, **c**, is depicted with the bond between the water molecule and the substrate partially formed. The oxonium ion that is initially produced is rapidly deprotonated to give the final alcohol product.

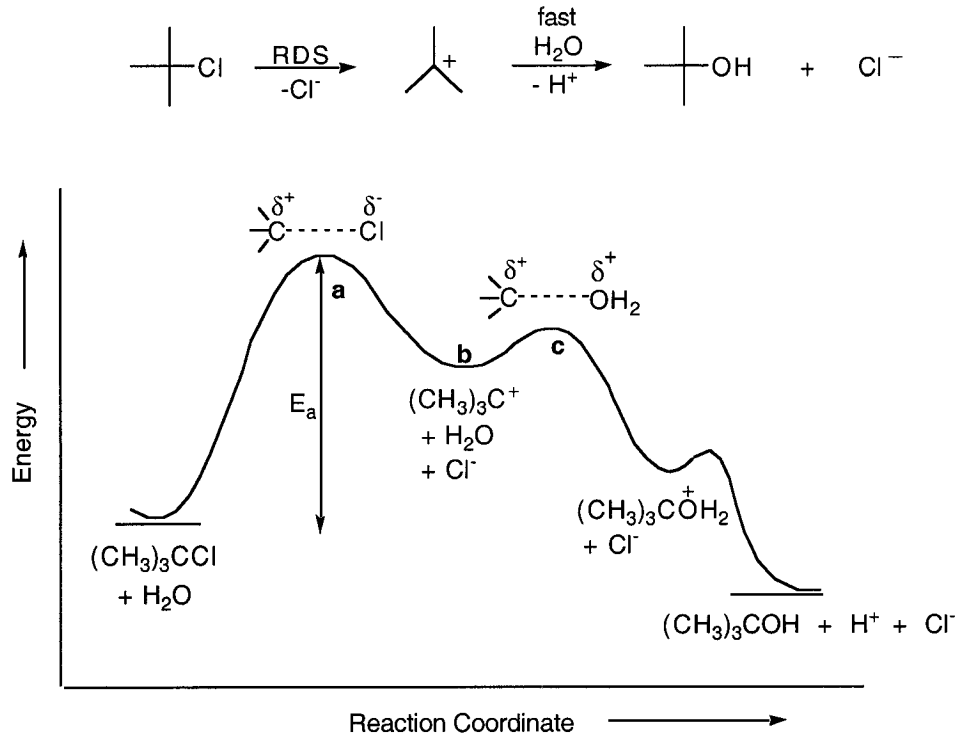

Figure 1-1. Illustrative representation of the energy profile associated with the reaction of *tert*-butyl chloride with water that proceeds *via* an S_N1 mechanism. The diagram shows two key transition states, **a** and **c**, separated by one intermediate structure, the carbocation that lies in an energy well **b**. The rate-determining step involves the energy climb from the reactants to transition state **a** which has the greatest activation energy, E_a.

S_N1-type processes are heavily dependent on the ionizing strength of the solvent due to the polar nature of the reaction. In this mechanism, the primary kinetic influence of the medium lies in its ability to solvate the starting and transition state structures, and the extent of these interactions will depend in part on the relative charge densities in each of these states. A substitution reaction in which the reactant is uncharged will be favoured in polar solvents due to efficient solvation and hence stabilization of the incipient charge in the transition structure. In such a case, an ionizing medium is expected to decrease the activation energy and in doing so, increase the rate of substitution, Figure 1-2 (A). Conversely however, if the starting material possesses a charge density that is greater than in the transition state where dispersion has already

started to occur, increasing solvent polarity will likely raise the activation barrier by providing more stabilization to the reactant relative to the transition structure. This last scenario is depicted in Figure 1-2 (B).

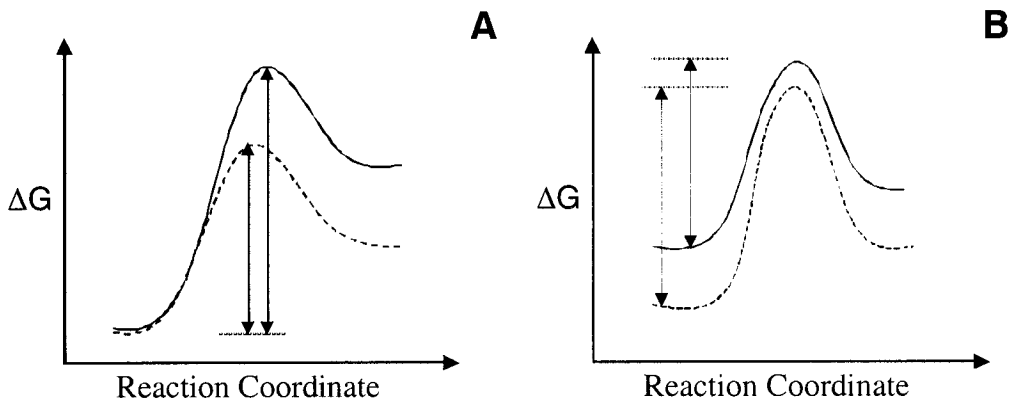

Figure 1-2. Energy vs. reaction coordinate diagrams for reactions taking place in a (——) less polar solvent, and (- - - -) polar solvent. (A) Reaction in which the transition state possesses more charge density than the reactant(s) benefits from a polar medium by lowering the activation barrier. (B) Reaction in which the reactant(s) is more polar than the transition state, leading to a higher activation barrier in the polar solvent.

Among the most ionizing solvents are water, 1,1,1,3,3,3-hexafluoro*iso*propanol (HFIP) and 2,2,2-trifluoroethanol (TFE). These last two solvents are particularly unique because unlike water, they are relatively non-nucleophilic. HFIP and TFE are therefore especially well suited for mechanistic studies in which carbocations and other positively charged intermediates are generated as their non-nucleophilic nature expands the lifetimes of these transient species.

The ability of the leaving group to leave (nucleofugality) also plays a part in the kinetics of an S_N1 mechanism. For neutral substrates, the leaving group develops a partial negative charge in the transition state and a good nucleofuge is one capable of efficiently dispersing the charge density. A leaving group's propensity toward ionization can be assessed *via* the pK_a value of its conjugate acid, with nucleofugality increasing

with decreasing pK_a value. Table 1-1 lists some common leaving groups and their relative rate of solvolysis for 1-phenylethyl esters and halides in 80% aqueous ethanol at 75 °C.[36] Among the halides, leaving ability increases in the order of $F^- < Cl^- < Br^- < I^-$ as charge dispersal improves with increasing atomic radii. However, superior nucleofuges include mesylate, tosylate and triflate due to extensive charge delocalization. Substituents that are strong bases such as –OH, -OR and $–NH_2$ are poor leaving groups but can be made more reactive by protonation to give $-OH_2^+$, $-ORH^+$, and $-NH_3^+$.

Table 1-1. Relative rates of solvolysis of 1-phenethyl esters and halides in 80% aqueous ethanol at 75 °C.[37]

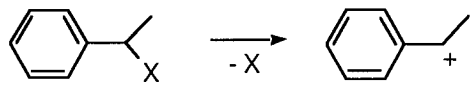

X	k_{het}/s^{-1}	k_{rel}
$H_3C-C(=O)-O^-$	3.1×10^{-9}	1.4×10^{-6}
F^-	2×10^{-8}	9.0×10^{-6}
Cl^-	2.2×10^{-3}	1
$F_3C-C(=O)-O^-$	5.5×10^{-3}	2.5
Br^-	3.1×10^{-2}	14
I^-	2×10^{-1}	91

Mesylate, Ms	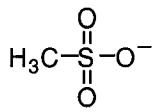	6.7×10	3.0×10^4
Tosylate, Ts	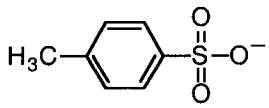	8.1×10	3.7×10^4
Triflate, Tf	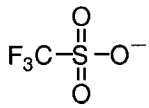	3.0×10^5	1.4×10^8

1.2.2 The Limiting S_N2 Mechanism

One of the key features of the limiting S_N2 (substitution, nucleophilic, bimolecular) mechanism is that the reaction takes place in a single step. As the nucleophile approaches, it donates an electron pair and bonds to the substrate while the leaving group simultaneously dissociates, as illustrated in eq. 1.7. Ideally, nucleophilic attack occurs from a position that is 180° away from the departing leaving group. Consequently, a limiting S_N2 reaction always proceeds *via* inversion of configuration.[38-40]

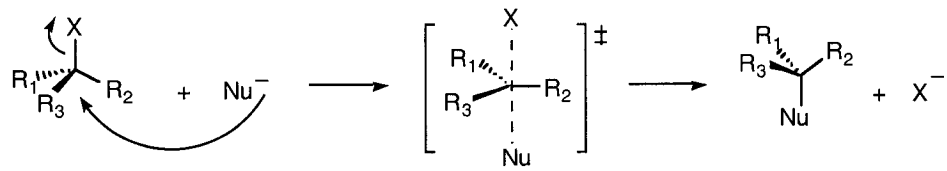

(1.7)

Since an S_N2 substitution unfolds in a single step, the reaction rate is dependent on the concentration of both the substrate and the attacking nucleophile, giving rise to second-order kinetics. The rate can therefore be expressed as $\frac{d[P]}{dt} = k[CR_1R_2R_3X][Nuc]$, where k is the second-order rate constant. The reaction of chloroethane with sodium hydroxide is known to occur *via* an S_N2 mechanism and its

energy profile is schematically represented in Figure 1-3. As is characteristic of this mechanism, the Scheme reveals a single activation barrier and the absence of any intermediate species. The configuration of the transition state **d** reflects the concertedness of the process, consisting of a 'penta-coordinated' carbon partially bonded to the leaving group (chloride) and the attacking nucleophile (hydroxide).

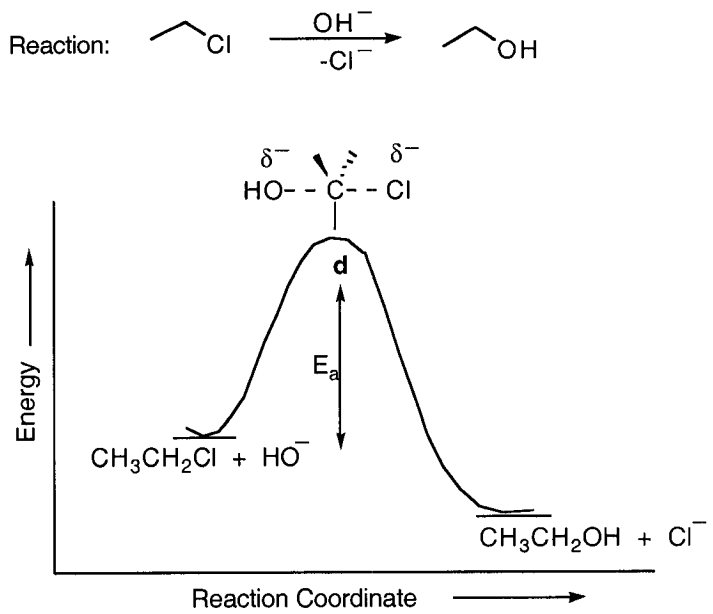

Figure 1-3. The S_N2 energy profile for the reaction of chloroethane with the hydroxide ions, consisting of a single 'penta-coordinated' transition state **d** in which the bond to the leaving group is partially broken and that to the nucleophile is partially formed.

1.2.3 Substitution Reactivity: From Closed to Open Shell Substrates

Consider the generic structure **20** presented in Scheme 1-4 where X designates a leaving group such as chloride or bromide. From a purely structural perspective, the lack of substitution at the reaction centre leads to the prediction that this molecule will undergo loss of X *via* an S_N2 rather than S_N1 mechanism. The cation generated during an S_N1 mechanism of **20** would be primary and highly unstable due to localization of the

positive charge on the carbon (hyperconjugation is possible but provides little stabilization). Contrarily, a primary carbon presents little hindrance for nucleophilic attack resulting in the concurrent dissociation of the carbon-leaving group bond, *i.e.* an S_N2 mechanism.

Scheme 1-4

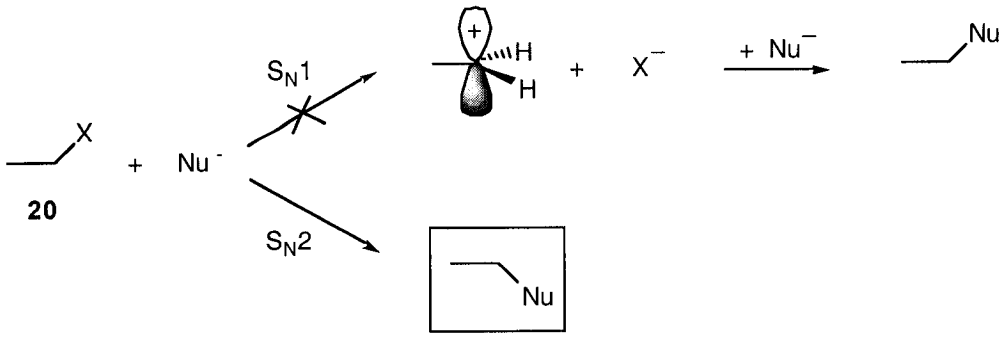

The situation becomes very different however when considering the allylic counterpart of this molecule, substrate **21** presented Scheme 1-5. While nucleophilic substitution of **21** *via* an S_N1 mechanism also yields a primary carbocation, the reaction is expected to proceed more readily due to additional resonance stabilization provided to the cation by the double bond. This is a result of the symmetry allowed interaction of the cationic centre with the p orbitals of the π-bond delocalizing the positive charge over three atoms instead of one. The presence of a double bond adjacent to the substitution site therefore modifies the energetics of this S_N1 reaction by decreasing the energy of the carbocation intermediate and lowering the activation barrier for the heterolysis reaction.

With substrate **21**, bimolecular nucleophilic substitution can occur in one of two ways as a result of the adjacent π-bond now present. A classic S_N2 reaction can take place whereby the nucleophile directly attacks the carbon bearing the leaving group X to produce the substitution product. However, the nucleophile also has the option of

Scheme 1-5

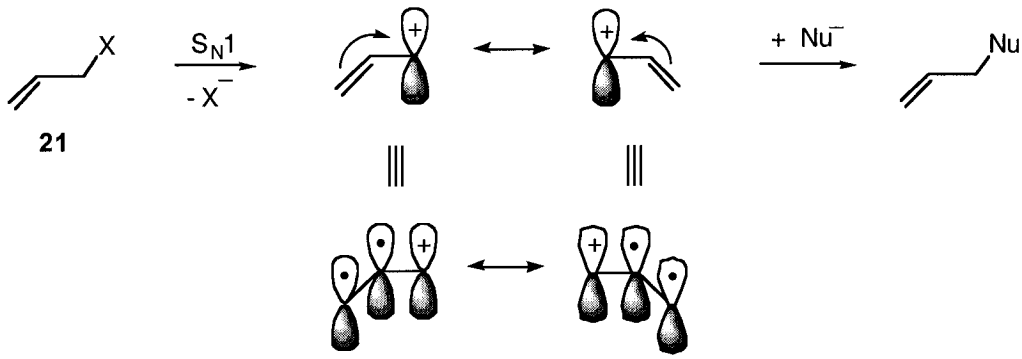

attacking the terminal carbon of the double bond, a process designated by the abbreviation S_N2' and which is illustrated in Scheme 1-6. In this reaction, all of the characteristic features of the S_N2 mechanism are conserved, hence the preservation of the name.

Scheme 1-6

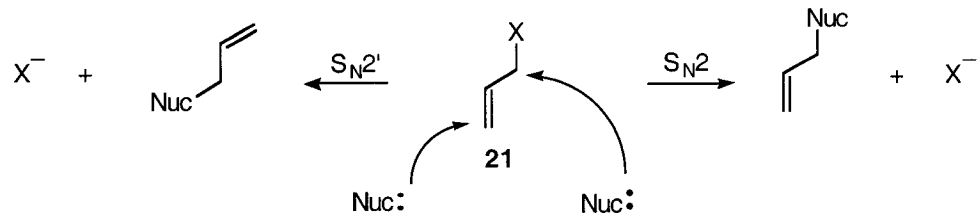

Lastly consider substrate **1**, previously introduced, in which the double bond has now been replaced by a $^{\bullet}CH_2$ group. Such molecules possessing a potential leaving group adjacent to a singly occupied molecular orbital (SOMO) are generally referred to as β-substituted radicals. Like substrates **20** and **21**, radical **1** is a ground-state molecule but an important point of difference is its increased energy level relative to the closed shell analogue due to the radical centre. In other words, **1** possesses all of the inherent reactivity often associated with unpaired spin molecules, categorizing it as a highly reactive intermediate.

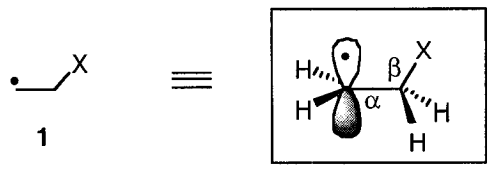

1

Do β-substituted radicals exhibit S_N1 and S_N2-type reactivity and if so, under what conditions? How do the dynamics of an open shell substrate such as **1** vary from analogous closed shell systems like **20** and **21**, and what is the influence of the radical centre? These are some of the questions that physical organic chemists have raised and in the last thirty years or so, many have aimed their research efforts at uncovering some of the answers. The following section provides a brief overview of the current understanding of the reactivity of β-substituted radicals, species that are the heart of the work described later in this thesis. Special emphasis will be given toward S_N1-type reactivity of these radicals as it is of direct relevance to the β-heterolysis reaction investigated.

1.3 Reactivity of β-Substituted Radicals

1.3.1 $S_{RN}2$ and $S_{RN}2'$ Mechanisms

For β-substituted radicals to exhibit S_N2-type reactivity, the process must kinetically compete against typical homolytic processes such as radical-radical recombination, disproportionation reactions, hydrogen atom abstraction and even homolysis. For example, in nitrogen saturated acetonitrile (AcN), Scaiano *et al.* have observed that following irradiation of vicinal bromides, the β-substituted radicals undergo homolytic cleavage of the carbon–bromine bond to yield a neutral olefin product, eq. 1.8 (X = Br).[41] In relatively nonpolar conditions, the chemistry of these β-substituted radicals is clearly dominated by the radical functionality.

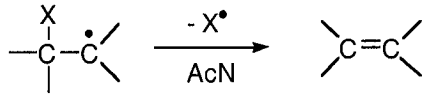

(1.8)

In 1994, theoretical calculations carried out by Zipse predicted that bimolecular nucleophilic substitutions are energetically feasible for β-substituted radicals. In an analogous fashion to the closed shell systems involving allylic substrates, Scheme 1-6, Zipse has suggested that nucleophilic attack on β-substituted radicals can occur *via* two different mechanisms. The nucleophile can attack the carbon bearing the leaving group or, alternatively, it can use its electron pair to bond with the adjacent radical centre with concomitant displacement of the leaving group. These two pathways are depicted in Scheme 1-7 and are labelled as $S_{RN}2$ and $S_{RN}2'$ according to Zipse's terminology.[42,43]

Scheme 1-7

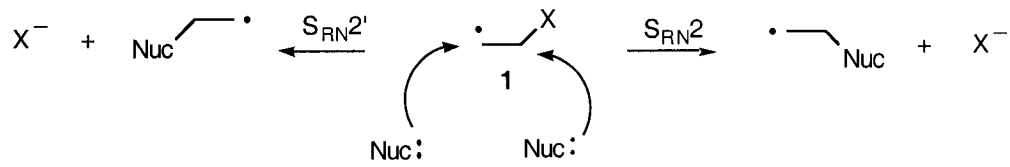

Moreover, theoretical calculations on the reaction of chloride with methyl chloride, allyl chloride and the β-chloroethyl radical revealed that the energy required for S_N2-type displacements is considerably lower in open shell systems compared to closed shell analogues, Scheme 1-8.[43,44] Zipse attributed these findings to the "mixed homolytic/heterolytic character of the dissociation process in open shell systems."

Scheme 1-8

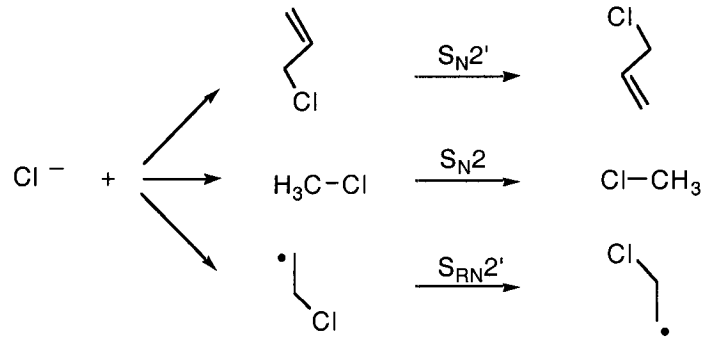

A survey of the literature uncovered very little conclusive evidence that β-substituted radicals exhibit S_N2-type reactivity. However, experimental support was provided in 1997 by Choi and co-workers, who studied β-(phosphatoxy)alkyl radical **23**, Scheme 1-9, a subset of β-ester radicals whose general structure is represented by **22**.[45]

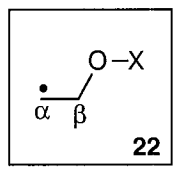

X = -C(O)R, $-SO_2R$, $-P(O)(OR)_2$

It was concluded that radical **23** exhibits $S_{RN}2'$ reactivity when generated in tetrahydrofuran by laser flash photolysis (LFP) in the presence of 1-octanol, Scheme 1-9. The alternative S_N1-type mechanism in which the unimolecular, rate-determining loss of phosphate is followed by nucleophilic attack on the radical cation **25** was ruled out on the basis of the second-order kinetics obtained. A bimolecular rate constant of 2×10^6 M^{-1} s^{-1} for the reaction of **23** with 1-octanol was determined for the formation of the benzylic radical product **24**. Moreover, styrene-type radical cations like **25** have well-characterized spectra with strong absorption bands near 350 and 600 nm,[46] neither of which were observed by the authors.

Scheme 1-9

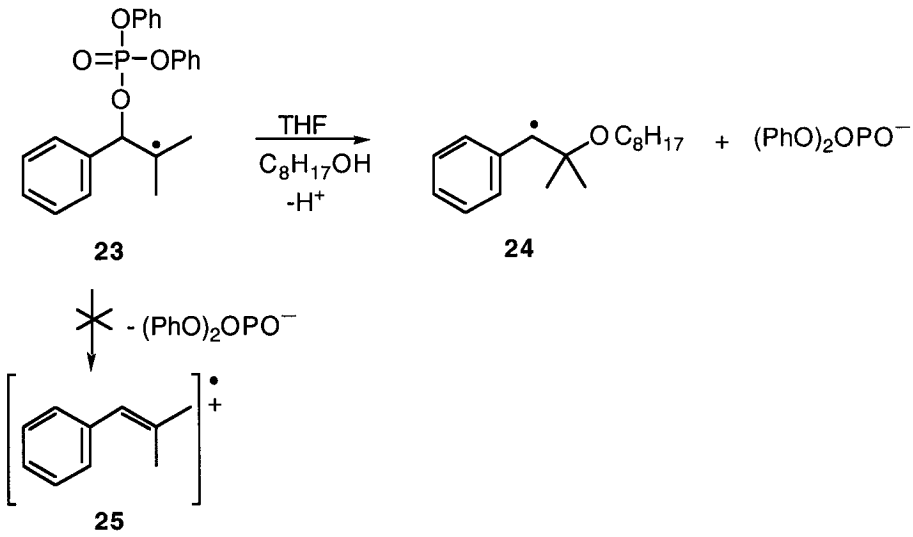

1.3.2 Unimolecular Substitution and the β-Heterolysis Reaction

The literature is comparatively more abundant with concrete examples of β-substituted radicals that undergo heterolytic loss of X^- to form an olefin-type radical cation as previously introduced in Scheme 1-1. The unimolecular ionization of the β-leaving group is also referred to as the *β-heterolysis reaction* and does not specify the nature of the radical cation chemistry that follows. However, in the instance where the β-heterolysis reaction is rate-determining and is rapidly ensued by nucleophilic attack on the radical cation, Scheme 1-10, the process becomes the unimolecular equivalent of the $S_{RN}2$ mechanism presented earlier, Scheme 1-7.

As a logical progression to his use of the term $S_{RN}2$ to describe a bimolecular nucleophilic substitution reaction of β-substituted radicals, Zipse refers to the unimolecular counterpart as $S_{RN}1$.[43,47] However, the use of this term is misleading since the abbreviation $S_{RN}1$ has previously been designated to the radical chain mechanism presented in Scheme 1-11 which bears no similarity.[48-51] In the 'true' $S_{RN}1$

Scheme 1-10

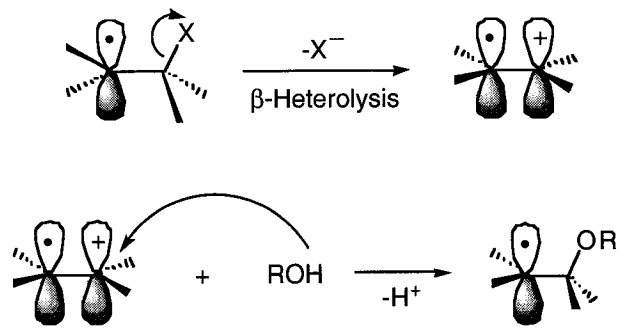

mechanism, an electron transfer to the substrate occurs in the first step that acts as a catalyst for the subsequent heterolytic loss of the halide anion to yield a neutral radical. Nucleophilic attack on the radical rapidly ensues to form another radical anion that subsequently gives up an electron to another reactant. In this last step, the substituted product is generated and the chain reaction is propagated. Throughout this introduction, the unimolecular substitution reaction depicted in Scheme 1-10 will be referred to $S_{RN}1^*$, so as to distinguish it from the $S_{RN}1$ mechanism outlined in Scheme 1-11.

Scheme 1-11

$$R{-}X + e^- \longrightarrow [R{-}X]^{\bullet -}$$

$$[R{-}X]^{\bullet -} \longrightarrow R^\bullet + X^-$$

$$R^\bullet + Nuc^- \longrightarrow [R{-}Nuc]^{\bullet -}$$

$$[R{-}Nuc]^{\bullet -} + R{-}X \longrightarrow R{-}Nuc + [R{-}X]^{\bullet -}$$

The objective of the work presented in the current thesis was to investigate the β-heterolysis reaction (Scheme 1-1), that is also the first step of an $S_{RN}1^*$ mechanism as defined above, Scheme 1-10. The rest of this introduction will therefore focus on a selection of published work that has lead to the current understanding of the ionic fragmentation of β-substituted radicals in solution.

1.3.2.1 Acid-Catalyzed Heterolysis of Simple β-Hydroxyalkyl Radicals

The earliest evidence in support of the β-heterolysis reaction stems from investigations into the reactivity of simple alcohols in aqueous medium following hydrogen atom abstraction by free radicals.[52-56] Early interest in these substrates can in part be attributed to their suitability as mimetic compounds for more complicated biological macromolecules such as carbohydrates and nucleic acids, both of which have been shown to be vulnerable toward radiation-induced free radical damage.[23,57,58]

A seminal reaction that received particular attention back in the 1960s is the oxidation of ethane-1,2-diol by hydroxyl radicals in acidic aqueous solutions, eq. 1.9. Independently, Livingston and Buley studied this reaction at low pH and both concluded, with evidence from electron spin resonance (ESR) measurements, that formylmethyl radical **27** was being produced.[59,60] This important finding, later supported by further product[57,61] and pulse-radiolysis studies,[56] revealed that the initially formed α,β-dihydroxyethyl radical **26** undergoes a proton-catalyzed dehydration to give the carbonyl-conjugated radical **27**.

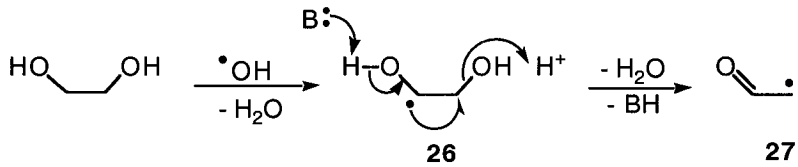

(1.9)

As shown in eq. 1.9, a concerted mechanism was originally postulated but subsequently challenged. On the basis of numerous follow-up studies, it was suggested that radical **27** is in fact formed *via* the intermediacy of radical cation **28**, that is *via* heterolytic cleavage of the protonated radical, eq. 1.10.[52,56]

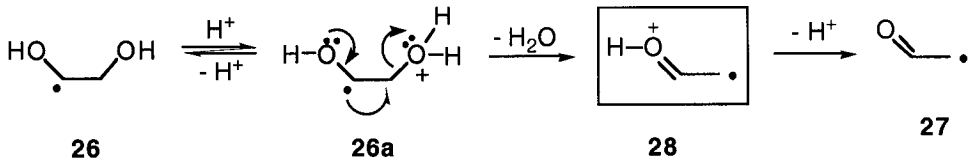

(1.10)

Further evidence of the acid-catalyzed β-heterolysis mechanism came from the work of Gilbert *et al.* who carried out combined pulse radiolysis and ESR spectroscopy experiments on 2-chloroethanol in acidic aqueous medium.[55] Following the formation of radical **29** *via* hydrogen abstraction from the substrate molecule, radical substitution products **32** and **33** were identified, in addition to the anticipated conjugated radical **31**, Scheme 1-12. The detection of radicals **32** and **33** was viewed by the authors as strong support for heterolytic loss of chloride leading to the radical cation intermediate **30**. Radicals **32** and **33** were concluded to be products of an $S_{RN}1^*$ mechanism, formed by subsequent nucleophilic attack by water on **30**, followed by deprotonation.

Scheme 1-12

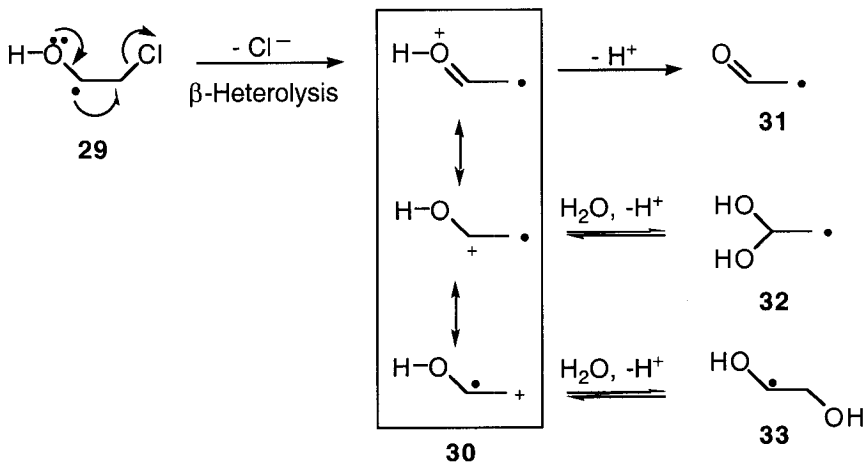

The availability of kinetic data for these types of reactions remains limited but rate constants that have been measured support the β-heterolysis mechanism based on the observed electronic influence of substituents.[53,54,56] In 1986, Steenken employed the

direct pulse-radiolysis method to determine rate constants for the acid-catalyzed dehydration of a variety of β-hydroxyl radicals in water (note, however, that they do not specify which radical isomer undergoes β-heterolysis). The bimolecular rate constant k_{cat} for the acid-catalyzed dehydration of radicals generated from cyclohexane-1,2-diol **34**, 1.2×10^9 M^{-1} s^{-1}, and butane-2,3-diol **35**, 9.8×10^8 M^{-1} s^{-1} are significantly higher than for 2-methoxyethanol **36**, for which k_{cat} was determined to be 2.2×10^6 M^{-1} s^{-1}.[54]

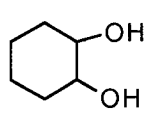

34

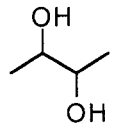

35

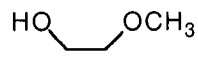

36

These large substituent effects are consistent with a reaction in which a highly polarized transition state is produced. As observed, rate constants for the β-heterolysis reaction are greater for compounds bearing electron donating alkyl groups, *viz.* **34** and **35**. These results strongly support a positively charged transition state leading to a radical cation intermediate, both of which can be stabilized by the inductive effect of the alkyl linkages. Conversely, k_{cat} is found to be smaller for substrates such as **36** that have no additional alkyl groups. The authors emphasized that these results provide strong evidence that a major factor governing the acid-catalyzed heterolysis of water is the thermodynamic stability of the radical cation produced.

It has been suggested that the orientation of the β-hydroxy group relative to the singly occupied p-orbital plays an important role in the β-heterolysis reaction. It is known for instance that α,β-dioxygen-substituted radicals have a propensity to adopt an orientation in which the β-oxy group is eclipsed with the SOMO.[62,63] This eclipsed geometry is demonstrated with the α,β-dihydroxyethyl radical **37** and is thought to occur due to the combination of the resonance electron donating effect of the α-oxy

group and the inductive electron withdrawing effect of the β-oxy substituent. These electronic interactions lead to resonance structures **38a-c** that result in a delocalization of the electron density on the reacting radical.

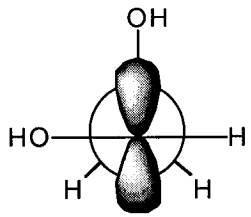

37

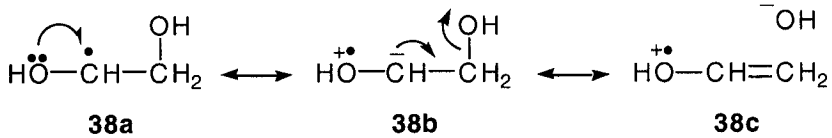

38a **38b** **38c**

The eclipsed conformation adopted by α,β-dioxygen substituted radicals such as **37** is highly favorable for heterolytic loss of β-H_2O. In this preferred geometry, the radical is already oriented for efficient overlap between the SOMO and the incipient cationic p-orbital in the transition state, Scheme 1-1. Moreover, in a manner proportional to the contribution of canonical structure **38c**, the radical will possess a resemblance to the transition state of the β-heterolysis reaction, resulting in a shift of the energy maximum to an earlier position along the reaction coordinate. Lastly, it is worth noting that α,β-dioxygen-substituted radicals possessing additional alkyl substituents may lead to an increase in the rate of β-heterolysis since steric interactions are likely to lock the structure into the favoured eclipsed conformation.

In 1978, experimental evidence for the postulated intermediary radical cation finally surfaced with the work of Behrens *et al.* who were the first to demonstrate that the heterolytic cleavage of β-chloride from the α,α-dialkoxy radical **39** leads directly to the 1,1-dimethoxyethylene radical cation **40**, as determined by ESR and conductivity measurements, eq. 1.11.[64] Interestingly, the direct detection of radical cation **40c** is a testament to its stability since it did not react with water over the observation period of a few milliseconds. This is certainly due to the additional stabilizing effect of the two

geminal α-methoxy groups. The conformation of this radical cation was later established to be as shown in structure **40d**.[65]

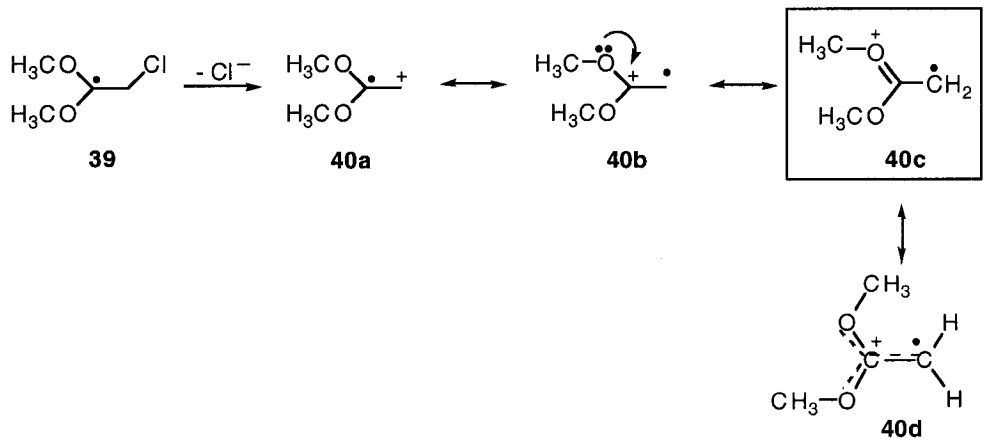

(1.11)

1.3.2.2 Acid-Catalyzed Heterolysis of Simple β-Ester Radicals

Gilbert and workers were also the first to suggest that acid-catalyzed β-heterolysis was also a viable pathway for β-(acyloxy)alkyl radicals whose generic structure is shown below, **41**.[55]

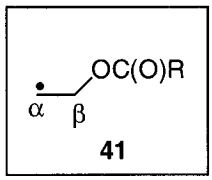

At pH 5.2, hydrogen abstraction of 2-methoxyethyl acetate led principally to β-substituted radical **42** but by increasing the acidity of the solution to pH 1, they found that the ESR spectrum attributed to radical **42** decreased in intensity in favor of the substitution product **44**, eq. 1.12. Without direct evidence, a radical cation has been invoked as the intermediate in this case *via* an $S_{RN}1^*$ mechanism: the acetate group cleaves heterolytically to yield a radical cation **43**, followed by the nucleophilic attack of water and deprotonation to form radical **44**. Interestingly, the addition of water was

found to occur regioselectively at the carbon bearing the methoxy group, presumably because of the greater positive charge density existing at this site.

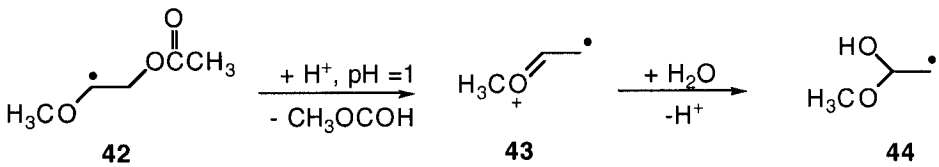

42 43 44 (1.12)

In an elaborate study using pulse radiolysis and time-resolved conductimetry, Schulte-Frohlinde *et al.* investigated the reactivity of a variety of β-(acetoxy)alkyl radicals, *viz.* **45** to **48**.

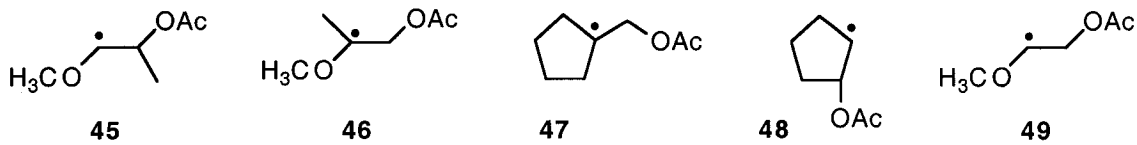

45 46 47 48 49

From ESR spectroscopic observations, they found that the hydrolysis reaction was too fast for these reactant radicals to be observed in acidic aqueous medium. In stark contrast however, radicals **45** to **48** were sufficiently long-lived in acetone for their spectra to be recorded.[66] This solvent effect was found to be consistent with a mechanism in which heterolytic loss of acetic acid yields an initial radical cation, followed by hydration, a process expected to accelerate with increasing solvent polarity. In a highly ionizing solvent like water, radical cation formation occurs so readily that depletion of the initially formed radicals prevented their detection. In a less polar solvent like acetone, heterolysis is decelerated due to poor solvation thereby extending the lifetime of the β-(acetoxy)alkyl radical. Substituent effects were also noted, as radicals **45** and **46** hydrolyzed ≥ 350 times faster than **49** due to the additional methyl group, irrespective of its position at either the α or β carbon to the radical.

Among β-ester radicals, β-phosphatoxy substituted radicals are of special interest due to their relevance as model compounds for the study of radiation-induced DNA damage, as well as DNA degradation by anti-cancer agents such as bleomycin and enediyne antibiotics.[27] Cleavage of alkylphosphate bonds have been observed following hydrogen abstraction from aqueous alkylphosphates,[67,68] polyhydroxyalkyl-phosphates,[69-71] carbohydrate phosphates,[72-75] nucleotides[76,77] and DNA.[64]

Some of the earliest chemical studies include work carried out by Steenken *et al.* who, in 1974, studied the reactions of glycerol phosphates with hydroxyl radicals in aqueous solutions, Scheme 1-13.[71] From ESR measurements, they concluded that β-phosphatoxy radicals such as **51**, generated by hydrogen abstraction of glycerol-1-phosphate, undergo rapid pH-independent phosphate ester cleavage to form radical **52** that was detected across the pH range investigated, pH 1-9. Once again however, elimination occurs at such a rate that by ESR techniques, **51** was not detected.

Scheme 1-13

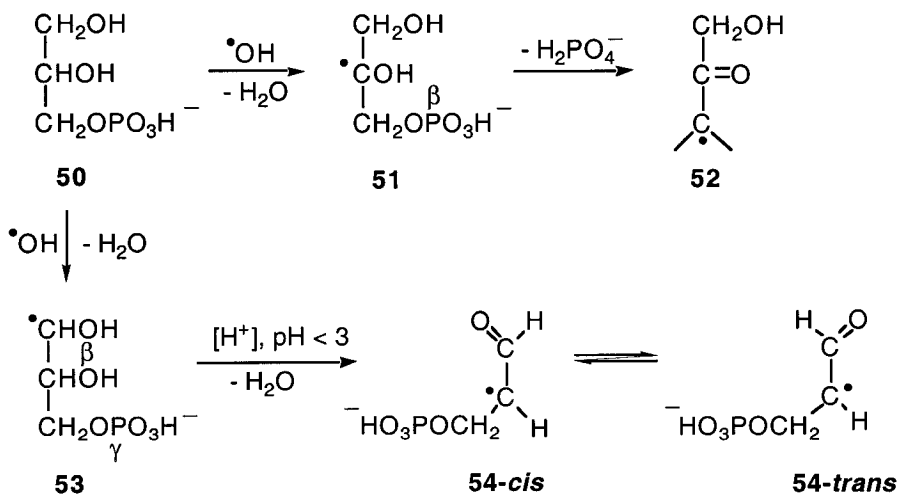

Interestingly, at a pH below 3, the spectra of geometrical isomers **54-*cis*** and **54-*trans*** were observed, leading the authors to suggest acid-catalyzed elimination of the

β-hydroxy group from γ-phosphatoxy radical **53**. These findings highlight not only the necessity for the nucleofuge to be at the β-position to the radical for β-heterolysis to occur, but also the increased catalytic requirement of OH^- relative to $H_2PO_4^-$ for ionization.

In their ground breaking experiments, Schulte-Frohlinde and Sonntag were the first to suggest the cleavage of the carbon phosphate bond as an important event in the radical induced strand breaks of DNA in aqueous solution.[78] A few years later, in 1978, Behrens and co-workers carried out a detailed study on β-phosphatoxy radicals which revealed that the rate of ionization was dependent on the degree of charge on the phosphate group and the extent of substitution of the initial β-substituted radical.[79] For example, under slightly acidic conditions, the rate constant for heterolysis of radical **55** was approximately 10^6 s^{-1}. In comparison, radicals **56** and **57**, with the singly and doubly charged phosphate groups, the rate constants dropped to ~10^3 s^{-1} and < 1 s^{-1} respectively, Scheme 1-14.

Scheme 1-14

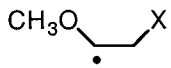

55 X = OPO_3H_2

56 X = OPO_3H^-

57 X = OPO_3^{2-}

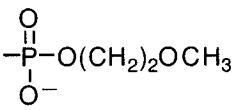

58 X = $O-P(=O)(O^-)-O(CH_2)_2OCH_3$

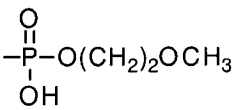

59 X = $O-P(=O)(OH)-O(CH_2)_2OCH_3$

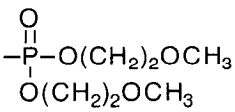

60 X = $O-P(=O)(O(CH_2)_2OCH_3)-O(CH_2)_2OCH_3$

The study also showed that diesters **58** and **59** undergo heterolysis with rate constants slightly faster than **56** and **55**, respectively, with triester **60** having the largest rate constant, $k_{het} > 4 \times 10^7\ s^{-1}$.

1.3.2.3 The Uncatalyzed β-Heterolysis Reaction

Although significant effort has been directed towards the study of acid-catalyzed ionization of β-substituted radicals, the dynamics of the analogous uncatalyzed β-heterolysis process remains comparatively unexplored. Sufficient evidence does exist, however, to suggest that this reaction is an important mechanistic pathway for β-substituted radicals.

One of the earliest experimental evidence for uncatalyzed β-heterolysis was published in 1982 by Koltzenburg *et al.* who investigated in aqueous solutions the reactivity of various aliphatic radicals substituted at the β-position with halogens, trialkylphosphates, alkylmethanesulfonates and dialkylsulfates.[80] Using their pulsed radiolysis/time resolved conductivity techniques, measurements revealed a rapid increase in conductivity subsequent to the generation of β-substituted radicals. This was assigned to the rapid formation of acid resulting from the decay of the β-substituted radicals by a solvolysis-type mechanism as concluded by the hydroxy products identified, Scheme 1-15.

Scheme 1-15

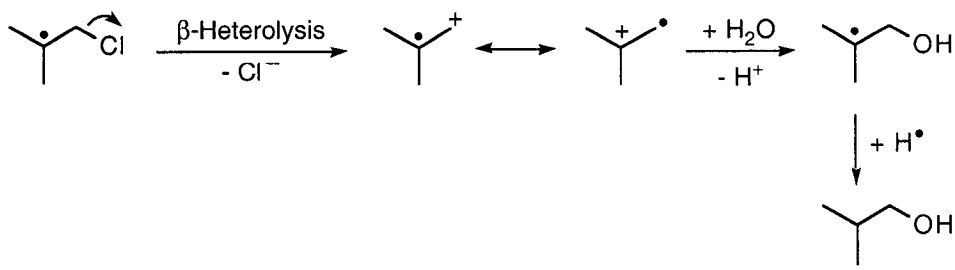

The calculated rate constants for acid formation showed a strong dependence on the degree of substitution at both the radical centre and the carbon attached to the leaving group. For example, the β-substituted radical generated from 1-chloropropane, **61**, produced an increase in conductivity with a rate constant < 10^2 s^{-1} but this value increased to 3.5×10^4 s^{-1} when the substrate contained an additional methyl group at the radical centre, **62**. Similarly, an extra methyl group at the carbon bearing the leaving group in radical **63** further accelerated the increase in conductivity and raised the rate constant to 3.5×10^5 s^{-1}.

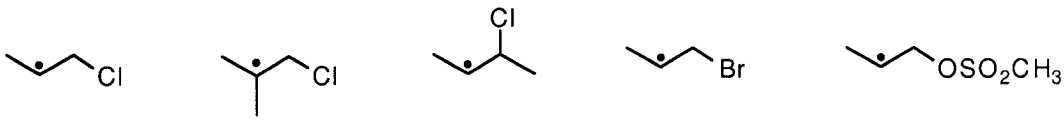

61 **62** **63** **64** **65**

Rate constants were also found to vary according to the leaving ability of the β-group. Relative to radical **61** which loses a chloride anion, a higher rate constant of 7×10^3 s^{-1} was calculated for radical **64** for the loss of bromide. The rate constant further rises to 2×10^5 s^{-1} for radical **65** in which the leaving group is methylsulfonate (or mesylate). These results support an $S_{RN}1^*$ mechanism in which the build-up of positive charge on the carbon bearing the leaving group is stabilized by the addition of electron donating alkyl groups. As bond dissociation progresses, the transition state is also stabilized by good dispersal of the incipient negative charge on the leaving group which increases in the order Cl^- < Br^- < $CH_3O_2SO^-$ and parallels the increase in rate constants observed.[80]

One of the more astonishing findings to come out of this study is that the rate of hydrolysis in aqueous solution of these β-substituted radicals is several orders of magnitude faster than their alkyl counterparts containing the same leaving group. For example, radical **62** solvolyzes with a rate constant of 3.5×10^4 s^{-1} at 22 °C, while the

alkyl analogue *tert*-butyl chloride ionizes *via* the more familiar S_N1 mechanism with a rate constant of 6.4×10^{-3} s^{-1} at 15 °C, Figure 1-1.[81] The presence of a radical centre adjacent to the leaving group causes an acceleration of the rate constant by a factor of 5.5×10^6!

In 1988, Koltzenburg *et al.* subsequently provided some of the first conclusive evidence of uncatalyzed $S_{RN}1^*$ reactivity, and therefore of the uncatalyzed β-heterolysis reaction, exhibited by β-sulfatoxyalkyl radicals.[82] Employing pulse radiolysis or LFP to generate sulfate radical anions, subsequent addition to a variety of cyclohexenes was found to be close to diffusion-controlled, leading to the β-substituted radicals of interest. Rate constants k_{het} were established for the subsequent substitution reaction to produce β-hydroxyalkyl radicals as exemplified in eq. 1.13.

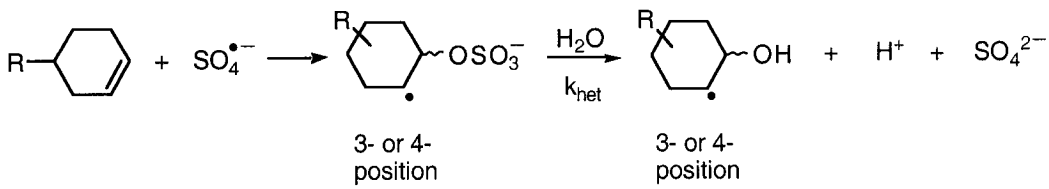

(1.13)

Dramatic substituent effects were observed in the values of k_{het}, calculated to be 8.4×10^3 s^{-1} and $> 5 \times 10^6$ s^{-1} for radicals **66** and **67**, respectively. These results are in agreement with a reaction that has a significant accumulation of positive charge in the transition state that is stabilized by the electron donating ability of an additional methyl group. However, an $S_{RN}1^*$ mechanism was confirmed on the basis of stereochemical evaluation of the products that supported the formation of a largely solvent separated radical cation/sulfate ion pair **68**.

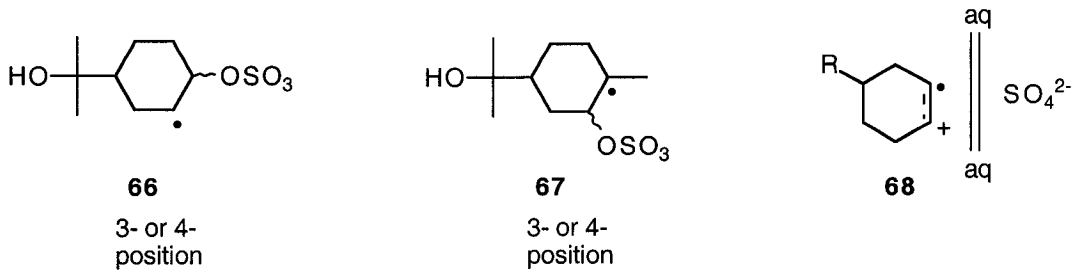

One of the first publications to provide direct observation of radical cation formation *via* β-heterolysis comes from the Cozens group who in 1997, carried out a thorough investigation into the reactivity of carbon-centered 1-arylalkyl radicals substituted at the β-position. Their work has shown that uncatalyzed heterolysis of the carbon-leaving group bond occurs rapidly in highly ionizing solvent conditions.[83] For example, laser photolysis of 2-bromo-1(4-methoxyphenyl)propyl acetate **69** in ionizing solvents such as water, TFE, and HFIP, leads to the corresponding β-substituted radical **70**, which subsequently undergoes rapid ionization of the β-bromo group. The first-order rate constants, k_{-Br-}, for this process were measured and range from 10^6 to 10^8 s^{-1}, eq. 1.14. Occurrence of this S_N1-type ionization of the β-group was confirmed through the direct observation of the styrene radical cation **71**, which is the primary product of the β-heterolysis reaction.

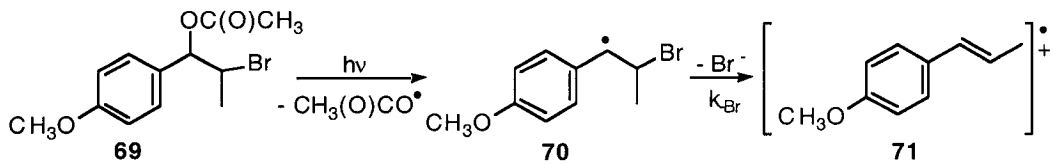

(1.14)

The rate of the β-heterolysis process was found to be strongly influenced by the nature of the reaction medium. To illustrate this point, upon photogeneration of the β-chloro-4-methoxyphenethyl radical **73**, ionization ensued forming **74** with a rate constant of 5.1×10^5 s^{-1} in nitrogen saturated AcN containing 33% TFE, eq. 1.15.

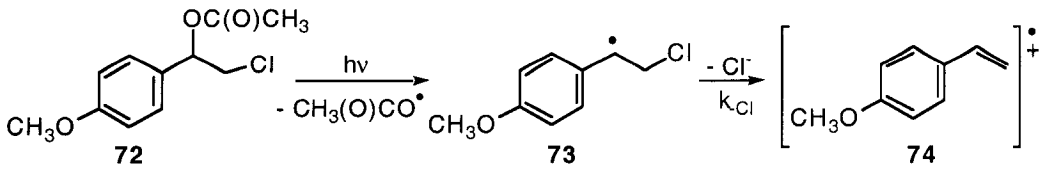

(1.15)

Increasing the content of TFE to 50%, and subsequently to 83%, resulted in a significant increase in the rate constant for the heterolysis reaction to 6.4×10^5 s^{-1} and 2.3×10^6 s^{-1}, respectively. Finally, in neat TFE, heterolytic cleavage of the β-chloro group was further accelerated, with a kinetic constant measured at 1.1×10^7 s^{-1}. However, in a weakly ionizing solvent such as neat AcN, there was no evidence of heterolytic cleavage of the β-group, eq. 1.16.

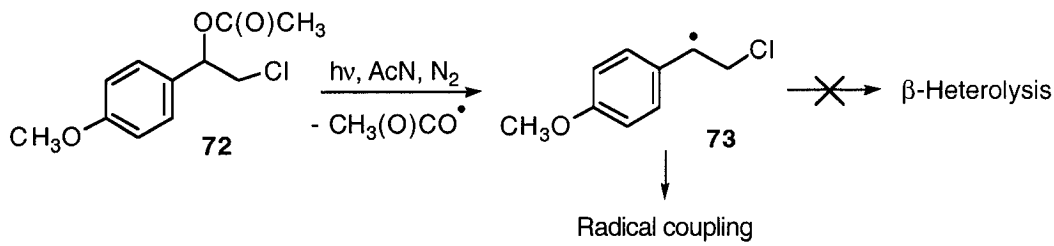

(1.16)

These results clearly exposed the reaction's inherent sensitivity toward the nature of the solvent, and in particular, to its ionizing ability. The failure to observe the formation of the radical cation in AcN suggests that β-heterolysis occurs at a rate that is too slow to compete against other available reaction pathways. Indeed, the radicals were found to decay in a second-order manner, suggesting that radical-radical coupling is the major decay pathway against which the β-heterolysis reaction cannot compete.

This study also probed the effect that various aromatic substituents have on the kinetics of the β-heterolysis process. While the *para*-methoxy-β-chloro and β-bromo substituted radicals were found to readily undergo uncatalyzed ionization in HFIP and TFE ($k_{het} \sim 10^6$-10^8 s^{-1}), the *para*-methyl and unsubstituted analogues revealed no

detectable levels of the corresponding radical cations, evidence that β-heterolysis was not prominent, eq. 1.17.

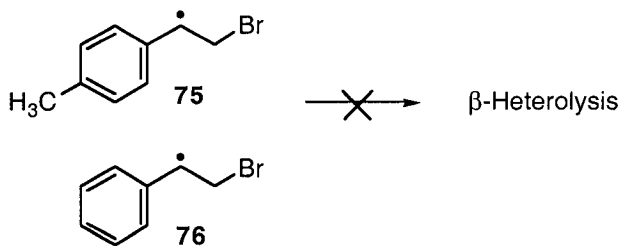

(1.17)

Furthermore, despite the wide range of ionization strengths of the solutions irradiated, the lifetime of radicals **75** and **76** did not alter and decayed in a second-order manner in each solvent. These results were explained by suggesting that the electronic nature of the substituent attached to the phenyl ring was capable of being transmitted through the radical centre to the cationic site, thereby affecting the stability of the radical cation and hence the rate of β-heterolysis.

It was also suggested that under ionizing conditions, the observed rate constant for the reaction of the 4-methoxystyrene radical cation **74**, with nucleophiles such as bromide or chloride that are also good leaving groups, can be affected by the kinetics of the reverse β-heterolysis process. In other words, the resulting 4-methoxystyrene radical cation resulting from β-heterolysis of the β-substituted radical can be reversibly attacked by the addition of bromide due to bromide's dual ability to attack electrophiles and behave as a good leaving group. Consequently, it is believed that the rate of nucleophilic addition to the radical cation, and hence the extent of addition product formed, is related to the magnitude of the reverse heterolysis reaction.

The most recent publication pertaining to the β-heterolysis reaction is by Horner *et al.* who investigated the reactions of α-methoxy-β-phosphatoxyalkyl radicals and calculated rate constant for their ionization in AcN and solvent mixtures of AcN/TFE.[84,85] β-Substituted radicals **77a** and **77b** were generated by photoinduced

homolytic cleavage of the appropriate precursor compounds. Both radicals subsequently underwent uncatalyzed ionization of the β-phosphate group to form radical cation **78**, that then cyclized to give product **79**, Scheme 1-16. For these particular radicals, heterolysis was calculated to be the rate-determining step hence time-resolved detection of the cyclization products allowed for rate constants to be determined under a variety of conditions.

Scheme 1-16

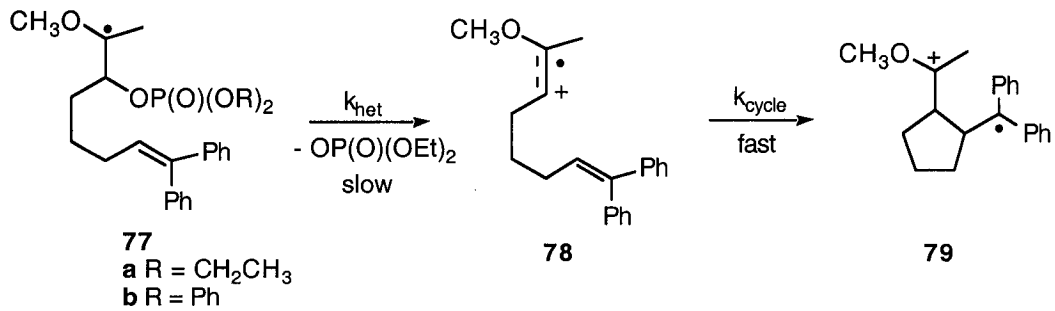

77
a R = CH_2CH_3
b R = Ph

78

79

Results revealed that the yield of the distonic radical cation product **79** was consistently greater in the more polar solvent.[84,85] For example, the yield of product **79** generated by radical **77a** increased from 14% to 42%, 65% and 70% as the solvent was changed from AcN to 0.5% TFE/AcN, 1% TFE/AcN, and 2.5% TFE/AcN, respectively. This trend was also mirrored in the rate constants calculated for the heterolytic dissociation of $^{\cdot}OPO(OCH_2CH_3)_2$ of radical **77a**, ranging from 3.9×10^7 s^{-1} to $> 2 \times 10^8$ s^{-1} in AcN to a 2.5 TFE%/AcN mixture, respectively.

A leaving group effect was also observed in this study, with the yield of **79** being consistently higher for **77b** than for **77a**, even though the same olefin-type radical cation is formed in the two reactions.[84,85] In AcN for instance, a product yield of 85% was calculated when the nucleofuge was $^{\cdot}OPO(OPh)_2$, radical **77b**, but decreased to 50% when the phosphate group was substituted with ethyl groups, $^{\cdot}OPO(OCH_2CH_3)_2$, radical

77a. In agreement with these observations, ionization of the diphenylphosphate group was consistently faster than for the elimination of the diethylphosphate group under the same solvent condition. For example, in neat AcN, k_{het} for **77a** was measured as 3.9×10^7 s^{-1} but k_{het} for **77b** was found to be faster than the temporal resolution of the equipment used, that is $> 2 \times 10^8$ s^{-1}.

It was suggested that these results support the β-heterolysis mechanism in which phosphate elimination from the β-substituted radicals leads directly to radical cation formation. Solvent effects were in agreement with this, with the rate of heterolysis being faster in AcN/TFE mixtures that are better able to solvate the build-up of charge in the transition state of the β-heterolysis mechanism. Similarly, the faster rate constants measured for the diphenylphosphate leaving group, relative to the diethylphosphate group is consistent with an S_N1-type mechanism with charge separation in the transition state. Delocalization of the negative charge is more significant in the presence of two phenyl rings due to the possibility of extensive resonance interaction. A parallel can also be drawn between the nucleofugality of the phosphate groups and the acidity of their conjugates acid, with the diphenylphosphoric acid being 1 pK_a unit more acidic than diethylphosphoric acid.[86]

Similar kinetic trends have previously been observed in the β-heterolysis reaction of β-phosphatoxyalkyl radicals such as **80** and **81**, which differ only with their leaving groups.[87]

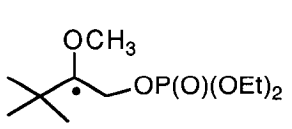

80

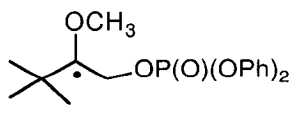

81

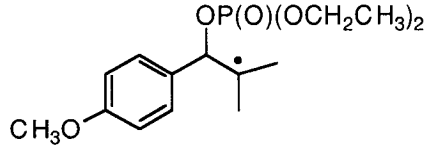

82

Rate constants calculated for the ionization of the phosphate group were found to increase with increasing solvent polarity. For radical **80**, no reaction was

observed in neat AcN but a k_{het} value of 2.0×10^6 s^{-1}, 2.7×10^6 s^{-1} and $> 1 \times 10^6$ s^{-1} was calculated in AcN mixtures containing 4.5%, 5% and 90% TFE, respectively. In contrast, radical **81** did ionize in neat AcN with $k_{het} = 8.5 \times 10^6$ s^{-1}, as well as in 5% TFE for which k_{het} was greater than the detection limit of the instrument, that is $> 2 \times 10^7$ s^{-1}.[87] A solvent effect was also observed in the study of radical **82** for which no radical cation was detected in neat tetrahydrofuran, but diffusively free ions were observed in more polar solvents such as AcN.[87]

1.3.3 1,2-Migration of β-(Ester)alkyl Radicals

There now exists ample evidence confirming that esters and related functional groups such as phosphates and sulfonates, adjacent to a radical centre can undergo 1,2-radical migrations. The mechanism of such rearrangements is believed to be solvent dependent but results in a net interchange of functionality at the two participating carbons, as exemplified in eq. 1.18 with the migration of an β-acetoxy group. Under some conditions, such rearrangements were found to be reversible. It can be readily appreciated that the position of the equilibrium is dictated by the relative stability of the two radicals and the strength of the C—O bonds.[88]

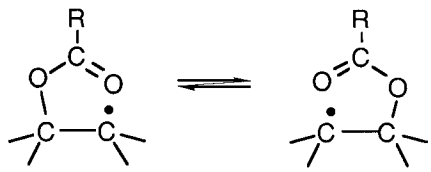

(1.18)

Surzur and Teissier provided the first examples of such rearrangements in their investigation of the dibenzoyl peroxide initiated addition of ethyl cyanoacetate to isoprenyl acetate, Scheme 1-17.[89,90] As anticipated from a simple addition reaction, they observed product **83** but moreover, they isolated **84** from addition followed by 1,2-migration of the ester function.

Scheme 1-17

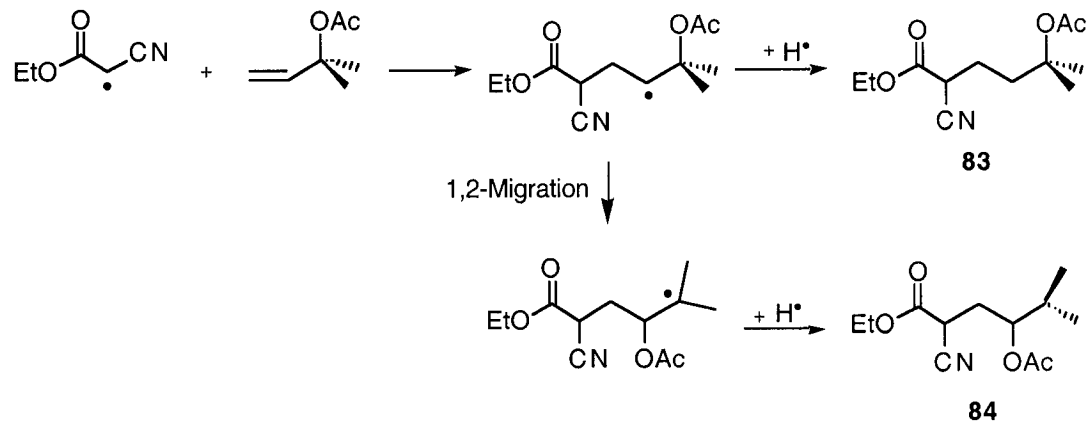

Rate constants for the 1,2-migration of radicals **85** and **86** were among the first to be calculated, Scheme 1-18.[91] Migration of the acetate group in **85** was found to occur with a similar rate constant, $k = 5.1 \times 10^2\ s^{-1}$, to the rearrangement of radical **86**, $k = 2.5 \times 10^2\ s^{-1}$, in which a phenyl ring is attached to the ester group.[92] Interestingly, when the aryl substituent is at position R_2 rather than R_1, as is the case in radical **87**, the rate constant for the migration of the acetate group increases to $4.1 \times 10^4\ s^{-1}$.[91]

Scheme 1-18

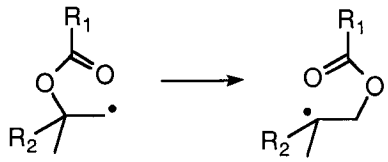

85	**88**	$R_1 = CH_3$, $R_2 = CH_3$
86	**89**	$R_1 = Ph$, $R_2 = CH_3$
87	**90**	$R_1 = CH_3$, $R_2 = Ph$

Examples of β-(phosphatoxy)alkyl radical rearrangement were uncovered independently by Crich and Yao,[93] as well as the Giese group[94] in 1993. Crich's discovery of the migration reaction in Scheme 1-19 exposed that the rearrangement of a

β-phosphate group could be driven by the formation of stabilized benzylic radicals from primary radicals.

Scheme 1-19

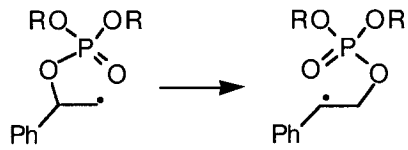

91 R = Ph **93**
92 R = CH_2CH_3 **94**

The formation of a tertiary radical from a primary one is also a sufficient driving force for the migration reaction, eq. 1.19, but formation of a secondary from a primary radical is not, as shown in reaction eq. 1.20.[95] This pattern of reactivity is consistent with that seen in the acyloxy series. As also the case for the acyloxy shift, the basic stereoelectronic requirement for migration of the phosphate group is periplanar orientation of the scissile C—O bond with the initial radical.[95] In radicals **91** and **92**, the C—O bond must also be perpendicular to the plane of the aromatic ring in order to benefit from benzylic stabilization in the transition state.

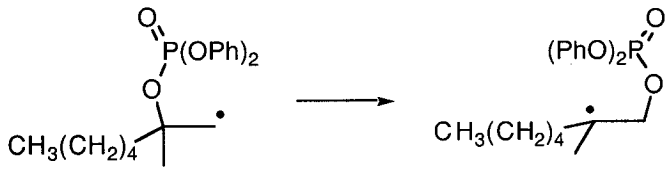

(1.19)

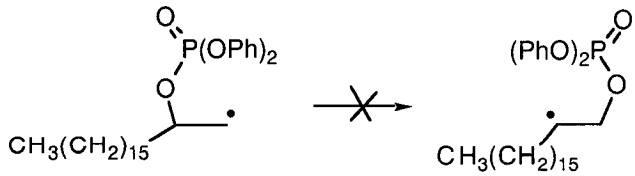

(1.20)

While little kinetic data has been determined for the phosphatoxy shift, the available data suggests that rate constants for migration of phosphate is faster than for the acyloxy group. For instance, the rate constant for the rearrangement of **91** in benzene,

calculated to be 8.0×10^5 s^{-1}, is several orders of magnitude greater than those recorded for comparable acyloxy migration in benzene, Scheme 1-19.[96] Interestingly, rate constants were also influenced by the nature of the migrating phosphate group. The value of k for the rearrangement of (diethylphosphatoxy)alkyl radical **92** was found to be almost two orders of magnitude lower than for the diphenylphosphate group, **91**.[96]

Sulfonate esters are also candidates for this type of radical rearrangement, as established by Crich and Filzen who found that the migration of radical **95** occurs quantitatively, eq. 1.21. Rate constants were not determined but the very high yields of migration product suggest that these are comparable to the diphenylphosphate shift and probably $\geq 10^5$ s^{-1} at 80 °C.[97]

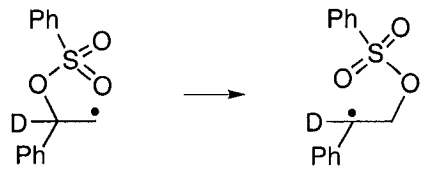

95 **96** (1.21)

Currently, the general consensus is that these 1,2-rearrangements occur by more than one mechanism, suggesting that the nature of the transition state changes according to solvent and substitution of the substrate.[98] Figure 1-4 illustrates a schematic summary of β-(ester)alkyl radical chemistry.[99] In between the two extremes of this spectrum, characterized by the β-(ester)alkyl radicals that are 'inert' to fragmentation and rearrangement, and those that fragment entirely (i.e. the β-heterolysis reaction), we encounter the various transition states believed to be possible during β-(acyloxy)alkyl radical rearrangement. A thorough review has been published by Beckwith *et al.*[99]

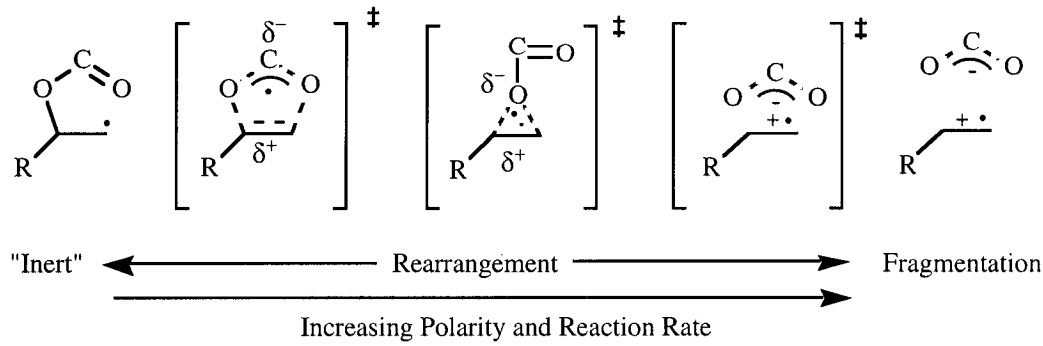

Figure 1-4. A schematic summary of β-(ester)alkyl radical chemistry, highlighting the range of transition states possible in rearrangement reactions of the acyloxy group.[99]

1.4 Scope of Thesis

This thesis describes an investigation into the kinetics and general dynamics of ionization of β-substituted phenethyl radicals in solution at room temperature. The work was carried out using nanosecond LFP, a technique that allows fast generation of transients and real-time detection *via* absorption spectroscopy.

The results are divided into two chapters based on whether the β-heterolysis reaction studied was uncatalyzed or acid-catalyzed. Thus in Chapter 2, the focus is on *para*-substituted β-mesylate phenethyl radicals that are generated in HFIP, TFE, AcN, water and methanol, as well as binary mixtures of these solvents. The discussion addresses the influence of solvent as well as electronic effects of substituents on the kinetics of the β-heterolysis reaction using physical organic chemistry tools, especially linear free energy relationships and the solvent polarity Y_X scale.

Chapter 3 presents the findings of an investigation into the acid-catalyzed β-heterolysis reaction of *para*-substituted β-hydroxy and β-diethylphosphatoxy phenethyl radicals. These experiments were carried out in HFIP, TFE and AcN, as well as mixtures prepared with a range of perchloric acid concentration. Bimolecular rate constants for the acid-catalyzed ionization of HO^- and $(CH_3CH_2O)_2(O)PO^-$ were determined, as well as

unimolecular acid-independent rate constants for the loss of H_2O and $(CH_3CH_2O)_2(O)POH$ at high acid concentration. Analysis of the results leads to a discussion about the catalytic requirement of the variously substituted radicals, the nucleofugality of the leavings group, the electronic influence of the substituent and the role of solvation in the kinetics of the β-heterolysis reaction in acidic media.

Lastly, Chapter 4 is dedicated to a full description of the experimental set-up, the organic synthetic procedures followed to generate the precursor compounds, as well as spectroscopic characterizations of these synthesized compounds.

CHAPTER 2
UNCATALYZED β-HETEROLYSIS

2.1 Introduction

Presented in this chapter are the results obtained from laser flash photolysis (LFP) experiments carried out on a series of methanesulfonate (mesylate) esters in a wide range of solvent mixtures. The principal aim of this work was to assess the reactivity of various *para*-substituted-β-mesylate phenethyl radicals **2(X)** in polar solvents toward the uncatalyzed β-heterolysis reaction as shown in Scheme 2-1.

Scheme 2-1

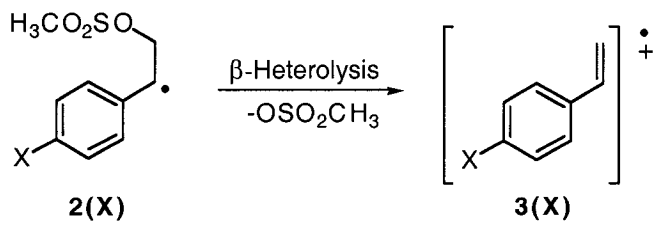

2(X) **3(X)**

X = Cl, H, F, CH_3, or OCH_3

An additional objective was to investigate the influence of solvent and substituents on the kinetics of this novel ionization reaction. Mechanistic insights were

further gained by subjecting the data to correlation analysis employing Y_{OMs} values to analyze the dependence of the reaction on solvent polarity and the σ^+ substituent parameter to measure the reaction's sensitivity to electronic effects.

2.1.1 Structural Design of the Precursor Compounds

As highly reactive intermediates, β-substituted radicals must be generated rapidly and in sufficient amounts to be detected spectroscopically. To this end, nanosecond LFP was employed throughout this study as it allows relatively high concentrations of transients to be generated within the < 10 ns laser excitation pulse and monitored using time-resolved absorption spectroscopy. The type of precursor required for these experiments must possess several key structural features, one of which is to be thermally stable in the range of solvent systems studied, at least for the time duration of the experiment. On the other hand, the precursor must possess a suitable chromophore and be designed such that upon 266 or 308 nm laser excitation, the compound undergoes the desired photochemistry to generate the target species, in this case the β-substituted radical **2(X)**.

The commercial availability of the starting materials precluded the use of a single precursor structure for all of the five aromatic substituents investigated. Consequently, the precursor compounds synthesized adopted one of two basic structures, as depicted in Scheme 2-2, where X denotes the aromatic substituent. The compounds synthesized include 2-(4-chlorophenyl)-3-oxobutylmethanesulfonate **1(Cl)**, 2-(4-fluoro-phenyl)-3-oxobutylmethanesulfonate **1(F)**, 2-(4-methoxyphenyl)-3-oxobutylmethane-sulfonate **1(OMe)**, 2,4-diphenyl-3-oxopentyl-1,5-dimethanesulfonate **1(H)**, and 2,4-bis(4-methylphenyl)-3-oxopentyl-1,5-dimethanesulfonate **1(Me)**, Scheme 2-2.

Scheme 2-2

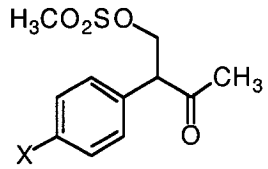

A

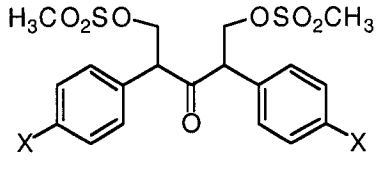

B

1(Cl) X = Cl
1(F) X = F
1(OMe) X = OCH_3

1(H) X = H
1(Me) X = CH_3

The choice of precursor structure was based on the known photochemical behavior of phenylacetone and dibenzylketone (DBK), both of which have been extensively studied in solution.[100-113]

Upon UV-excitation, phenylacetone is known to undergo a Norrish type I photocleavage (also referred to as α-cleavage) in which the C_α—CO bond breaks homolytically to generate a benzyl radical and an acetyl radical, as shown in eq. 2.1. The acetyl radical, which has a longest wavelength band at 215 nm,[114-117] undergoes decarbonylation to yield carbon monoxide gas and a methyl radical.[100,107] Neither the acetyl nor the methyl radicals are detected in these experiments as they absorb well below 280 nm. However, the benzyl radical can be readily observed in deoxygenated solutions and is known to have an absorption maximum near 316 nm.[118,119]

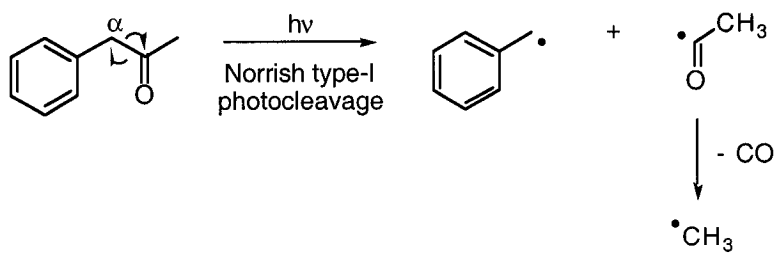

(2.1)

In a similar manner, the photochemistry of DBK is also characterized by α-cleavage with a high quantum yield of $\phi = 0.7$,[102,104] rendering this type of ketone a

convenient source of benzyl radicals. The mechanism outlined in Scheme 2-3 shows that upon UV-irradiation, absorption of light by DBK causes an $n \rightarrow \pi^*$ transition that promotes the molecule to an excited singlet state ($\tau_{singlet}$ ~ 3 ns)[104] before undergoing intersystem crossing to the excited-triplet state. α-Cleavage rapidly ensues ($k > 10^{10}$ s^{-1})[109,112] to generate a benzyl and phenacetyl radical, the latter of which absorbs at 275 nm.[111] The decarbonylation of the phenacetyl radical occurs rapidly with a rate constant $k_{CO} = 6.4 \times 10^6$ s^{-1} in isooctane, to yield a second benzyl radical.[111]

Scheme 2-3

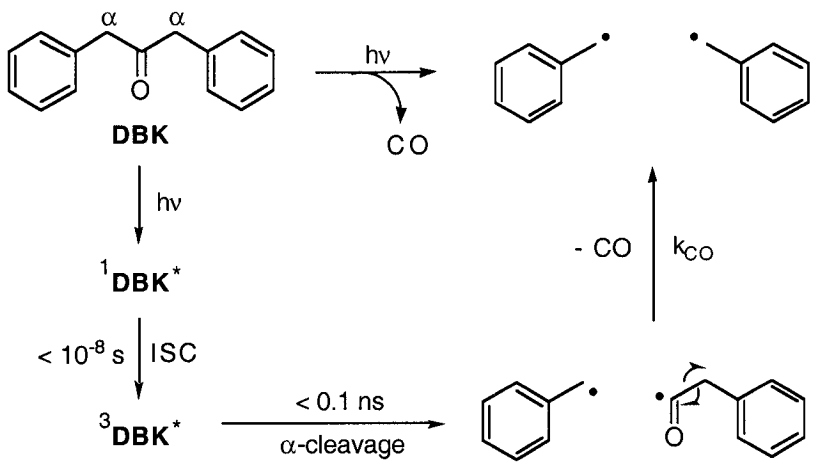

Based on the above, precursors presented in Scheme 2-2 with structures A and B were expected to undergo similar photochemistry in solution as phenylacetone or DBK upon 266 or 308 nm laser irradiation to yield the β-mesylate phenethyl radicals **2(X)** of interest.

2.2 Results

2.2.1 Laser Photolysis of Methanesulfonate Esters in Solution

2.2.1.1 Neat Acetonitrile

Figure 2-1 presents a transient absorption spectrum acquired immediately following 266 nm nanosecond laser excitation of precursor **1(Cl)** in nitrogen-saturated AcN. The significant change in optical density (ΔO.D.) detected at wavelengths below 300 nm indicates the formation of a transient species with an absorption maximum near 280 nm. Monitoring the changes in absorbance at 280 nm as a function of time generates the transient decay trace shown in Figure 2-2. Analysis of the data using non-linear least squares analysis revealed that the transient decays with second-order kinetics, with a value of $k_{obs} = 3.1 \times 10^5\ s^{-1}$. The observed rate constant calculated for a second-order decay of a radical is defined as $k_{obs} = k/\varepsilon l$, where k is the second-order rate constant ($M^{-1}\ s^{-1}$), ε is the molar extinction coefficient with units of $M^{-1}\ cm^{-1}$, and *l* represents the cell path length in cm. When using flash photolysis with kinetic absorption spectroscopy, second-order rate constants can only be calculated when ε values for the transient species are known. Since it is difficult to estimate the values of ε for transients, observed second-order rate constants for bimolecular reactions are often reported as defined above, with units of s^{-1}.[120,121] The transient was found to be relatively long-lived and detectable for approximately 0.3 ms under nitrogen conditions, but is rapidly quenched in the presence of oxygen, Figure 2-1.

Benzylic radicals are known to have an absorption maximum in the low UV region, with the 4-chlorobenzyl radical absorbing near 280 nm.[118,119] It is also well established that oxygen efficiently scavenges benzylic radicals at close to the diffusion-controlled limit in both aqueous and organic solvents.[122] For example, the second-order rate constant for the reaction of 4-chlorobenzyl radicals with oxygen is reported to be $2.0 \times 10^9\ M^{-1}\ s^{-1}$ in *n*-hexane.[119] Based on these criteria, the transient detected in

nitrogen-purged AcN is identified as the β-mesylate-4-chlorophenethyl radical **2(Cl)** produced by the photo-induced α-homolytic fragmentation of precursor **1(Cl)** *via* the Norrish type I mechanism as shown in Scheme 2-4.

Scheme 2-4

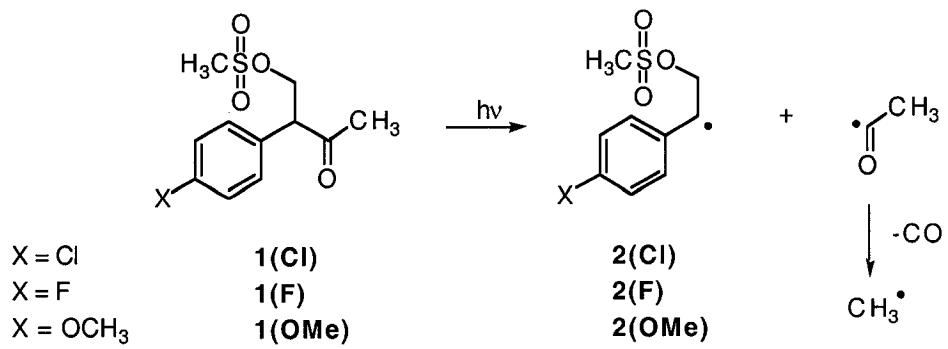

As shown in Figure 2-3 (b) and (d), LFP of the phenylacetone derivatives **1(F)** and **1(OMe)** in AcN also generate transient absorption spectra with strong absorption below 300 nm. In both cases the transient is completely quenched with the addition of oxygen to the sample but moreover, the transient spectra (b) and (d) are similar to those for the 4-fluoro and 4-methoxybenzyl radical in solution, respectively.[83,118,119,123] Based on the above, the transients are identified as the β-mesylate-4-fluorophenethyl radical **2(F)** in spectrum (b) and the β-mesylate-4-methoxyphenethyl radical **2(OMe)** in spectrum (d).

Laser irradiation of DBK precursors **1(H)** and **1(Me)** in AcN produced similar results. In Figure 2-3 (a), the time-resolved spectrum produced upon 266 nm LFP of **1(H)** shows a strong absorption at and below 270 nm as well as a shoulder at 316 nm, an absorption profile which fully resembles that reported for the structurally similar benzyl radical.[118,119] The transient signals generated are therefore attributed to the β-mesylate phenethyl radical **2(H)**. Similarly, a strong absorption band is observed around 280 nm in the transient absorption spectrum recorded after 266 nm laser photolysis of **1(Me)**.

Once again, the profile coincides with that of the 4-methylbenzyl radical and the transient responsible for the spectrum in Figure 2-3 (c) is identified as the β-mesylate-4-methylphenethyl radical **2(Me)**.[118,119,123] As illustrated in Scheme 2-5, radicals **2(H)** and **2(Me)** are produced by photoinduced α-cleavage of the triplet ketone precursor following 266 nm laser irradiation to yield a primary acyl/benzyl radical pair. Subsequent decarbonylation of the acyl radical occurs to yield a second β-mesylate radical of interest. Spectra collected in oxygenated AcN showed complete quenching of the absorption bands assigned to the β-mesylate radicals **2(H)** and **2(Me)**, as expected since carbon-centered radicals are known to react rapidly with oxygen.

Scheme 2-5

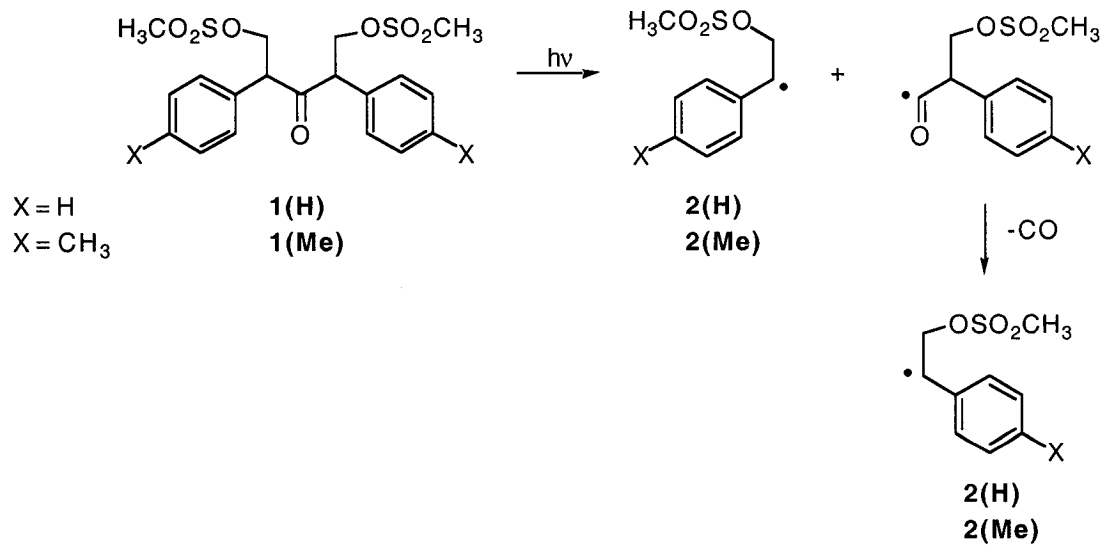

While the spectra presented in Figure 2-3 confirm that the anticipated Norrish type I photochemistry is indeed taking place, they also provide evidence that no transients other than radicals **2(X)** are produced in AcN. It is clear therefore that these β-substituted radicals do not readily undergo ionization of the β-mesylate group in this solvent. Decay traces acquired at the absorbing wavelength of each radical fit second-order kinetics

suggesting that their decay pathway is *via* a bimolecular mechanism such as radical-radical coupling.

2.2.1.2 HFIP/TFE Mixtures

Subjecting precursor **1(Cl)** to 266 nm LFP in a highly ionizing solvent like HFIP affords more interesting results. Taken under nitrogen-saturated conditions, the spectra presented in Figure 2-4 show the 280 nm absorption maximum previously assigned to radical **2(Cl)** decaying as a function of time, along with two additional absorption bands whose intensities increase as a function of time. The new band at 370 nm is approximately triple the intensity of the second new band centered at 630 nm. Kinetic measurements at these two wavelengths reveal an identical first-order rate constant, $k_{het} = 3.0 \times 10^6\ s^{-1}$ for the increase in absorbance as a function of time. This strongly suggests that the two absorption bands originate from the same transient. Moreover, the value of k_{het} was found to match the first-order rate constant calculated for the concurrent decay of the radical **2(Cl)** at 280 nm, where $k_{decay} = 3.0 \times 10^6\ s^{-1}$, Figure 2-5.

The spectral profile obtained in Figure 2-4 closely resembles those generated by styrene-type radical cations that are known to have strong absorption bands around 350 and 600 nm with an approximate 3:1 intensity ratio, respectively. The experimental results therefore provide strong evidence that in nitrogen-purged HFIP, the photogenerated radical **2(Cl)** undergoes subsequent loss of the β-mesylate group to yield the 4-chlorostyrene radical cation **3(Cl)**, Scheme 2-6.[83]

Scheme 2-6

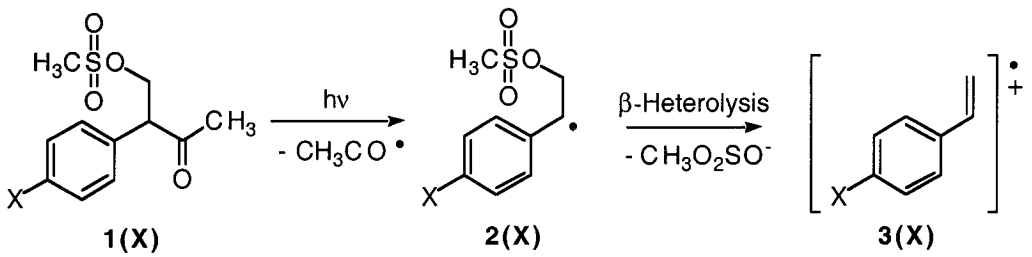

1(X) **2(X)** **3(X)**

X = Cl, F, or OCH_3

Additional support for the above mechanism is obtained by comparing Figure 2-4 to the transient absorption spectrum of the 4-chlorostyrene radical cation formed by other means. It is well established that styrene-type radical cations are readily produced *via* an electron transfer mechanism in the presence of the chloranil triplet, which is known to be an excellent electron acceptor.[124] Laser photolysis at 308 nm of chloranil in nitrogen-saturated HFIP in the presence 4-chlorostyrene leads to the transient spectra in Figure 2-6. The spectra show strong absorption bands at 370 and 630 nm due to the 4-chlorostyrene radical cation **3(Cl)** generated by an electron transfer reaction from 4-chlorostyrene to the triplet excited chloranil, eq. 2.2. Consistent with the electron transfer mechanism is the presence of strong absorbance at 420 and 450 nm, the known maxima for the chloranil radical anion.[125]

Further evidence for the β-heterolysis mechanism outlined in Scheme 2-6 is provided with the observation that in oxygen-saturated HFIP, 266 nm laser irradiation of **1(Cl)** results in the almost complete disappearance of the absorption bands at 370 and 630 nm assigned to radical cation **3(Cl)**, Figure 2-7. Since the reactivity of styrene-type radical cations has been shown to be insensitive to oxygen concentration,[46] the inhibited formation of **3(Cl)** cannot be attributed to the rapid trapping of the radical cation by oxygen. Rather, this outcome supports a mechanism in which the radical cation is generated from an oxygen-sensitive precursor. Indeed, carbon-centered radicals similar

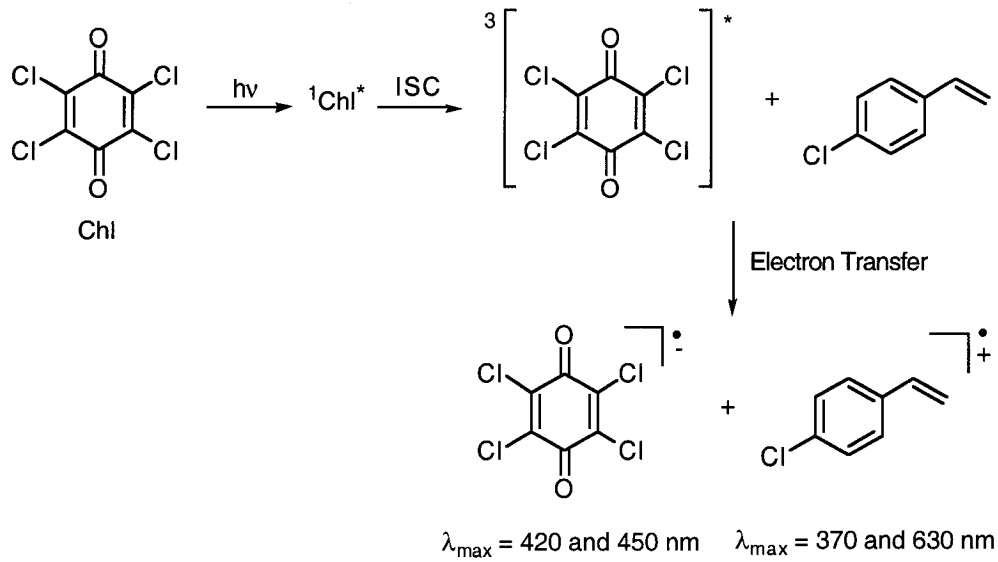

(2.2)

to **2(Cl)** are known to react rapidly with oxygen[122,126] and this quenching reaction provides an alternative decay route against which the kinetics of the β-heterolysis reaction cannot compete, Scheme 2-7.

Scheme 2-7

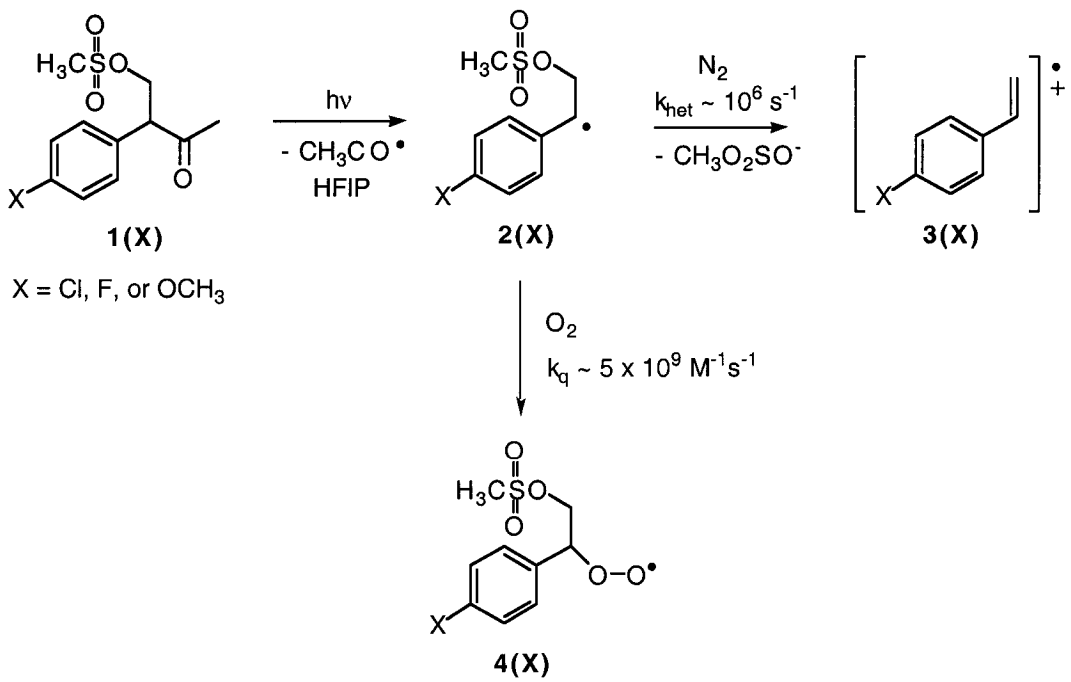

When precursor **1(Cl)** was laser irradiated at 266 nm in nitrogen-saturated HFIP in the presence of varying concentrations of bromide, the observed rate constant for the decay observed at 630 nm was found to increase with increasing bromide concentration, Figure 2-8. This confirms that, as expected, the transient responsible for the absorption bands at 370 and 630 nm possesses a cationic centre that can be attacked by a nucleophile such as bromide. Moreover, the second-order rate constant calculated from the slope is $k_{Br} = 1.1 \times 10^{10}\ M^{-1} s^{-1}$, a value that is in agreement with the known rate constant for the quenching of styrene-type radical cations with bromide.[46]

The fact that the 4-chlorostyrene radical cation was not detected in AcN yet successfully generated in HFIP infers that its formation *via* β-heterolysis is heavily dependent on the nature of the solvent. To explore this effect more thoroughly, an initial study was carried out to measure the kinetics of the ionization reaction in various HFIP/TFE solvent mixtures. As a first experiment, precursor **1(Cl)** was dissolved in a solution of nitrogen-saturated 70% HFIP/30% TFE and spectra were collected after 266 nm laser irradiation of the sample, Figure 2-9. The absorption band observed near 280 nm and assigned to radical **2(Cl)** decays while the 370 and 630 nm maxima of the 4-chlorostyrene radical cation are simultaneously growing in with time. These observations are consistent with the mechanism presented in Scheme 2-6 in which the β-substituted radical undergoes loss of the mesylate group to yield **3(Cl)**. Several kinetic traces showing the build-up of the radical cation in a variety of HFIP/TFE mixtures are superimposed in Figure 2-10. Inspection of these growth curves reveals that the maximum change in optical density, a value proportional to the maximum concentration of radical cation **3(Cl)**, increases with increasing HFIP content. It can also be noted that the initial rise of the signal becomes progressively steeper as the HFIP content is increased from 40% to 100%. This unquestionable solvent effect is confirmed upon kinetic analysis of the traces, the result of which is plotted in Figure 2-11. In

50% HFIP/50% TFE, a rate constant of $9.2 \times 10^5\ s^{-1}$ is calculated for the formation of radical cation **3(Cl)**, a value which triples to $3.0 \times 10^6\ s^{-1}$ when the experiment is carried out in neat HFIP. Accurate growth rate constants could not be determined in mixtures containing less than 50% HFIP due to minimal changes in optical density.

The second precursor investigated was the unsubstituted DBK derivative **1(H)**. Spectra acquired immediately following 266 nm laser photolysis of **1(H)** in 70% HFIP/30% TFE under nitrogen-saturated conditions are presented in Figure 2-12 and show similar characteristics to those previously described for precursor **1(Cl)**. The decay of radical **2(H)** seen at 280 nm follows first-order kinetics and is concurrent with the first-order growth of the styrene radical cation **3(H)** responsible for the two absorption maxima seen at 350 and 600 nm, Figure 2-13. The spectral characteristics attributed to the radical cation are in agreement with those reported in the literature.[46,119] As expected for the β-heterolysis mechanism designated in Scheme 2-8, the presence of oxygen results in quenching of the absorption bands generated by both the radical and radical cation.

Selected kinetic traces illustrating the build-up of the styrene radical cation in various HFIP/TFE solvent mixtures are provided in Figure 2-14. The observed rate constants obtained by fitting the growth curves to a monoexponential function are summarized in Figure 2-15. As can be seen, the rate constant almost triples in value from $2.6 \times 10^6\ s^{-1}$ in 50% HFIP/50% TFE to $7.5 \times 10^6\ s^{-1}$ in neat HFIP.

Scheme 2-8

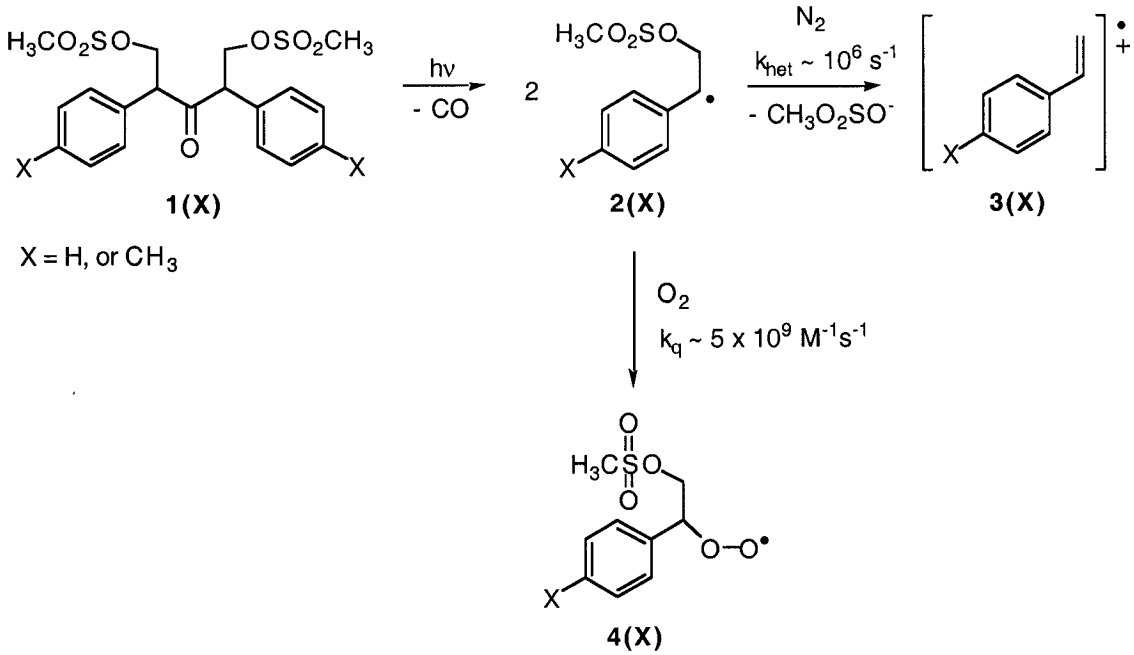

The spectra presented in Figure 2-16 were attained by subjecting the fluorinated precursor **1(F)** to 266 nm LFP in nitrogen-saturated 80% HFIP/20% TFE. Once again, the spectra show an absorption band near 280 nm due to radical **2(F)** that decays while changes in O.D. increase with time at 355 and 585 nm. The location of these two absorption bands and their relative intensities are characteristic of the 4-fluorostyrene radical cation **3(F)** and, consistent with this identification, the bands grow in with the same calculated first-order rate constant of $k_{het} = 3.7 \times 10^6\ s^{-1}$, Figure 2-17.[46] Evidence that radical **2(F)** is indeed the precursor to radical cation formation *via* the β-heterolysis mechanism shown in Scheme 2-6 is obtained by adding oxygen to the sample. Spectra subsequently collected under these conditions reveal complete quenching of the transient signals. Since oxygen is a potent radical scavenger and styrene-type radical cations are known to be insensitive to oxygen concentration on the nanosecond timescale, it is suggested that rapid, irreversible trapping of radical **2(F)** by

oxygen kinetically inhibits the ionization pathway. This also rationalizes why the radical cation **3(F)** is not observed in oxygen-saturated solutions.

Representative kinetic traces of the growth of **(3F)** at 585 nm are compiled in Figure 2-18 and clearly show the influence of solvent composition on the amount of radical cation formation as well as k_{het}. While the initial build-up in ΔO.D. is slow in 40% HFIP/60% TFE, the rise in signal at 585 nm is much sharper and more intense in neat HFIP. These observations were then quantified by fitting the kinetic traces and plotting the calculated rate constant k_{het} as a function of HFIP content in nitrogen-purged TFE, Figure 2-19. In 40% HFIP/60% TFE, k_{het} was calculated to be $2.5 \times 10^6 s^{-1}$ and continued to increase in value up to $1.1 \times 10^7 s^{-1}$ for the ionization of the radical **2(F)** in neat HFIP. This represents a factor of four increase in k_{het} over the range in solvent composition investigated.

To determine whether or not the phenylacetone or DBK precursor backbone has any influence on the β-heterolysis kinetics, 2,4-bis(4-fluorophenyl)-3-oxopentylmethanesulfonate **1(F)-DBK** was synthesized and subjected to 308 nm LFP in a series of HFIP/TFE mixtures, eq. 2.3. The spectra presented in Figure 2-20 clearly show two absorption bands at 355 and 585 nm growing in with time and are assigned to the 4-fluorostyrene radical cation **3(F)**.[46] The absorption peak associated with the radical **2(F)** previously observed near 280 nm was not detected since this wavelength is too close to the 308 nm laser wavelength employed in these experiments. Exemplary kinetic traces showing the rise in signal detected at 355 nm are provided in Figure 2-21 (a) in a variety of HFIP/TFE mixtures. The series of rate constants acquired for precursors **1(F)-DBK** and **1(F)** are combined in Figure 2-21 (b). Both sets of rate constants measured for the growth of the radical cation **3(F)** are virtually identical. These results suggest that the structural differences between the precursors A and B (Scheme 2-2) used in this study do not noticeably affect the kinetics of the β-heterolysis reaction.

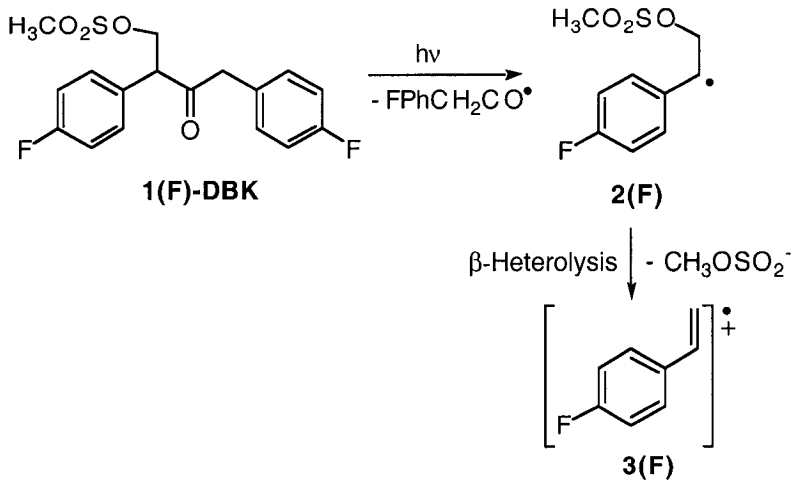

(2.3)

In a 30% HFIP/70% TFE mixture, the ionization of the methylated radical **2(Me)** was investigated following 266 nm laser irradiation of its precursor **1(Me)** in nitrogen-saturated conditions, Figure 2-22. The transient absorption spectra recorded display the characteristic 280 nm absorption maximum of radical **2(Me)** decaying with time, while two additional absorption bands at 350 and 590 nm simultaneously increase in intensity. These two transient signals at 350 and 590 nm are confidently assigned to the 4-methylstyrene radical cation **3(Me)**.[46] Monitoring changes in optical density at 280 nm as a function of time generates a decay trace from which a first-order rate constant of 2.7×10^7 s^{-1} was calculated which closely matches the first-order rate constant associated with the growth of **3(Me)** at both 350 and 590 nm, $k_{het} = 3.6 \times 10^7$ s^{-1}, Figure 2-23. These results are consistent with the β-heterolysis mechanism outlined in Scheme 2-8 where the radical cation is generated from heterolytic loss of the β-mesylate group in this case from radical **2(Me)**. Also in agreement is the successful quenching of the radical cation absorption bands in oxygenated solution due to rapid trapping of **2(Me)** *via* oxygen thereby preventing the radical from undergoing the slower ionization process.

Figure 2-24 presents a few selected time-resolved kinetic traces illustrating the rise in absorption at 590 nm due to **3(Me)** in various HFIP/TFE solvent mixtures.

Solvent effects once again play an important role in the kinetics of formation of the radical cation, with the initial rise in absorption appearing substantially faster in 50% HFIP/50% TFE mixtures than in neat TFE. The growth of the radical cation *via* β-heterolysis of **2(Me)** was detected across the entire HFIP/TFE solvent range with a growth rate constant of $4.1 \times 10^6 s^{-1}$ in neat TFE, a value that increases by a factor of fourteen to $5.7 \times 10^7 s^{-1}$ in neat HFIP, Figure 2-25. These results show that unlike **2(Cl)**, **2(H)** and **2(F)**, ionization of radical **2(Me)** takes place even under less ionizing conditions such as neat TFE.

A similar study was done with the 4-methoxy derivative **1(OMe)** and the findings also suggest that radical **2(OMe)** readily undergoes heterolytic loss of the mesylate group in neat TFE, Figure 2-26. The time-resolved transient spectra obtained following 308 nm laser irradiation of **1(OMe)** in nitrogen conditions, show the characteristic absorption bands at 350 and 590 nm with a 3:1 intensity ratio associated with the 4-methoxystyrene radical cation **3(OMe)**.[46,83] Time-resolved kinetic traces acquired at 350 and 590 nm show the extremely rapid rise in signal as a result of radical cation formation *via* the β-heterolysis reaction of **2(OMe)**. A first-order rate constant of $6.7 \times 10^7 s^{-1}$ was calculated from the trace recorded at 590 nm, Figure 2-27, which does not show interference from fluorescence effects as seen in the trace monitored at 350 nm. Quenching of these two absorption bands with the addition of oxygen to the sample provides good evidence that the radical precedes the formation of the radical cation, Scheme 2-6. Since the value of k_{het} calculated in neat TFE is at the limit of the time-resolution of the laser system, no additional attempts were made to study the ionization of **2(OMe)** in the more polar HFIP/TFE mixtures.

2.2.1.3 HFIP/Acetonitrile Mixtures

As stated previously, the growth of the 4-methoxystyrene radical cation in HFIP/TFE mixtures was too fast to be resolved by the nanosecond laser system employed. This consequently motivated a further study in which the precursors were laser irradiated in solvent compositions of lower polarity in an attempt to slow down the ionization process. This section therefore describes the results obtained from a systematic investigation into the dynamics of the β-heterolysis reaction in various HFIP/AcN compositions.

The work began with 266 nm laser irradiation of **1(OMe)** in nitrogen-saturated 50% HFIP/50% AcN to immediately establish whether in this less polar medium, growth of the radical cation could be detected. As shown in Figure 2-28, photolysis resulted in the formation of radical **2(OMe)** with a decaying absorption maximum at 290 nm, as anticipated from a Norrish type I photohomolysis of the precursor molecule, Scheme 2-4. The two additional absorption maxima observed in the spectra are confidently assigned to the 4-methoxystyrene radical cation **3(OMe)** as described earlier. Interestingly, the spectra also show an isosbestic point around 320 nm, a region of overlap between the absorption spectrum of the radical and that of the radical cation. The presence of an isosbestic point is indicative that the rate of change in absorption at this wavelength is zero as the rate of decay of the radical coincides with the rate of growth of the radical cation. This is further confirmed from the time-resolved kinetic traces in Figure 2-29 from which the decay rate constant for the radical was found to match that obtained for the growth of the radical cation, $k_{het} = 9.1 \times 10^6\ s^{-1}$. This observation, along with the complete quenching of the radical cation absorption bands under oxygenated conditions, is consistent with the mechanism designated by the β-heterolysis reaction outlined in Scheme 2-6. It is clear from these results that replacing TFE with AcN as the co-solvent in HFIP has a drastic effect on the rate constant for ionization of radical **2(OMe)**. In

equal volumes of HFIP/AcN, the β-heterolysis is sufficiently decelerated to permit direct time-resolved detection of radical cation formation that was not possible in HFIP/TFE mixtures. Such solvent effects are also apparent when the HFIP/AcN ratio is systematically increased as shown in Figures 2-30 and 2-31. In a solvent mixture containing 10% HFIP/90% AcN, the rate constant calculated for formation of the radical cation is 9.0×10^5 s^{-1}. The value of k_{het} continues to increase as the HFIP content is increased, and shows particular acceleration in solutions containing > 40% HFIP. For example, in 70% HFIP/30% AcN, the k_{het} has increased by a factor of approximately 60 to a value of 5.8×10^7 s^{-1}, Figure 2-31.

Laser flash experiments carried out at 266 nm with precursor **1(Me)** in nitrogen-saturated 80% HFIP/20% AcN generated transient absorption spectra with maxima at 360 and 600 nm that both increase with time as the 280 nm absorption of radical **2(Me)** decays, Figures 2-32 and 2-33. The location of the absorption bands at 350 and 590 nm is consistent with the identification of the transient as the 4-methylstyrene radical cation[46] **3(Me)** whose formation is also found to be completely quenched upon addition of oxygen to the sample. This provides strong evidence that the **3(Me)** radical cation is generated from the oxygen-sensitive radical **2(Me)** upon heterolytic cleavage of the β-mesylate group, Scheme 2-8. The kinetic traces compiled in Figure 2-34 once again indicate a significant solvent effect, although formation of the radical cation was only detected within the narrow range of 70% to 100% HFIP in AcN, Figure 2-35. The ionization of the methylated radical **2(Me)** generated rate constants for the growth of **3(Me)** that vary from 2.2×10^6 s^{-1} in 70% HFIP/30% AcN to 5.5×10^7 s^{-1} in neat HFIP.

In these less polar solvent mixtures, the fluorinated radical **2(F)** was also found to undergo ionization of its β-mesylate group in solvent composition containing no less than 80% HFIP in AcN. For example, 308 nm laser excitation of precursor **1(F)** in nitrogen-purged 95% HFIP/5% AcN resulted in the spectra presented in Figure 2-36.

The characteristic absorption peaks of the 4-fluorostyrene radical cation **3(F)** are detected at 355 and 585 nm and increase in intensity after the laser pulse. The time-resolved kinetic traces provided in Figure 2-37 show the build-up of signal at 355 and 585 nm generated by the radical cation with a similar rate constant of $k_{het} = 7.4 \times 10^6\ s^{-1}$ and $7.6 \times 10^6\ s^{-1}$, respectively. Once again, solvent composition plays a key role in the rise time and magnitude of the signal detected at 585 nm, Figure 2-38. In 82.5% HFIP/17.5% AcN, the rate constant is calculated as $3.0 \times 10^6\ s^{-1}$ and increases to $1.1 \times 10^7\ s^{-1}$ in neat HFIP, Figure 2-39. In the case of experiments carried out in solvent mixtures with lower than 80% HFIP content, kinetic analysis could not be made accurately due to the weakness or complete absence of radical cation absorption.

Upon 266 nm laser photolysis of precursor **1(H)** in nitrogen-purged 95% HFIP/5% AcN, maximum changes in optical density were found at 350 and 600 nm as seen in the spectra presented in Figure 2-40. Rate constants calculated for the rise in absorption at these two wavelengths were found to be identical with a k_{het} value of $4.9 \times 10^6\ s^{-1}$, Figure 2-41. From the location of these maxima and their simultaneous growth with time, the transient responsible for these signals is identified as the styrene radical cation **3(H)**.[46,119] As it is quenched in the presence of oxygen, formation of **3(H)** is likely preceded by a species that is sensitive to oxygen concentration. These observations are consistent with the mechanism outlined in Scheme 2-8 in which the benzyl-type radical **2(H)** is first photogenerated and subsequently undergoes thermal β-heterolysis to yield the styrene radical cation. The influence of solvent composition on its formation *via* the β-heterolysis reaction is apparent from the time-resolved kinetic traces of the growth of **3(H)** in varying concentrations of HFIP content in AcN, Figure 2-42. In neat HFIP, the rise of the signal monitored at 600 nm is significantly steeper than that obtained in 90% HFIP/10% AcN. This solvent effect is confirmed and quantified by analysis of the kinetic traces to give the observed rate constant for the

growth of **3(H)**. The results are compiled in Figure 2-43 and clearly show that as the HFIP content increases, so does the corresponding first-order growth rate constant for the formation of the radical cation. This value ranges between 2.8×10^6 s^{-1} and 6.3×10^6 s^{-1} for the β-heterolysis process in 90% HFIP/10% AcN and neat HFIP, respectively.

Lastly, the chlorinated precursor **1(Cl)** was subjected to 266 nm LFP in HFIP/AcN solvent mixtures. An initial spectral profile was obtained upon laser excitation of **1(Cl)** in nitrogen-saturated 98.3% HFIP/1.7% AcN and is presented in Figure 2-44. The transient absorption spectra reveal three absorption maxima, one of which is at 280 nm and attributed to the radical **2(Cl)**. As the absorption signal of this transient decays with time, the bands centered around 370 and 630 nm simultaneously increase in intensity with the same first-order rate constant, $k_{het} = 3.1 \times 10^6$ s^{-1}, Figure 2-45. Furthermore, the reactive transient responsible for these signals is efficiently quenched by oxygen, as is the radical band at 280 nm. The growth at 370 and 630 nm can confidently be attributed to the formation of the 4-chlorostyrene radical cation **3(Cl)**.[118,119]

The solvent effects on the ionization of radical **2(Cl)** are made evident by the kinetic traces presented in Figure 2-46 for the growth of the radical cation. The traces show tremendous variation in the initial build-up of the signal as well as in the maximum ΔO.D. value, in spite of the relatively small range of HFIP/AcN mixtures investigated. The corresponding first-order rate constants for the β-heterolysis reaction are presented in Figure 2-47 and show an increase in the rate constant k_{het}, from 2.3×10^6 s^{-1} in 94.4% HFIP to 3.2×10^6 s^{-1} in 99.0% HFIP in AcN.

2.2.1.4 TFE/Acetonitrile Mixtures

Time-resolved transient absorption spectra collected upon 266 nm laser excitation of precursor **1(OMe)** in nitrogen-saturated 50% TFE/50% AcN distinctly show

the decay of radical **2(OMe)** at 290 nm and the concomitant growth of the radical cation **3(OMe)** at 350 and 590 nm, Figure 2-48. The corresponding time-resolved kinetic traces at these wavelengths show that the first-order decay of the radical matches the first-order growth rate constant of $k_{het} = 4.5 \times 10^6\ s^{-1}$ calculated at 350 and 590 nm, Figure 2-49.

Selected kinetic traces obtained in nitrogen-purged AcN containing 20% to 70% TFE are presented in Figure 2-50 and show the drastic difference in the rate constant for the β-heterolysis process as the solvent composition (and hence polarity) changes. The influence of solvent composition on the kinetics of the β-heterolysis reaction are particularly noticeable in this set of experiments; in neat TFE, radical **2(OMe)** ionizes with a rate constant of $6.7 \times 10^7\ s^{-1}$, a value 88 times faster than that obtained in 10% TFE/90% AcN, in which k_{het} is calculated to be $7.6 \times 10^5\ s^{-1}$, Figure 2-51.

Laser irradiation of precursor **1(Me)** at 266 nm in nitrogen-purged TFE/AcN mixtures also generated evidence of radical cation formation. Spectra acquired in neat TFE show the characteristic absorption bands at 360 and 600 nm of **3(Me)** which increase in intensity as the absorption at 280 nm of radical **2(Me)** decays simultaneously in a first-order manner, Figures 2-52 and 2-53. These bands are completely quenched with the addition of oxygen to the sample, strong evidence that formation of the radical cation is preceded by an oxygen sensitive precursor. This observation is consistent with the β-heterolysis mechanism outlined in Scheme 2-8. Evidence for the ionization reaction was found in AcN mixtures containing between 80% and 100% TFE content. However, the growth curves detected at 600 nm for the build-up of the radical cation **3(Me)** showed significant variation in rise time and intensity according to the TFE content of the solvent mixture, Figure 2-54. These observations are quantified by analyzing the time-resolved kinetic traces and plotting the calculated rate constants for the ionization reaction of radical **2(Me)** as a function of TFE content, Figure 2-55. A rate constant of $1.2 \times 10^6\ s^{-1}$ was calculated in 80% TFE/20% AcN and this value almost

triples to 3.4×10^6 s^{-1} in neat TFE. In TFE/AcN solvent mixtures containing less than 80% TFE, signals were too weak to accurately determine k_{het}.

The β-ionization of radicals **2(Cl)** and **2(H)** was found not to take place in TFE/AcN solvent mixtures as the corresponding radical cations are not detected. Laser flash photolysis experiments carried out with precursors **1(Cl)** and **1(H)** in neat TFE gave the spectra presented in Figures 2-56 and 2-57. In both cases, only the β-substituted radicals **2(Cl)** and **2(H)** are observed and decay in a second-order manner. Moreover, lifetimes of these radicals were unaffected by changes in solvent ionizing ability. These observations infer that the principal decay pathway of these radicals is *via* a nonpolar mechanism such as radical-radical recombination. Since neat TFE is more polar than any of the TFE/AcN combinations, no further study was carried out with **1(Cl)** and **1(H)** in this solvent system.

2.2.1.5 Water/Acetonitrile Mixtures

The transient absorption spectra provided in Figure 2-58 were obtained upon 266 nm laser irradiation of **1(OMe)** in nitrogen-purged 30% water/70% AcN. The spectral profile reveals the decay of an absorption maximum at 290 nm associated with radical **2(OMe)**, along with the growth of the 4-methoxystyrene radical cation observed at 350 and 590 nm. Once again, an isosbestic point is easily identifiable around 310 nm as the rate for the decay of the radical matches that of the growth of the radical cation **3(OMe)**, $k_{het} = 5.7 \times 10^6$ s^{-1}, Figure 2-59. The time-resolved kinetic traces clearly demonstrate an increase in the rate constant for the growth of the radical cation, and thus for the β-heterolysis reaction, in solvent mixtures containing higher water content, Figure 2-60. The measured kinetic rate constants are plotted as a function of water content in nitrogen-purged AcN, Figure 2-61. In 10% water/90% AcN, k_{het} has a calculated value of 1.9×10^6 s^{-1} and increases to 6.5×10^7 s^{-1} in 80% water/20% AcN,

representing an increase of 34 times.

2.2.1.6 Water/Methanol Mixtures

Precursor **1(OMe)** was also subjected to LFP in nitrogen-saturated water/methanol mixtures due to the availability of Y_{OMs} values in this solvent system. A few selected kinetic traces acquired upon 266 nm laser excitation of **1(OMe)** are shown in Figure 2-62 and clearly illustrate the increase in the rate constant for the growth of the radical cation in solvent mixtures of increasing water content. The rate constants calculated in these experiments for the growth of **3(OMe)** are plotted in Figure 2-63 as a function of water content in nitrogen-saturated methanol. The value of k_{het} for the ionization of radical **2(OMe)** clearly increases as the water content of the solvent increases. In neat methanol, k_{het} has a value of 7.8×10^6 s^{-1} and rises by a factor of 6.5 to 5.1×10^7 s^{-1} in 50% water/50% methanol.

2.2.1.7 The Decarbonylation Reaction

Experiments were also carried out to determine whether the decarbonylation reaction shown in Scheme 2-5 interferes with the kinetic measurements used to calculate rate constants for the ionization of β-substituted radicals **2(H)** and **2(Me)**. To this end, precursor **1(H)** was subjected to 266 nm laser irradiation in nitrogen-saturated AcN or HFIP. The objective was to determine whether the formation of the second benzyl-type radical could be observed. Figures 2-64 (a) presents a time-resolved kinetic trace of radical **2(H)** at 316 nm in AcN, and reveals that in this solvent, the radical is fully formed during the laser pulse. No subsequent growth is observed, showing that the decarbonylation reaction is complete within the time duration of the laser pulse. A similar experiment was carried out with radical **2(H)** in HFIP, Figure 2-64 (b). In this case, some delayed growth at 280 nm due to decarbonylation is observed with a very fast

rate constant of $k_{CO} = 6.7 \times 10^7\ s^{-1}$. This rate constant is similar to that measure for decarbonylation of the similar α-methylphenacetyl radical, $k_{CO} = 4.9 \times 10^7\ s^{-1}$, eq. 2.4.[106,108]

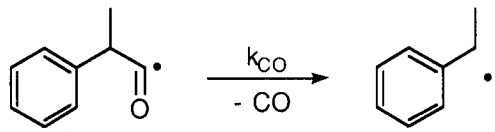

(2.4)

However, this k_{CO} value is still faster than the k_{het} value determined for the ionization of the radical **2(H)** in neat HFIP and thus will not interfere with the kinetic measurements.

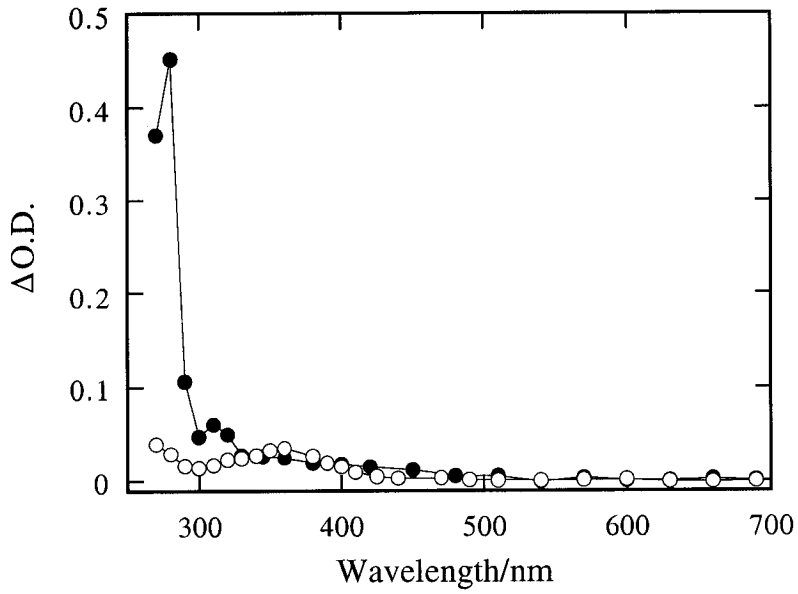

Figure 2-1. Transient absorption spectra obtained 0.21 μs after 266 nm laser irradiation of 2-(4-chlorophenyl)-3-oxobutylmethanesulfonate **1(Cl)** in (●) nitrogen-saturated and (○) oxygen-saturated acetonitrile.

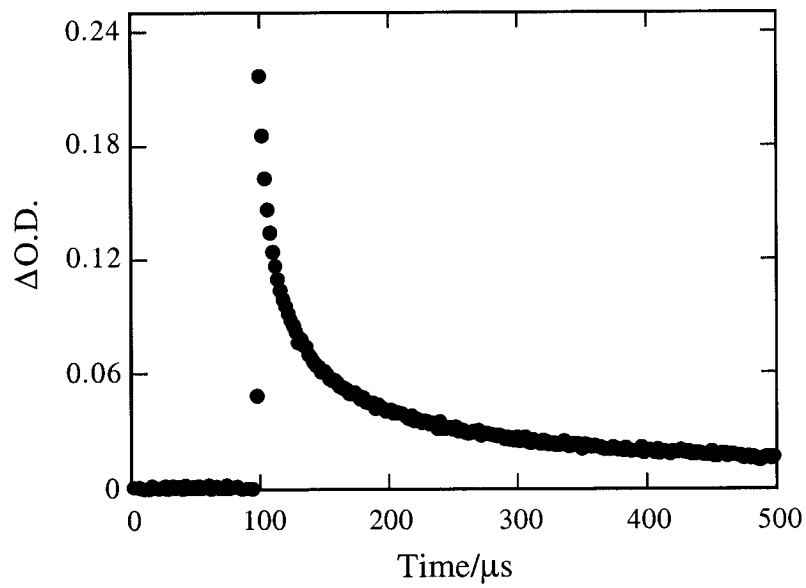

Figure 2-2. Time-resolved second-order decay trace detected at 280 nm after 266 nm laser irradiation of 2-(4-chlorophenyl)-3-oxobutylmethanesulfonate **1(Cl)** in nitrogen-purged acetonitrile.

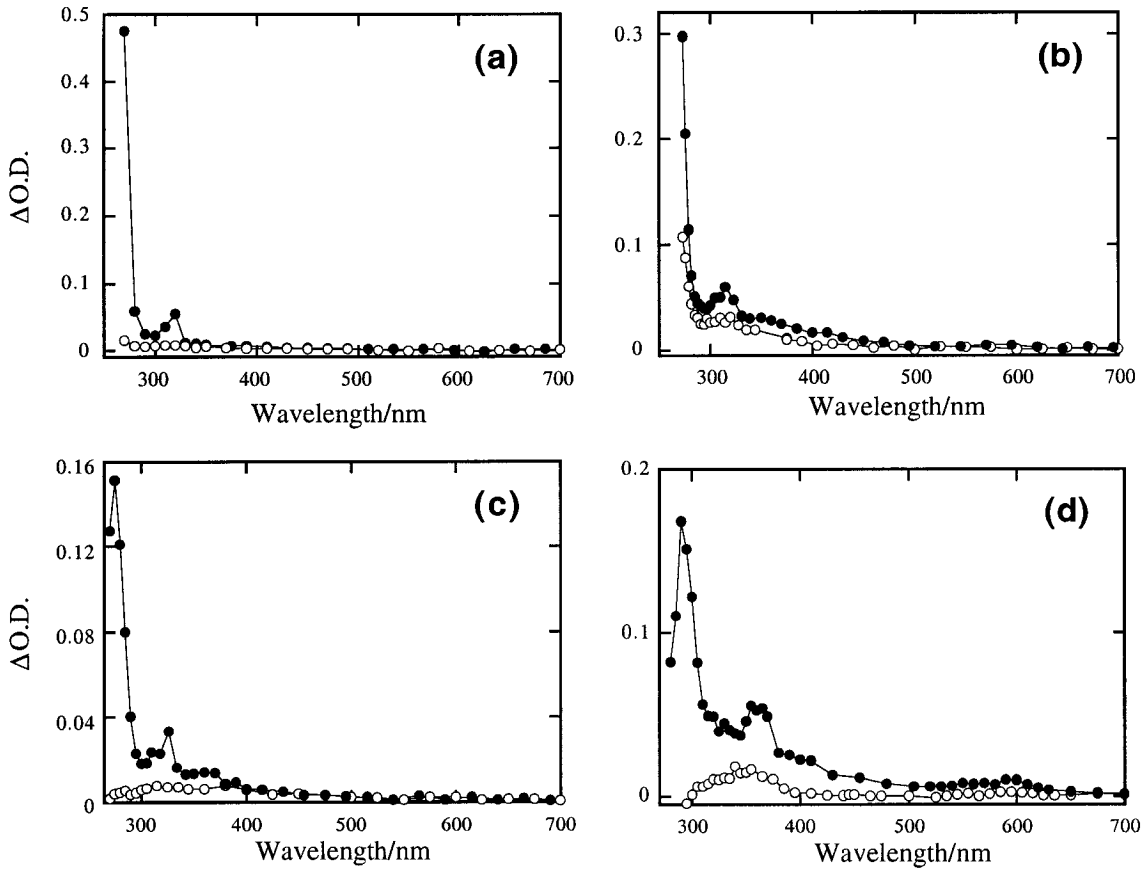

Figure 2-3. Transient absorption spectra obtained after 266 nm laser irradiation of (a) 2,4-diphenyl-3-oxopentyl-1,5-dimethanesulfonate **1(H)**, (b) 2-(4-fluorophenyl)-3-oxobutylmethanesulfonate **1(F)**, (c) 2,4-bis(4-methylphenyl)-3-oxopentyl-1,5-dimethanesulfonate **1(Me)**, and (d) 2-(4-methoxyphenyl)-3-oxobutylmethanesulfonate **1(OMe)** in (●) nitrogen-saturated and (○) oxygen-saturated acetonitrile.

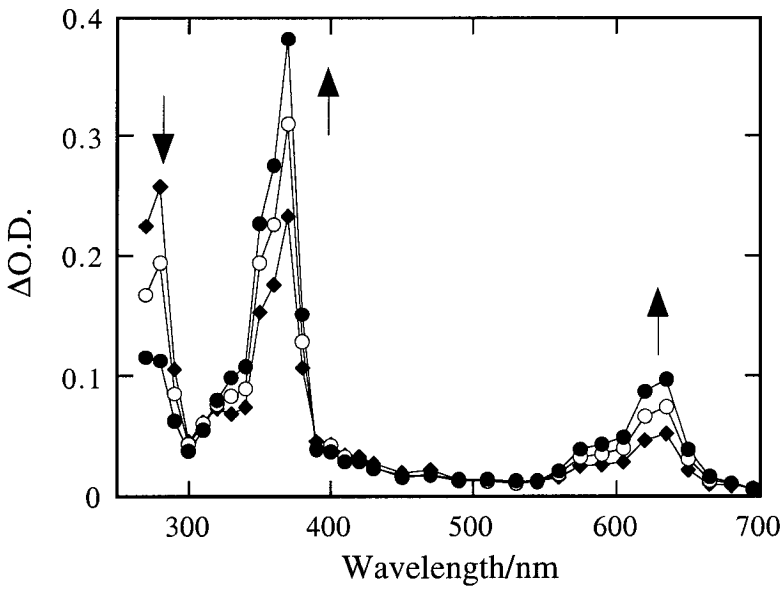

Figure 2-4. Transient absorption spectra obtained after 266 nm laser irradiation of 2-(4-chlorophenyl)-3-oxobutylmethanesulfonate **1(Cl)** in nitrogen-saturated HFIP. Spectra were recorded (◆) 0.19 μs, (○) 0.32 μs, and (●) 0.62 μs after the laser pulse.

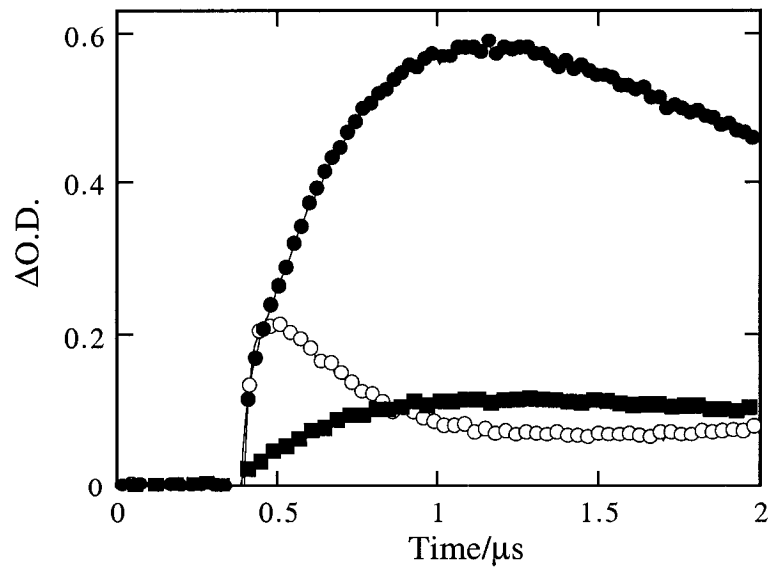

Figure 2-5. Time-resolved kinetic traces at (○) 280 nm, (●) 370 nm, and (■) 630 nm following 266 nm laser excitation of 2-(4-chlorophenyl)-3-oxobutylmethanesulfonate **1(Cl)** in nitrogen-saturated HFIP.

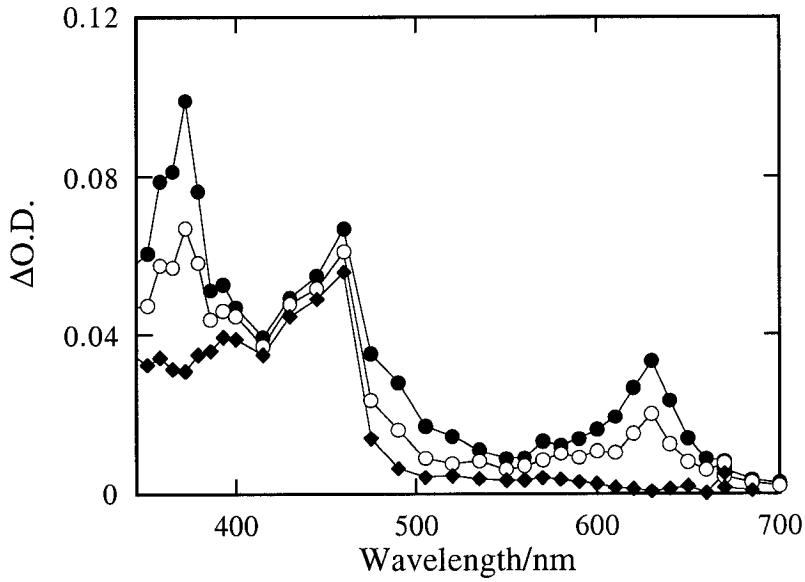

Figure 2-6. Transient absorption spectra obtained after 308 nm laser irradiation of chloranil in the presence 4-chlorostyrene in nitrogen-saturated HFIP. Spectra were collected (●) 0.12 μs, (○) 0.18 μs, and (◆) 0.80 μs after the laser pulse.

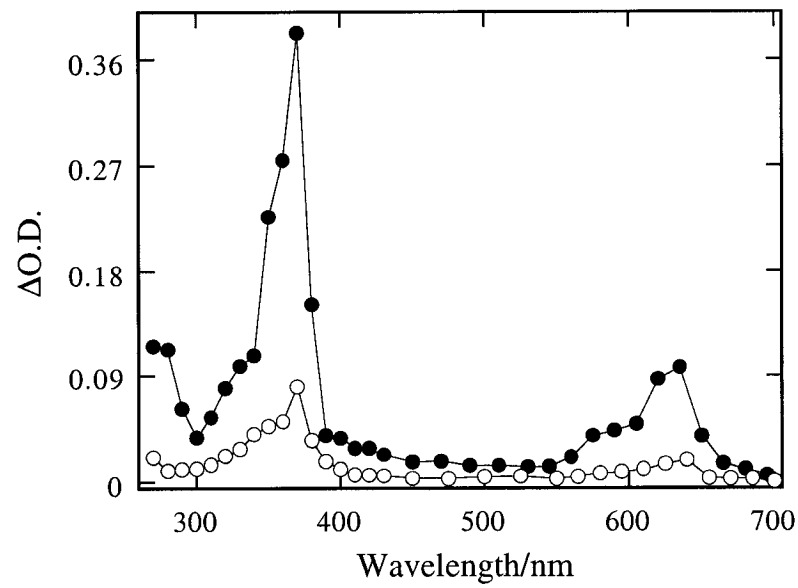

Figure 2-7. Transient absorption spectra obtained 0.62 μs after 266 nm laser irradiation of 2-(4-chlorophenyl)-3-oxobutylmethanesulfonate **1(Cl)** in (●) nitrogen-saturated and (○) oxygen-saturated HFIP.

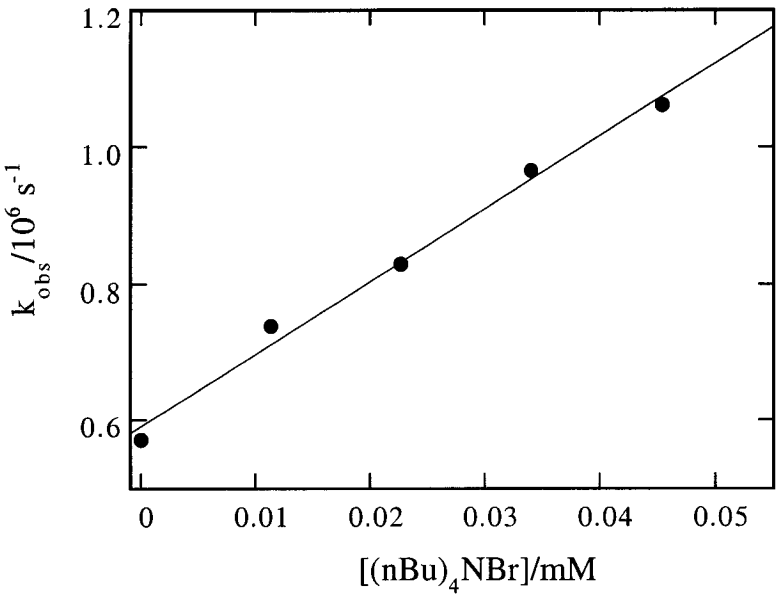

Figure 2-8. Relationship between the rate constant for the decay of the 4-chlorostyrene radical cation **3(Cl)** after 266 nm laser photolysis of 2-(4-chlorophenyl)-3-oxobutylmethanesulfonate **1(Cl)** and tetrabutylammonium bromide concentration in nitrogen-saturated HFIP. From the slope of the plot, a value of $1.1 \times 10^{10}\ M^{-1}\ s^{-1}$ was calculated for the quenching rate constant, k_q.

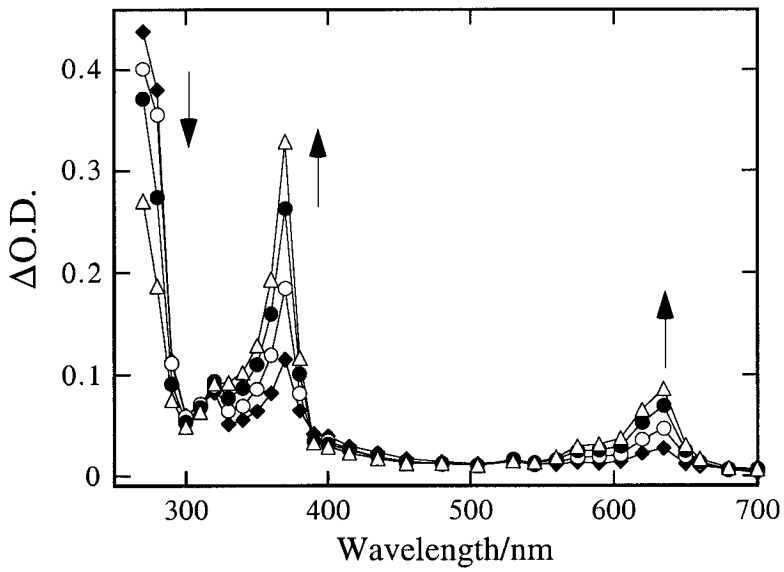

Figure 2-9. Transient absorption spectra obtained in nitrogen-saturated 70% HFIP/30% TFE after 266 nm laser irradiation of 2-(4-chlorophenyl)-3-oxobutylmethanesulfonate **1(Cl)**. Spectra were recorded (◆) 0.13 μs, (○) 0.31 μs, (●) 0.59 μs, and (Δ) 1.1 μs after the laser pulse.

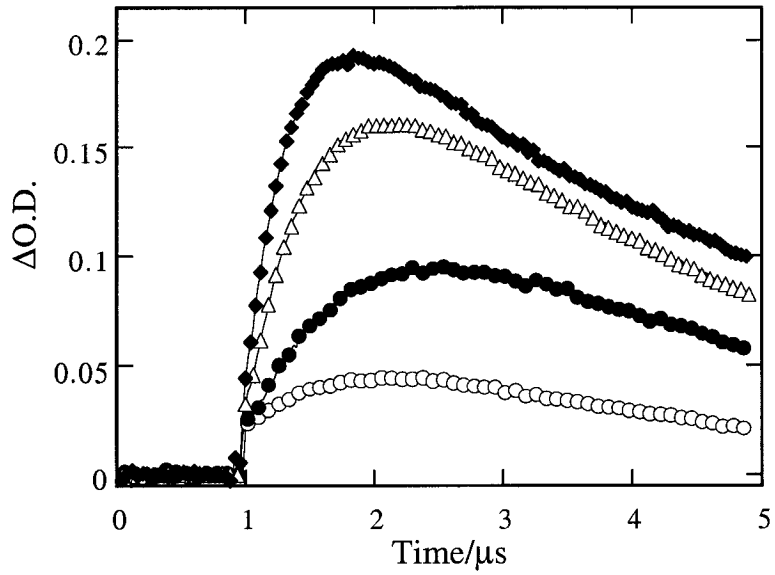

Figure 2-10. Time-resolved kinetic traces monitored at 630 nm showing the growth of the 4-chlorostyrene radical cation **3(Cl)** after 266 nm laser irradiation of 2-(4-chlorophenyl)-3-oxobutylmethanesulfonate **1(Cl)** in nitrogen-saturated HFIP/TFE mixtures containing (○) 40%, (●) 60%, (Δ) 80%, and (◆) 100% HFIP.

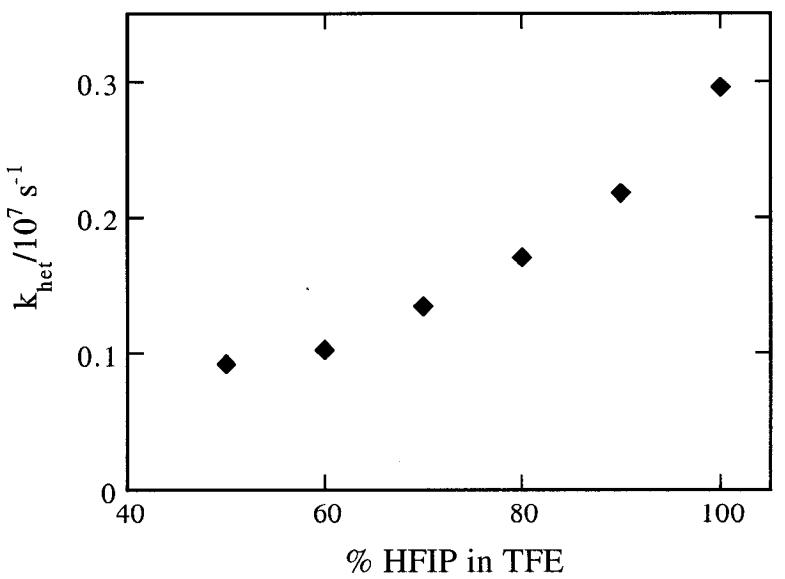

Figure 2-11. Observed rate constant for the growth of the 4-chlorostyrene radical cation **3(Cl)** after 266 nm laser excitation of 2-(4-chlorophenyl)-3-oxobutylmethanesulfonate **1(Cl)** as a function of HFIP content in nitrogen-saturated TFE.

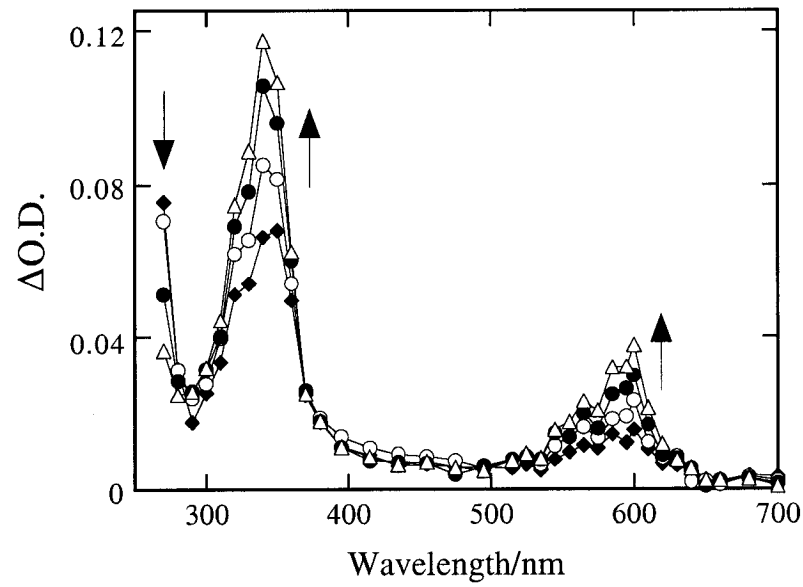

Figure 2-12. Transient absorption spectra after 266 nm laser irradiation of 2,4-diphenyl-3-oxopentyl-1,5-dimethanesulfonate **1(H)** in nitrogen-saturated 70% HFIP/30% TFE. Spectra were recorded (◆) 0.066 μs, (○) 0.17 μs, (●) 0.33 μs and (Δ) 0.65 μs after the laser pulse.

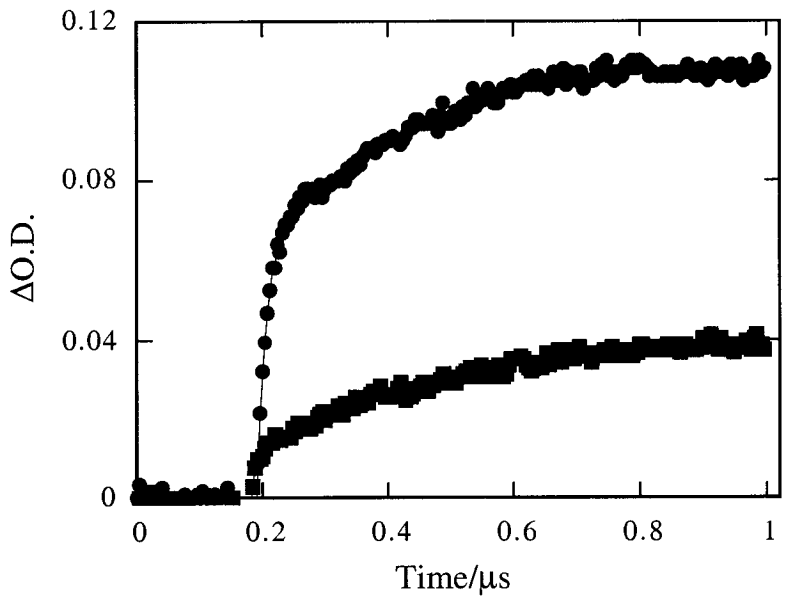

Figure 2-13. Time-resolved kinetic traces at (●) 350 nm and (■) 600 nm following 266 nm laser excitation of 2,4-diphenyl-3-oxopentyl-1,5-dimethanesulfonate **1(H)** in nitrogen-saturated 70% HFIP/30% TFE.

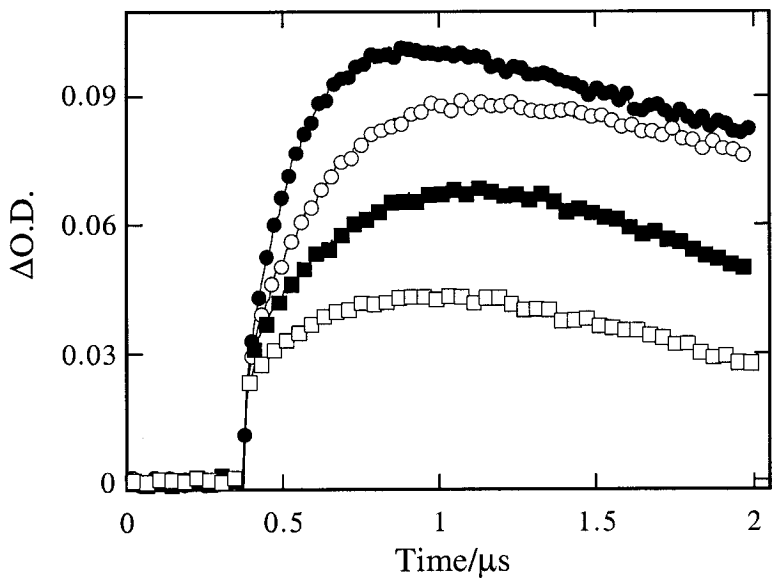

Figure 2-14. Time-resolved kinetic traces showing the growth of the styrene radical cation **3(H)** at 600 nm observed after 266 nm laser irradiation of 2,4-diphenyl-3-oxopentyl-1,5-dimethanesulfonate **1(H)** in nitrogen-saturated HFIP/TFE mixtures containing (□) 50%, (■) 60%, (○) 80%, and (●) 100% HFIP.

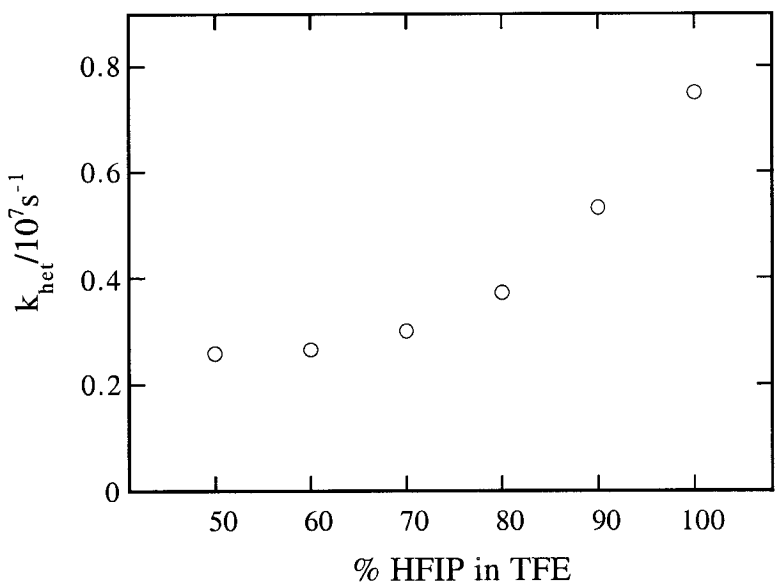

Figure 2-15. Observed rate constant for the growth of the styrene radical cation after 266 nm laser excitation of 2,4-diphenyl-3-oxopentyl-1,5-dimethanesulfonate **1(H)** as a function of HFIP content in nitrogen-saturated TFE.

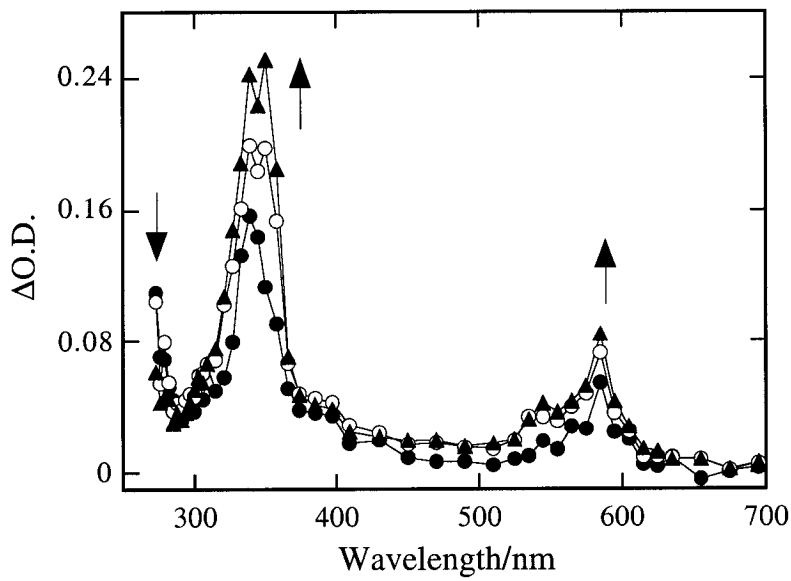

Figure 2-16. Transient absorption spectra obtained in nitrogen-saturated 80% HFIP/20% TFE upon 266 nm laser excitation of 2-(4-fluorophenyl)-3-oxobutylmethanesulfonate **1(F)**. Spectra were recorded (●) 0.086 μs, (○) 0.18 μs and (▲) 0.34 μs after the laser pulse.

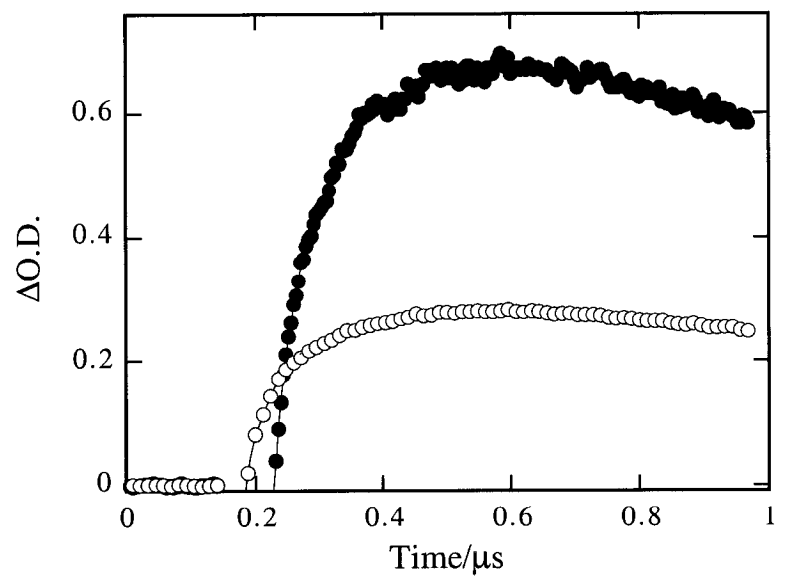

Figure 2-17. Time-resolved kinetic traces collected at (●) 355 nm and (○) 585 nm in nitrogen-saturated 80% HFIP/20% TFE upon 266 nm laser irradiation of 2-(4-fluorophenyl)-3-oxobutylmethanesulfonate **1(F)**.

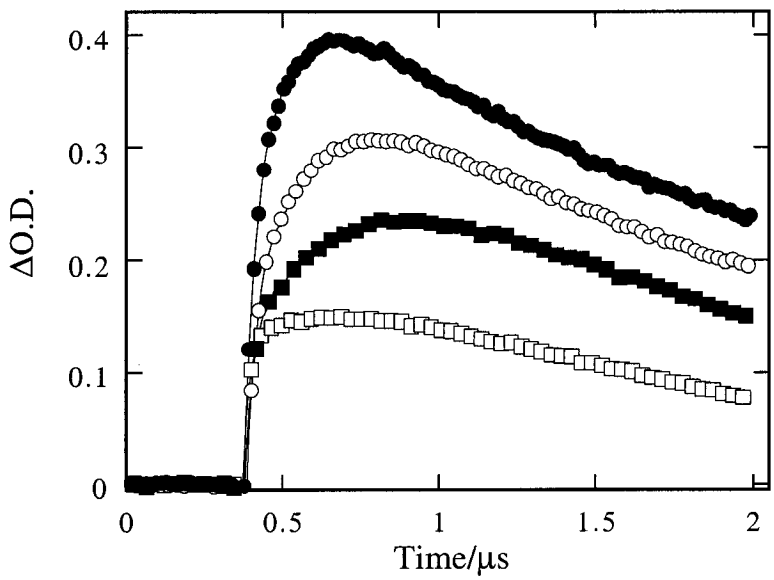

Figure 2-18. Time-resolved kinetic traces collected at 585 nm showing the growth of the 4-fluorostyrene radical cation **3(F)** after 266 nm laser irradiation of 2-(4-fluorophenyl)-3-oxobutylmethanesulfonate **1(F)** in nitrogen-saturated HFIP/TFE mixtures containing (□) 40%, (■) 60%, (○) 80%, and (●) 100% HFIP.

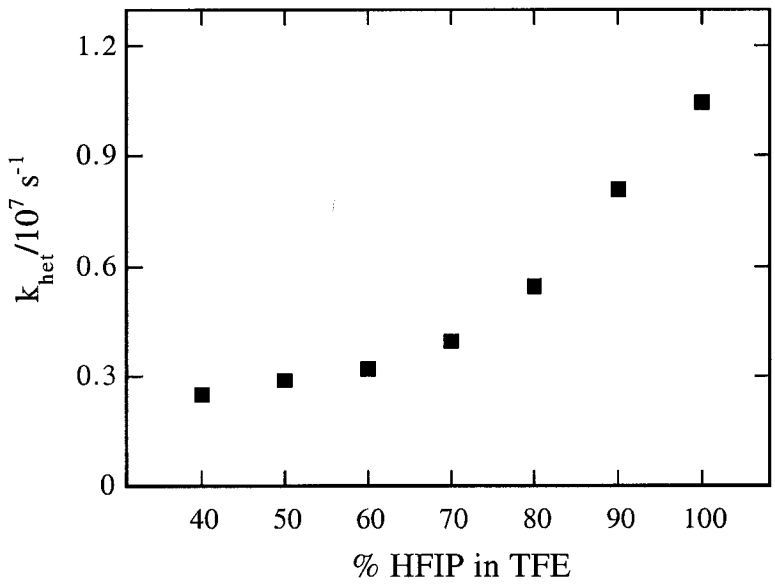

Figure 2-19. Observed rate constant for the formation of the 4-fluorostyrene radical cation **3(F)** monitored at 585 nm following 266 nm laser excitation of 2-(4-fluorophenyl)-3-oxobutylmethanesulfonate **1(F)** as a function of HFIP content in nitrogen-saturated TFE.

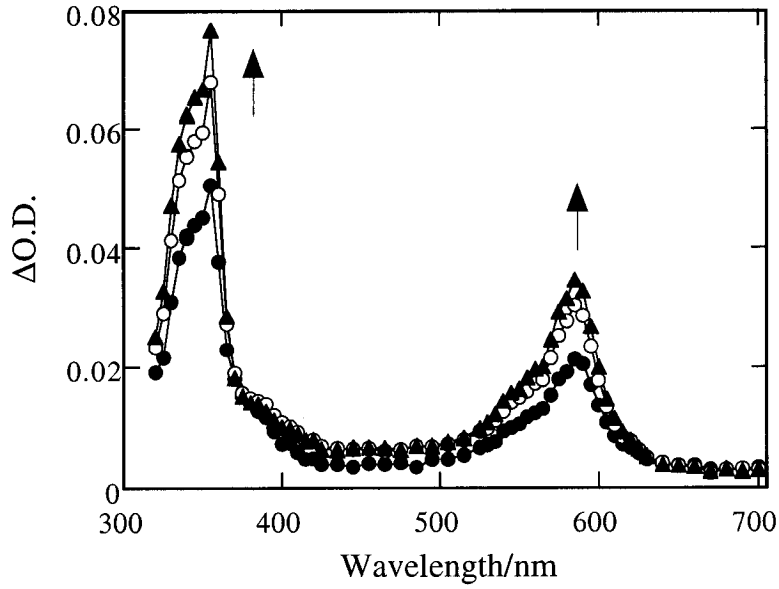

Figure 2-20. Transient absorption spectra obtained in nitrogen-saturated 80% HFIP/20% TFE after 308 nm laser excitation of 2,4-bis(4-fluorophenyl)-3-oxopentyl-methanesulfonate **1(F)-DBK**. Spectra were recorded (●) 0.072 μs, (○) 0.18 μs and (▲) 0.31 μs after the laser pulse.

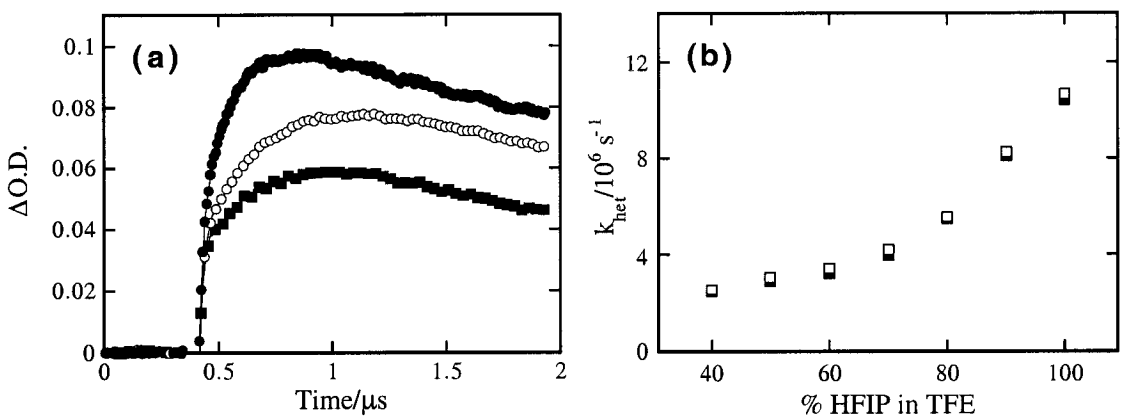

Figure 2-21. (a) Time-resolved growth curves at 355 nm observed after 308 nm laser irradiation of 2,4-bis(4-fluorophenyl)-3-oxopentylmethanesulfonate **1(F)-DBK** in nitrogen-saturated HFIP/TFE mixtures containing (□) 50%, (○) 60%, and (●) 90% HFIP. (b) Observed rate constant for the growth of the 4-fluorostyrene radical cation in nitrogen-saturated TFE as a function of HFIP content generated by (■) 266 nm and (□) 308 nm laser photolysis of (■) 2-(4-fluorophenyl)-3-oxobutylmethanesulfonate **1(F)** and (□) 2,4-bis(4-fluorophenyl)-3-oxopentylmethanesulfonate **1(F)-DBK**.

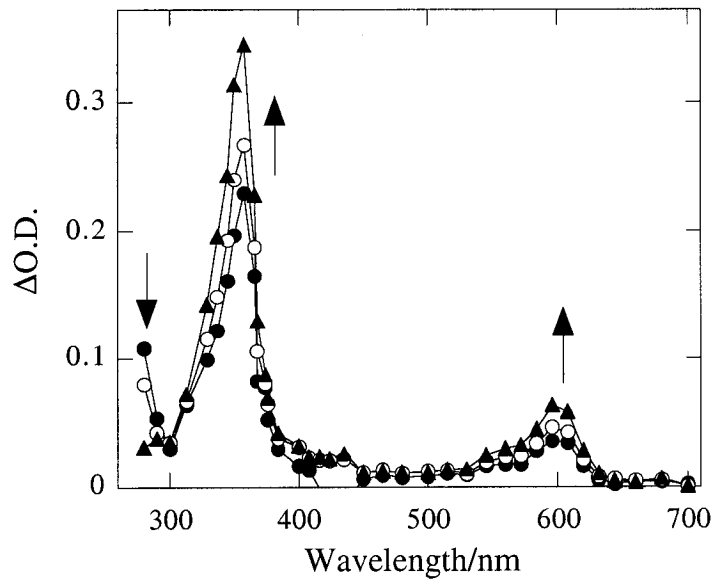

Figure 2-22. Transient absorption spectra recorded upon 266 nm laser irradiation of 2,4-bis(4-methylphenyl)-3-oxopentyl-1,5-dimethanesulfonate **1(Me)** in nitrogen-saturated 30% HFIP/70% TFE. Spectra were recorded (●) 0.066 μs, (○) 0.10 μs, and (▲) 0.30 μs after the laser pulse.

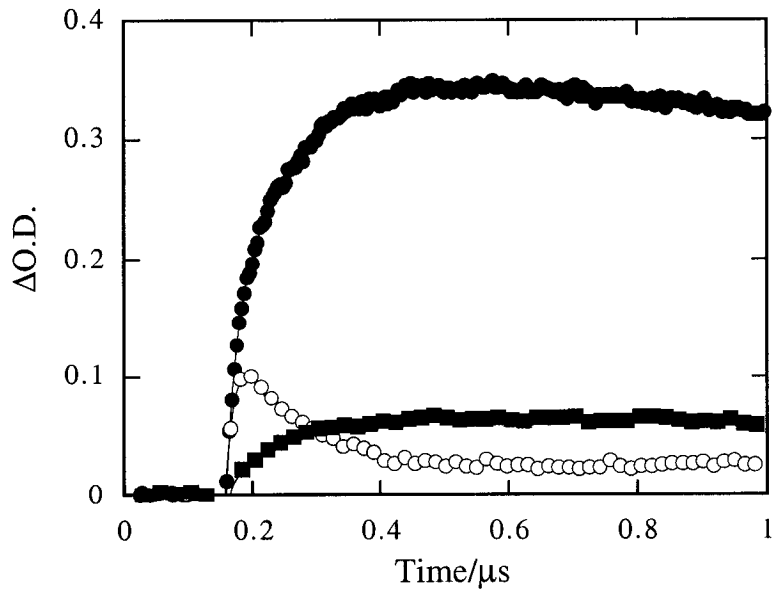

Figure 2-23. Time-resolved kinetics traces recorded at (○) 280 nm, (●) 350 nm, and (■) 590 nm following 266 nm laser irradiation of 2,4-bis(4-methylphenyl)-3-oxopentyl-1,5-dimethanesulfonate **1(Me)** in nitrogen-saturated 30% HFIP/70% TFE.

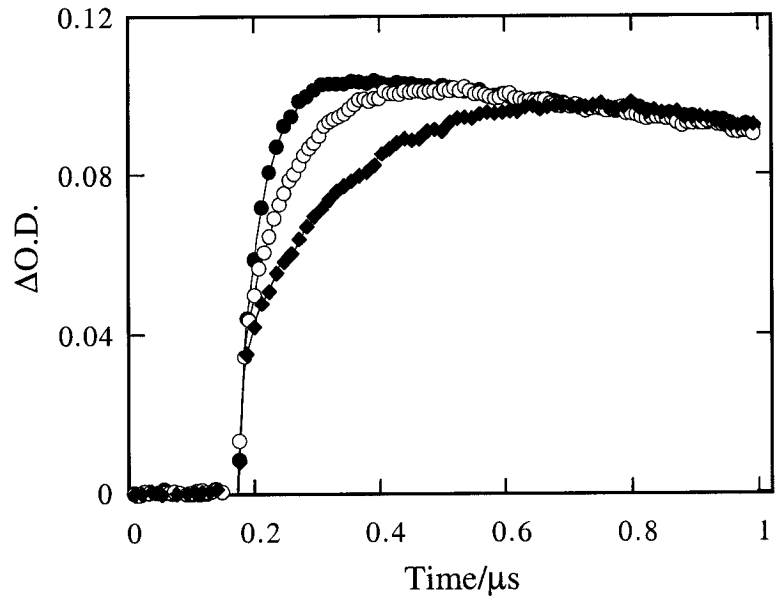

Figure 2-24. Time-resolved growth curved detected at 590 nm after 266 nm laser irradiation of 2,4-bis(4-methylphenyl)-3-oxopentyl-1,5-dimethanesulfonate **1(Me)** in nitrogen-saturated HFIP/TFE mixtures containing (◆) neat TFE, (○) 30% HFIP and (●) 50% HFIP.

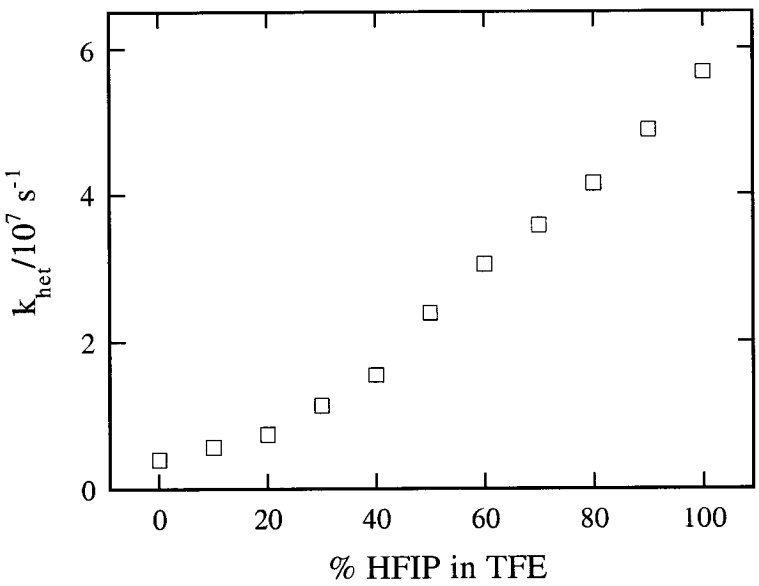

Figure 2-25. Rate constant for the growth of the 4-methylstyrene radical cation **3(Me)** following 266 nm laser excitation of 2,4-bis(4-methylphenyl)-3-oxopentyl-1,5-dimethanesulfonate **1(Me)** as a function of HFIP content in nitrogen-saturated TFE.

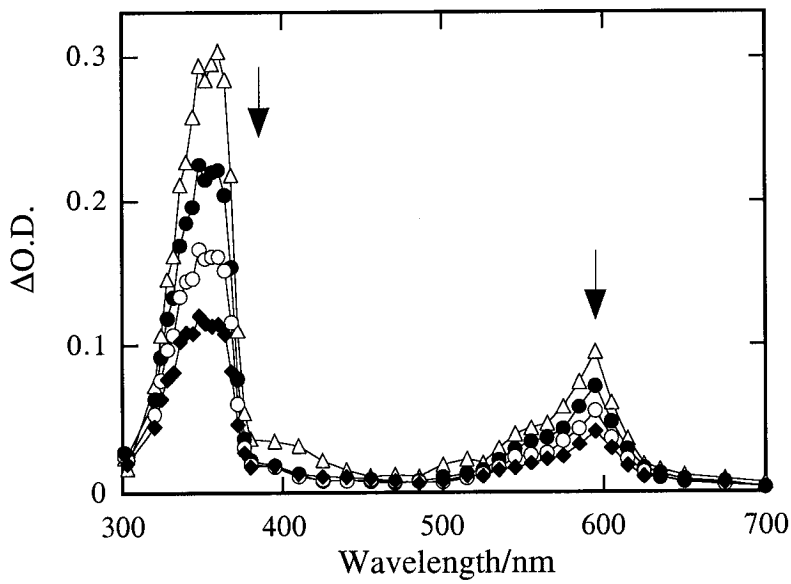

Figure 2-26. Transient absorption spectra recorded after 308 nm laser irradiation of 2-(4-methoxyphenyl)-3-oxobutylmethanesulfonate **1(OMe)** in nitrogen-saturated TFE. Spectra were recorded (Δ) 0. 60 μs, (●) 3.9 μs, (○) 8.6 μs, and (◆) 14.8 μs after the laser pulse.

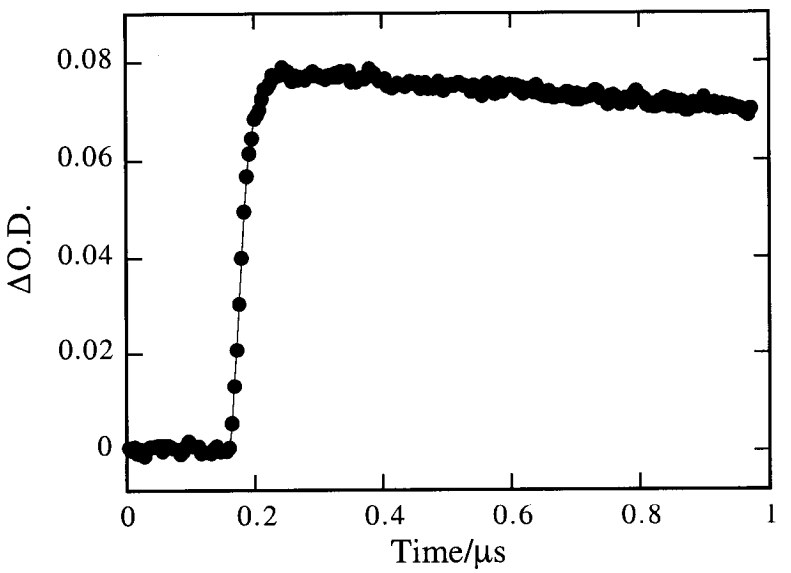

Figure 2-27. Time-resolved kinetic traces monitored at 590 nm after 308 nm laser flash photolysis of 2-(4-methoxyphenyl)-3-oxobutylmethanesulfonate **1(OMe)** in nitrogen-saturated TFE.

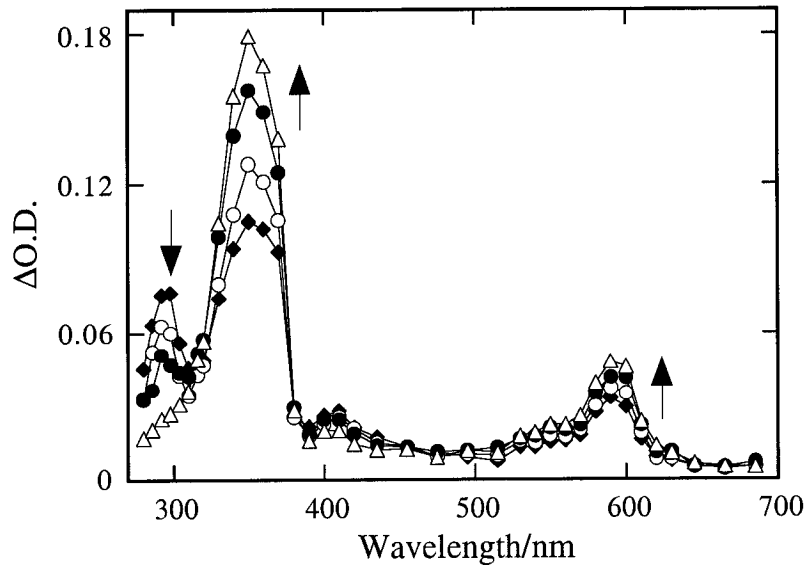

Figure 2-28. Transient absorption spectra obtained after 266 nm laser photolysis of 2-(4-methoxyphenyl)-3-oxobutylmethanesulfonate **1(OMe)** in nitrogen-saturated 50% HFIP/50% AcN. Spectra were recorded (◆) 0.082 μs, (○) 0.13 μs, (●) 0.21 μs, and (Δ) 0.45 μs after the laser pulse.

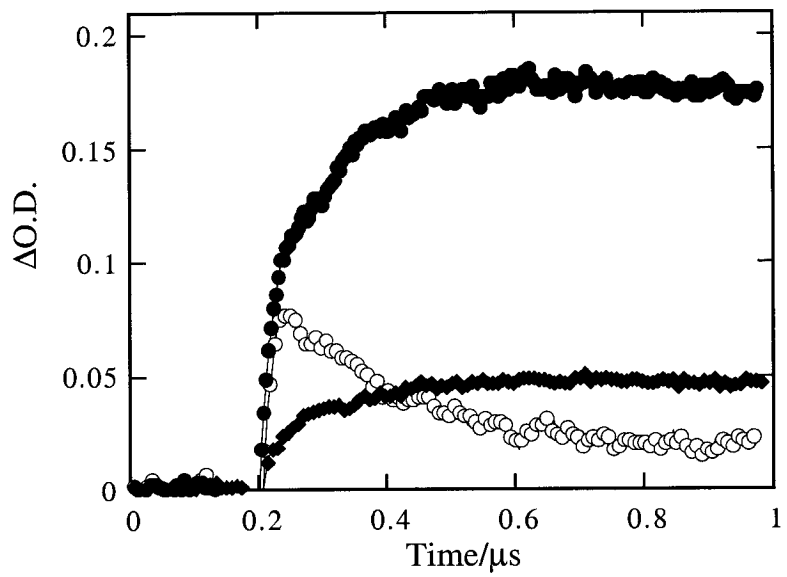

Figure 2-29. Time-resolved kinetic traces observed after 266 nm laser photolysis of 2-(4-methoxyphenyl)-3-oxobutylmethanesulfonate **1(OMe)** in nitrogen-saturated 50% HFIP/50% AcN. Traces were recorded at (○) 290 nm, (●) 350 nm and (◆) 590 nm.

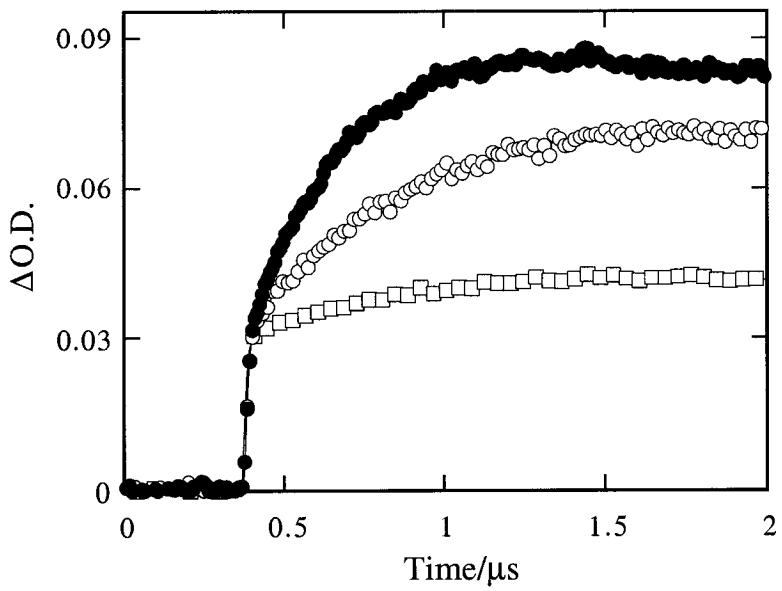

Figure 2-30. Time-resolved growth curves observed at 590 nm after 266 nm laser irradiation of 2-(4-methoxyphenyl)-3-oxobutylmethanesulfonate **1(OMe)** in nitrogen-saturated HFIP/AcN mixtures containing (□) 10%, (○) 20%, and (●) 30% HFIP.

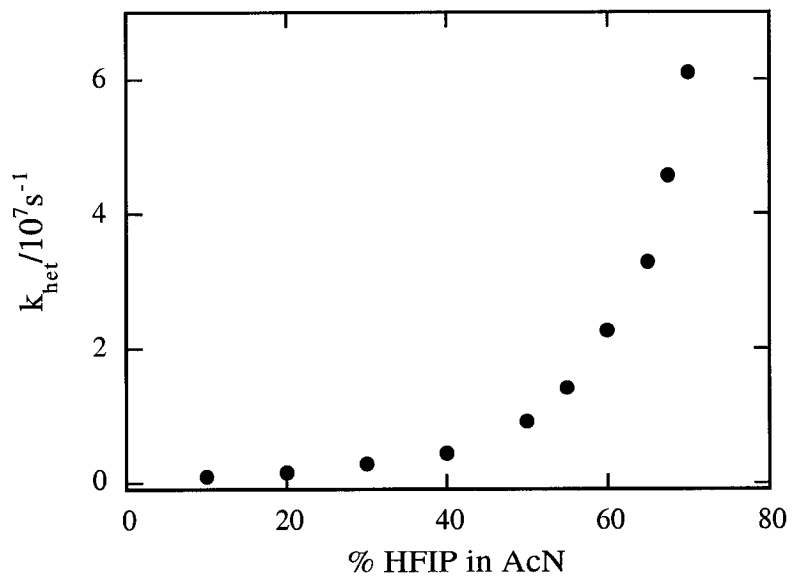

Figure 2-31. Observed rate constant for the formation of the 4-methoxystyrene radical cation **3(OMe)** after 266 nm laser irradiation of 2-(4-methoxyphenyl)-3-oxobutylmethanesulfonate **1(OMe)** as a function of HFIP content in nitrogen-saturated acetonitrile.

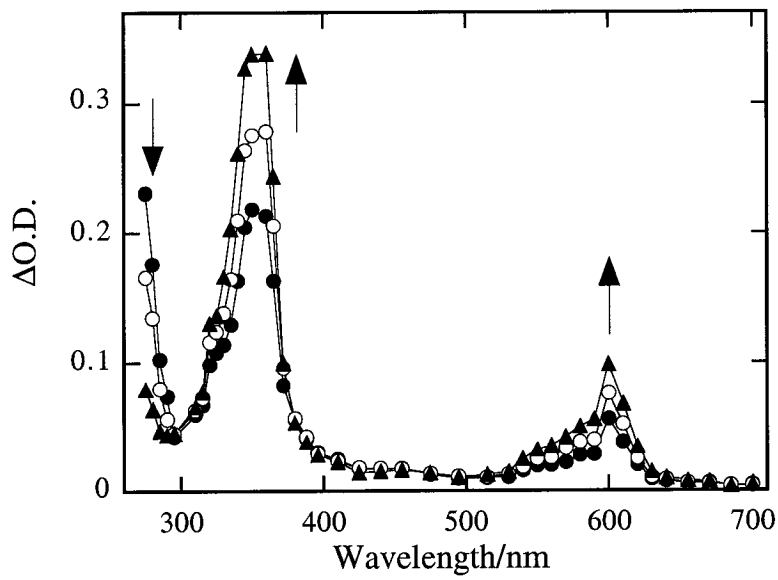

Figure 2-32. Transient absorption spectra collected upon 266 nm laser irradiation of 2,4-bis(4-methylphenyl)-3-oxopentyl-1,5-dimethanesulfonate **1(Me)** in nitrogen-saturated 80% HFIP/20% AcN. Spectra were recorded (●) 0.11 μs, (○) 0.22 μs, and (▲) 0.58 μs after the laser pulse.

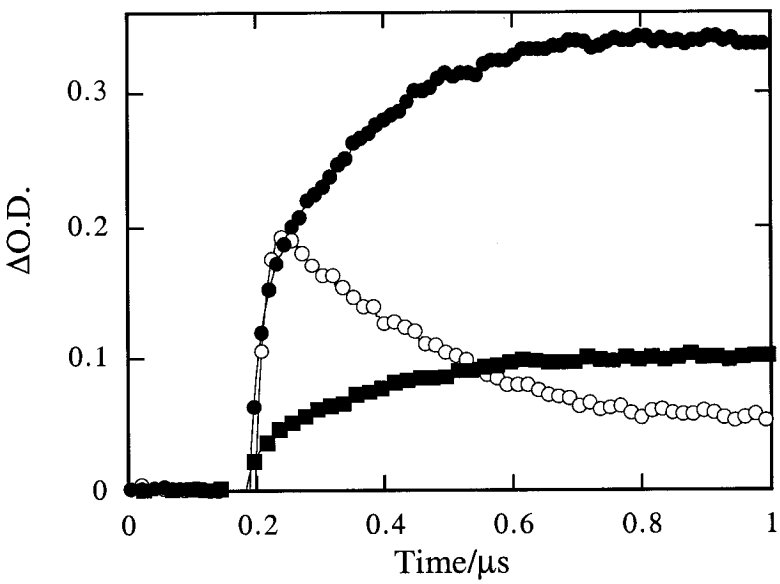

Figure 2-33. Time-resolved kinetic traces monitored at (○) 280 nm, (●) 360 nm, and (■) 600 nm after 266 nm laser irradiation of 2,4-bis(4-methylphenyl)-3-oxopentyl-1,5-dimethanesulfonate **1(Me)** in nitrogen-saturated 80% HFIP/20% AcN.

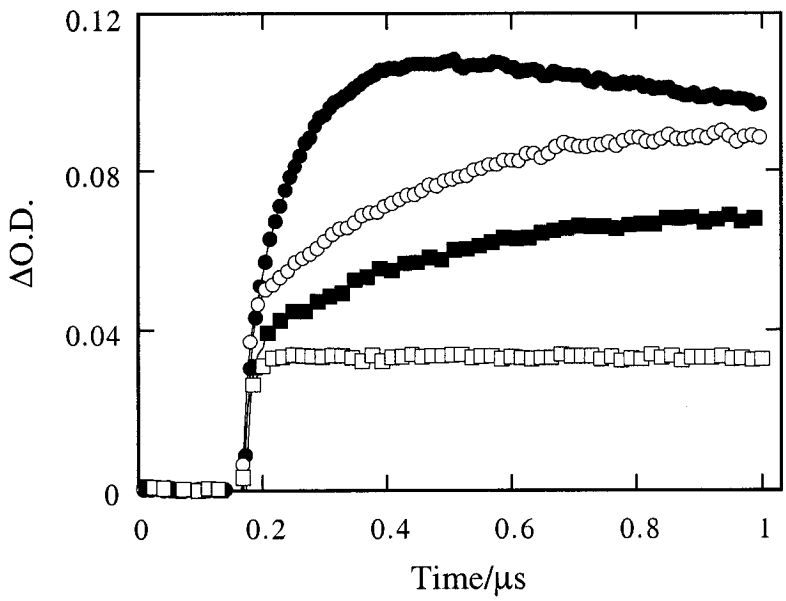

Figure 2-34. Time-resolved kinetic traces showing the growth of the 4-methylstyrene radical cation **3(Me)** upon 308 nm laser irradiation of 2,4-bis(4-methylphenyl)-3-oxopentyl-1,5-dimethanesulfonate **1(Me)** in nitrogen-saturated HFIP/AcN mixtures containing (□) 60%, (■) 70%, (○) 75%, and (●) 80% HFIP.

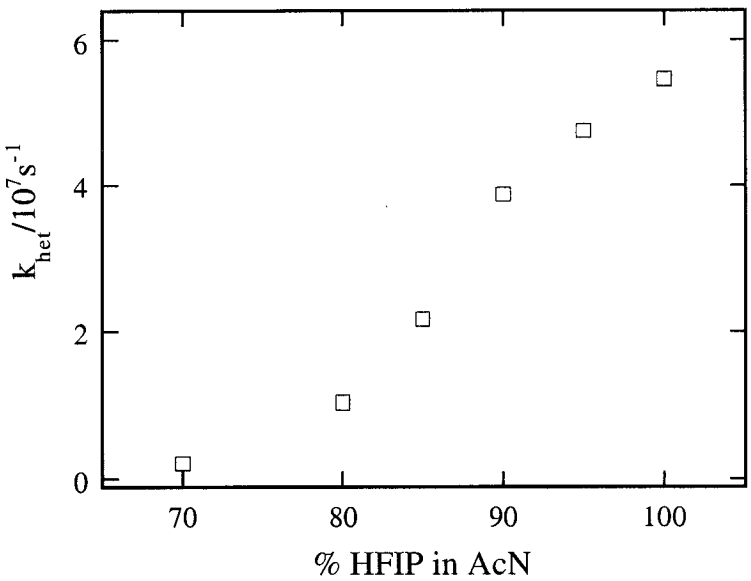

Figure 2-35. Rate constant for the growth of the 4-methylstyrene radical cation **3(Me)** after 266 nm laser irradiation of 2,4-bis(4-methylphenyl)-3-oxopentyl-1,5-dimethanesulfonate **1(Me)** as a function of HFIP content in nitrogen-saturated acetonitrile.

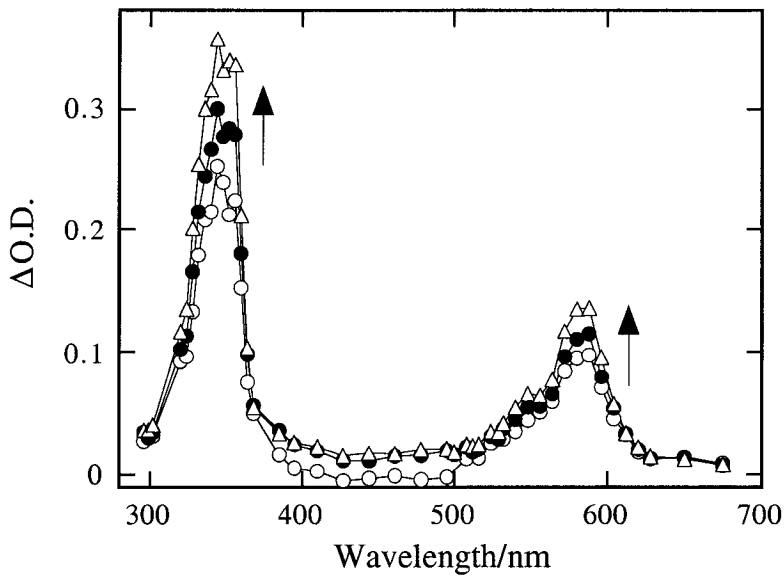

Figure 2-36. Transient absorption spectra obtained after 308 nm laser irradiation of 2-(4-fluorophenyl)-3-oxobutylmethanesulfonate **1(F)** in nitrogen-purged 95% HFIP/5% AcN. Spectra were recorded (O) 0.086 μs, (●) 0.13 μs, and (Δ) 0.33 μs following the excitation pulse.

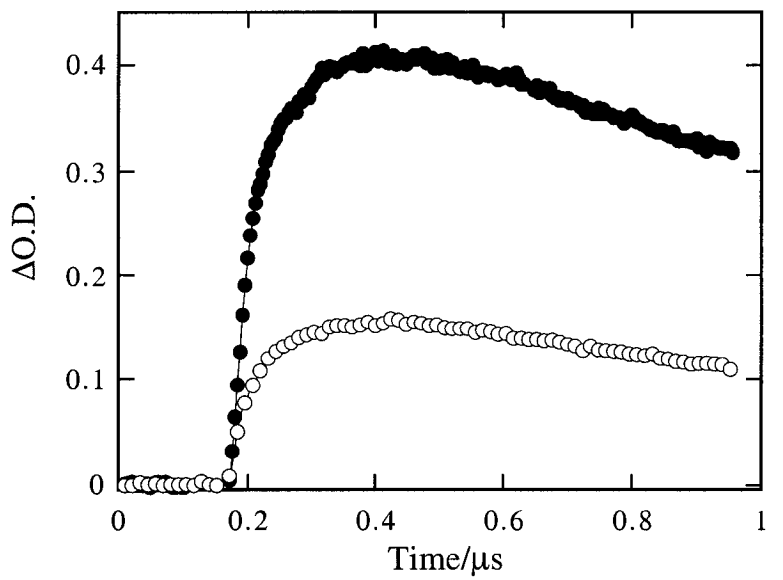

Figure 2-37. Time-resolved kinetic traces collected at (O) 585 nm and (●) 355 nm following 308 nm laser irradiation of 2-(4-fluorophenyl)-3-oxobutylmethanesulfonate **1(F)** in nitrogen-purged 95% HFIP/5% AcN.

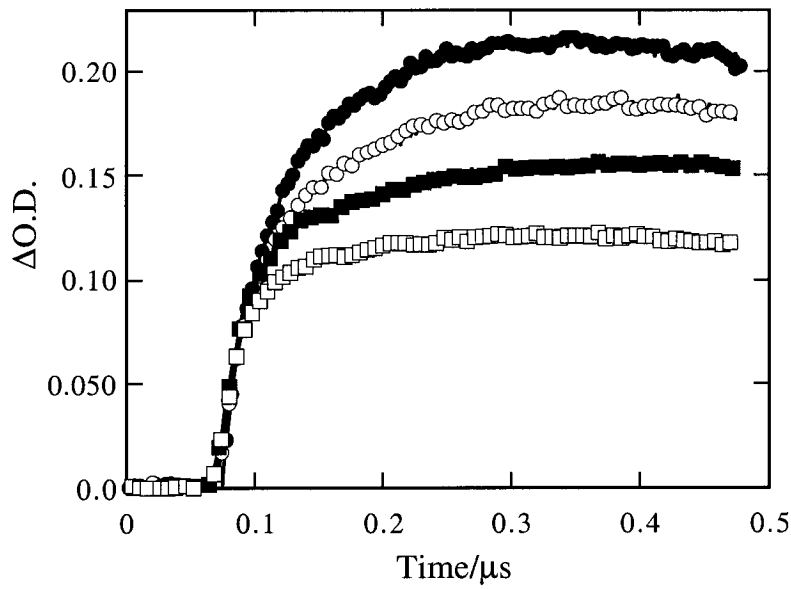

Figure 2-38. Time-resolved growth curves observed at 585 nm after 308 nm laser irradiation of 2-(4-fluorophenyl)-3-oxobutylmethanesulfonate **1(F)** in nitrogen-saturated HFIP/AcN mixtures containing (□) 82.5%, (■) 85%, (○) 90%, and (●) 95% HFIP.

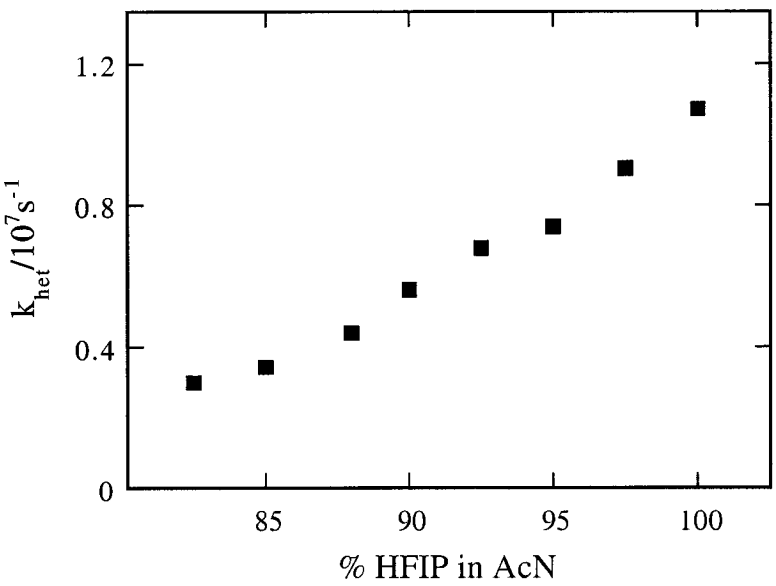

Figure 2-39. Observed rate constant for the growth of the 4-fluorostyrene radical cation **3(F)** after 308 nm laser photolysis of 2-(4-fluorophenyl)-3-oxobutylmethanesulfonate **1(F)** as a function HFIP content in nitrogen-saturated acetonitrile.

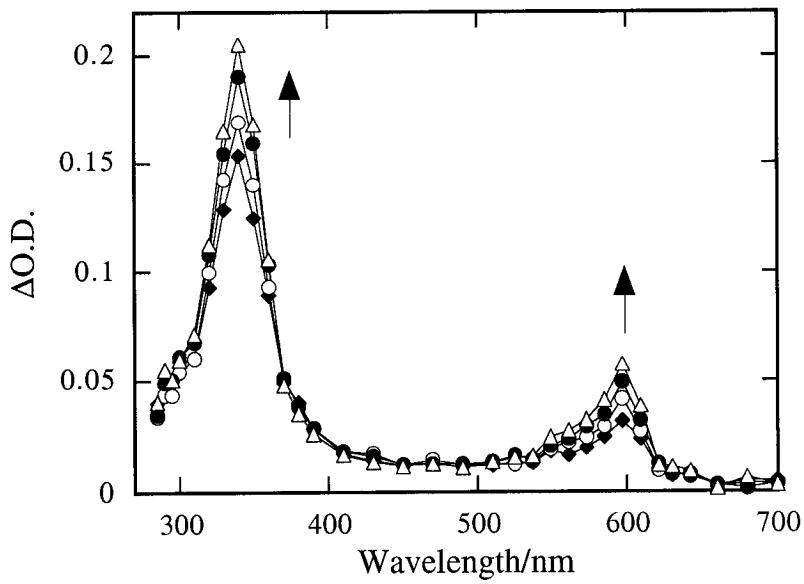

Figure 2-40. Transient absorption spectra obtained after 266 nm laser irradiation of 2,4-diphenyl-3-oxopentyl-1,5-dimethanesulfonate **1(H)** in nitrogen-saturated 95% HFIP/5% AcN. Spectra were recorded (●) 0.080 μs, (◆) 0.14 μs, (○) 0.21 μs, and (Δ) 0.38 μs after the laser pulse.

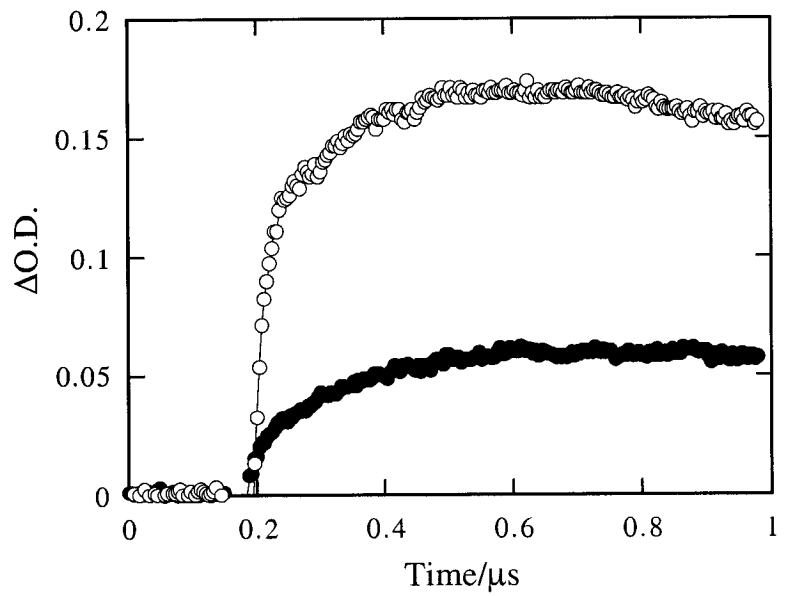

Figure 2-41. Time-resolved kinetic traces at (○) 350 nm, and (●) 600 nm following 266 nm laser excitation of 2,4-diphenyl-3-oxopentyl-1,5-dimethanesulfonate **1(H)** in nitrogen-saturated 95% HFIP/5% AcN.

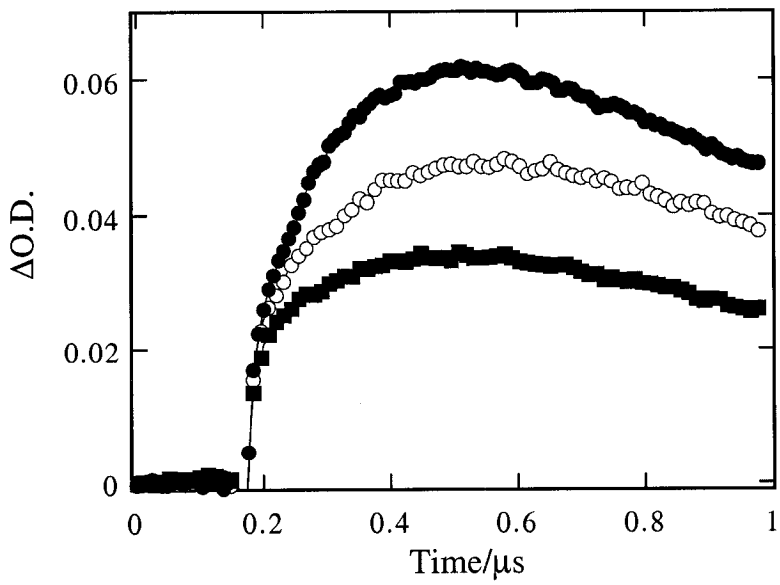

Figure 2-42. Time-resolved growth curved recorded at 600 nm after 266 nm laser irradiation of 2,4-diphenyl-3-oxopentyl-1,5-dimethanesulfonate **1(H)** in nitrogen-saturated HFIP/AcN mixtures containing (■) 90%, (○) 93%, and (●) 100% HFIP.

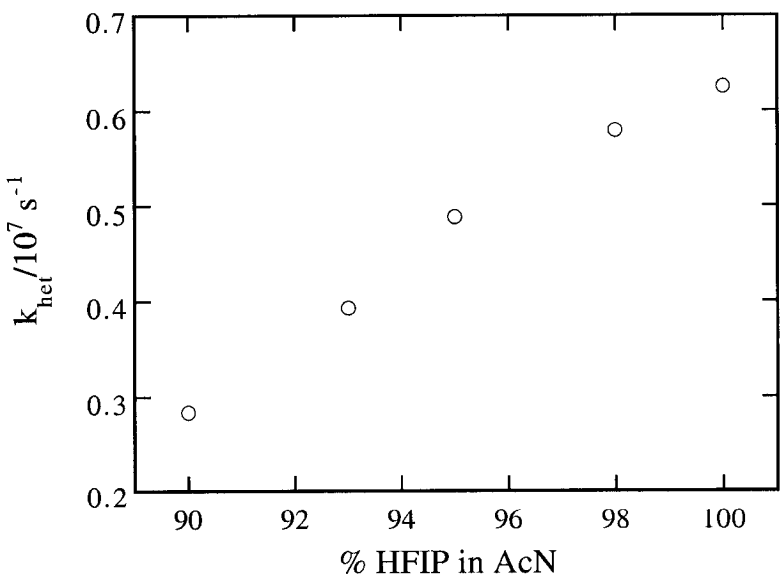

Figure 2-43. Observed rate constant for the growth of the styrene radical cation following 266 nm laser excitation of 2,4-diphenyl-3-oxopentyl-1,5-dimethanesulfonate **1(H)** as a function of HFIP content in nitrogen-saturated acetonitrile.

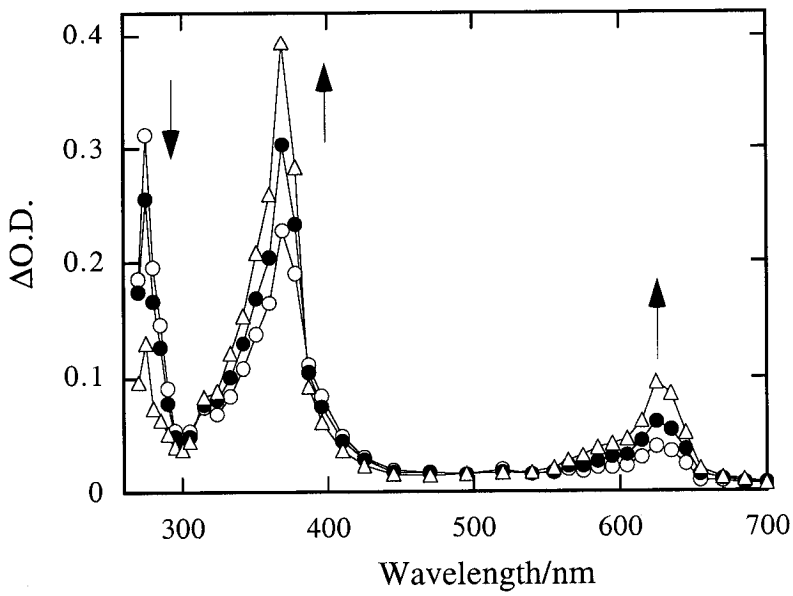

Figure 2-44. Transient absorption spectra obtained after 266 nm irradiation of 2-(4-chlorophenyl)-3-oxobutylmethanesulfonate **1(Cl)** in nitrogen-saturated 98.3% HFIP/1.7% AcN. Spectra were recorded (○) 0.14 μs, (●) 0.26 μs, and (Δ) 0.68 μs after the laser pulse.

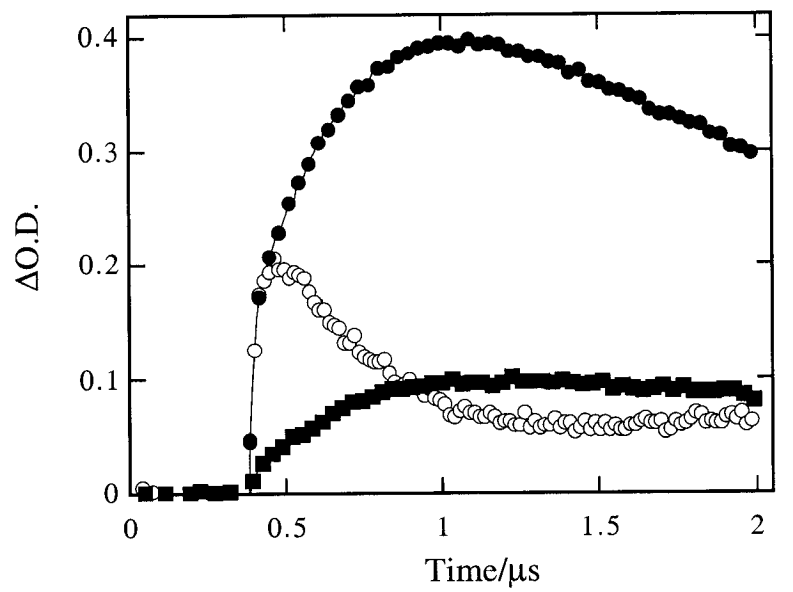

Figure 2-45. Time-resolved kinetic traces at (○) 280 nm, (●) 370 nm, and (■) 630 nm following 266 nm excitation of 2-(4-chlorophenyl)-3-oxobutylmethanesulfonate **1(Cl)** in nitrogen-saturated 98.3% HFIP/1.7% AcN.

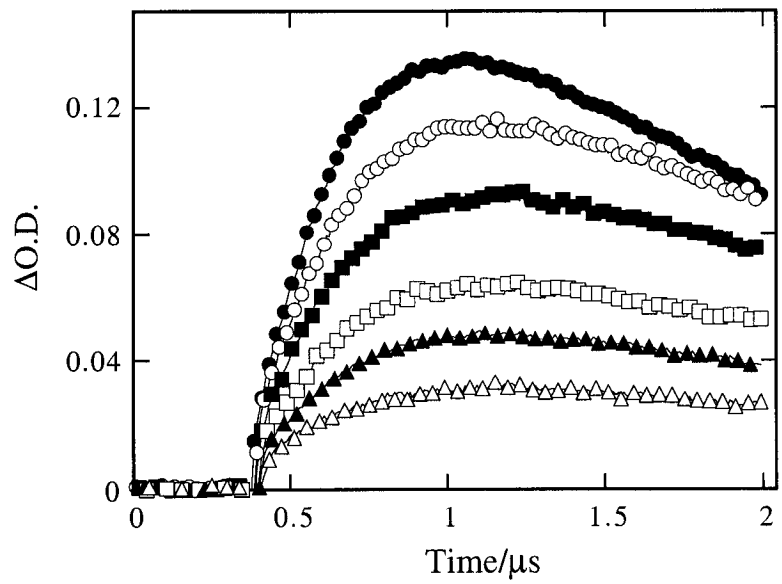

Figure 2-46. Time-resolved growth curves observed at 630 nm following 266 nm laser irradiation of 2-(4-chlorophenyl)-3-oxobutylmethanesulfonate **1(Cl)** in nitrogen-saturated HFIP/AcN mixtures containing (Δ) 94.4%, (▲) 95.7%, (□) 96.3%, (■) 97.0%, (○) 97.7%, and (●) 98.3% HFIP.

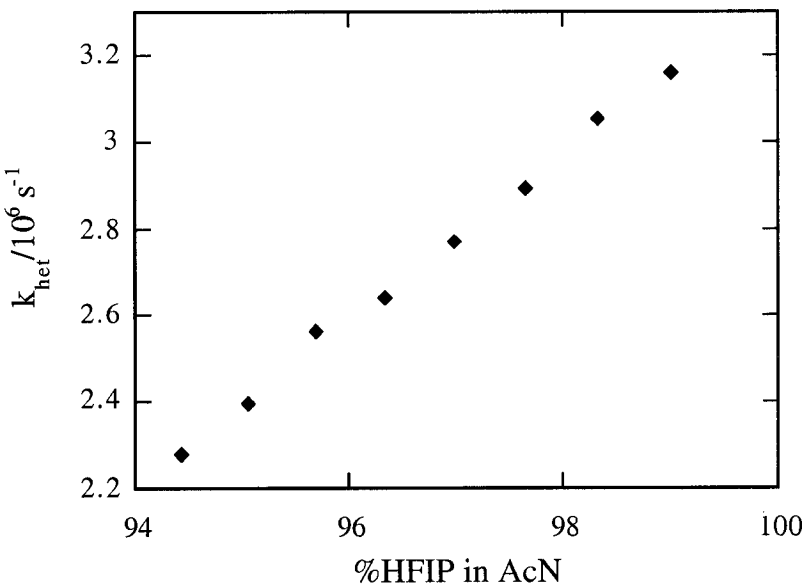

Figure 2-47. Observed rate constant for the growth of the 4-chlorostyrene radical cation **3(Cl)** observed after 266 nm laser excitation of 2-(4-chlorophenyl)-3-oxobutylmethanesulfonate **1(Cl)** and presented as a function of HFIP content in nitrogen-saturated acetonitrile.

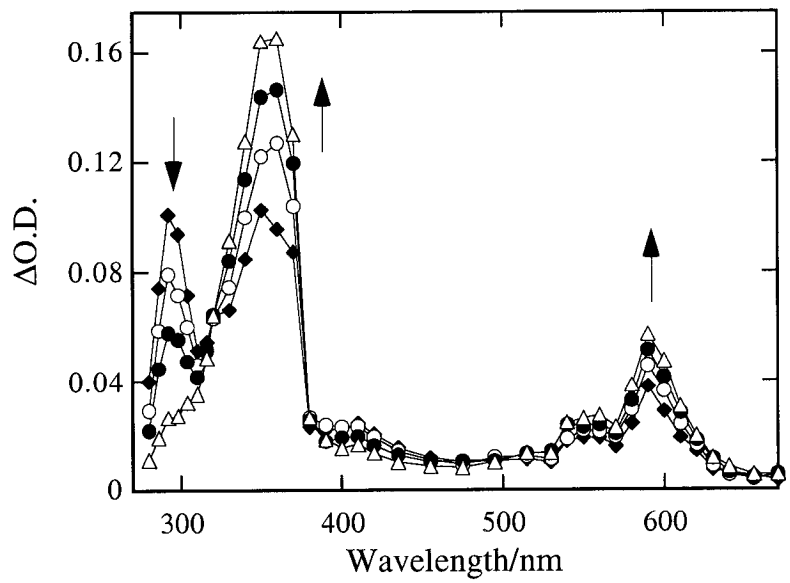

Figure 2-48. Transient absorption spectra obtained following 266 nm laser irradiation of 2-(4-methoxyphenyl)-3-oxobutylmethanesulfonate **1(OMe)** in nitrogen-saturated 50% TFE/50% AcN. Spectra were recorded (◆) 0.08 μs, (○) 0.17 μs, (●) 0.28 μs, and (Δ) 0.67 μs after the laser pulse.

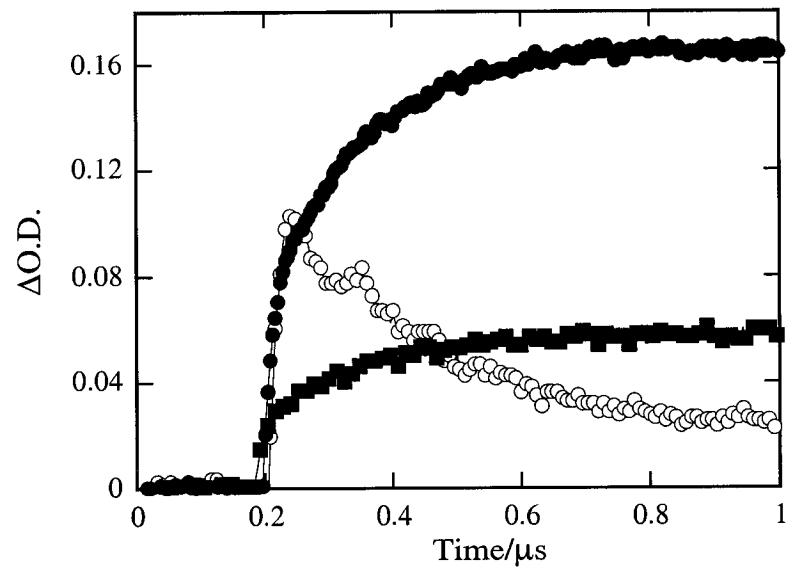

Figure 2-49. Time-resolved traces obtained after 266 nm laser flash photolysis of 2-(4-methoxyphenyl)-3-oxobutylmethanesulfonate **1(OMe)** in nitrogen-saturated 50% TFE/50% AcN. Traces were recorded at (○) 290 nm, (●) 350 nm, and (■) 590 nm.

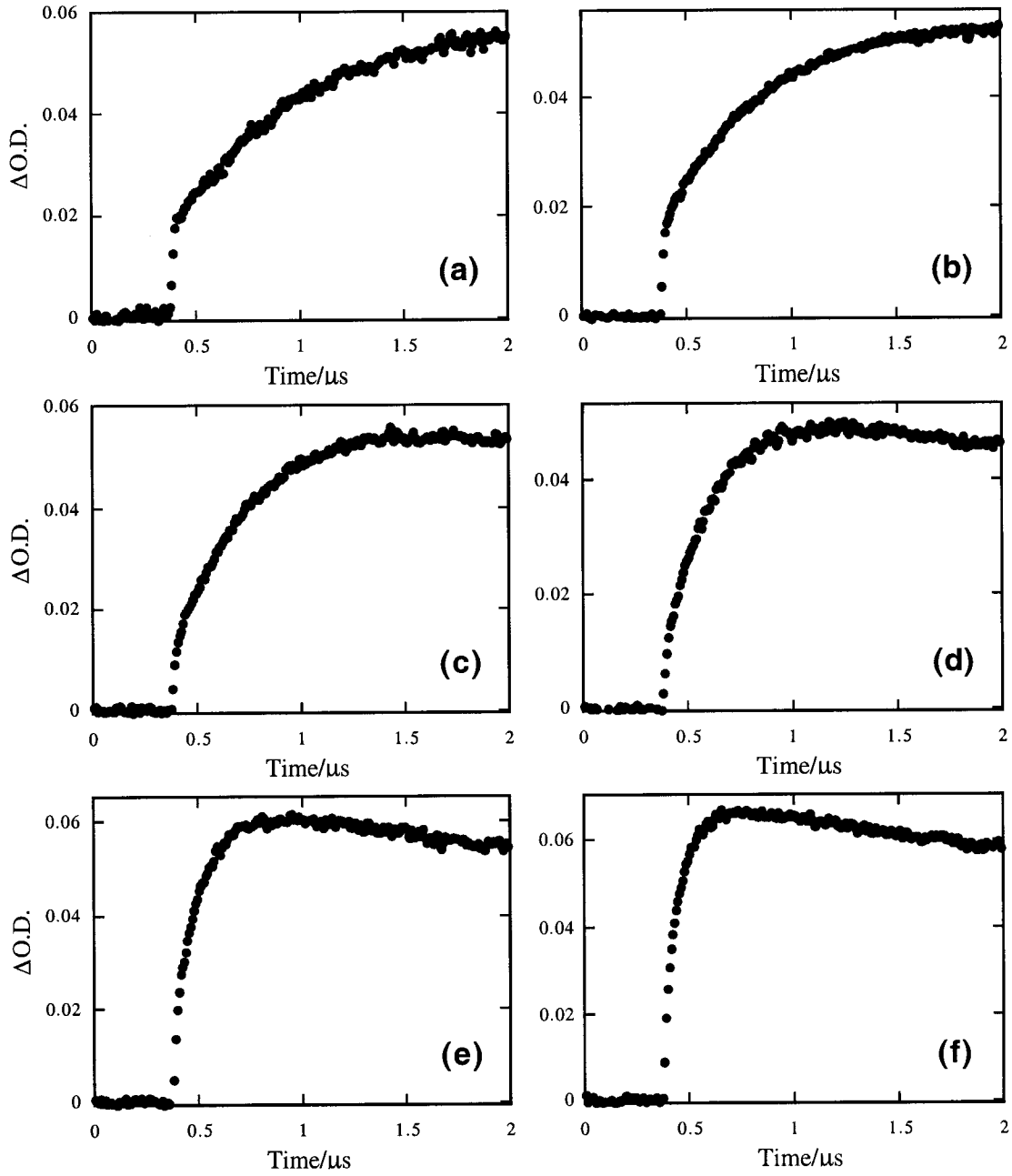

Figure 2-50. Time-resolved growth curves generated by absorption at 590 nm of the 4-methoxystyrene radical cation **3(OMe)** in TFE/AcN solvent mixtures containing (a) 20%, (b) 30%, (c) 40%, (d) 50%, (e) 60%, and (f) 70% TFE. Traces were obtained upon 266 nm laser irradiation of 2-(4-methoxyphenyl)-3-oxobutylmethanesulfonate **1(OMe)**.

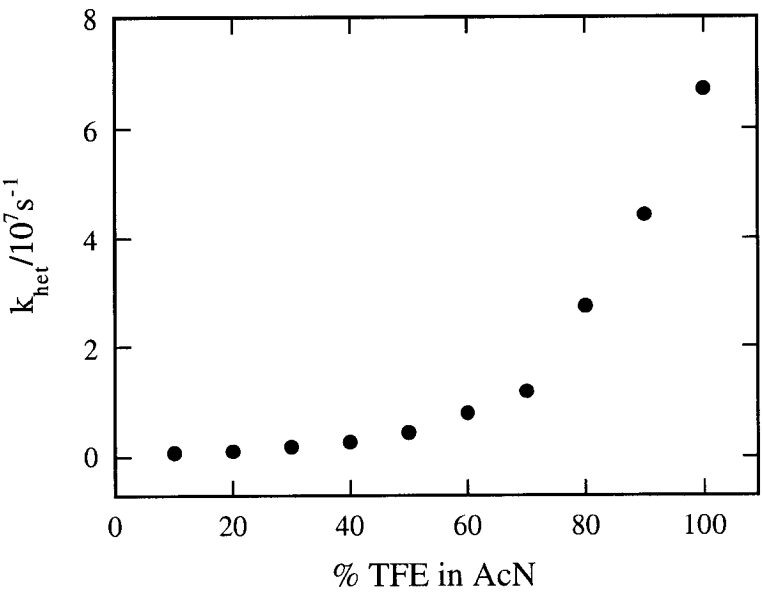

Figure 2-51. Observed rate constant for the build-up of the 4-methoxystyrene radical cation **3(OMe)** after 266 nm laser irradiation of 2-(4-methoxyphenyl)-3-oxobutylmethanesulfonate **1(OMe)** and presented as a function of TFE content in nitrogen-saturated acetonitrile.

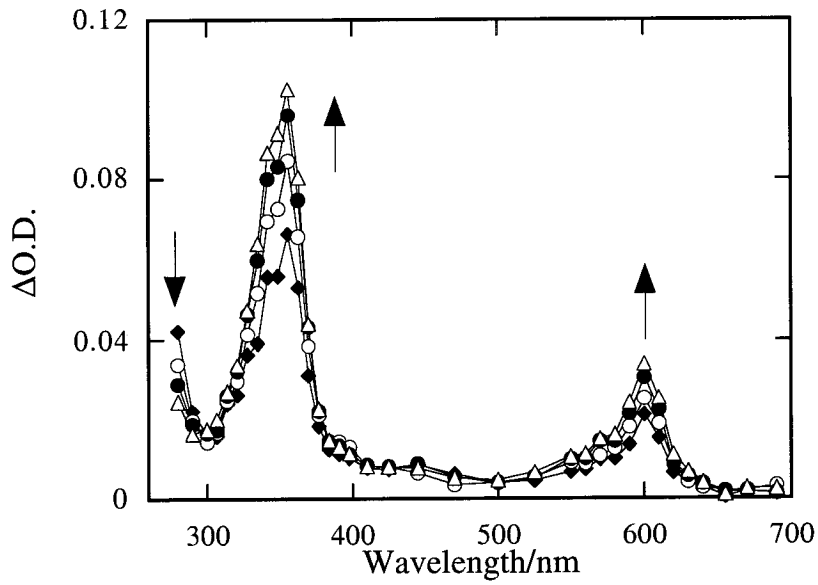

Figure 2-52. Transient absorption spectra collected following 266 nm laser irradiation of 2,4-bis(4-methylphenyl)-3-oxopentyl-1,5-dimethanesulfonate **1(Me)** in nitrogen-saturated TFE. Spectra were recorded (◆) 0.16 μs, (○) 0.24 μs, (●) 0.36 μs, and (Δ) 0.61 μs after the laser pulse.

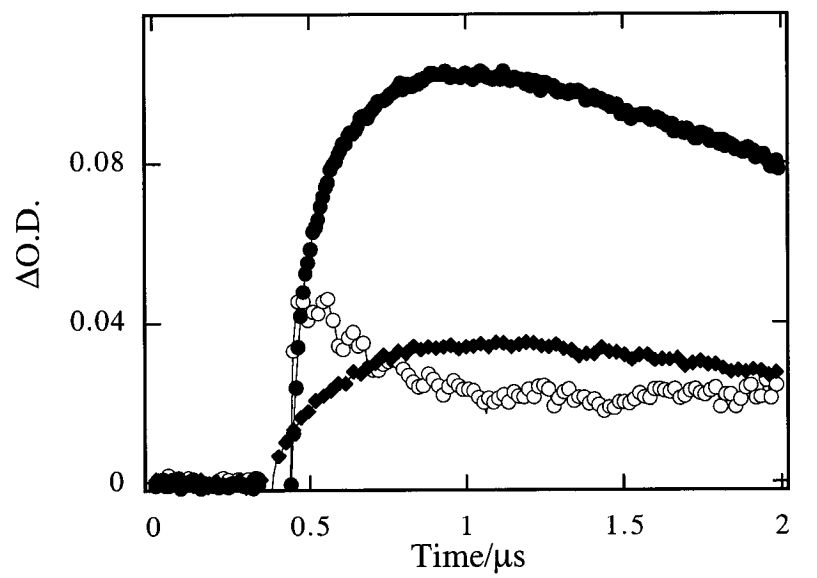

Figure 2-53. Time-resolved kinetic traces monitored at (○) 280 nm, (●) 360 nm and (◆) 600 nm following 266 nm laser flash photolysis of 2,4-bis(4-methylphenyl)-3-oxopentyl-1,5-dimethanesulfonate **1(Me)** in nitrogen-saturated TFE.

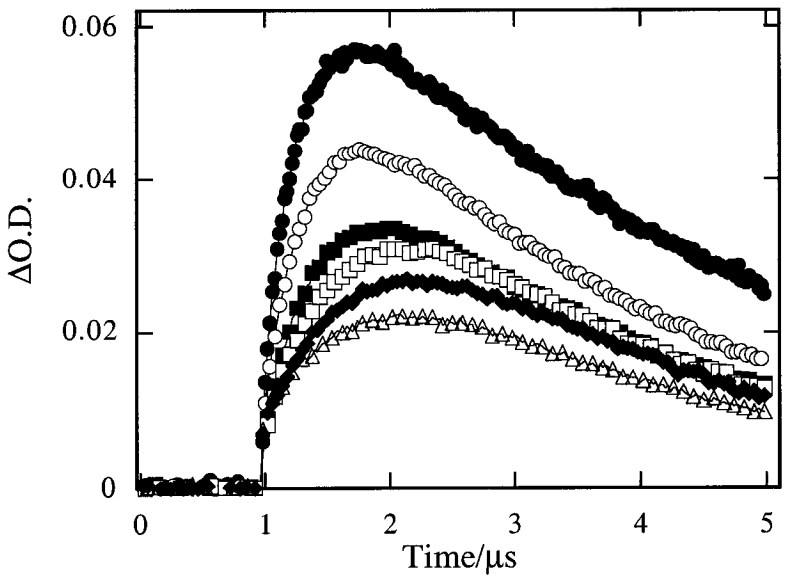

Figure 2-54. Time-resolved growth curves observed at 600 nm following 266 nm laser irradiation of 2,4-bis(4-methylphenyl)-3-oxopentyl-1,5-dimethanesulfonate **1(Me)** in nitrogen-saturated AcN containing (Δ) 80%, (◆) 85%, (□) 90%, (■) 95%, (○) 97%, and (●) 100% TFE.

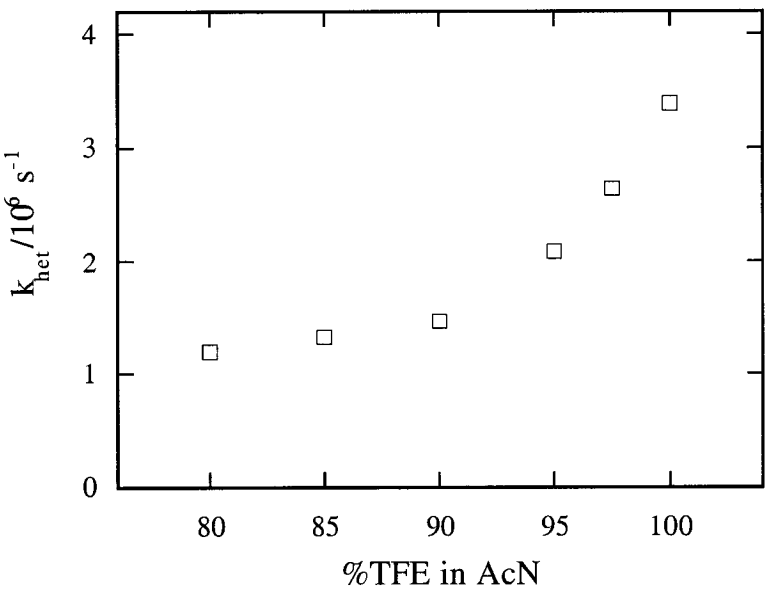

Figure 2-55. Observed rate constant for the build-up of the 4-methylstyrene radical cation **3(Me)** after 266 nm laser irradiation of 2,4-bis(4-methylphenyl)-3-oxopentyl-1,5-dimethanesulfonate **1(Me)** and presented as a function of TFE content in nitrogen-saturated acetonitrile.

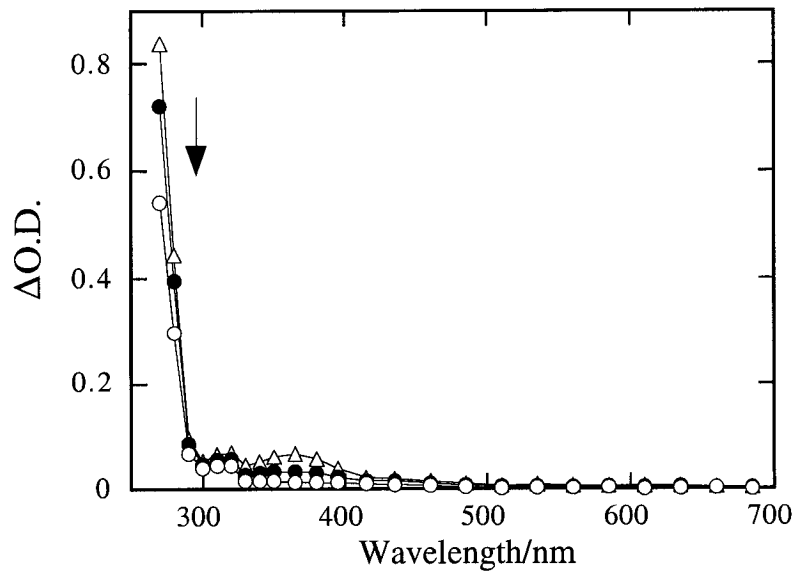

Figure 2-56. Transient absorption spectra obtained after 266 nm laser irradiation of 2-(4-chlorophenyl)-3-oxobutylmethanesulfonate **1(Cl)** in nitrogen-saturated TFE. Spectra were recorded (Δ) 0.29 μs, (●) 1.30 μs, and (○) 3.81 μs after the laser pulse.

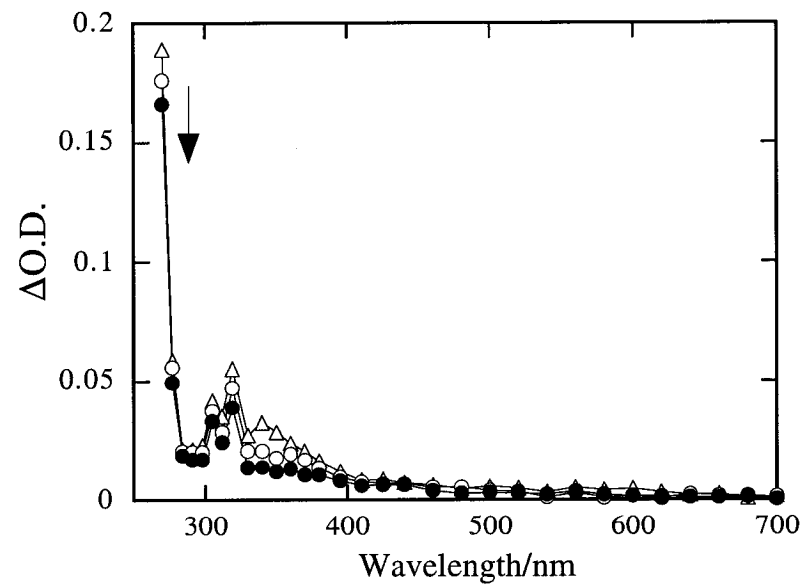

Figure 2-57. Transient absorption spectra collected after 266 nm laser flash photolysis of 2,4-diphenyl-3-oxopentyl-1,5-dimethylsulfonate **1(H)** in nitrogen-saturated TFE. Spectra were recorded (Δ) 0.092 μs, (○) 0.56 μs, and (●) 1.54 μs after the laser pulse.

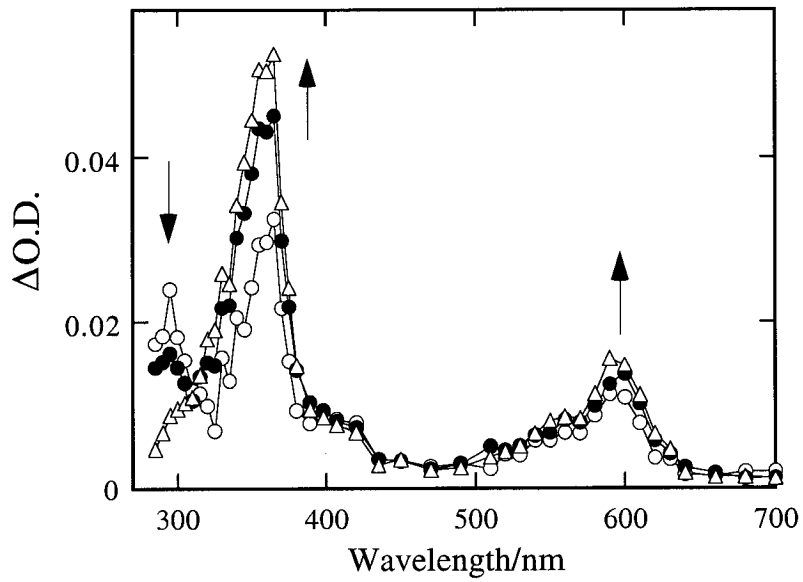

Figure 2-58. Transient absorption spectra generated after 266 nm laser irradiation of 2-(4-methoxyphenyl)-3-oxobutylmethanesulfonate **1(OMe)** in nitrogen-saturated 30% water/70% acetonitrile. Spectra were recorded (●) 0.16 μs, (○) 0.26 μs and (Δ) 0.53 μs after the laser pulse.

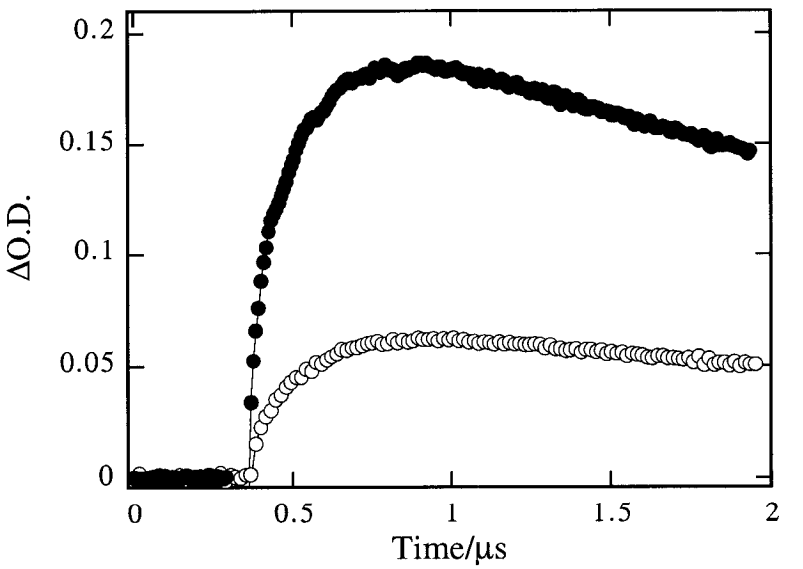

Figure 2-59. Time-resolved kinetic traces at (●) 350 nm and (○) 590 nm collected after 266 nm laser irradiation of 2-(4-methoxyphenyl)-3-oxobutylmethanesulfonate **1(OMe)** in nitrogen-saturated 30% water/70% acetonitrile.

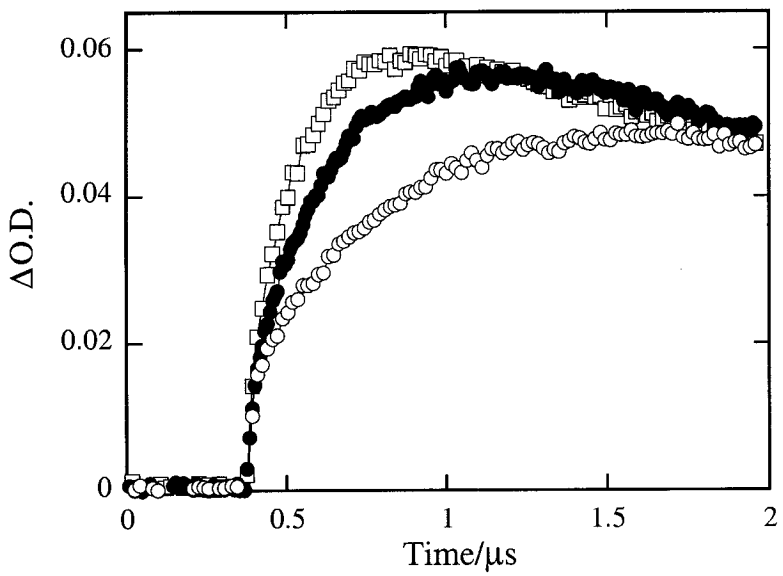

Figure 2-60. Time-resolved kinetic traces at 590 nm showing the growth of the 4-methoxystyrene radical cation following 266 nm laser irradiation of 2-(4-methoxyphenyl)-3-oxobutylmethanesulfonate **1(OMe)** in water/acetonitrile mixtures containing (○) 10%, (●) 20%, and (□) 30% water.

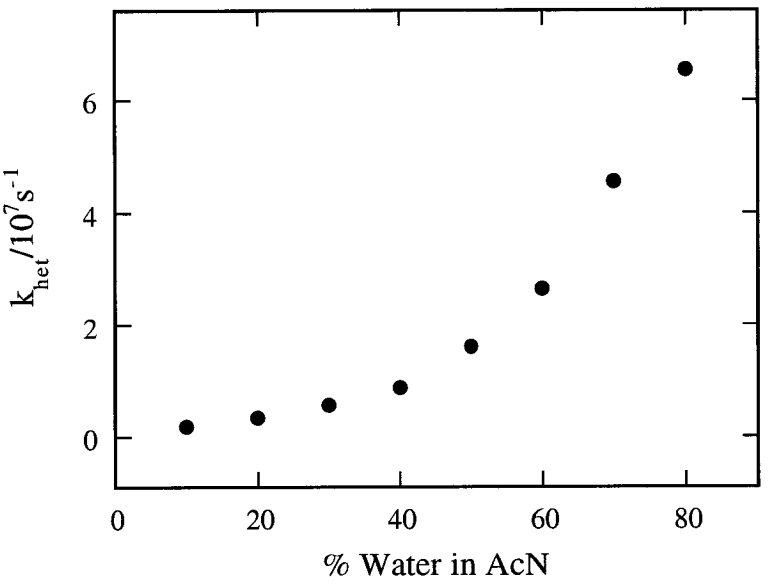

Figure 2-61. Observed rate constant for the growth of the 4-methoxystyrene radical cation **3(OMe)** at 590 nm observed after 266 nm laser irradiation of 2-(4-methoxyphenyl)-3-oxobutylmethanesulfonate **1(OMe)** and presented as a function of water content in nitrogen-saturated acetonitrile.

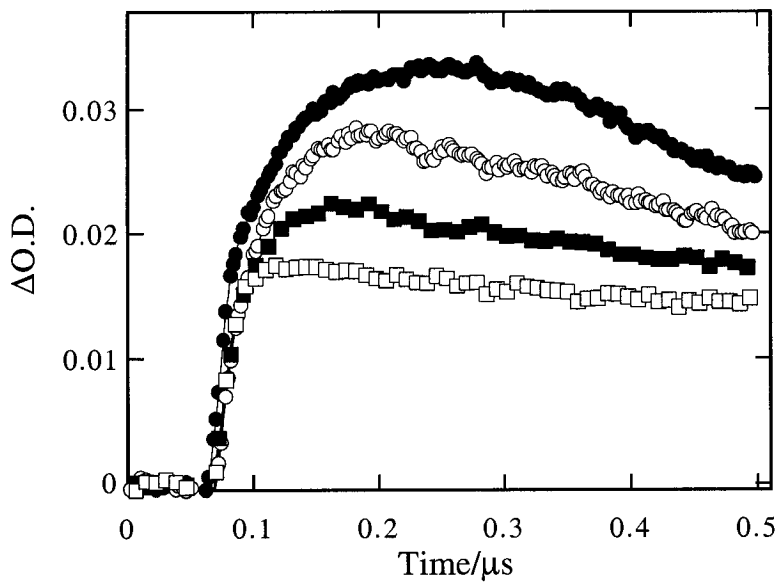

Figure 2-62. Time-resolved growth curves detected at 590 nm following 266 nm laser photolysis of 2-(4-methoxyphenyl)-3-oxobutylmethanesulfonate **1(OMe)** in nitrogen-saturated water/methanol mixtures containing (●) 10%, (○) 30%, (■) 40%, and (□) 60% water.

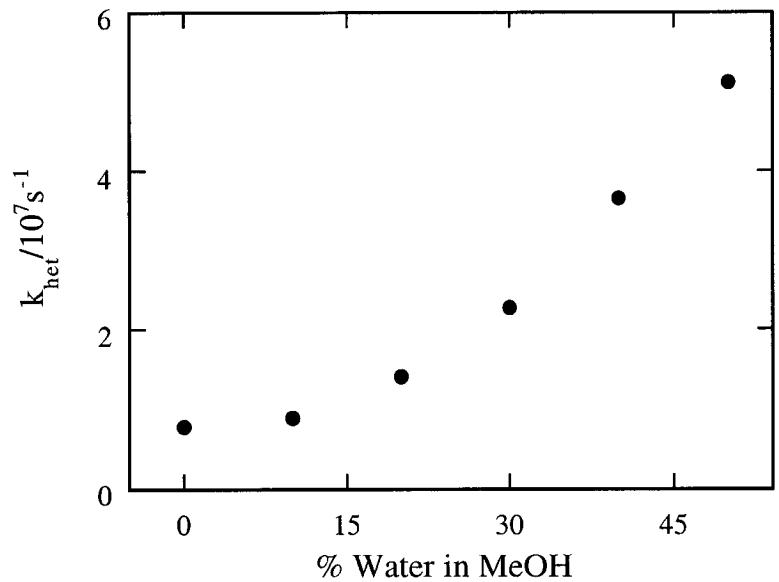

Figure 2-63. Observed rate constant for the growth of the 4-methoxystyrene radical cation following 266 nm laser photolysis of 2-(4-methoxyphenyl)-3-oxobutylmethanesulfonate **1(OMe)** presented as a function of water content in nitrogen-purged methanol.

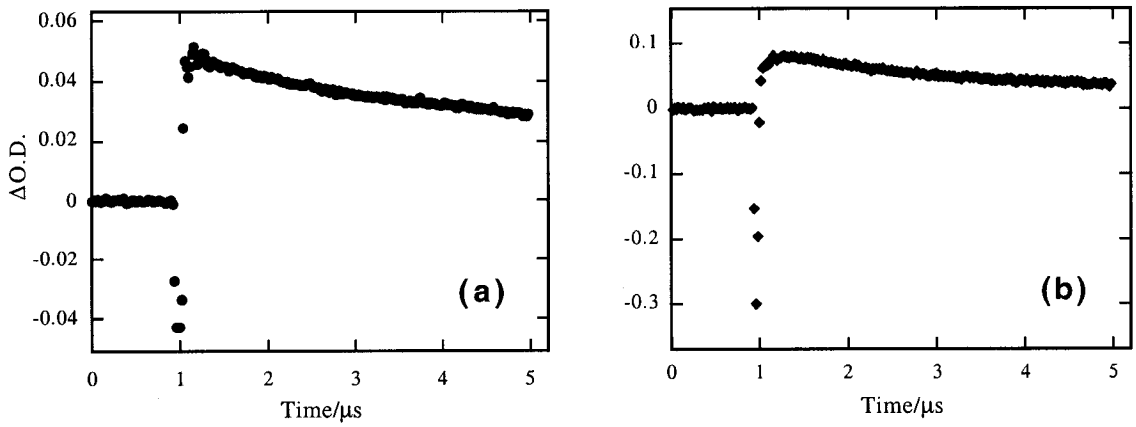

Figure 2-64. Time-resolved kinetic traces monitored at 316 nm for 2,4-diphenyl-3-oxopentyl-1,5-dimethanesulfonate **1(H)** in (a) acetonitrile and (b) HFIP following 266 nm laser flash photolysis.

2.3 Discussion

Spectroscopic evidence and kinetic calculations make it clear that the reactivity of substituted β-mesylate radicals **2(X)** is heavily dependent on the properties of the medium in which they are generated, Scheme 2-9.

Scheme 2-9

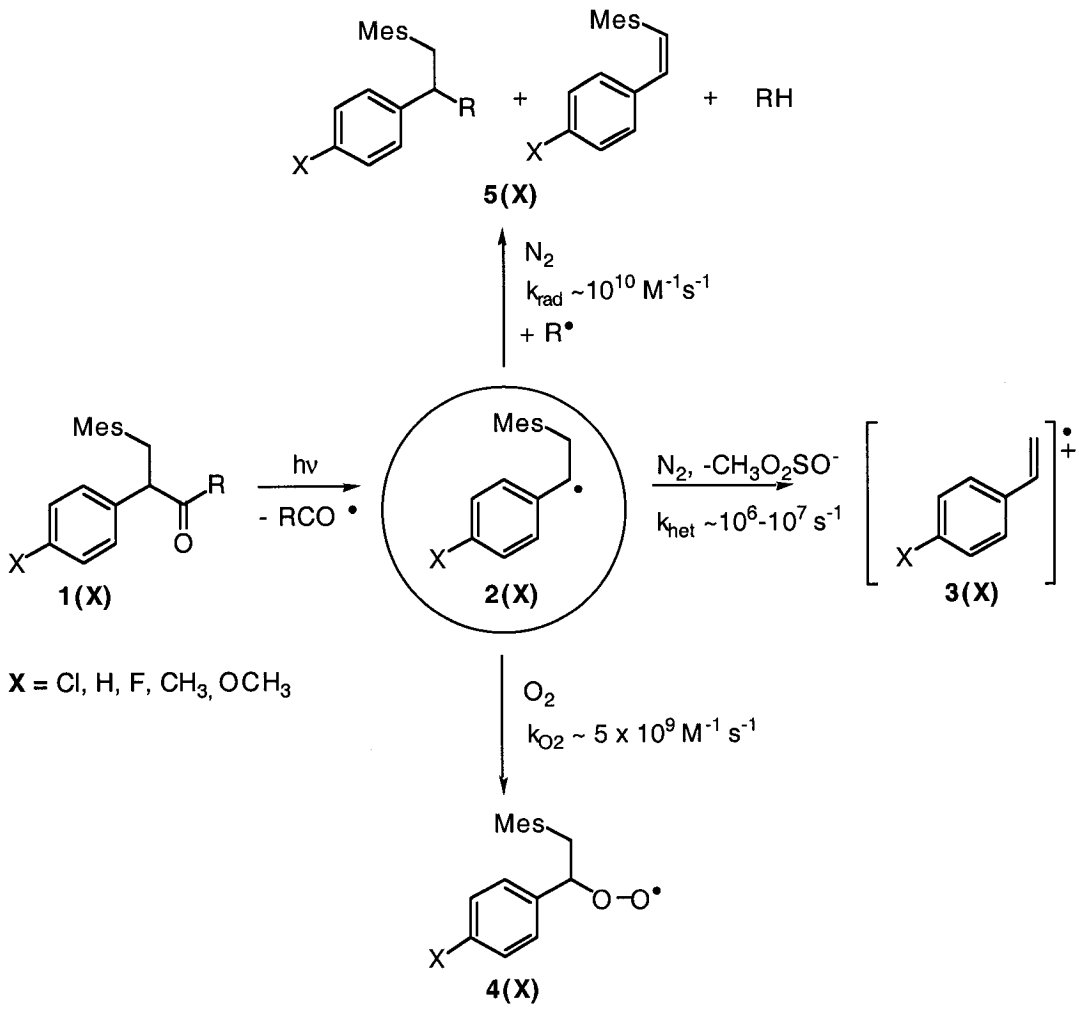

When formed in nitrogen-purged AcN, radicals **2(X)** were found to be relatively long-lived and to decay in a second-order fashion. This kinetic behavior suggests that reaction pathways such as radical-radical recombination and disproportionation predominate to give spin-paired products **5(X)**. The results presented no evidence to indicate that in AcN radicals **2(X)** undergo heterolytic loss of the

β-mesylate group, suggesting that this reaction is kinetically too slow to compete with radical-radical coupling. These findings can be explained by taking a closer look at the solvation requirements of the two reactions. Open shell reactions typically show minimal (if any) dependence on solvent effects since the reacting species remain neutral throughout the reaction. Contrarily, the β-heterolysis process yields formally charged products, namely a radical cation/anion pair. As heterolysis of the carbon-leaving group bond progresses, charge separation polarizes the radical substrate upon reaching the transition state. The energies of the transition state and products, and in turn the value of k_{het}, will be strongly influenced by the solvent's ability to provide stabilizing interactions. With the β-heterolysis reaction being highly dependent on solvation, the activation barrier for the ionization of the β-mesylate group in AcN likely remains too high for it to compete kinetically against the bimolecular radical-radical recombination.

In a highly ionizing solvent such as HFIP where charge formation is facilitated through efficient solvation, the lifetimes of radicals **2(X)** are much shorter than in AcN and the decay of the radicals follows first-order kinetics under nitrogen-saturated conditions. Time-resolved growth of the radical cations **3(X)** monitored at characteristic absorption bands near 350 and 600 nm provides convincing evidence that in HFIP the principal decay pathway for radicals **2(X)** is *via* the β-heterolysis reaction. Unlike AcN, the strong ionizing ability of HFIP provides additional stability to the polarized transition state as well as to the charged products, resulting in a significant lowering of the activation energy for this process. The rate constants calculated for this ionization process were determined to be in the order of 10^6-10^7 s^{-1}. (It is worth clarifying that while the magnitude of k_{rad} is at the diffusion-controlled limit, ~ 10^{10} M^{-1} s^{-1}, the rate of this bimolecular process is proportional to k_{rad}[**2(X)**][R], where R is another molecule of **2(X)**, or another radical generated during α-cleavage. Since the radicals generated within the

laser flash are in low concentrations, the overall rate of radical coupling is slow relative to the β-heterolysis process.)

Upon the addition of oxygen to solutions in which radical cation formation had previously been observed under nitrogen conditions, the transient signals of radicals **2(X)** and radical cations **3(X)** were entirely quenched. As an efficient scavenger of carbon-centered radicals, oxygen is expected to react with radicals **2(X)** at close to the diffusion-controlled limit resulting in an observed rate constant exceeding that of the β-heterolysis reaction. Rate constants k_{O2} for the quenching of benzyl-type radicals are reported within the range of 1.6-4.9 $\times$ 10^9 M^{-1} s^{-1} and are not very sensitive to solvent.[126] With a quenching process close to the diffusion-controlled limit available to the radicals in oxygenated conditions, the end result is rapid and irreversible depletion of **2(X)** to form peroxyl radicals **4(X)**. Under such conditions, the radical cation was not detected since the ionization reaction cannot compete kinetically.

2.3.1 Structural Electronic Effects

The results of this study show that an unquestionable correlation exists between the electronic nature of the aromatic substituent and the magnitude of the rate constants calculated for the ionization of radicals **2(X)**. To emphasize the point, Figure 2-65 shows the time-resolved growth of the radical cation in nitrogen-saturated 70% HFIP/30% TFE for four of the radicals studied, **2(Cl)**, **2(H)**, **2(F)**, and **2(Me)**. It is evident from these kinetic traces that the rise in signal, corresponding to radical cation formation *via* the β-heterolysis reaction, is strongly affected by the aromatic substituent X. Under otherwise identical experimental conditions, k_{het} for the β-heterolysis reaction jumps from 1.3 $\times$ 10^6 s^{-1} for the ionization of radical **2(Cl)** to 3.6 $\times$ 10^7 s^{-1} for the ionization of radical **2(Me)**. In this specific example, the electronic effect of the methyl group relative to chlorine increases k_{het} by a factor of approximately 30. It is this degree

of influence that the aromatic substituent imposes on the kinetics of ionization that is particularly interesting since the reaction site, and therefore the developing cationic centre, is separated from the aryl ring by a benzylic $CH^{\bullet}$ group.

The electronic nature of the substituent and its impact on the overall rate of heterolysis of the β-mesylate radicals can be fully appreciated from Figure 2-66 in which all of the rate constants k_{het} calculated for radical cation formation in HFIP/TFE solvent mixtures are overlaid. With this comparative view of the data, it is quickly apparent that radicals **2(OMe)** and **2(Me)** ionize much faster relative to **2(Cl)**, **2(F)** and **2(H)**. The kinetic data clearly shows that for a particular HFIP/TFE solvent mixture, the magnitude of k_{het} increases as the substituent changes in the order of Cl < H < F < Me < OMe.

It is also obvious from Figure 2-66 that all five radicals do not ionize across the entire HFIP/TFE solvent range studied. Beginning with radical **2(Cl)**, the time-resolved growth of the radical cation was only detected in solvent mixtures containing greater than 50% HFIP in TFE. Ionization was found to occur in a similar solvent range for radicals **2(H)** and **2(F)**, in HFIP/TFE solutions containing between 40% and 100% HFIP. Interestingly however, formation of radical cation **3(Me)** was detected across the entire HFIP/TFE solvent range, including neat TFE as well as neat HFIP. In sharp contrast, the ionization of radical **2(OMe)** in neat TFE was already at the time resolution limit of the instrumental set-up, with k_{het} calculated to be 6.7×10^7 s^{-1}.

Substituent effects are also apparent from the kinetic data obtained in HFIP/AcN mixtures for the ionization of radicals **2(X)**, Figure 2-67. The rate constants show a similar trend to that observed in HFIP/TFE solutions. In a given HFIP/AcN mixture containing 80% HFIP and greater, radical **2(Me)** systematically ionizes with a rate constant that is approximately an order of magnitude greater than **2(F)**, **2(H)**, and **2(Cl)**. For instance, in 95% HFIP/5% AcN, k_{het} was calculated to be 4.8×10^7 s^{-1} for the ionization of **2(Me)** and 7.4×10^6 s^{-1}, 4.9×10^6 s^{-1}, and 2.4×10^6 s^{-1} for the ionization of

radicals **2(F)**, **2(H)**, and **2(Cl)**, respectively. Once again, growth of the 4-methoxystyrene radical cation **3(OMe)** in HFIP/AcN mixtures could only be resolved in solvent mixtures of much lower polarity, in this case containing 70% HFIP or less. A point of overlap is found however in 70% HFIP/30% AcN, in which k_{het} for the ionization of radical **2(OMe)** is calculated to be $5.7 \times 10^7\ s^{-1}$, a value that is almost 30 times faster when compared to $k_{het} = 2.2 \times 10^6\ s^{-1}$ determined for the ionization of **2(Me)**. This accelerating effect of the methoxy substituent relative to the methyl group was also observed in neat TFE, but interestingly, to a much smaller extent. The ionization of **2(OMe)** was calculated to be only 16 times faster than for **2(Me)**, with values of k_{het} of $6.7 \times 10^7\ s^{-1}$ and $4.1 \times 10^6\ s^{-1}$ respectively, Figure 2-66.

These results provide more than ample evidence that the electron donating or withdrawing capacity of the aromatic substituent influences the kinetics of the β-heterolysis reaction of the radicals **2(X)** investigated. In an attempt to quantify the sensitivity of this ionization reaction toward electronic substituent effects, the kinetic data was subjected to linear free-energy correlation analysis (LFER) using σ and σ^+ substituent parameters.[127] These are used to generate Hammett-type plots that are based on the relationships shown in eq. 2.5. Here, K is the equilibrium constant and k is the rate constant for the reaction of interest, ρ is a reaction constant that reflects the sensitivity of the reaction towards electronic substituent effects, and σ is a substituent parameter developed from a standard reaction.[128,129]

$$\log k = \rho\sigma \qquad \text{or} \qquad \log K = \rho\sigma \tag{2.5}$$

The first correlation plot shown in Figure 2-68 (a), presents the logarithm of k_{het} measured in neat HFIP for the β-heterolysis reaction of radicals **2(Me)**, **2(F)**, **2(H)** and **2(Cl)** as a function of Hammett's σ substituent constants. These parameters were

derived from the acidity constants, K, measured for a series of substituted benzoic acids in water at 25 °C, eq. 2.6.[128]

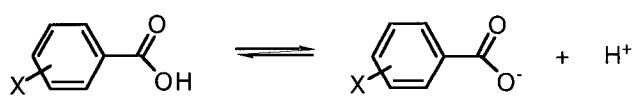

(2.6)

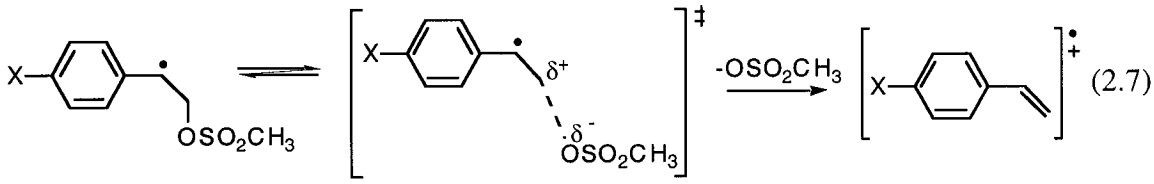

(2.7)

A priori reasons for correlating the ionization of radicals **2(X)** with σ constants are based on a key structural feature shared between the β-heterolysis process, eq. 2.7, and the deprotonation of benzoic acids: both reaction sites are located one atom removed from the benzylic position. In the mechanism of ionization of benzoic acids, no through-resonance is possible between the aromatic ring and the reaction centre. Therefore, if the radical centre does not participate in the β-heterolysis mechanism, it would be reasonable to expect, based on structural similarities, that the extent of electronic influence imposed by the aryl substituent on the kinetics of the β-heterolysis reaction would be similar to that observed for the reference reaction shown in eq. 2.6. If indeed this was the case, a linear correlation would be expected between the body of kinetic data calculated for the β-ionization reaction and the σ parameters. However, as shown in Figure 2-68 (a), the linear regression fit with the σ scale is poor and indicates that a free-energy correlation does not exist between these two reaction series.

In contrast, when the same kinetic data for the β-heterolysis reaction is plotted as a function of the substituent parameter σ^+, an excellent linear relationship is attained (R = 0.999), as can be seen from Figure 2-68 (b). Developed by Brown and Okamoto,

the reference reaction from which the σ^+ parameters are derived is the solvolysis of *para*-substituted cumyl chlorides in 90% aqueous acetone, eq. 2.8.[130]

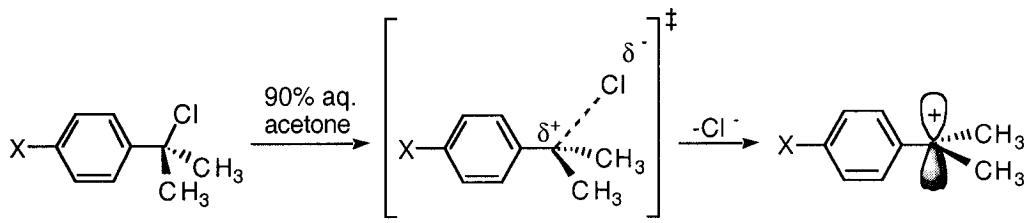

(2.8)

It can be recognized that this ionization reaction progresses *via* a classical S_N1 mechanism. At the transition state, the C—Cl bond is partially broken resulting in some degree of charge separation. In this particular substrate, the positive charge density develops on a benzylic carbon and as a result, can be efficiently delocalized throughout the π-system of the ring. As a direct consequence of this, the solvolysis of cumyl chlorides is strongly influenced by the electronic nature of the aromatic substituent because of through resonance with the incipient cationic centre. The σ^+ scale is therefore expected to correlate with reactions in which extensive delocalization of positive charge occurs in the transition state. It follows then that finding a linear relationship between the β-heterolysis reaction and the σ^+ scale suggests the existence of some conjugative interaction during the ionization of β-substituted radicals. Since the reaction centre in the ionization of radicals **2(X)** is one carbon removed from the benzylic position, there must be some degree of overlap between the singly occupied orbital and the incipient positive charge in the transition state, as depicted in eq. 2.9. Such orbital interaction would result in through-resonance and rationalizes why the electronic nature of the aromatic substituent exhibits such a strong influence on the kinetics of the β-heterolysis reaction.

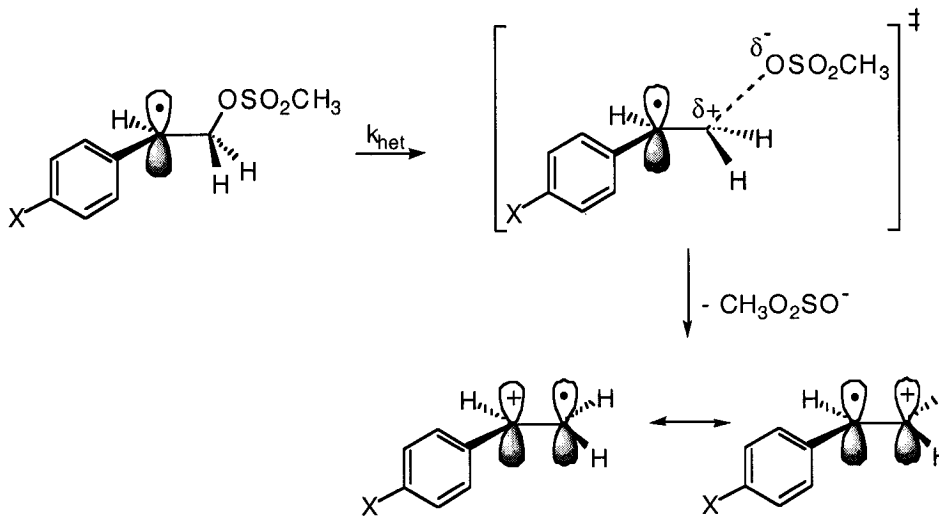

(2.9)

The validity of this mechanism can be assessed by taking a closer look at the influence of a substituent such as fluorine that has the capacity to be both electron withdrawing by induction and electron donating through resonance. The kinetic calculations show that in the ionization of radical **2(F)** in HFIP, fluorine acts predominantly as an electron donating group since the rate constants for β-heterolysis are systematically greater relative to those measured for the unsubstituted radical **2(H)**, as previously shown in Figures 2-66 and 2-67. In order for fluorine to exhibit electron donating abilities, conjugation between the ring's π-system and the cationic centre must therefore exist and is made possible by the intermediacy of the singly occupied orbital at the benzylic position. In other words, as the carbon-oxygen bond begins to break heterolytically, the carbon atom gradually rehybridizes from sp^3 to sp^2, with the positive charge gradually accumulating in the developing unhybridized p-orbital. In the transition state, some degree of overlap is thus possible between the distorted sp^2/sp^3 hybridized cationic centre and the singly occupied p-orbital at the adjacent benzylic carbon, thereby permitting delocalization of the positive charge throughout the π-network. Consistent with this mechanism, the electron density donated by the fluorine atom, albeit minimal

relative to a methoxy group, assists in stabilizing the cationic centre and lowers the energy of the transition state.

As previously mentioned, this is reflected experimentally with an increased rate constant for the ionization of **2(F)** relative to the unsubstituted radical **2(H)** under otherwise identical conditions. Interestingly, one of the differences between the σ and σ^+ scale deals with the fluorine substituent since in the ionization of benzoic acids, fluorine can only be electron withdrawing by induction and by definition, an EWG is given a positive value, 0.062. In contrast, in the solvolysis of cumyl chlorides, fluorine is electron donating by resonance and as an EDG, is given a negative value, -0.071.[131]

In all solvent systems investigated, the chlorinated radical generated the slowest rate constants for the ionization of the β-mesylate group. As an aromatic substituent, the ability of chlorine to act as an EDG is overshadowed by its electronegativity. As radical **2(Cl)** reaches the transition state, chlorine's electron withdrawing effect through the σ-framework causes destabilization of the cationic centre and increases its energy. The barrier to β-heterolysis is consequently elevated and results in the slower rate constants calculated for the ionization of **2(Cl)**.

The methyl group is a substituent incapable of resonance interaction but which in HFIP/TFE and HFIP/AcN solvent systems, leads to a significant enhancement in the value of k_{het} relative to H, Cl and F as substituents. This is simply explained by the methyl group's inductive electron donating ability that assists in the stabilization of the cationic centre both in the transition state and in the resulting radical cation. Compared to fluorine, a methyl group is significantly more electron donating and accordingly, rate constants calculated for the ionization of **2(Me)** are considerably higher than for the ionization of **2(F)**.

While the growth of the 4-methoxystyrene radical cation could not be resolved in neat HFIP, the mechanism outlined in eq. 2.9 rationalizes why radical **2(OMe)** ionizes

with rate constants well above all others measured, and in solvent compositions of much lower polarity. The methoxy group is known to be electron withdrawing by induction but strongly electron donating by resonance. From the results, it is clear that during the ionization of **2(OMe)**, the latter effect dominates. Since the lone electron pairs on oxygen increase the ring's π-electron density, the presence of the *para*-methoxy group provides substantial electronic stabilization to the forming cationic centre in the transition state through the overlap of the radical centre with both the reaction site and the aromatic ring.

2.3.1.1 Kinetic Effect: Variation of $\Delta G^{\ddagger}$

In discussing the influence of substituent electronic effects on rates of reaction, important interactions to consider involve the initial and transition structures, since changes in energy for either or both of these two states will affect the activation barrier for the reaction in question.[132] In the current context, the initial state is a highly reactive but neutral radical which undergoes heterolytic stretching of the carbon-leaving group bond that eventually leads to a radical cation/anion pair. Transmission of substituent electronic effects through the benzyl radical centre is expected to have little effect on the energy of the initial radical since it does not bear a charge. Comparatively, the electronic nature of the substituent will have significant impact on the stability of the transition state that possesses some degree of polarization. If the overall effect of the substituent is to provide electron density, such as in the case of the 4-methoxy group, the transition state will be affected favorably by a decrease in energy, resulting in a smaller activation barrier represented by $\Delta G^{\ddagger}$ in Figure 2-69. This is consistent with the observed increase in the overall rate constant for the β-heterolysis reaction of radical **2(OMe)** relative to radical **2(H)**.

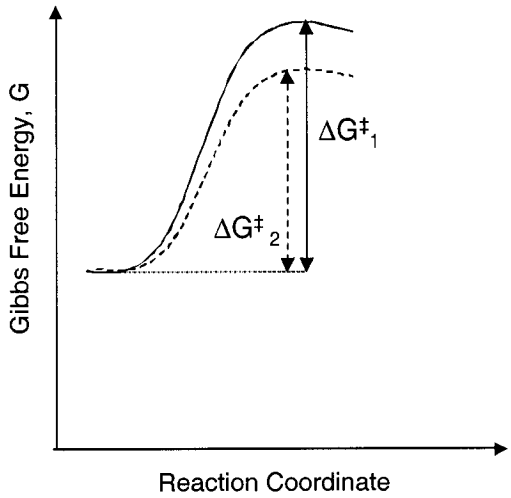

Figure 2-69. Energy versus reaction coordinate diagram illustrating two reaction profiles with isoenergetic initial states but varying transition state energy level. Stabilization of the transition state leads to a reduced $\Delta G^{\ddagger}$ (Gibbs energy change in going from the initial to the activated state), $\Delta G^{\ddagger}_1$ (solid line) > $\Delta G^{\ddagger}_2$ (dotted line).

A substituent that lowers the energy of the transition structure should also stabilize the products of the ionization reaction relative to the reactants, since the former consists of a radical cation/anion pair. In fact, the stabilizing effect of an EDG is expected to be more important for the product than for the transition state in which the positive charge is only partial. Therefore, an electron donating substituent is both *kinetically* and *thermodynamically* favorable to the β-heterolysis reaction by decreasing the value of $\Delta G^{\ddagger}$, the difference in free energy between the transition and initial state, and decreasing the value of $\Delta G°$, the change in free energy between the initial and final state, Figure 2-71.

2.3.1.2 Thermodynamic Effect: Variation of ΔG° and T.S.‡ Structure

A corollary of the changes in ΔG° caused by substituents is a shift in the position of the transition state along the reaction coordinate. These assumptions are based on rules originally formulated by Hammond, one of which states that changes in energy made along the reaction coordinate result in a shift of the transition state toward the end that is raised, away from the end that is lowered.[133]

A shift in the position of the transition state due to these structural changes of the substrate explains in part why the β-heterolysis reaction was not observed across the same solvent range for all radicals investigated. For **2(F)**, **2(H)** and **2(Cl)**, the radical cation formation was detected under very similar solvent conditions, in both HFIP/TFE and HFIP/AcN mixtures, with the **2(Cl)** radical particularly limited to highly ionizing mixtures, Figures 2-66 and 2-67. While none of these radicals undergo the β-heterolysis reaction in neat TFE, this solvent along with even less polar TFE/AcN mixtures was favorable for the ionization of radicals **2(Me)** and **2(OMe)**. The rate constant for the β-heterolysis reaction of these radicals as a function of TFE content in nitrogen-purged AcN is presented in Figure 2-70. From this graph, it is clear once again that radical **2(OMe)** ionizes in significantly less polar mixtures relative to **2(Me)** and with a rate constant approximately one order of magnitude greater, $k_{het} \sim 10^7\ s^{-1}$. Furthermore, the ionization of **2(OMe)** was observed in almost all TFE/AcN mixtures studied, but radical **2(Me)** only exhibited heterolytic reactivity between 80% to 100% TFE content in AcN.

These observations can be partly rationalized by the relative position of the two transition states. With chlorine as the substituent, ionization of radical **2(Cl)** is the slowest, followed by the unsubstituted and the fluorinated radical. The small changes in the rate constant calculated for the ionization of these radicals suggests minimal stabilizing or destabilizing effects on the energy of the products by F and Cl, respectively relative to the unsubstituted radical **2(H)**. Consequently, it is reasonable to assume that

the position of the transition state in going from Cl, H to F moves only slightly to an earlier position. The differences in the charge density experienced by these transition states are likely minimal and this is reflected in their solvation requirements of each reaction. As mentioned, all three radicals ionize in similar, highly ionizing solvent mixtures containing a minimum content of 40% HFIP in TFE, and a minimum of 80% HFIP in AcN. In contrast, the suddenly large increase in rate constants calculated for the ionization of **2(Me)** and particularly of **2(OMe)** could indicate a more drastic shift in the transition state to earlier positions along the reaction coordinate. It is reasonable to suggest that the earliest transition state occurs during the ionization of **2(OMe)** for which the methoxy substituent provides the most efficient stabilization to the activated complex as well as to the products. The transition state consequently possesses less charge density and in accordance with this, the reaction exhibits less sensitivity to the solvent's ability to provide additional stabilizing forces. The favorable electronic effect of the methoxy group and its effect on the relative position of the transition state partly explains why the β-heterolysis reaction of radical **2(OMe)** is only resolved in relatively nonpolar mixtures of AcN containing 70% HFIP or less, and in neat TFE.

The electronic effect of the substituent on the energy of the products of the β-heterolysis reaction, and the consequential shift of the transition state is illustrated in the energy versus reaction coordinate diagrams shown in Figure 2-71.[132,133]

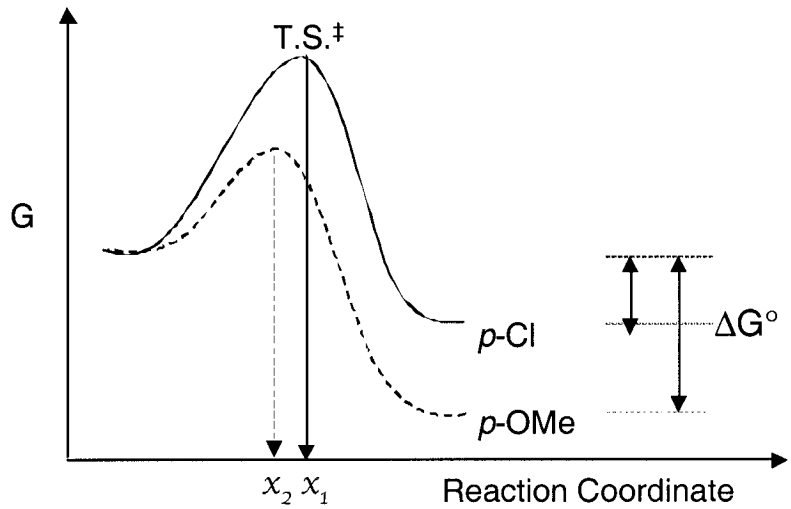

Figure 2-71. Effect of an EWG such as chlorine (solid line) and EDG such as methoxy (dashed line) on the energetics of the β-heterolysis mechanism. An EDG provides additional stabilization to the transition state and the products, resulting in an earlier transition state along the reaction coordinate, shifting it from x_1 to x_2 towards the reactants.

Hammett-type plots could equally be established for the kinetic data acquired in HFIP/TFE mixtures containing 60%, 70%, 80%, and 90% HFIP for radicals **2(Me)**, **2(F)**, **2(H)**, and **2(Cl)**, and are presented in Figure 2-72. In all four solvent systems, a linear relationship was achieved between the rate constant k_{het} for the ionization reaction and the σ^+ substituent parameter. Pertinent mechanistic information can also be gained from the slope (ρ^+) of a Hammett-type correlation plot. While its negative sign indicates the nature of the charge build-up in the transition state, the magnitude of ρ^+ reflects the degree of sensitivity of the reaction towards substituent electronic effects. Since EDGs are assigned positive σ^+ values and EWGs are given negative σ^+ values, the negative slopes obtained from the plots in Figure 2-72 infer that the rate constant for the ionization of the β-substituted radicals **2(X)** decelerates as the electron withdrawing capacity of the substituent increases. In agreement with this, a negative slope also indicates the build-up of positive charge in the transition state, as is indeed the case during the heterolytic cleavage of the carbon-leaving group bond. The values of the slopes are included in each

of the plots presented in Figure 2-72 and range from -3.02 to -3.49. From these values, it can be concluded that the β-heterolysis reaction exhibits a moderately high sensitivity to substituent electronic effects. From the mechanism shown in eq. 2.9, this is expected since orbital overlap between the cationic centre and the SOMO permits some degree of conjugation with the ring and acts as an open channel for the electronic nature of the substituent to interact with the reaction centre. Nevertheless, it is worth noting that the β-heterolysis reaction shows less sensitivity to electronic effect in HFIP/TFE mixtures than the solvolysis of the *para*-substituted cumyl chlorides in 90% aqueous acetone for which $\rho^+ = -4.62$. This discrepancy can simply be explained by the fact that there is less electronic transmission during the β-heterolysis reaction than in the course of the solvolysis of cumyl chlorides. In the later case, the reaction site is at the benzylic carbon where the electronic influence of the substituent can directly interact with the developing cationic centre. However, during the ionization reaction of the β-mesylate phenethyl radicals **2(X)**, the cationic centre does not form at the benzylic site but on the carbon adjacent to it. Despite some extent of overlap between the partial positive charge and the SOMO in the transition state, substituent electronic effects are likely dampened by the added distance away from the ring. Alternatively, the reduced sensitivity of the β-heterolysis reaction to electronic effects of substituents may be related to the inherently faster rate of this reaction relative to the S_N1 solvolysis. An earlier transition state along the reaction coordinate in the course of the ionization of radicals **2(X)** would lead to a transition structure with less charge separation and thus reduced electronic requirements for stabilization.

2.3.1.3 Variation of ρ^+ with Solvent

An intriguing result unveiled by this study is that the magnitude of ρ^+ measured for the ionization of radicals **2(X)** increases as the ionizing ability of the solvent mixtures decreases (for solvent properties, see Table A1 in Appendix). It can be seen in Figure 2-72 that as the HFIP/TFE ratio becomes progressively smaller, ρ^+ becomes increasingly more negative. Values of -3.02, -3.19, -3.32, -3.41 and -3.49 were obtained for data measured in 100%, 90%, 80%, 70% and 60% HFIP, respectively. This trend is also observed with the slopes of two additional Hammett-type plots presented in Figure 2-73 for the kinetic data acquired in AcN mixtures containing 95% and 90% HFIP. Once again, the best linear correlation was obtained by plotting the rate constants against the Brown-Okamoto σ^+ substituent parameter. As the solvent polarity decreases, that is as the HFIP content in AcN is reduced from 95% to 90%, ρ^+ becomes increasingly more negative, going from -3.13 to -3.68. It is also interesting to highlight that as the co-solvent is changed from 10% TFE/90% HFIP to 10% AcN/90% HFIP, the magnitude of ρ^+ increases from -3.19 to -3.68 respectively, representing a dramatic difference of 0.49 in the value of the slopes.

All of the calculated ρ^+ values discussed above are plotted in Figure 2-74 as a function of HFIP content with TFE or AcN as the co-solvent. These results provide a unique insight into the balance that exists between the reaction's sensitivity to electronic and solvent effects, two factors that play a pivotal role in the overall rate of the β-heterolysis reaction for radicals **2(X)**. Figure 2-74 distinctly shows that as the solvent composition becomes increasingly ionizing with greater HFIP content, the β-heterolysis reaction becomes less sensitive to substituent electronic effects, as though muffled by the increasing efficiency with which the solvent stabilizes the transition state through solvation effects. Conversely, as the medium becomes less polar, the importance of electronic stabilization by the substituent increases, as observed with the

increasing absolute values of ρ^+. As previously mentioned, this effect is particularly drastic in HFIP/AcN mixtures.

The value of ρ^+ correlates directly with the amount of charge transmission between the aromatic substituent and the reaction centre. However, the solvent must also modify the amount of charge localized on C_α as a result of C_α-X heterolytic stretching in the transition state. Subsequently, the observed solvent-dependence of ρ^+ can be interpreted[131,134] to mean that changes in solvent composition alter the extent of ionic character in the transition state and therefore adjust the requirements for electronic stabilization at the energy maximum. The reaction's sensitivity toward electronic substituent effects therefore changes and is reflected in the magnitude of the ρ^+ value. Stabilizing solvent interactions also influence the energy of the products and cause a shift in the position of the transition state in a manner consistent with the Hammond postulate.[133] Thus in the highly polar environment provided by HFIP, the transition state is efficiently stabilized by solvation and its energy lowered by this effect. Stabilization of the products relative to the reactants also occurs and results in an earlier transition state. In the less ionizing environment provided, for example, by a solution of 60% HFIP/40% TFE, the transition structure is expected to be later and more product-like. Changes in the ionizing ability of the medium translates into varying degrees of charge separation at the transition state and consequently, varying demands on electronic stabilization. If the transition state in neat HFIP is assumed to be earlier along the reaction coordinate, bond dissociation has not progressed as far by the time the free energy maximum is reached and consequently, the transition structure exhibits less charge separation. This in turn results in a reduced demand for electronic stabilization by the substituents, as observed with a smaller ρ^+ value of -3.02. Conversely, in a significantly less polar medium provided by a solvent mixture containing 90% HFIP/10% AcN, the transition state is suggested to occur

comparatively later along the reaction coordinate. At this point, the carbon-leaving group bond has dissociated to a greater extent and leads to a transition state structure with greater charge separation and therefore, with an enhanced sensitivity to electronic stabilization from the substituents. In agreement with this, ρ^+ is calculated to be significantly greater with a value of –3.68.

Such solvent effects on the reaction constant ρ^+ have also been reported for the solvolysis of substituted cumyl chlorides but in widely different solvents that include methanol (ρ^+ = -4.82), ethanol (ρ^+ = -4.67), acetone (ρ^+ = -4.54), and isopropanol (ρ^+ = -4.43).[135] However, from these values of ρ^+, no significant relationship could be established against the ionizing ability as defined by the Y_{Cl} scale.[136] This could be explained by the fact that the solvents compared in this study differ not only in their polarity, but in other important solvent properties such as polarizability and hydrogen bonding capabilities. The observed changes in ρ^+ may then reflect changes in solvent properties other than polarity. It is therefore difficult to compare this data with the values ρ^+ obtained for the β-heterolysis reaction in a range of binary solvent mixtures with only subtle differences. Nevertheless, the literature does provide examples of reactions in which the magnitude of ρ^+ decreases with increasing ionizing ability of the solvent, such as for the ionization of substituted benzoic acids in aqueous alcohols and of substituted anilines in aqueous ethanol.[137,138]

2.3.2 Solvent Effects

The influential role of solvent composition on the kinetics of the β-heterolysis reaction has already been partly addressed in the previous section. These solvent effects are once again evident in Figure 2-75 which illustrates the rate constant for ionization of the β-mesylate-4-methoxyphenethyl radical **2(OMe)** as a function of water content in two different co-solvents, AcN and methanol. The general trend found in both binary

mixtures is that k_{het} for radical cation formation *via* the β-heterolysis reaction increases with increasing water content. However, it is obvious that the ionization rate constants are faster with solutions containing methanol as the co-solvent rather than AcN with otherwise identical water content. The rate constant for the growth of the 4-methoxystyrene radical cation **3(OMe)** in 10% aqueous AcN is $1.9 \times 10^6 s^{-1}$ and increases to a value of $6.5 \times 10^7 s^{-1}$ in 80% aqueous AcN. In neat methanol $k_{het} = 7.8 \times 10^6 s^{-1}$ and increases by a factor of 6.5 to a value of $5.1 \times 10^7 s^{-1}$ in 50% aqueous methanol. It is emphasized that in these series of experiments, the substrate structure and leaving group were kept identical. The changes in rate constant observed can therefore only be attributed to the changing ionizing strength of the binary mixtures studied. The results presented in Figure 2-75 exemplify the extent to which solvent can accelerate the β-heterolysis reaction. The rate constant for the ionization of **2(OMe)** showed a factor of 34 increase in value on going from 10% to 80% aqueous AcN.

The majority of the medium effects observed on the rates of ionization can be attributed to the differential solvation of reactants and activated complexes, and the extent of this effect will depend on the intermolecular forces between solute and surrounding solvent molecules. Solvent interactions at play can include for example, electrostatic and polarization forces, as well as hydrogen bonding.[139] The complexity of these solvation interactions is beyond the scope of this thesis but a general definition of "ionizing" power of the solvent, which chemists often interchange with the term "polarity", is helpful for the following discussion. According to Reichardt, polarity can be adequately defined as "the overall solvation capability (or solvation power) of solvents, which in turn depends on the action of all possible, specific and nonspecific, intermolecular interactions between solute ion or molecules and solvent molecules, excluding however, those interactions leading to definite chemical alterations of the ions or molecules of the solution (such as protonation, oxidation, reduction, chemical complex

formation, etc.)."[139] This definition continues to gain increasing support within the scientific community.[140,141] Interestingly however, not one physical solvent parameter such as dielectric constant or dipole moment for example, has been found to be sufficient to quantitatively describe solvent polarity. This has consequently led to a number of empirical parameters of solvent polarity based on carefully selected, well-understood and highly solvent-dependent chemical reactions. This is the basis of why the Y scale was originally developed by Winstein *et al.* in 1948 to be a measure of a solvent's ionizing power.[136,142]

It is well established that S_N1-like mechanisms exhibit high solvent-dependence due to the polar nature of the reaction and, to varying degrees, of the transition state. The kinetic effect of solvent "ionizing power" on such reactions can be assessed with the Y_X scale, an adaptation of the original Grunwald-Winstein equation[142,143] that takes into account the nature of the leaving group X, eq. 2.10. In this equation, *m* is a substrate parameter that reflects the degree to which its ionization is sensitive to the ionizing power of the solvent. In other words, it is a measure of the extent to which the solvolysis occurs unassisted, free from anchimeric and nucleophilic solvent participation. Y_X represents the solvent parameter (where X is the leaving group) that is a measure of its ionizing ability, and k_0 and k are rate constants for the reaction of interest in 80% aqueous ethanol and in the solvent of choice, respectively.

$$\mathrm{Log}(k/k_0) = mY_X \tag{2.10}$$

With the use of eq. 2.10, the kinetic data for the β-heterolysis reaction can be correlated with data for the solvolysis of a "standard" compound, namely the 2-adamantyl X system.

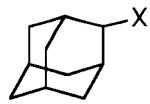

2-Adamantyl Substrate

This substrate was specifically chosen because its caged structure sterically inhibits backside attack, resulting in a solvolysis reaction that is free of nucleophilic assistance and thus highly dependent on solvent ionizing power. Observed changes in the rate constant for the solvolysis of 2-adamantyl X as a function of solvent composition should therefore only be a measure of the solvent's polarity. As will be shown, the β-heterolysis reaction is correlated with the Y_{OMs} scale which is based on the solvolysis of 2-adamantyl mesylate.[136] The values of Y_{OMs} therefore represent a measure of the ionizing strength of the medium during solvolysis of the mesylate group but are available only for a limited range of solvent mixtures. Table 2-1 presents the Y_{OMs} parameters used in Figure 2-76 and show that the values increase as ionizing power of the solvent increases, i.e. as the methanol/water ratio decreases. Table 2-1 also provides the corresponding values for the Y_{Cl} and Y_{Br} parameters referred to later on in the text. It is worthwhile noting that the values of Y_X for a specific solvent system vary according to the nature of the leaving group due to differential solvation of X^- in eq. 2.11. Therefore when assessing a reaction's sensitivity to ionizing power of the solvent with the use of the Y_X scale, the leaving group must be kept the same.

$$(R\text{-}X)_{solvated} \rightarrow (R^+)_{solvated} + (X^-)_{solvated} \qquad (2.11)$$

Table 2-1. Y_X values of solvent ionizing power defined for the solvolysis of 2-adamantyl mesylate, chloride and bromide at 25°C in methanol/water mixtures.[136]

Solvent Composition (%v/v water)	Y_{OMs}	Y_{Br}	Y_{Cl}
MeOH	-1.17	-1.12	-1.2
90% MeOH	-0.30	-0.14	-0.2
80% MeOH	0.39	0.70	0.67
70% MeOH	0.98	1.42	1.46
60% MeOH	1.54	2.04	2.07
50% MeOH	2.05	2.61	2.70
40% MeOH	2.50	3.14	3.25
30% MeOH	2.95	3.61	3.73
20% MeOH	3.32	3.94	4.10

Regression analysis of log k_{het} values, obtained for the formation of the 4-methoxystyrene radical cation **3(OMe)** in aqueous methanol mixtures, plotted as a function of Y_{OMs} reveals an excellent linear relationship (R = 0.998), and a slope *m* of 0.33, Figure 2-76. The lack of correlation dispersion suggests that the two reaction series show proportional responses to changes in solvent ionizing power, confirming that the loss of the β-mesylate group proceeds *via* an S_N1-type mechanism as proposed earlier. Further implied is that the degree of charge separation in the transition state associated with the β-heterolysis reaction of radical **2(OMe)** parallels that of the more familiar S_N1-type solvolysis of 2-adamantyl mesylate as the water/methanol ratio of the mixtures is varied.

While *m* values often reflect the degree to which a substrate undergoes unassisted ionization, with *m* being unity for fully unassisted ionization reactions (defined as such for the solvolysis of 2-adamantyl substrate), this interpretation is not fitting to explain the low *m* values encountered in the current study. If the β-heterolysis reaction studied had substantial nucleophilic assistance, direct detection of radical cation

formation would not have been possible, and yet it was. Moreover, some upward dispersion of the kinetic data for the β-heterolysis reaction would likely have been observed in the Winstein-Grunwald plot (Figure 2-76) since the rate constants would have shown some enhancement from this nucleophilic solvent assistance.

An *m* value of 0.33 as calculated implies that the β-heterolysis reaction is less sensitive to solvent ionizing strength relative to the limiting S_N1 mechanism encountered in typical solvolysis reactions. However, in the heterolysis of β-substituted radicals, the substrate is a highly reactive intermediate and consequently, the rates of ionization are exceptionally faster than normal S_N1 reactions. As mentioned, rate constants for the ionization of radicals **2(X)** range from 10^5 to 10^7 s^{-1} and are even greater for the methoxy derivative. According to the Hammond postulate, these extremely fast reactions are likely exothermic and have an early transition state in which heterolytic bond dissociation between the carbon and sulfonate leaving group is not as advanced.[133] The resulting transition structure at the free energy maximum is therefore less polar than expected for a typical S_N1 ionization reaction, and would account for the reduced sensitivity to the solvent's ionizing strength.

If solvation influences the stability of the transition state, it follows therefore that the nature of the leaving group must be an equally important part of the equation alongside with the solvation of the radical cation.[144,145] This is addressed in more detail in the following section.

2.3.3. Leaving Ability of the β-Group

In the course of the β-heterolysis reaction of radicals **2(X)**, the leaving group becomes more negatively charged in the transition state. A good leaving group therefore is one that is able to stabilize that negative charge through efficient delocalization. The dispersion of the charge on the anion directly affects the solvation requirement of the

transition structure and can consequently lead to changes in its energy and position along the reaction coordinate for the β-heterolysis process.

To better understand the effect of the leaving group on the β-heterolysis reaction, the current results on the reactivity of the β-mesylate-4-methoxyphenethyl radical (referred to more specifically as **2(OMe)-OMs** in this section) in aqueous methanol mixtures are compared to previous work carried out in our laboratory on the related β-bromo- and β-chloro-4-methoxyphenethyl radicals, **2(OMe)-Br** and **2(OMe)-Cl**, Scheme 2-10.[83]

Scheme 2-10

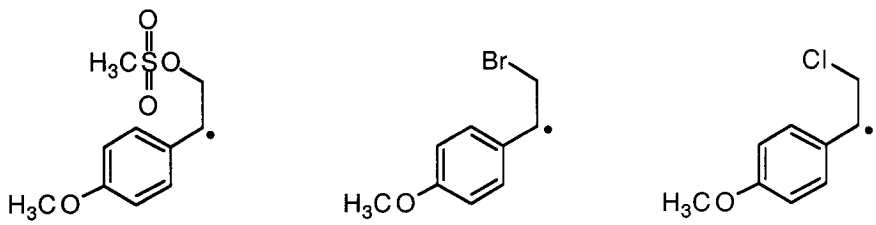

2(OMe)-OMs **2(OMe)-Br** **2(OMe)-Cl**

The rate constants for the ionization of these three radicals are shown in Figure 2-77. In nitrogen-saturated aqueous methanol mixtures, it is evident that the β-heterolysis process is strongly affected by the nature of the leaving group; rate constants measured for the mesylate derivative are consistently faster than those determined for bromide and chloride compounds. As anticipated, the order of reactivity of these radicals, **2(OMe)-Cl < (OMe)-Br < 2(OMe)-OMs**, parallels the leaving ability of the groups that itself is dependent on the stability of the corresponding anion, $Cl^- < Br^- < CH_3O_2SO^-$. This trend is also observed in AcN mixtures containing water, TFE and HFIP as co-solvents, as shown in Figures 2-78 to 2-80. This order of reactivity is consistent with results found in numerous mechanistic studies on S_N1-type reactions.[81] While bromide is known to be a better leaving group relative to chloride, the mesylate

group is superior to both due to its greater ability, following heterolysis, to stabilize the negative charge through resonance.

In an opposing trend to the leaving ability of the groups, the sensitivity of the β-heterolysis reaction to solvent ionizing ability, as measured by *m*, decreases as we consider Cl^- (*m* = 0.56), Br^- (*m* = 0.45) then $CH_3O_2SO^-$ (*m* = 0.33), Figure 2-76. These results support the notion that solvation of the anion leaving group is an important contributor to solvent effects observed on the kinetics of the β-heterolysis reaction. In other words, the solvent owes its ionizing power more to its ability to provide electrophilic assistance to the departure of the anion than to its ability to solvate the incipient cationic centre.[131] Thus in the case of the mesylate leaving group whose anion is unusually stable relative to chloride and bromide, solvation is not so critical and this is reflected in the small *m* value calculated. Similarly, the *m* value for bromide is smaller than that calculated for chloride as the negative charge on bromide is comparatively more diffuse and will require less solvation.

The relatively high reactivity of the mesylate β-substituted radical relative to the chloro and bromo derivatives towards β-heterolysis, under otherwise identical conditions, can also provide an insight into the nature of the transition states relative to one another. As the methanesulfonate anion is best equipped to disperse the negative charge, it is lower in energy. Thus, the transition state for the β-heterolysis of radical **2(OMe)-OMs** is likely lower in energy than for the chloro and bromo derivatives. The stability of the anion product also affects position of the transition state and as discussed earlier, the more it is stabilized internally, the further the position of the transition state is shifted towards the reactant, Figure 2-71. Thus decreasing values of *m* as the leaving group is improved from Cl^-, Br^- to $CH_3O_2SO^-$ can also be interpreted to mean that the transition state structure becomes increasingly reactant-like and the extent of charge

build-up due to bond dissociation is reduced. Consequently, the reaction's sensitivity to solvation effects is lessened and the *m* values are correspondingly smaller, as observed.

A reaction's sensitivity to the nucleofugality of the leaving group can efficiently be assessed by establishing relative rate constants, k_{rel}, for the nucleofuges studied. In the limiting S_N1 ethanolysis of the 1-adamantyl system in which nucleophilic solvent assistance is prohibited, Scheme 2-11, rate constants for the ionization step have been found to vary widely according to the nature of leaving group X. Values of k_{rel} for chloride, bromide and mesylate were calculated to be 1, 40 and 1.0×10^6, respectively.[146]

Scheme 2-11

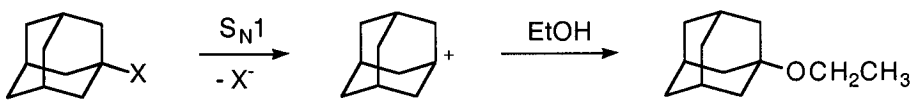

X	k/s^{-1}	k_{rel}
Cl^-	2.5×10^{-11}	1
Br^-	1.0×10^{-9}	40
$CH_3O_2SO^-$	2.5×10^{-5}	1.0×10^6

The drastic increase in k_{rel} between the halogen nucleofuges and the mesylate group clearly shows the extent to which the solvolysis reaction depends on the leaving group's ability to stabilize the negative charge density. In sharp contrast, the k_{rel} values obtained for the β-heterolysis reaction of radicals **2(OMe)-X** in 30% water/70% methanol, Scheme 2-12, were determined to be 1, 9, and 17, where again X is chloride, bromide, and mesylate, respectively.

Scheme 2-12

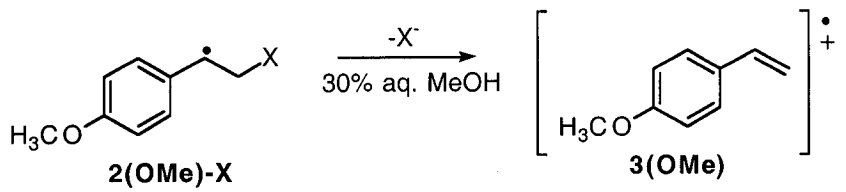

2(OMe)-X **3(OMe)**

X	k/s^{-1}	k_{rel}
Cl^-	1.3×10^6	1
Br^-	1.2×10^7	9
$CH_3O_2SO^-$	2.3×10^7	17

While the trend is the same for both reactions, with rate constants increasing in the order $Cl^- < Br^- < CH_3O_2SO^-$, the nucleofugality of the leaving group has a much greater impact on the kinetics of the solvolysis of the 1-adamantyl system. The relatively small differences in the k_{rel} values calculated for the β-heterolysis reaction of radicals **2(OMe)-X** provide further support for a transition state that is reached sooner along the reaction coordinate relative to an S_N1 mechanism under limiting conditions. During the ionization of radicals **2(OMe)-X**, it is postulated that heterolysis of the carbon-leaving group bond is still in its early stages by the time the energy maximum is reached. Since the negative charge density localized on the nucleofuge is then less significant, the β-heterolysis reaction exhibits a reduced sensitivity to the leaving group's ability to disperse the charge. An early, reactant-like transition state therefore rationalizes why the range of k_{rel} values calculated for the ionization of radicals **2(OMe)-X** is small despite the drastically different nucleofugalities of the leaving groups investigated.

2.3.4 Rate Enhancing Effect of the Radical Centre

In previous work carried out in this laboratory, the ionization of bromide and chloride from β-substituted arylethyl radicals **2(OMe)-Br** and **2(OMe)-Cl** were found to occur with first-order rate constants that exceeded $1 \times 10^8\ s^{-1}$ in water and HFIP. The magnitude of these rate constants was found to be substantially greater than traditionally

encountered for the analogous S_N1-type reactions. For instance, the ionization of 4-methoxyphenethyl chloride[147] in 20% aqueous AcN was found to proceed 4600 times slower, with a rate constant of ~ 1000 s^{-1}, eq. 2.12, compared to the rate constant of 4.6×10^6 s^{-1} calculated for the ionization of the β-chloro-4-methoxyphenylpropyl radical[83] in 17% aqueous AcN, eq. 2.13.

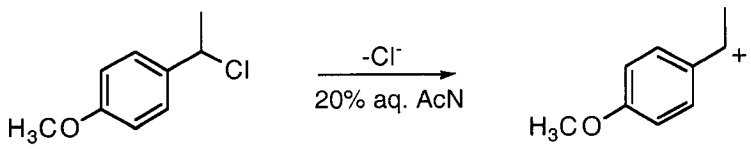

(2.12)

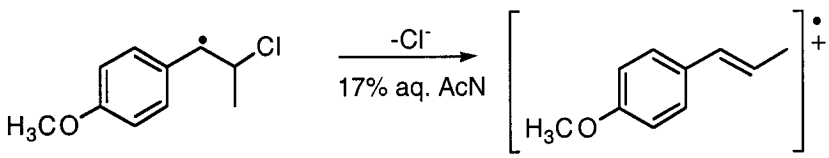

(2.13)

This rate accelerating effect is also found for the β-heterolysis reaction of the radicals **2(X)** which have been shown to occur with first-order rate constants ranging from 1×10^5 s^{-1} to values greater than 1×10^8 s^{-1}. For example, the rate constant for the ionization of 4-methoxybenzyl mesylate in neat ethanol was calculated to be 2.7×10^{-1} s^{-1}, eq. 2.14.[148] Comparatively, the ionization of radical **2(OMe)** was determined to have a rate constant of 7.8×10^6 s^{-1} in neat methanol, eq. 2.15, representing an increase of approximately 10^7. This rate acceleration can largely be attributed to the lower stability of the radical substrate **2(OMe)** relative to 4-methoxybenzyl mesylate. That is, the starting material **2(OMe)** is already a reactive intermediate that is likely to be considerably closer in energy to the radical cation product than 4-methoxybenzyl mesylate is to the 4-methoxybenzyl cation. As a result, the thermodynamic component of the activation barrier will be reduced, and the reaction progresses with an enhanced rate constant.

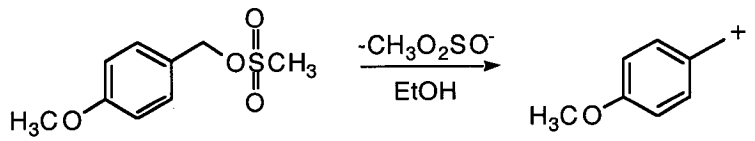

(2.14)

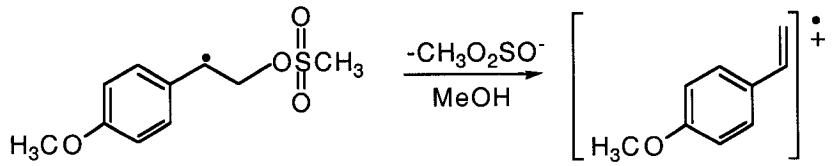

2(OMe) 3(OMe)

(2.15)

2.4 Conclusions

From the kinetic data collected in this investigation, a more complete mechanistic profile of the β-heterolysis reaction has emerged. Together, the results suggest that the ionization of β-mesylate phenethyl radicals **2(X)** is a process in which the transition state is reached early along the reaction coordinate, as concluded from the reduced sensitivity of the reaction toward solvation effects. Moreover, based on the large rate constants calculated which are in the order of 10^5-10^7 s^{-1}, it is reasonable to predict with the use of the Hammond postulate, that the β-heterolysis reaction is in fact exothermic. These findings diverge significantly from what is known about the analogous closed-shell S_N1 mechanism in which the rate-determining ionization step is endothermic for neutral substrates that ionize to form a fully charge cation.

Despite differences in the position of the transition state and hence the degree of cationic character at the energy maximum between the closed and open shell ionization, the β-heterolysis reaction was found to exhibit classical S_N1 characteristics. Rate constants for the heterolytic loss of the β-mesylate group increased with solvent ionizing strength as well as with electron donating substituents on the aromatic ring, as expected for a reaction in which there is significant build-up of positive charge density in

the transition structure. The study also confirmed that as the ionization of radicals **2(X)** progresses and the transition state is reached, an overlap gradually develops between the cationic centre and the orbital housing the unpaired electron. This subsequently leads to through-resonance interaction involving the π-system of the ring and rationalizes why the electronic nature of the aromatic substituent has such a strong influence on the value of k_{het} despite the distance between the substituent and the reaction site. When the overlap between the HOMO and the developing cationic centre is favorable, such as when the ring is substituted with a *para*-methoxy group, the effect of the radical can be viewed as a form of 'anchimeric' assistance to the departure of the leaving group.

While the β-heterolysis reaction and S_N1 ionization both involve heterolytic bond dissociation, the data presented in this chapter highlight the extent to which the presence of a β-radical centre group changes the energetics and the overall dynamics of the heterolysis process.

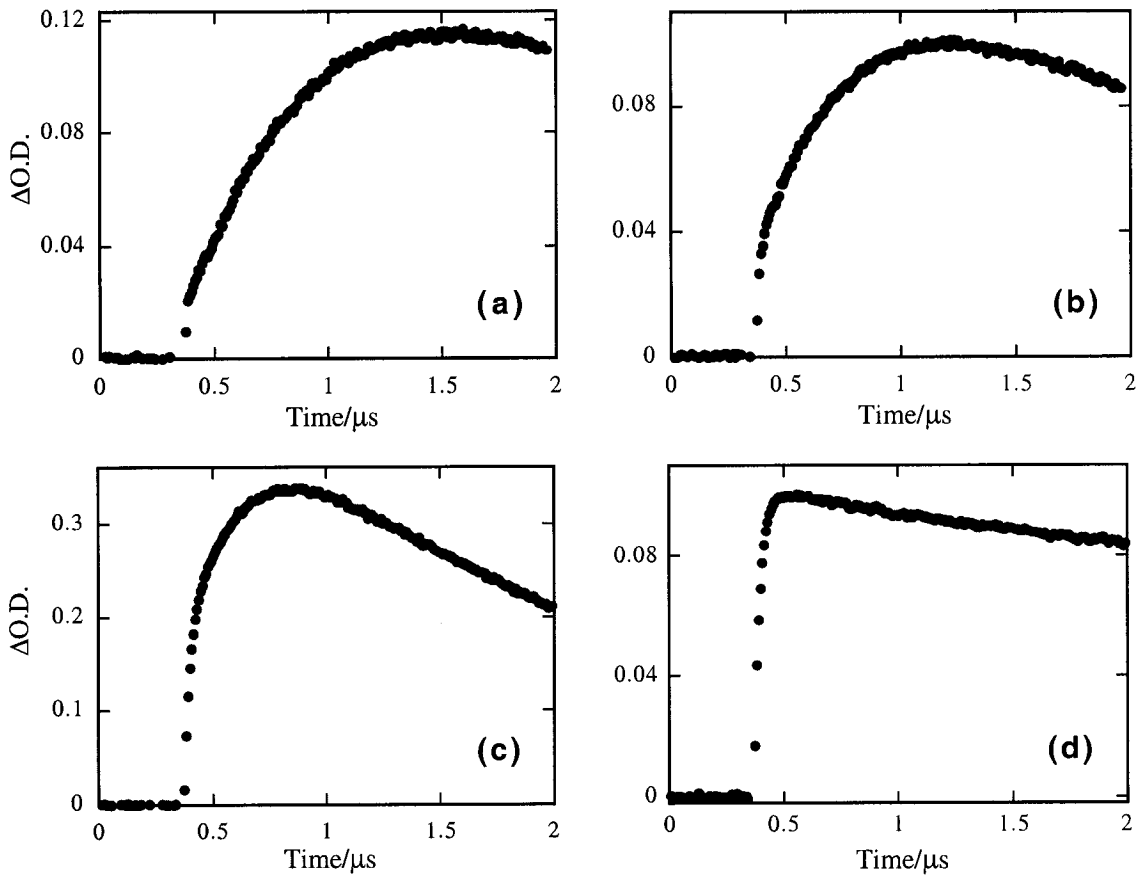

Figure 2-65. Time-resolved growth of substituted styrene radical cations **4(X)** generated upon β-heterolysis of radicals (a) **2(Cl)**, (b) **2(H)**, (c) **2(F)**, and (d) **2(Me)** in nitrogen-saturated 70% HFIP/30% TFE.

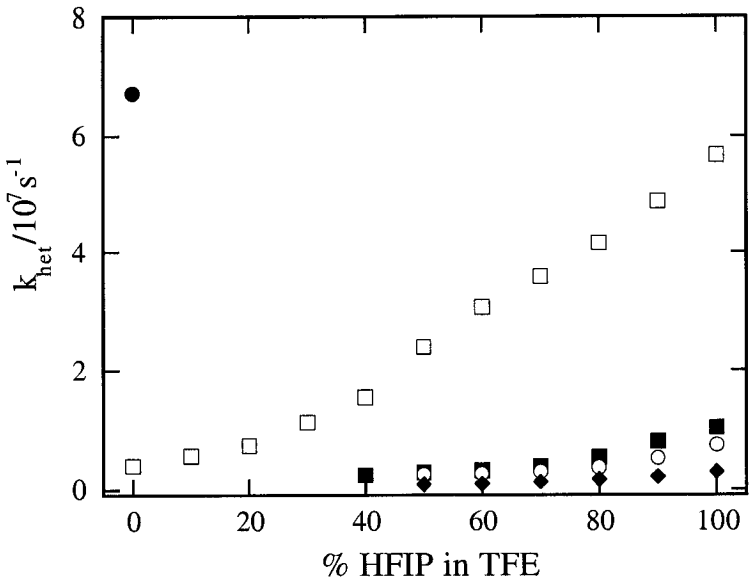

Figure 2-66. Rate constants for the growth of the (●) 4-methoxystyrene, (□) 4-methylstyrene, (■) 4-fluorostyrene, (○) styrene and (◆) 4-chlorostyrene radical cation as a function of HFIP content in TFE, following 266 nm laser flash photolysis in nitrogen-saturated conditions.

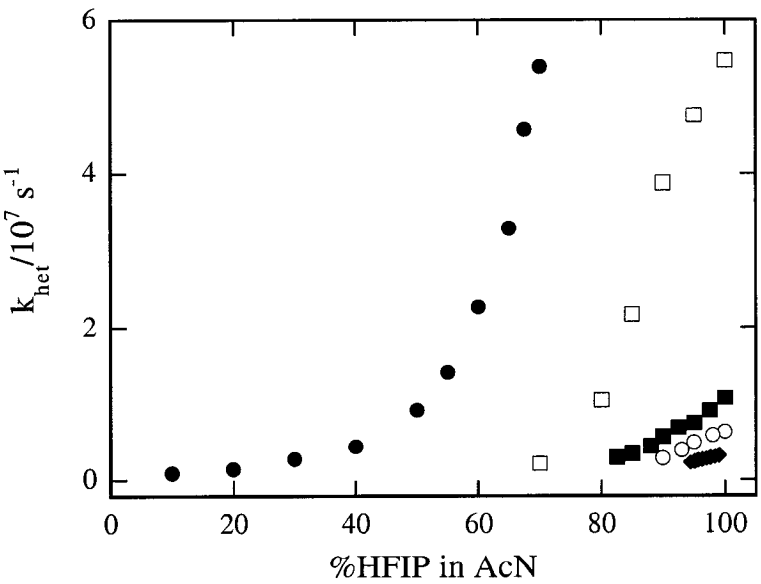

Figure 2-67. Rate constants for the growth of the (●) 4-methoxystyrene, (□) 4-methylstyrene, (■) 4-fluorostyrene, (○) styrene and (◆) 4-chlorostyrene radical cation as a function of HFIP content in acetonitrile, following 266 nm laser flash photolysis in nitrogen-saturated conditions.

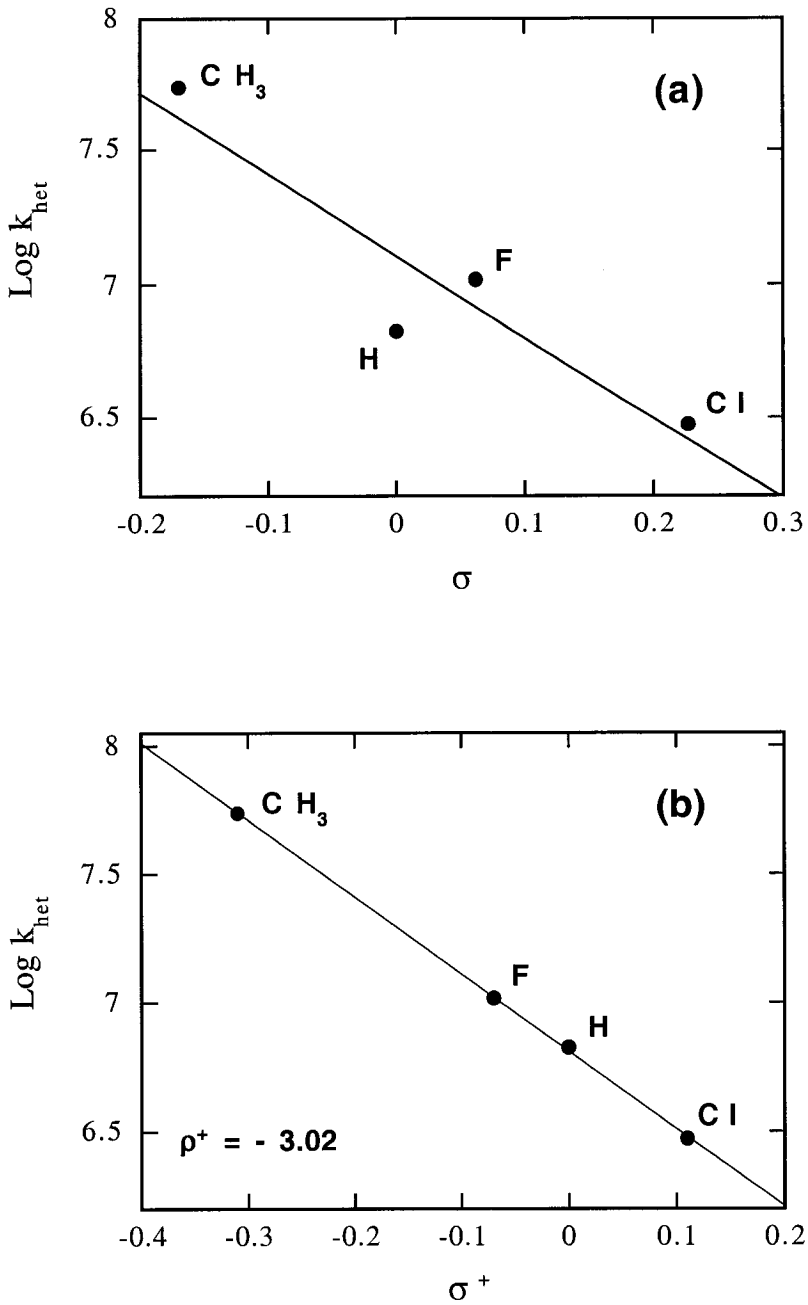

Figure 2-68. Hammett-type correlation analysis using (a) Hammett σ and (b) Brown-Okamoto σ^+ parameters for the ionization of mesylate from radicals **2(Me)**, **2(F)**, **2(H)**, and **2(Cl)** in nitrogen-saturated HFIP.

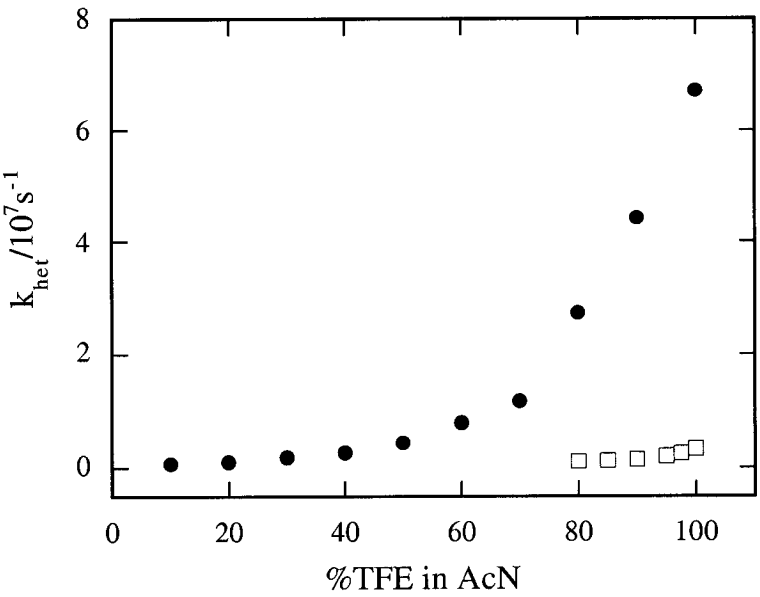

Figure 2-70. Rate constant for the growth of the radical cation after 266 nm laser irradiation of (●) 2-(4-methoxyphenyl)-3-oxobutylmethanelsulfonate **1(OMe)** and (□) 2,4-bis(4-methylphenyl)-3-oxopentyl-1,5-dimethanesulfonate **1(Me)** and presented as a function of TFE content in nitrogen-saturated acetonitrile.

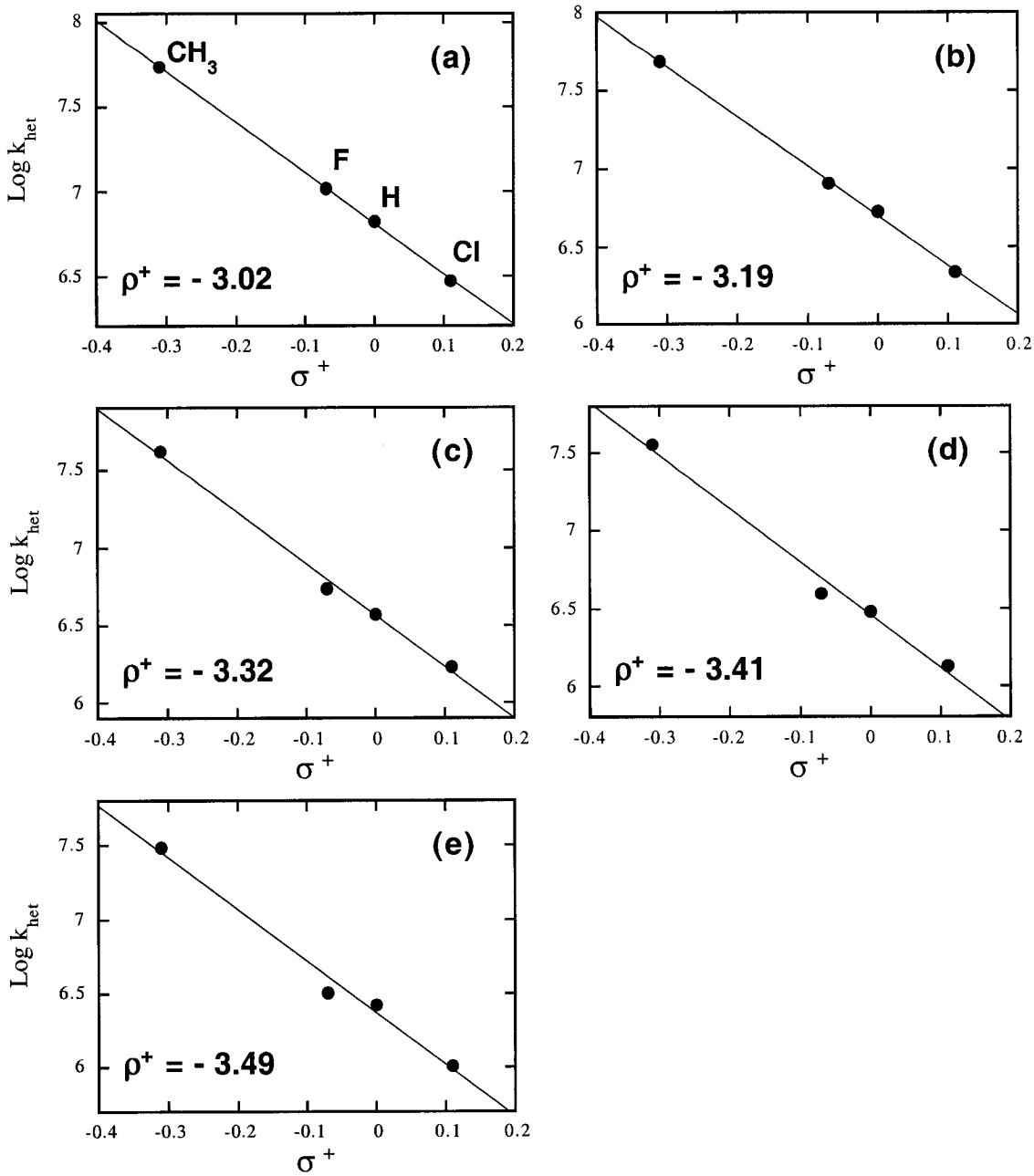

Figure 2-72. Log of rate constants measured for the ionization of the β-mesylate-4-methyl, 4-fluoro, unsubstituted, and 4-chlorophenethyl radical in nitrogen-purged HFIP/TFE mixtures containing (a) 100%, (b) 90%, (c) 80%, (d) 70%, and (e) 60% HFIP, presented as a function of the Brown-Okamoto σ^+ parameters.

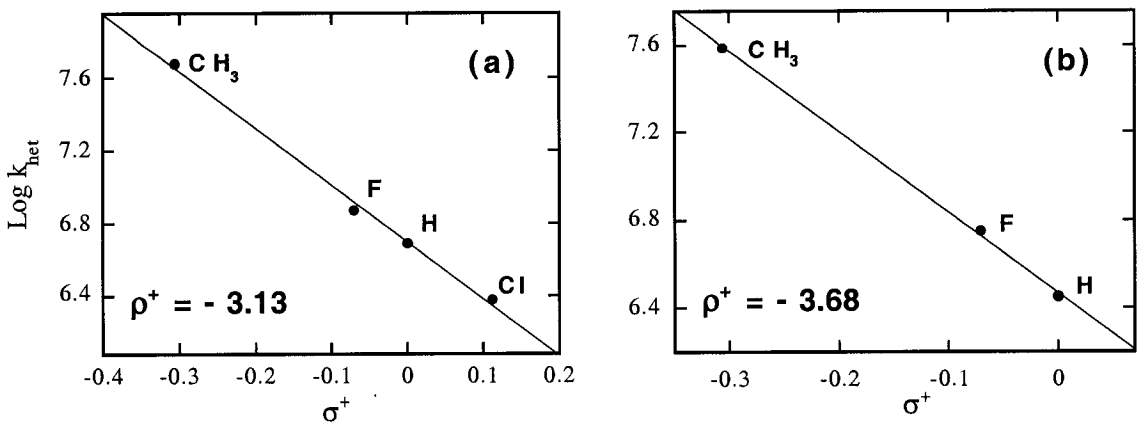

Figure 2-73. Log of rate constants measured for ionization of *para*-substituted β-mesylatephenethyl radicals **2(X)** in nitrogen-purged HFIP/TFE mixtures containing (a) 95% HFIP/5% AcN and (b) 90% HFIP/10% AcN, presented as a function of the Brown-Okamoto σ^+ parameters.

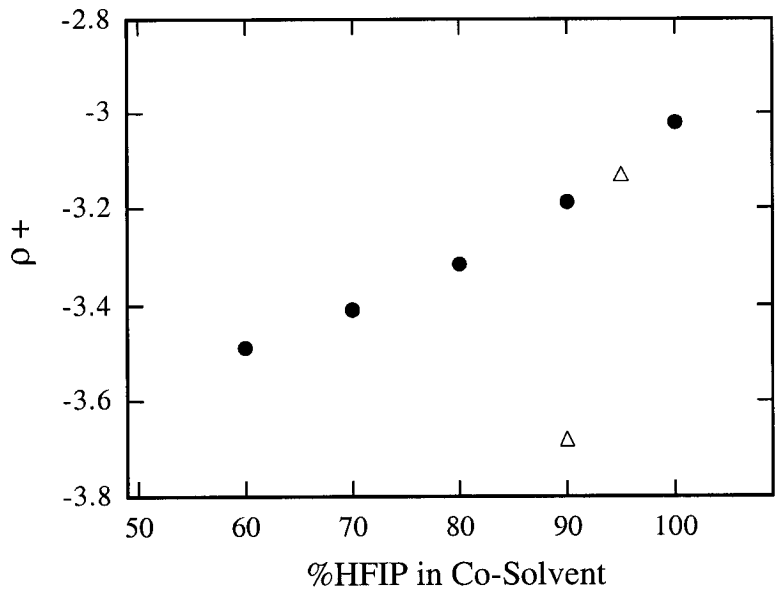

Figure 2-74. Slopes (ρ^+) calculated from the Hammett-type analysis using the Brown-Okamoto σ^+ substituent parameters and presented as a function of HFIP content in nitrogen-saturated (●) TFE and (Δ) acetonitrile.

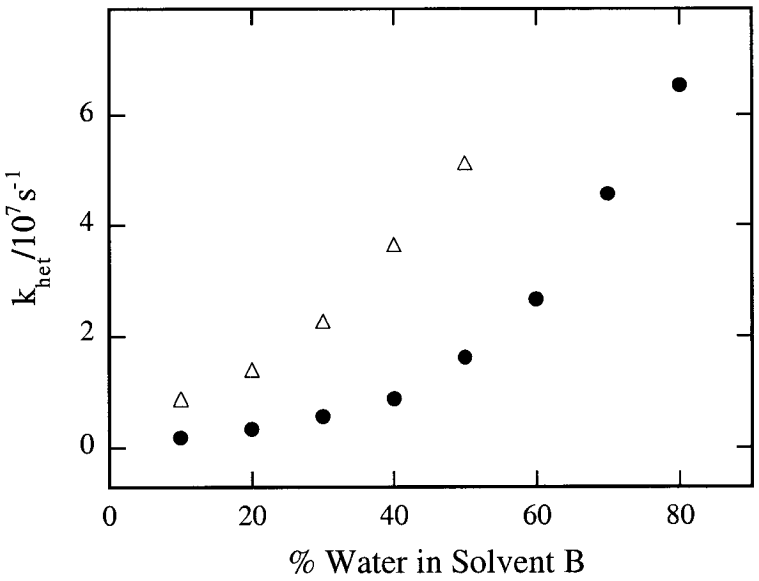

Figure 2-75. Growth of the 4-methoxystyrene radical cation **3(OMe)** measured at 590 nm upon 266 nm laser irradiation of 2-(4-methoxyphenyl)-3-oxobutyl-methanesulfonate **1(OMe)** as a function of water content in nitrogen-saturated (●) acetonitrile and (Δ) methanol.

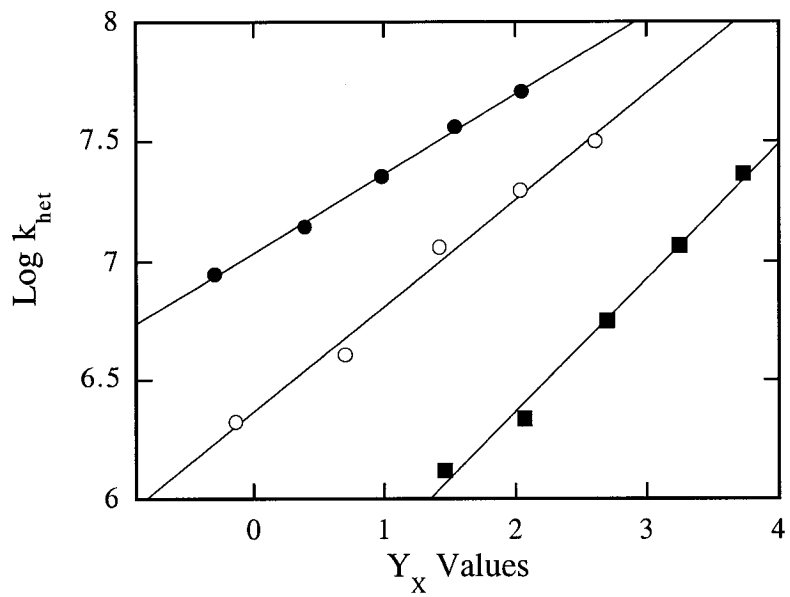

Figure 2-76. Relationship between the observed rate constant for the β-ionization of the (●) β-mesylate-4-methoxyphenethyl radical (R = 0.998, Y_{Oms}, m = 0.33), (○) β-bromo-4-methoxyphenethyl radical (Y_{Br}, m = 0.45), and (■) β-chloro-4-methoxyphenethyl radical (Y_{Cl}, m = 0.56) as a function of the solvent ionizing ability (Y_X values) of methanol/water mixtures.

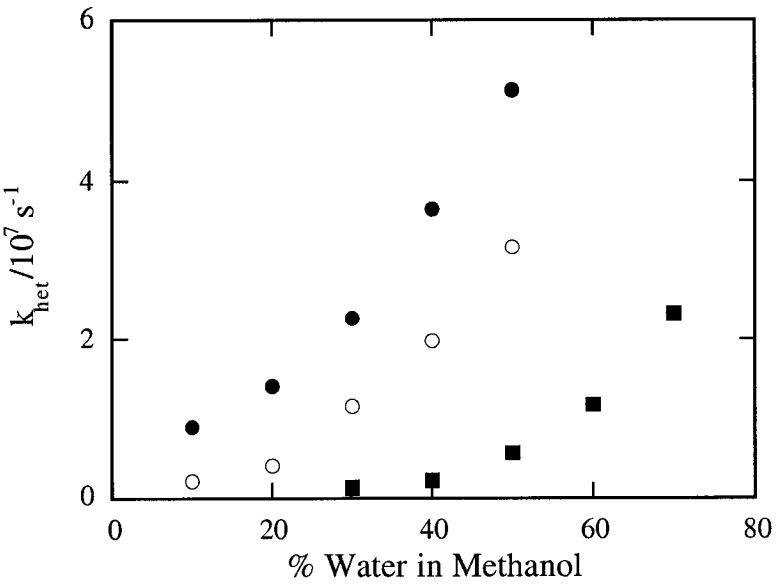

Figure 2-77. Observed rate constant for the growth of the 4-methoxystyrene radical cation upon ionization of the (●) β-mesylate-4-methoxyphenethyl radical, (○) β-bromo-4-methoxyphenethyl radical, and (■) β-chloro-4-methoxyphenethyl radical in methanol/ water mixtures.

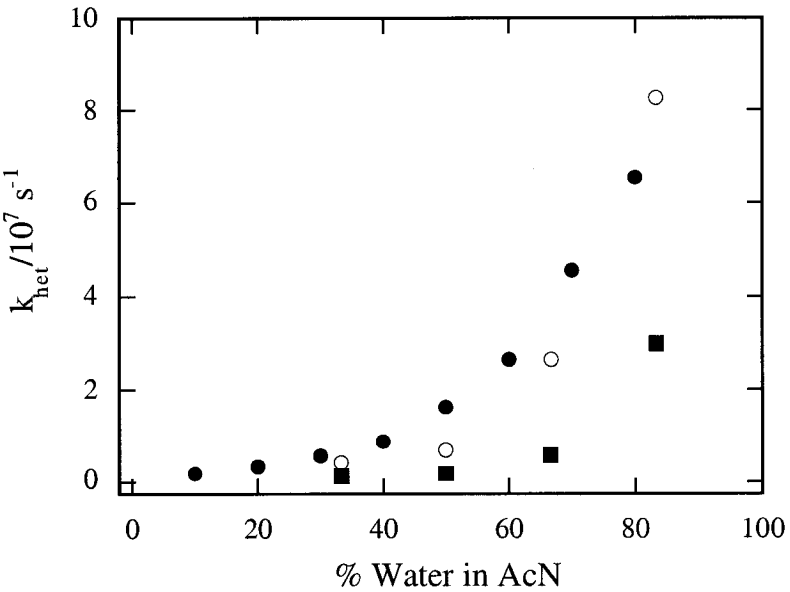

Figure 2-78. Growth of the 4-methoxystyrene radical cation **3(OMe)** measured at 600 nm upon 266 nm irradiation of (●) 2-(4-methoxyphenyl)-3-oxo-butylmethanesulfonate, (○) 1-acetoxy-2-bromo-1-(4-methoxyphenyl)ethane, and (○) 1-acetoxy-2-chloro-1-(4-methoxyphenyl)ethane as a function of water content in nitrogen-saturated acetonitrile.

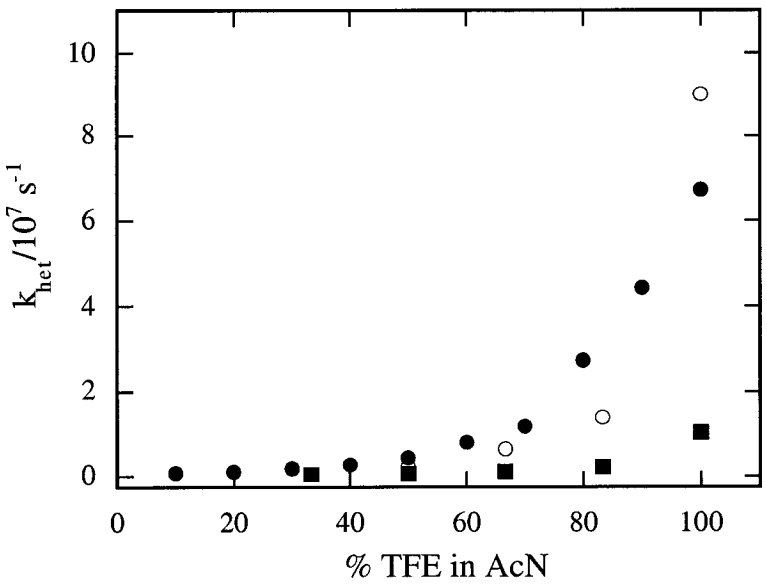

Figure 2-79. Growth of the 4-methoxystyrene radical cation **3(OMe)** measured at 600 nm upon 266 nm irradiation of (●) 2-(4-methoxyphenyl)-3-oxo-butylmethanesulfonate, (○) 1-acetoxy-2-bromo-1-(4-methoxyphenyl)ethane, and (■) 1-acetoxy-2-chloro-1-(4-methoxyphenyl)ethane as a function of TFE content in nitrogen-saturated acetonitrile.

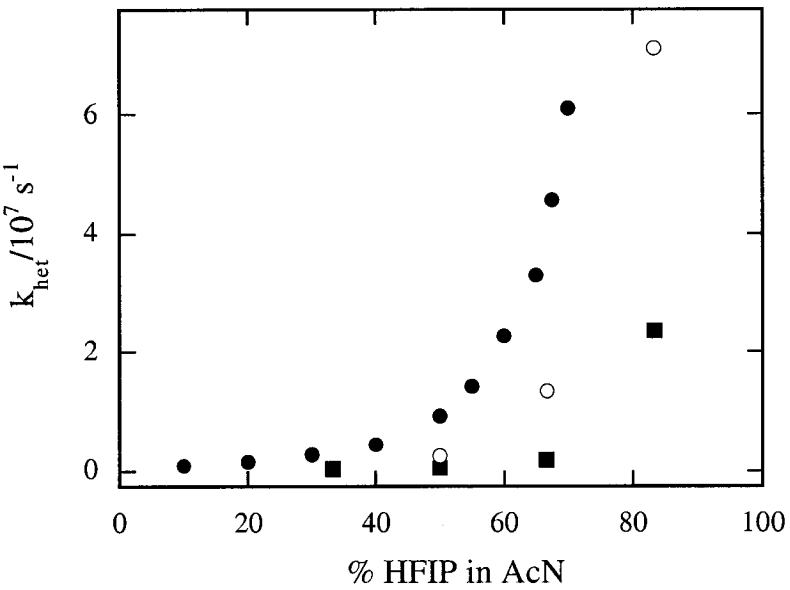

Figure 2-80. Growth of the 4-methoxystyrene radical cation **3(OMe)** measured at 600 nm upon 266 nm irradiation of (●) 2-(4-methoxyphenyl)-3-oxo-butylmethanesulfonate, (○) 1-acetoxy-2-bromo-1-(4-methoxyphenyl)ethane, and (■) 1-acetoxy-2-chloro-1-(4-methoxyphenyl)ethane as a function of HFIP content in nitrogen-saturated acetonitrile.

CHAPTER 3

ACID-CATALYZED β-HETEROLYSIS

3.1 Introduction

This chapter focuses on the acid-catalyzed β-heterolysis reaction that is associated with various enzymatic reactions, such as those mediated by ethanolamine deaminase,[3,12,149] diol dehydrase,[3,11] and ribonucleotide reductase.[4,16,17] The principal objective of this work was to investigate how the kinetics of the acid-catalyzed β-heterolysis process are influenced by electronic substituent effects and the acid strength of the medium. Solvent effects on the ionization of β-substituted radicals were studied in neat HFIP, TFE and AcN, as well as in various TFE/AcN mixtures acidified with perchloric acid. Lastly, the nucleofugality of the β-group was assessed by studying the acid-catalyzed ionization of the β-hydroxy (β-OH) and β-diethylphosphate (β-$OP(O)(OEt)_2$) group in the same range of acidic solvents.

The first half of this chapter describes the work carried out on the acid-catalyzed reaction of β-OH-*para*-substituted phenethyl radicals **7(X)**, Scheme 3-1.

Scheme 3-1

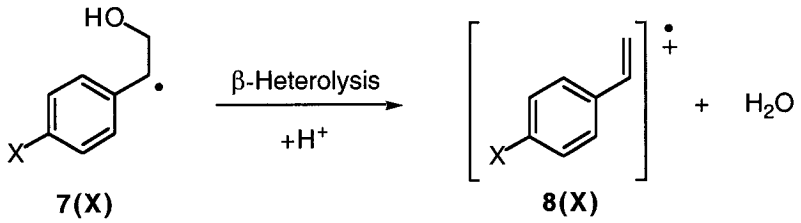

7(X) **8(X)**

X = Cl, H, F, CH_3, or OCH_3

The precursors synthesized for this investigation are shown in Scheme 3-2 and include 2,4-bis(4-chlorophenyl)-1,5-dihydroxy-3-pentanone **6(Cl)**, 2,4-diphenyl-1,5-dihydroxy-3-pentanone **6(H)**, 2,4-bis(4-methylphenyl)-1,5-dihydroxy-3-pentanone **6(Me)**, 3-(4-fluorophenyl)-4-hydroxy-2-butanone **6(F)**, 3-(4-methoxy-phenyl)-4-hydroxy-2-butanone **6(OMe)**. As in Chapter 2, the structure of the precursors adopted one of two carbon backbones (designated below as A and B) according to the commercial availability of the starting materials.

Scheme 3-2

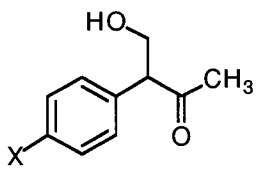

A

6(F) X = F
6(OMe) X = OCH_3

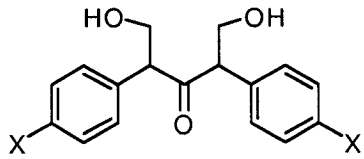

B

6(Cl) X = Cl
6(H) X = H
6(Me) X = CH_3

The results discussed in the second half of this chapter explore the reactivity of the β-diethylphosphate-4-methoxyphenethyl radical **10(OMe)** in a variety of solvent systems. Radical **10(OMe)** was generated photolytically by 266 nm laser irradiation of the precursor compound, 2-(4-methoxyphenyl)-3-oxobutyldiethylphosphate **9(OMe)**.

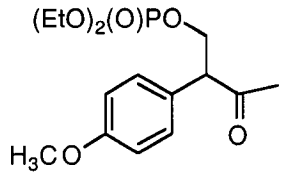

9(OMe)

The primary goal was to investigate the heterolytic cleavage of the β-OP(O)(OEt)$_2$ group, eq. 3.1. Special emphasis was placed on studying this reaction in the same acidic solutions found favorable for the ionization of the β-OH radical **7(OMe)** in order to draw conclusions about the influence of nucleofugality on the rate constants of the acid-catalyzed β-heterolysis process.

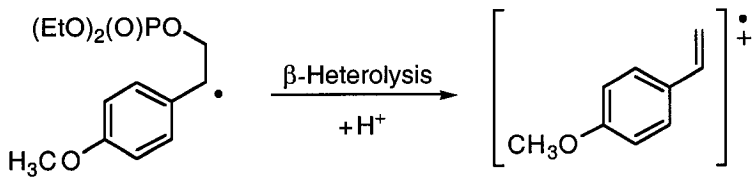

10(OMe) **11(OMe)** (3.1)

3.2 Results

3.2.1 Laser Photolysis of Alcohol and Diol Precursors in Solution

3.2.1.1 Neat Solvents: Acetonitrile, TFE, and HFIP

As shown in Figure 3-1, 266 nm laser flash photolysis of precursor **6(Cl)** in nitrogen-saturated AcN generates a transient with an absorption maximum near 280 nm. A time-resolved kinetic trace subsequently collected at this wavelength is presented in Figure 3-2 and upon analysis, reveals that the transient responsible for this absorption decays in a second-order manner, with an observed rate constant $k_{obs} = 8.2 \times 10^5\ s^{-1}$. While this entity is relatively long-lived in nitrogen-purged AcN, it is rapidly quenched under oxygenated conditions, as evidenced by the mere residual absorption detected at

280 nm, Figure 3-1. The location of the absorption maximum, together with the behavior of the transient in the presence of oxygen, is reminiscent of benzylic-type radicals that absorb in the low UV region, with the 4-chlorobenzyl radical possessing an absorption maximum near 280 nm.[118,119] It is also well known that benzylic radicals are sensitive to radical scavengers and are rapidly trapped by oxygen.[119] As previously mentioned in Chapter 2, the behavior of dibenzylketones upon photolysis is well established and the excited molecules readily undergo α-cleavage to produce benzyl/acyl radical pairs.[102-104,108,109] Therefore, upon 266 nm laser photolysis, **6(Cl)** undergoes a C—CO homolytic bond cleavage to produce the β-OH radicals **7(X)** shown in Scheme 3-3.

Scheme 3-3

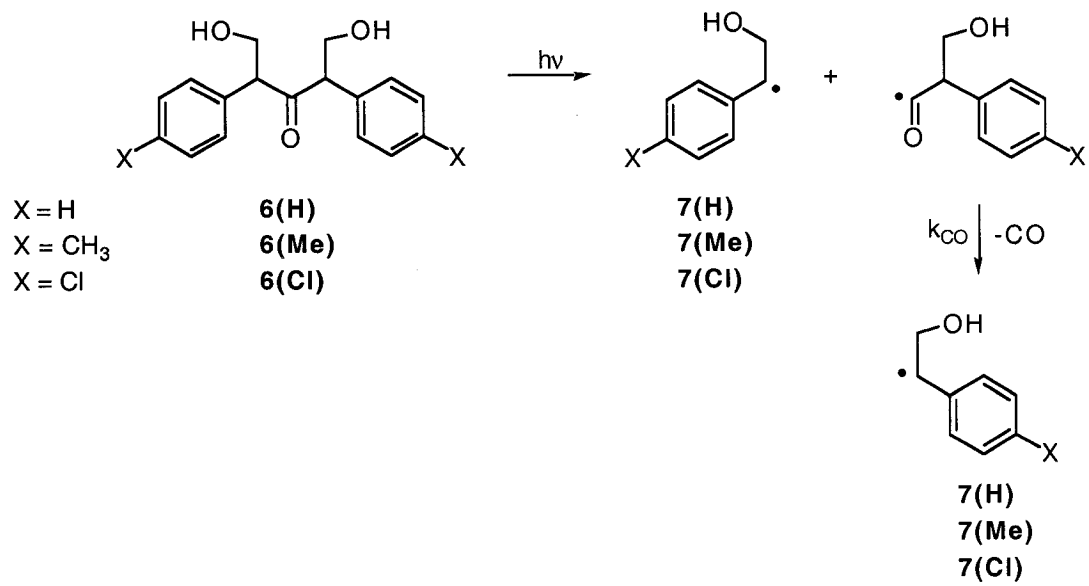

As designated by the Norrish Type I mechanism, the photodissociation comprises of a primary process involving the breakage of a C—CO bond. This occurs within the time duration of the laser pulse,[102,104] and yields the β-hydroxy-4-chlorophenethyl radical **7(Cl)** of interest and a phenacetyl radical. The secondary process

involves rapid decarbonylation of the phenacetyl radical fragment[106,107,111,112] to form CO and a second β-OH radical **7(Cl)**.

Laser flash photolysis at 308 nm of compounds **6(H)** and **6(Me)** in nitrogen-saturated AcN resulted in similar spectral features, Figures 3-3 (a) and (b), as those described above. The transient absorption spectra show a maximum change in optical density near 300 nm that is completely quenched when laser irradiation is carried out in oxygenated AcN. The transients responsible for these absorption bands possess spectral profiles that closely resemble those reported for the benzyl radical and the 4-methylbenzyl radical, respectively.[118,119,150] The absorption maxima detected in these experiments are therefore attributed to the β-hydroxy phenethyl radical **7(H)** and the β-hydroxy-4-methylphenethyl radical **7(Me)**, respectively, generated according to the mechanism shown in Scheme 3-3.

The phenylacetone type precursors **6(F)** and **6(OMe)** generated similar results following 308 and 266 nm laser excitation, respectively, in nitrogen-saturated AcN. The transient absorption spectra, Figures 3-3 (c) and (d), reveal absorption bands near 300 nm which, in both cases, are quenched by the addition of oxygen to the solution. These transient signals closely match those reported for the similar 4-fluoro and 4-methoxybenzyl radicals[118,119] and are assigned to the corresponding radicals **7(F)** and **7(OMe)**. Upon exposure to ultraviolet light, phenylacetone is known to readily undergo Norrish Type I reactions to yield a benzyl/acetyl radical pair.[100] Laser irradiation of precursor **6(F)** or **6(OMe)** is thus expected to result in α-homolysis that generates two initial fragments: the β-OH radical of interest **7(X)** and an acetyl radical that rapidly decarbonylates to a methyl radical, Scheme 3-4.

Scheme 3-4

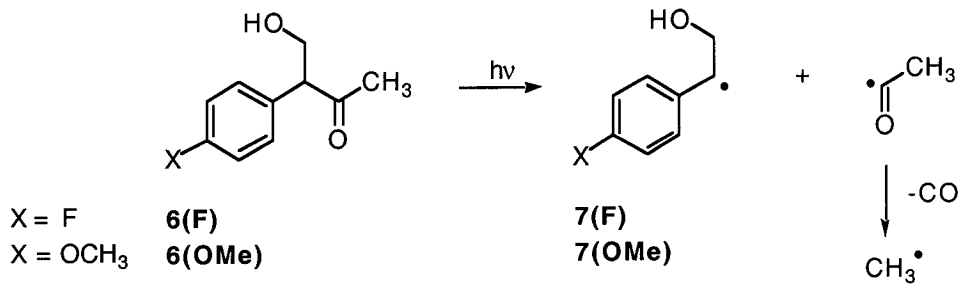

X = F **6(F)** **7(F)**
X = OCH_3 **6(OMe)** **7(OMe)**

Neither the acetyl radical (with a longest absorption band at 215 nm),[114,116,117] carbon monoxide or the methyl radical are detected in these experiments and therefore do not interfere with the spectroscopic measurements made to calculate kinetic data for the β-heterolysis reaction of radicals **7(F)** and **7(OMe)**.

Laser flash photolysis of precursors **6(Cl)**, **6(H)**, **6(Me)**, **6(F)**, and **6(OMe)**, in nitrogen-saturated TFE results in absorption maxima detected around 300 nm, Figure 3-4. The spectral profiles closely match those observed in nitrogen-saturated AcN and those published for the related *para*-substituted benzyl radicals[118,119] and can confidently be assigned to the corresponding β-OH radicals **7(X)**, as described above. As anticipated, the absorption signals generated by radicals **7(X)** are efficiently quenched with the addition of oxygen to the TFE sample.[119] In HFIP, the results presented in Figure 3-5 again imply that radicals **7(Cl)**, **7(H)**, **7(F)** and **7(Me)** are generated *via* photohomolysis of the corresponding precursor compounds following laser irradiation. It is noted however that the characteristic absorption band near 300 nm is not observed upon laser photolysis of **6(OMe)** in HFIP. Instead, a strong absorption is detected between 350 and 400 nm, a band that is quenched with the addition of oxygen to the solution. Although significantly weaker, a similar absorption band can be observed in a few other spectra presented in Figures 3-4 and 3-5. The transient responsible for this absorption signal was not conclusively identified but was not found to interfere with later experiments.

3.2.1.2 HFIP/Perchloric Acid Mixtures

Spectra obtained upon laser irradiation of precursors **6(X)** showed no evidence for the presence of the radical cations that would be generated as a result of heterolytic loss of the β-OH group from radicals **7(X)**. In light of these results, experiments were undertaken in solutions of HFIP containing various concentrations of perchloric acid.

The first precursor compound subjected to laser irradiation in acidic HFIP was **6(Cl)**. The transient absorption spectra presented in Figure 3-6 were obtained following 266 nm laser flash photolysis of **6(Cl)** in nitrogen-saturated HFIP containing 0.021 M perchloric acid. The spectra show an absorption maximum at 280 nm, previously assigned to radical **7(Cl)**. As this transient decays, two additional absorption maxima centered at 370 and 630 nm are detected and increase in intensity. The location of these absorption maxima at 370 and 630 nm, and their relative intensities, closely resemble the known absorption spectra of styrene-type radical cations which have strong absorption near 350 and 600 nm.[46,151] The spectral pattern observed in Figure 3-6 also matches that of the 4-chlorostyrene radical cation generated by an electron-transfer mechanism from 4-chlorostyrene to the triplet chloranil generated upon 308 nm excitation in nitrogen-saturated HFIP, Figure 2-6.

Kinetic measurements were subsequently carried out at 280, 370 and 630 nm following 266 nm laser irradiation of **6(Cl)** in nitrogen-saturated HFIP containing 0.021 M perchloric acid, Figure 3-7. Fitting the traces with a monoexponential function results in a first-order rate constant of $1.2 \times 10^6\ s^{-1}$ for the decay of radical **7(Cl)** at 280 nm, a value that closely matches the observed rate constant calculated for the increase in absorption at 370 and 630 nm, $1.1 \times 10^6\ s^{-1}$ and $1.3 \times 10^6\ s^{-1}$, respectively. Moreover, addition of oxygen resulted in the complete quenching of the transient signals, Figure 3-8. Within the timescale of these experiments, styrene-type radical cations are

insensitive to oxygen concentration; thus the disappearance of the 370 and 630 nm bands implies that **8(Cl)** is generated from an oxygen sensitive precursor. All of these observations are consistent with the acid-catalyzed β-heterolysis reaction mechanism shown in Scheme 3-5. The β-OH radical **7(Cl)** is initially produced *via* Norrish Type I cleavage of the excited precursor **6(Cl)**. Following protonation of the hydroxyl group on **7(Cl)**, the radical undergoes heterolytic breakage of the carbon-oxygen bond to yield water and the 4-chlorostyrene radical cation **8(Cl)**.

Scheme 3-5

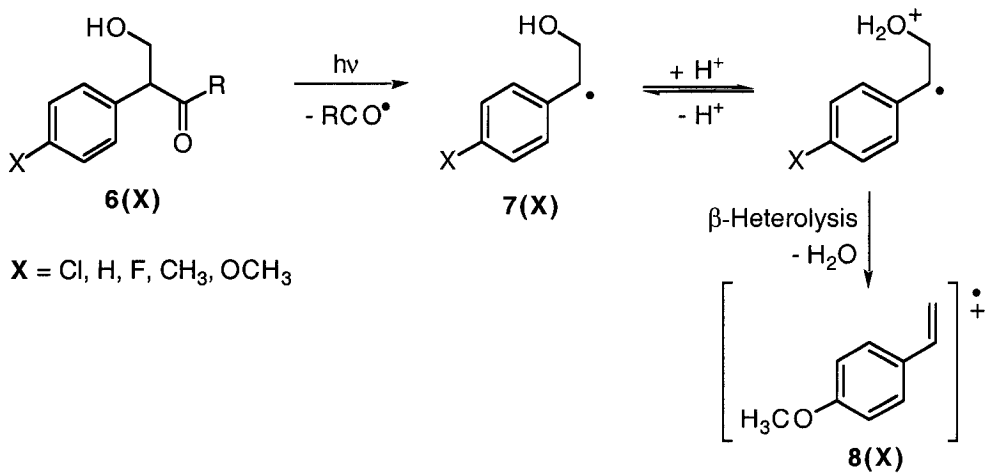

The above mechanism is given additional support with the time-resolved kinetic traces presented in Figure 3-9 showing changes in O.D. at 630 nm in solutions of HFIP containing various perchloric acid concentrations. It can be easily noted that as the concentration of acid increases, the rise of the kinetic trace becomes steeper, indicating that radical cation formation becomes faster with increasing acidity. In light of these results, a systematic study was carried out by 266 nm laser irradiation of **6(Cl)** in nitrogen-saturated in HFIP solutions containing between 0.0026 M to 0.31 M perchloric acid. The relationship between k_{obs} for the growth of the radical cation and perchloric acid concentration is shown in Figure 3-10.

A striking feature of Figure 3-10 is that k_{obs} does not increase indefinitely with increasing acid concentration. Over the range of acid strength investigated, the kinetic data show an obvious curvature that leads to an eventual plateau region where k_{obs} ceases to increase despite further addition of acid to the solution. This kinetic behavior suggests that two limiting mechanisms are in fact at play. In weakly acidic HFIP, within the range of 0.002-0.05 M perchloric acid, k_{obs} for radical cation formation becomes larger with increasing increments of acid to the solution. In this region of the plot, the correlation appears linear and the kinetics of the ionization process is undoubtedly acid-dependent. The rate constant for this reaction is therefore determined by the position of the pre-equilibrium that exists between the radical and the protonated radical, together with the β-heterolysis step itself, Scheme 3-5. The observed rate constant for this process therefore incorporates a concentration term for the acid, along with a second-order rate constant, $k_{obs} = k_{cat}[H^+]$. In HFIP solutions containing more than 0.05 M acid, it is clear that k_{obs} does not continue to increase in a linear manner and eventually levels off to a limiting value. In this instance, the rate constant for the β-heterolysis reaction becomes independent of acid concentration, meaning that the rate of the reaction is entirely determined by the rate at which the ionization process occurs, the final step in Scheme 3-5. The observed rate constant therefore simplifies to an expression that contains a first-order rate constant $k_{obs} = k_{het}$.

A kinetic expression that is consistent with Scheme 3-5 and with the observed acid catalysis at low concentrations of acid, and no catalysis at higher concentrations is shown in eq. 3.2. (This expression is derived in section 3.3.2).

$$k_{obs} = \frac{k_{cat}k_{het}[H^+]}{[H^+]k_{cat} + k_{het}} \qquad (3.2)$$

Both parameters k_{cat} and k_{het} can be obtained by non-linear least squares fitting of k_{obs} measured as a function of acid concentration. In doing so, a second-order rate constant of $k_{cat} = 1.1 \times 10^8\ M^{-1}\ s^{-1}$ is calculated for the acid-catalyzed ionization reaction of **7(Cl)** and a value of $3.6 \times 10^6\ s^{-1}$ is calculated for k_{het}, the acid-independent heterolysis reaction, Figure 3-10.

A similar approach was adopted to investigate the acid-catalyzed β-heterolysis reaction of β-OH radical **7(H)**. Laser irradiation of compound **6(H)** at 308 nm in nitrogen-saturated HFIP containing 0.0078 M perchloric acid led to the spectra provided in Figure 3-11. Along with a hint of absorption from radical **7(H)** near 290 nm, large changes in optical density at 350 and 600 nm dominate the spectra and increase with time. Fitting of the growth traces shown in Figure 3-12 leads to k_{obs} values of $1.8 \times 10^6\ s^{-1}$ and $1.7 \times 10^6\ s^{-1}$ for the rise in absorption at 350 and 600 nm, respectively, a strong indication that the absorption bands originate from the same transient. These results provide supporting evidence that the photogenerated radical **7(H)** ionizes *via* heterolytic loss of water to yield the styrene radical cation **8(H)** as shown in Scheme 3-5. This is further confirmed with the observed quenching of the radical cation in oxygenated solution due to rapid trapping of radical **7(H)** by oxygen. The selected kinetic traces in Figure 3-13 make it evident that the radical cation is formed by a mechanism that is acid-dependent; the growth curve observed at 600 nm rises faster in a solution of HFIP containing 0.017 M than 0.0046 M perchloric acid. The observed rate constants for the β-ionization reaction of radical **7(H)** are plotted as a function of perchloric acid concentration, Figure 3-14. Fitting of these data to eq. 3.2 gives a second-order rate constant of $k_{cat} = 3.3 \times 10^8\ M^{-1}\ s^{-1}$ for the acid-catalyzed β-heterolysis reaction and a value of $k_{het} = 7.6 \times 10^6\ s^{-1}$ for the first-order ionization rate constant that is independent of acid concentration.

The transient absorption spectra shown in Figure 3-15 were obtained following 308 nm laser flash photolysis of precursor **6(F)** in nitrogen-saturated HFIP containing 0.0049 M perchloric acid. Two absorption bands centered around 355 and 585 nm are detected and intensify with time following the laser pulse. Upon analysis of the corresponding kinetic traces collected at 355 and 585 nm, an identical first-order rate constant, $k_{obs} = 7.5 \times 10^5\ s^{-1}$, is calculated for the build-up of absorption at these wavelengths, Figure 3-16. In an oxygen-saturated solution of acidic HFIP, the signals at 355 and 585 nm are not observed upon laser photolysis of **6(F)**. This behavior, along with the location of the absorption maxima and their relative intensity, lead to the identification of the transient as the 4-fluorostyrene radical cation **8(F)** formed *via* heterolytic loss of water from radical **7(F)**. Figure 3-17 shows selected kinetic traces at 585 nm in acidic HFIP and reveals that the rise in signal is dependent on acid concentration, as expected for a mechanism that involves a protonation step. The observed rate constants for the acid-catalyzed dehydration of radical **7(F)** are presented in Figure 3-18 as a function of perchloric acid concentration. Fitting of these data to eq. 3.2 gives a second-order rate constant $k_{cat} = 2.1 \times 10^8\ M^{-1}\ s^{-1}$ and a first-order rate constant $k_{het} = 7.5 \times 10^6\ s^{-1}$.

Irradiation at 266 nm of precursor **6(Me)** dissolved in nitrogen-saturated HFIP containing 0.010 M perchloric acid led to the acquisition of the spectra presented in Figure 3-19. The absorption maximum noted at 280 nm is assigned to the 4-methylphenethyl radical **7(Me)** and decays while strong absorption bands at 360 and 600 nm increase with time. Time-resolved kinetic traces collected at these three absorption maxima are provided in Figure 3-20. Fitting each trace with a monoexponential expression established a first-order rate constant for the decay of the radical that matches the first-order rate constant $k_{obs} = 5.9 \times 10^6\ s^{-1}$ for the rise in signal at

360 and 600 nm. This kinetic data, combined with the location of the absorption maxima at 360 and 600 nm, led to the identification of the transient as the 4-methylstyrene radical cation[46] generated from radical **7(Me)** *via* the ionization of water as shown in Scheme 3-5. This mechanism is further supported by the fact that the radical cation is quenched in oxygenated solution due to trapping of the radical precursor by oxygen.

Selected time-resolved kinetic traces are provided in Figure 3-21 and show the build-up of signal at 600 nm due to **8(Me)** in various perchloric acid/HFIP mixtures. The changes in optical density observed after the laser pulse rise faster with time as the concentration of acid increases from 0.0013 M to 0.0044 M. Once again, this suggests that k_{obs} for the ionization of **7(Me)** is strongly influenced by the acidity of the HFIP solution. The values of k_{obs} calculated from the kinetic traces recorded at 600 nm are presented as a function of acid concentration in Figure 3-22. Subsequent analysis of these data using eq. 3.2 reveals a second-order rate constant of $k_{cat} = 6.8 \times 10^8\ M^{-1} s^{-1}$ for the acid-catalyzed β-heterolysis reaction and a value of $k_{het} = 3.8 \times 10^7\ s^{-1}$ for the first-order rate constant of the acid-independent ionization reaction.

Experiments were also carried out with precursor **6(OMe)** and Figure 3-23 presents a typical transient spectra acquired following 266 nm laser irradiation of this compound in acidic HFIP solutions. Two strong absorption bands at 350 and 590 nm are detected and found to initially intensify with time. From the time-resolved kinetic traces shown in Figure 3-24, the absorption bands at 350 and 590 nm are determined to increase with a similar first-order k_{obs} of $2.3 \times 10^6\ s^{-1}$ and $2.1 \times 10^6\ s^{-1}$, respectively. This strongly suggests that the absorption maxima originate from the same transient and based on the location of the signals, the species was identified as the 4-methoxystyrene radical cation **8(OMe)**.[46] Upon addition of oxygen to the solution, the bands at 350 and 590 nm disappeared, providing evidence that the radical cation emanates from radical **7(OMe)** by

heterolytic loss of water. The dependence of the β-heterolysis reaction on acid strength is nicely illustrated in Figure 3-25. Once more, the selected time-resolved kinetic traces for the growth of **8(OMe)** rise progressively faster with increasing acid content. Over the range of acid concentration studied, a linear relationship was found between k_{obs} for the build-up of the radical cation and acid concentration, Figure 3-26. Fitting of these data with a linear regression calculates a second-order rate constant k_{cat} of 7.8×10^8 M^{-1} s^{-1}. Attempts were made to measure rate constants for the heterolysis reaction at acid concentrations greater than 0.004 M perchloric acid but the signals associated with the growth of the radical cation became unusually weak, and no reliable measurements of k_{obs} could be obtained. The reasons for this situation were not investigated, and in the end, no measurements at concentrations above 0.004 M perchloric acid were made. A summary of the rate constants k_{het} and k_{cat} determined for radicals **7(X)** in HFIP/perchloric acid mixtures are summarized in Table 3-1.

Table 3-1. Rate constants for the acid-catalyzed (k_{cat}) and acid-independent (k_{het}) β-heterolysis reaction calculated for β-hydroxy-*para*-substituted radicals **7(X)** in HFIP/perchloric acid mixtures.

Radical	$k_{cat}/10^8$ M^{-1} s^{-1}	$k_{het}/10^6$ s^{-1}
7(Cl)	1.1±0.1	3.6±0.1
7(F)	2.1±0.3	7.5±0.5
7(H)	3.3±0.5	7.6±0.5
7(Me)	6.8±0.7	38.2±2.0
7(OMe)	7.8±0.3	-

3.2.2 Laser Photolysis of 3-(4-Methoxyphenyl)-4-hydroxy-2-butanone

3.2.2.1 TFE/Perchloric Acid Mixtures

As shown in Figure 3-27, 266 nm laser irradiation of **6(OMe)** in nitrogen-saturated TFE containing 0.022 M perchloric acid leads to the formation of radical **7(OMe)** whose absorption maximum can be seen at 290 nm decreasing with time. The spectra also show two additional bands that grow in at 350 and 590 nm and are assigned to the 4-methoxystyrene radical cation **8(OMe)**. Kinetic analysis of the time-resolved traces collected at 290, 350 and 590 nm reveals a rate constant of $k_{obs} = 2.1 \times 10^6\ s^{-1}$ associated with the growth curves at 350 and 590 nm and decay at 290 nm, Figure 3-28. Quenching of the radical and the radical cation observed under oxygenated conditions provides strong evidence that **8(OMe)** is formed *via* the acid-catalyzed β-heterolysis mechanism depicted in Scheme 3-5. Consistent with this mechanism, the rise in signal at 590 and 350 nm was found to be acid-dependent within the concentration range studied, Figure 3-29. With increasing acid concentration, the amplitude of the signal can be seen to increase and its build-up becomes faster following the laser pulse. The observed first-order rate constants for the growth at 590 nm are plotted in Figure 3-30 as a function of perchloric acid concentration. From the slope of the graph, a value of $k_{cat} = 8.3 \times 10^7\ M^{-1}\ s^{-1}$ is calculated for the second-order rate constant associated with the acid-catalyzed β-heterolysis reaction.

3.2.2.2 Acetonitrile/Perchloric Acid Mixtures

Laser irradiation at 308 nm of precursor **6(OMe)** in 0.0040 M perchloric acid in nitrogen-saturated AcN generates a transient absorption spectra with two maxima centered around 350 and 590 nm, the first band being approximately three times more intense than the second, Figure 3-31. The addition of oxygen to the sample results in almost complete quenching of these two absorption signals. The growth rate constants

calculated from the time-resolved kinetic traces collected at 350 and 590 nm, Figure 3-32, were found to be identical, $k_{obs} = 1.9 \times 10^6$ s^{-1}, suggesting that the signals likely originate from the same transient. These results are consistent with the formation of the 4-methoxystyrene radical cation **8(OMe)** *via* heterolytic cleavage of water from radical **7(OMe)**, as depicted in Scheme 3-5. Time-resolved kinetic traces monitored at 590 nm reveal a significant dependence on acid concentration, Figure 3-33, consistent with a mechanism in which the β-OH group is protonated prior to elimination. As can be seen, both the rise and the intensity of the signal increase as the acid concentration becomes stronger. The observed first-order rate constant for the growth of the radical cation is plotted as a function of acid concentration in Figure 3-34. A linear correlation can be observed at low concentrations of acid but the data suggest that a limiting rate constant exists for the β-heterolysis reaction at high acid concentrations. According to eq. 3.2, a value of $k_{cat} = 1.4 \times 10^9$ $M^{-1} s^{-1}$ was calculated for the acid-catalyzed rate constant and the rate constant for the uncatalyzed ionization reaction was found to be $k_{het} = 3.4 \times 10^6$ s^{-1}.

3.2.2.3 Acetonitrile/TFE Mixtures with Added Perchloric Acid

Rate constants determined earlier for the ionization of **7(OMe)** in acidic HFIP, TFE and AcN show significant dependence on the nature of the solvent. To further investigate the influence of solvent interactions on the kinetics of the acid-catalyzed β-heterolysis reaction, precursor **6(OMe)** was subjected to laser irradiation at 266 nm in various TFE/AcN mixtures acidified with perchloric acid, the results of which are presented in Figure 3-35. Rate constants for the growth of the 4-methoxystyrene radical cation were calculated from time-resolved kinetic traces monitored at 590 nm under nitrogen-saturated conditions. These were acquired over a range of acid concentrations

up to 0.06 M in AcN containing 25%, 50%, and 75% TFE. Figure 3-35 (a) shows the kinetic data acquired in 25% TFE/75% AcN which rapidly increases upon the addition of acid and then begins to level off in concentrations greater than 0.02 M. Similar results are observed in 50% TFE/50% AcN and 75% TFE/25% AcN, Figures 3-35 (b) and (c) respectively, except that k_{obs} shows a more gradual increase with increasing acid concentration. Analysis of all three sets of data was done according to eq. 3.2. Values for k_{het} and k_{cat} for the ionization of **7(OMe)** are summarized in Table 3.2 which also includes the values of k_{cat} in neat TFE and neat HFIP determined previously.

Table 3-2. Rate constants for the acid-catalyzed (k_{cat}) and acid-independent (k_{het}) β-heterolysis reaction calculated for the β-hydroxy-4-methoxyphenethyl radical **7(OMe)** in various solvents acidified with perchloric acid.

Solvent	$k_{cat}/10^8$ M^{-1} s^{-1}	$k_{het}/10^6$ s^{-1}
AcN	13.8±2	3.4±0.1
25% TFE in AcN	1.6±0.3	1.3±0.05
50% TFE in AcN	1.1±0.08	3.1±0.09
75% TFE in AcN	1.2±0.09	4.4±0.1
TFE	0.83±0.03	-
HFIP	7.8±0.3	-

3.2.3 Photolysis of 2-(4-Methoxyphenyl)-3-oxobutyldiethylphosphate

3.2.3.1 Neat Solvents: Acetonitrile, TFE, and HFIP

In nitrogen-purged AcN, 266 nm laser photolysis of 2-(4-methoxyphenyl)-3-oxobutyldiethylphosphate **9(OMe)** generates the transient absorption spectra presented in Figure 3-36. A transient species with a strong absorption at 290 nm is clearly seen following the laser pulse. Analysis of the kinetic trace at 290 nm determines that the signal decays in a second-order manner, Figure 3-36 inset. Moreover, the transient responsible for this absorption is rapidly quenched in the presence of oxygen, Figure 3-37. The location of the absorption maximum, along with its disappearance in oxygenated AcN, is consistent with the identification of the transient as the β-diethylphosphate-4-methoxyphenethyl radical **10(OMe)** generated photochemically *via* a Norrish Type I reaction as shown in eq. 3.3.

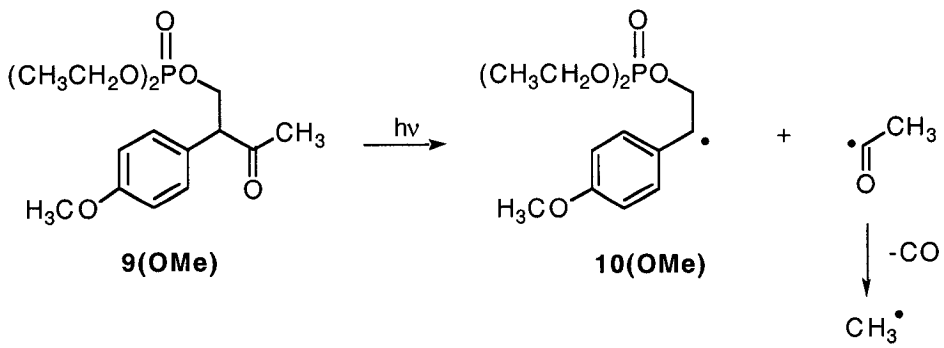

(3.3)

Similar results were observed upon LFP of precursor **9(OMe)** in nitrogen-saturated TFE, water and methanol. Again, the spectra consisted of an absorption band at 290 nm that was quenched under oxygen. Exposure of **9(OMe)** to 266 nm laser irradiation in nitrogen-saturated HFIP also yields radical **10(OMe)**, as evidenced from the 290 nm absorption band observed in the transient absorption spectra provided in Figure 3-38. However, additional maxima can also be observed near 350 and 590 nm and are characteristic of the 4-methoxystyrene radical cation **11(OMe)**.[46,83] Time-

resolved kinetic traces monitored at 290, 350 and 590 nm reveal that the radical decays in HFIP with first-order kinetics, Figure 3-38 inset. Moreover, the rate constant for its decay, $k_{decay} = 7 \times 10^5\ s^{-1}$, closely matches the observed rate constant for the first-order build-up monitored at 350 and 590 nm, $k_{obs} = 6.0 \times 10^5\ s^{-1}$. This strongly suggests that the radical is the direct precursor to the radical cation. The observation that all signals at 290, 350 and 590 nm are significantly quenched by oxygen, Figure 3-39, further indicates that the radical cation is derived from the radical. Together, these results provide evidence that in HFIP, the β-heterolysis reaction is a viable decay pathway for radical **10(OMe)**, eq. 3.4.

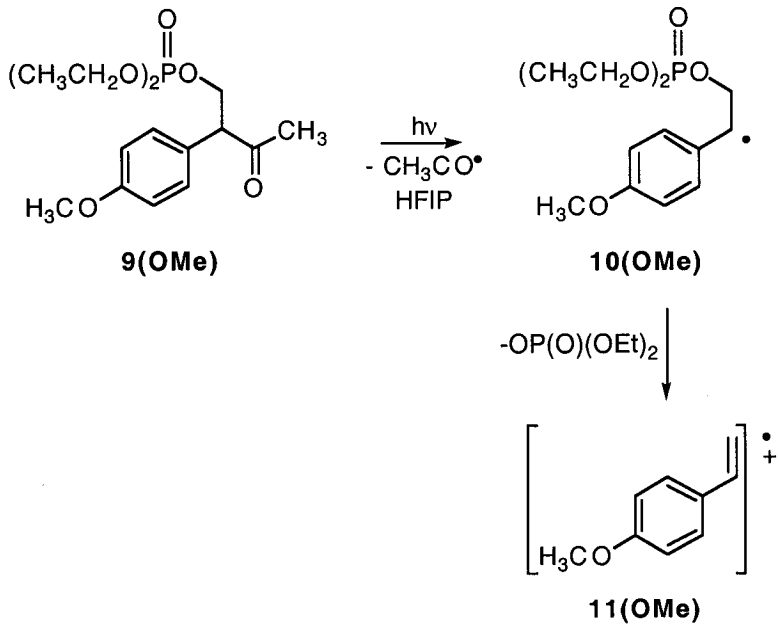

9(OMe) **10(OMe)** **11(OMe)** (3.4)

It is also noted that the spectra provided in Figure 3-38 show the presence of a transient species in addition to the radical and the radical cation. This is evident from the absorption band near 400 nm in nitrogen-saturated HFIP, Figure 3-38. However this transient, which was not identified, decays with kinetics that are different from the decay of the radical and the growth of the radical cation and did not influence the rate constants for the β-heterolysis reaction of radical **10(OMe)**.

As shown in Figure 3-39, oxygen did not provide complete quenching of radical cation formation. This behavior has been observed before[152] and has been attributed to very rapid formation of the radical cation by a mechanism distinct from thermal loss of the β-leaving group from the radical. One possibility is that the initially formed radical absorbs a second photon from the laser pulse to produce an excited radical that then very rapidly undergoes heterolysis of the leaving group, eq. 3.5.

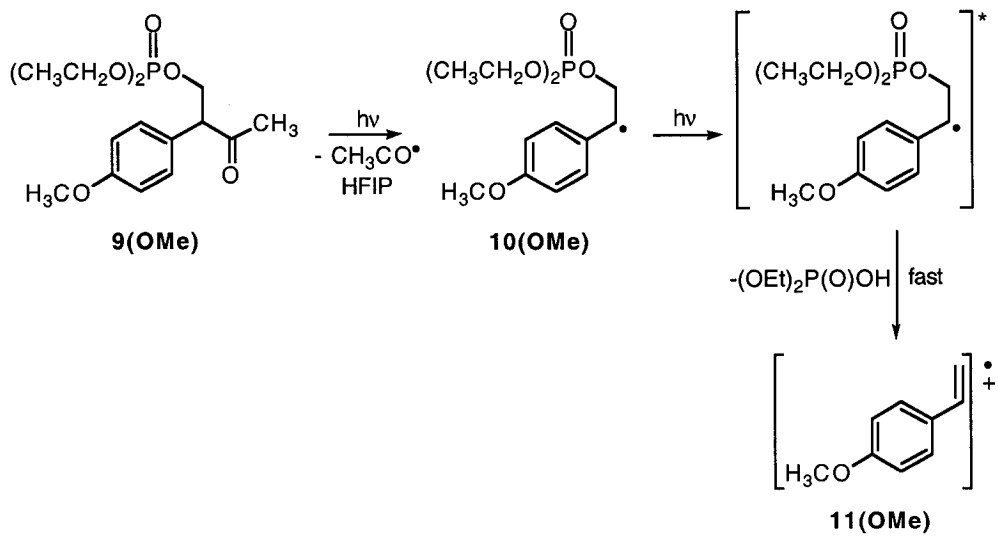

(3.5)

This process is likely to be faster than quenching of the excited radical by oxygen. Thus, a fraction of the radical cations will be observed immediately after the laser pulse, even in oxygenated solution. Two photon experiments with β-trifluoroacetate-4-methoxy-phenethyl radicals have demonstrated the feasibility of such an excited state process.[152] Two-photon experiments were not carried out in the present work.

3.2.3.2 HFIP/Perchloric Acid Mixtures

As a logical progression to this study, precursor **9(OMe)** was subsequently laser irradiated at 266 nm in HFIP acidified with perchloric acid. Experiments were carried out over a wide range of acid concentration (0.0002-0.1 M) but in all cases, the signals were too weak to pursue a systematic investigation under these conditions.

3.2.3.3 Acetonitrile/TFE Mixtures with Added Perchloric Acid

Laser irradiation of precursor **9(OMe)** at 266 nm in nitrogen-purged TFE containing 0.0039 M perchloric acid led to the transient absorption spectra shown in Figure 3-40. While an absorption band at 290 nm decays over the time windows chosen, a concurrent build-up in signal is observed at 350 and 590 nm. Spectra taken in oxygenated solution show that quenching occurs for all three absorption bands that were observed under nitrogen conditions. Equally revealing are the kinetic traces provided in Figure 3-41 showing the decaying absorption at 290 nm and the simultaneous rise at 350 and 590 nm. Kinetic calculations from these traces generates an identical first-order k_{obs} of 1.1×10^6 s^{-1} for the decay of each of the growth curves. These observations are consistent with the β-heterolysis mechanism as the principal decay pathway for radical **10(OMe)**, as shown in Scheme 3-6. Since the addition of acid is clearly a necessity for the ionization of radical **10(OMe)** in TFE, an acid-catalyzed mechanism is presented for the heterolytic loss of phosphoric acid. In this process, the initially formed radical is in equilibrium with its protonated form, and it is only the latter that subsequently undergoes ionization to give the 4-methoxystyrene radical cation.

Scheme 3-6

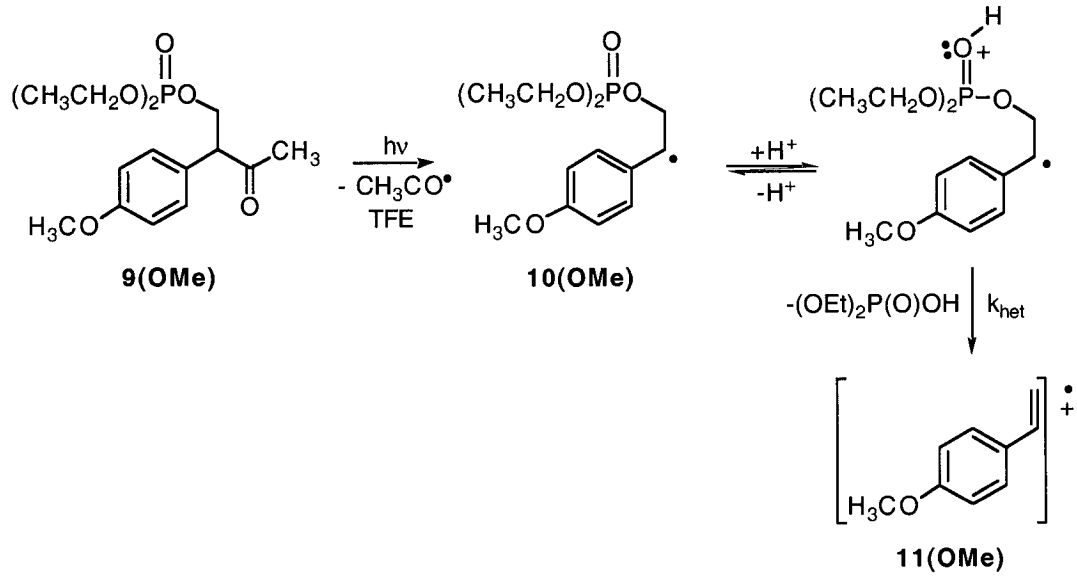

To investigate this further, precursor **9(OMe)** was subjected to 266 nm LFP in TFE containing a range of perchloric acid concentrations. Sample kinetic traces for the growth observed at 590 nm for the radical cation **11(OMe)** in various TFE/acid mixtures are provided in Figure 3-42. It is evident from these traces that the rate of the rise in signal, and therefore the growth of the radical cation *via* β-heterolysis, is dramatically influenced by the concentration of acid present in TFE. Experiments were systematically carried out in TFE solutions containing 0.0048 M to 0.058 M perchloric acid and values of k_{obs} calculated from the kinetic growth traces acquired at 590 nm are presented in Figure 3-43. When plotted as a function of acid concentration, it is apparent that within this concentration range, k_{obs} for the β-heterolysis reaction is linearly dependent on acid concentration. From the slope of this plot, the second-order rate constant for the acid-catalyzed ionization of **10(OMe)** in TFE is calculated as $k_{cat} = 2.3 \times 10^8\ M^{-1} s^{-1}$.

The following set of experiments was carried out to study the dynamics of the acid-catalyzed β-heterolysis reaction in AcN. Preliminary transient absorption spectra were taken in nitrogen-saturated AcN acidified with 0.008 M perchloric acid, following

266 nm laser photolysis of precursor **9(OMe)**, Figure 3-44. The results are similar to those previously observed in acidic TFE, with the 290 nm absorption band of the radical **10(OMe)** decaying while, concurrently, two strong absorption maxima at 350 and 590 nm increase in intensity with time. The quenching effect of oxygen on the radical band at 290 nm and of the signals at 350 and 590 nm can be explained by the acid-catalyzed β-heterolysis mechanism in which the radical cation is preceded by the β-substituted radical that is rapidly scavenged by oxygen. Further supporting evidence for the mechanism outlined in Scheme 3-6 is provided by kinetic analysis of traces monitored at 290, 350 and 590 nm, Figure 3-45. Values of k_{obs} calculated for the rise in absorption at 350 and 590 nm are not only identical with a value of 4.8×10^6 s^{-1}, but match the first-order decay rate constant for the radical, $k_{decay} = 4.8 \times 10^6$ s^{-1}. These results strongly imply that the radical decays *via* ionization of the β-phosphate group to generate the radical cation.

Selected kinetic traces for the build-up of signal at 590 nm following photolysis of **9(OMe)** in various AcN/acid mixtures are provided in Figure 3-46. These traces show that k_{obs} for the β-heterolysis reaction is highly dependent on the concentration of acid in AcN and is confirmed with Figure 3-47 (a). As previously seen in acidic TFE, k_{obs} increases with increasing acid concentration but rather than being linear, the data display a curvature over a similar range of acid concentration. This curvature suggests that k_{obs} does not increase indefinitely and that there exists a concentration of acid beyond which the rate constant no longer increases but rather levels off. These data were treated using eq. 3.2 in the same manner as described earlier and in this way, rate constants of $k_{cat} = 8.0 \times 10^8$ M^{-1} s^{-1} and $k_{het} = 1.6 \times 10^7$ s^{-1} were determined.

Similar experiments were carried out in acidic AcN/TFE solvent mixtures containing 25%, 50%, and 75% TFE. The results are presented in Figure 3-47 (b)-(d) and

as anticipated, all show an increase in k_{obs} as a function of acid in the various solvent systems studied. However, a noticeable difference is seen in the curvature generated by the data, indicating a change in the value of k_{cat} as well as k_{het}. These values were determined by fitting the data with eq. 3.2 and the results of these calculations are provided in Table 3-3.

Table 3-3. Rate constants for the acid-catalyzed (k_{cat}) and acid-independent (k_{het}) β-heterolysis reaction calculated for the β-diethylphosphate-4-methoxyphenethyl radical **10(OMe)** in TFE/AcN mixtures acidified with perchloric acid.

Solvent	$k_{cat}/10^8$ M^{-1} s^{-1}	$k_{het}/10^7$ s^{-1}
AcN	8.0±2.0	1.6±0.1
25% TFE in AcN	4.5±0.5	1.8±0.1
50% TFE in AcN	2.2±0.4	0.95±0.08
75% TFE in AcN	2.6±0.7	1.8±0.03
TFE	2.3±0.05	-

3.2.4 The Decarbonylation Reaction

Kinetic traces collected at the absorption wavelength of radicals **7(X)** immediately following 266 nm laser excitation confirm that radicals **7(Cl)**, **7(H)**, and **7(Me)** undergo rapid loss of CO and that the growth for the second equivalent β-hydroxy radical is faster than the time resolution of this laser system. These results were obtained in AcN as well as in the more polar solvent HFIP. From these results, it is concluded that the decarbonylation step does not interfere with subsequent kinetic measurements made on the β-heterolysis reaction of these radicals.

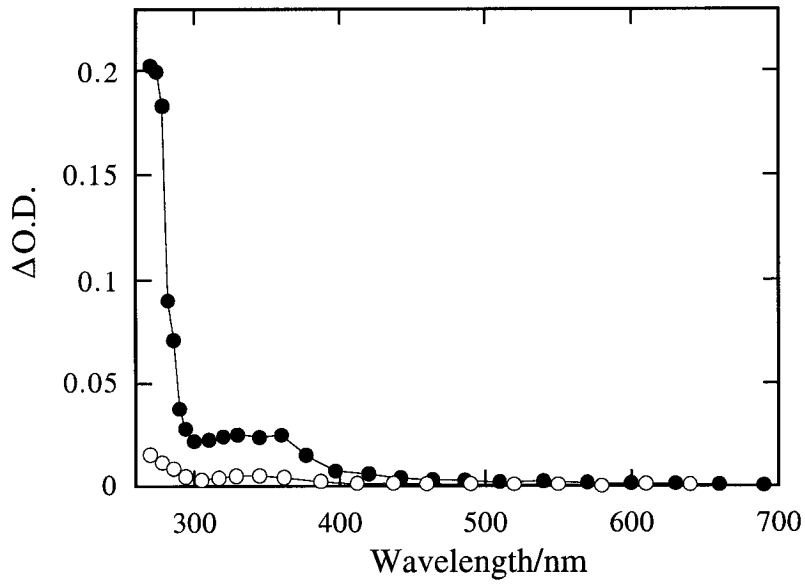

Figure 3-1. Transient absorption spectra obtained 0.60 μs after 266 nm laser irradiation of 2,4-bis(4-chlorophenyl)-1,5-dihydroxy-3-pentanone **6(Cl)** in (●) nitrogen-saturated and (○) oxygen-saturated acetonitrile.

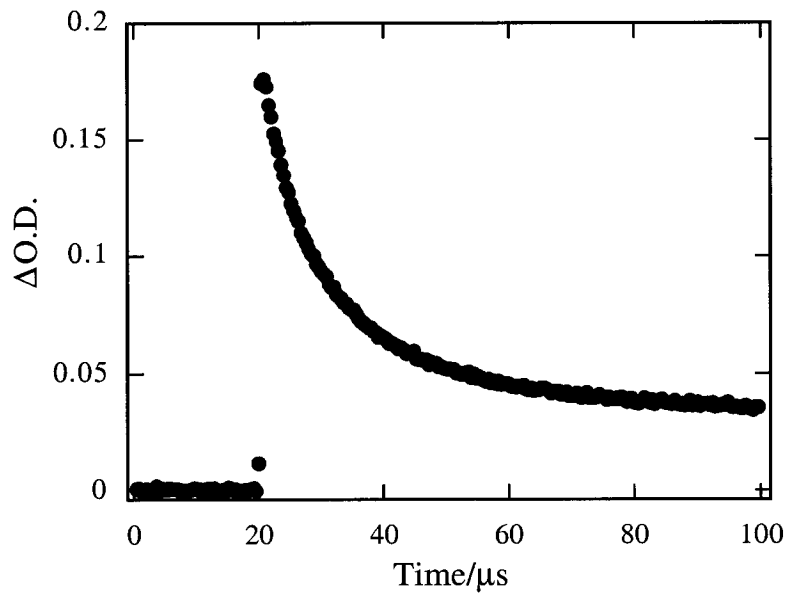

Figure 3-2. Time-resolved second-order decay trace measured at 280 nm after 266 nm irradiation of 2,4-bis(4-chlorophenyl)-1,5-dihydroxy-3-pentanone **6(Cl)** in nitrogen-purged acetonitrile.

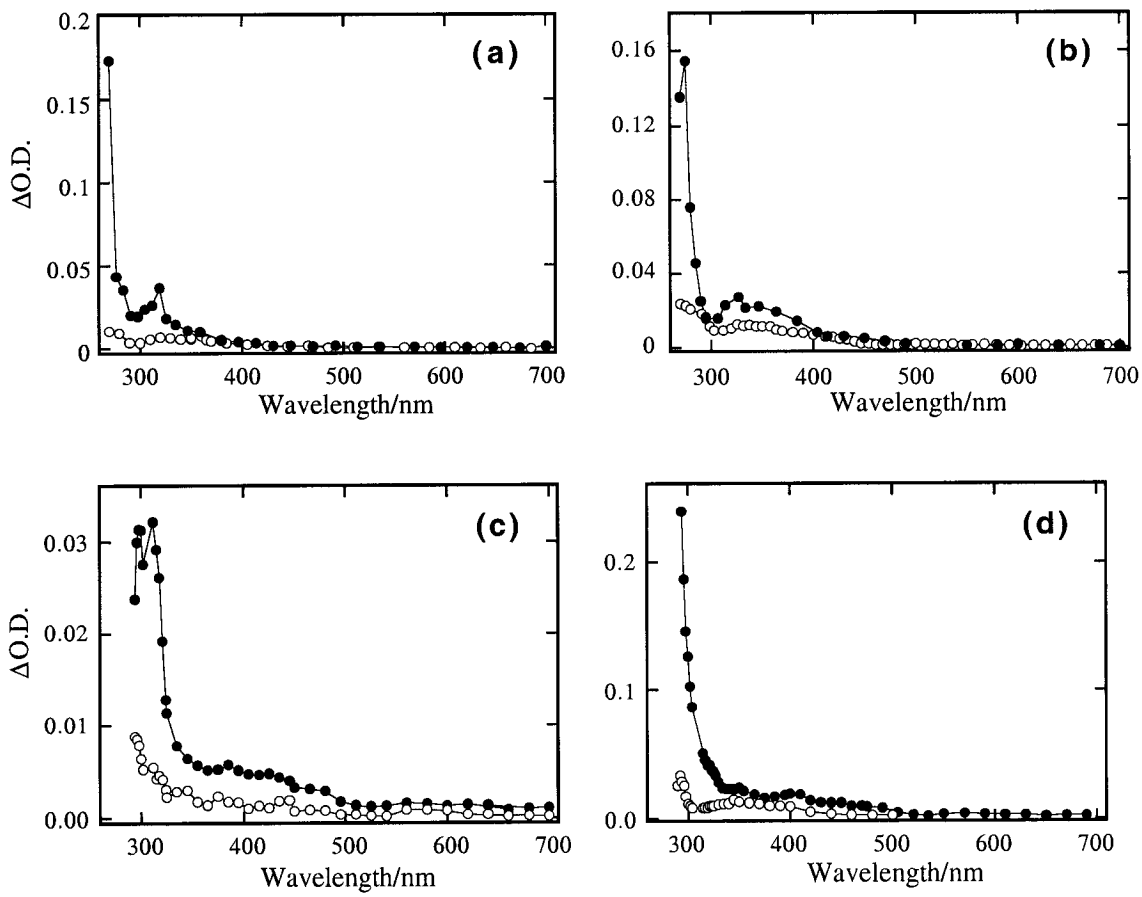

Figure 3-3. Transient absorption spectra obtained after 266 or 308 nm laser irradiation of (a) 2,4-diphenyl-1,5-dihydroxy-3-pentanone **6(H)**, (b) 2,4-bis(4-methylphenyl)-1,5-dihydroxy-3-pentanone **6(Me)**, (c) 3-(4-fluorophenyl)-4-hydroxy-2-butanone **6(F)**, and (d) 3-(4-methoxyphenyl)-4-hydroxy-2-butanone **6(OMe)** in (●) nitrogen-saturated and (○) oxygen-saturated acetonitrile.

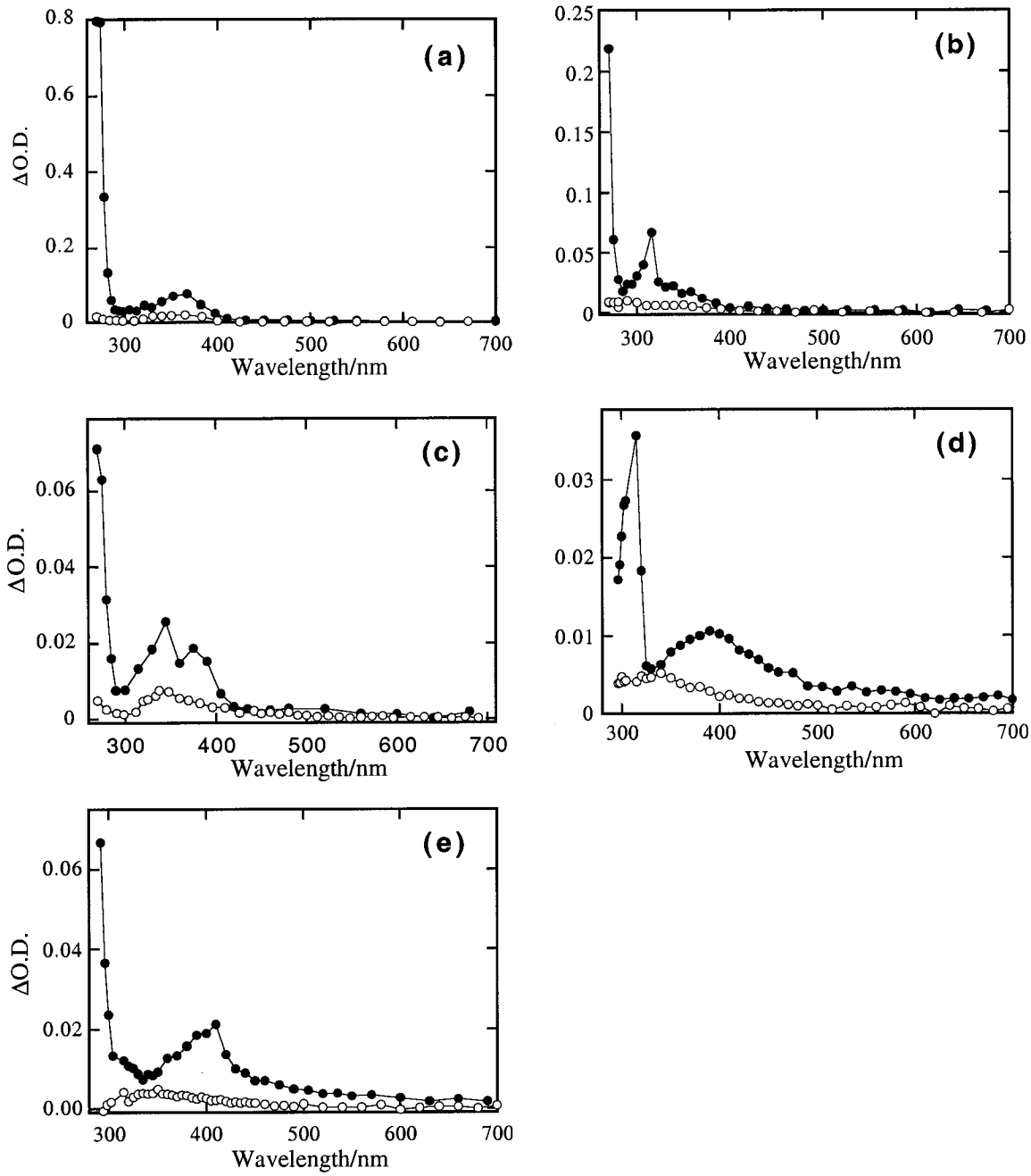

Figure 3-4. Transient absorption spectra obtained after 266 nm laser irradiation of (a) 2,4-bis(4-chlorophenyl)-1,5-dihydroxy-3-pentanone **6(Cl)**, (b) 2,4-diphenyl-1,5-dihydroxy-3-pentanone **6(H)**, (c) 2,4-bis(4-methylphenyl)-1,5-dihydroxy-3-pentanone **6(Me)**, (d) 3-(4-fluorophenyl)-4-hydroxy-2-butanone **6(F)**, and (e) 3-(4-methoxyphenyl)-4-hydroxy-2-butanone **6(OMe)** precursors in (●) nitrogen-saturated and (○) oxygen-saturated TFE.

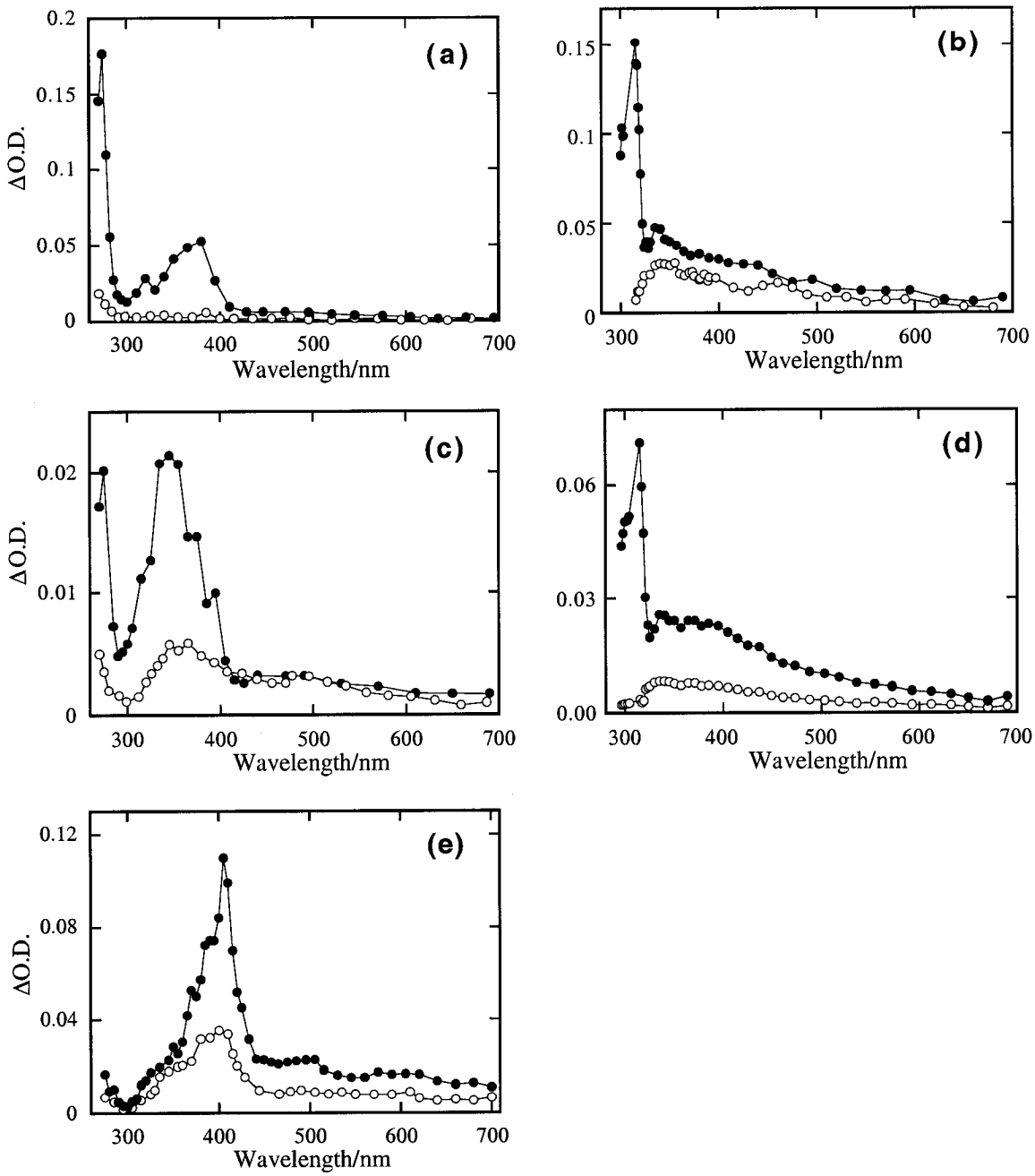

Figure 3-5. Transient absorption spectra obtained after 266 or 308 nm laser irradiation of (a) 2,4-bis(4-chlorophenyl)-1,5-dihydroxy-3-pentanone **6(Cl)**, (b) 2,4-diphenyl-1,5-dihydroxy-3-pentanone **6(H)**, (c) 2,4-bis(4-methylphenyl)-1,5-dihydroxy-3-pentanone **6(Me)**, (d) 3-(4-fluorophenyl)-4-hydroxy-2-butanone **6(F)**, and (e) 3-(4-methoxyphenyl)-4-hydroxy-2-butanone **6(OMe)** in (●) nitrogen-saturated and (○) oxygen-saturated HFIP.

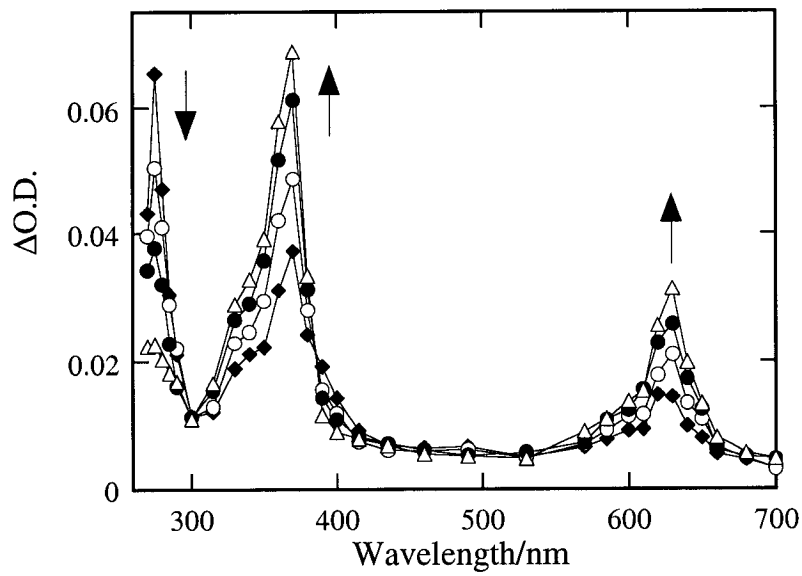

Figure 3-6. Transient absorption spectra obtained after 266 nm laser irradiation of 2,4-bis(4-chlorophenyl)-1,5-dihydroxy-3-pentanone **6(Cl)** in nitrogen-saturated HFIP containing 0.021 M perchloric acid. Spectra were recorded (◆) 0.24 μs, (○) 0.47 μs, (●) 0.83 μs, and (Δ) 1.6 μs following the laser pulse.

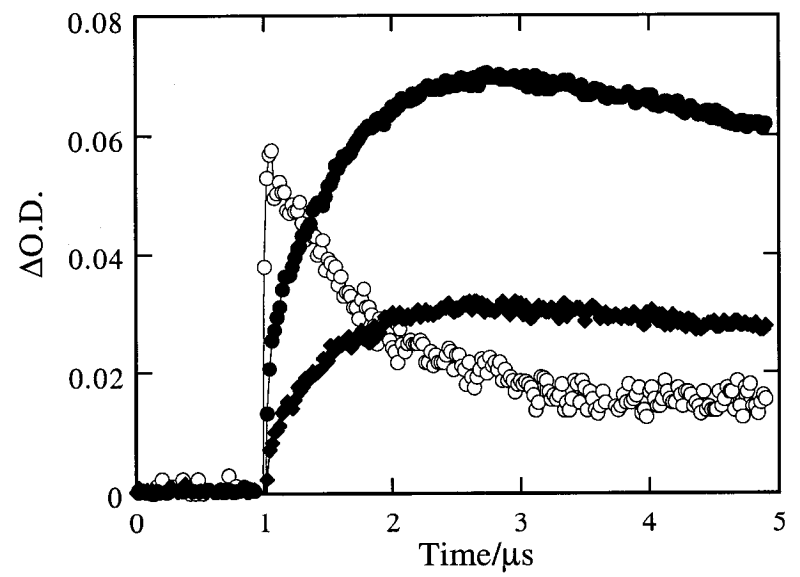

Figure 3-7. Time-resolved kinetic traces at (○) 280 nm, (●) 370 nm, and (◆) 630 nm following 266 nm excitation of 2,4-bis(4-chlorophenyl)-1,5-dihydroxy-3-pentanone **6(Cl)** in nitrogen-saturated HFIP containing 0.021 M perchloric acid.

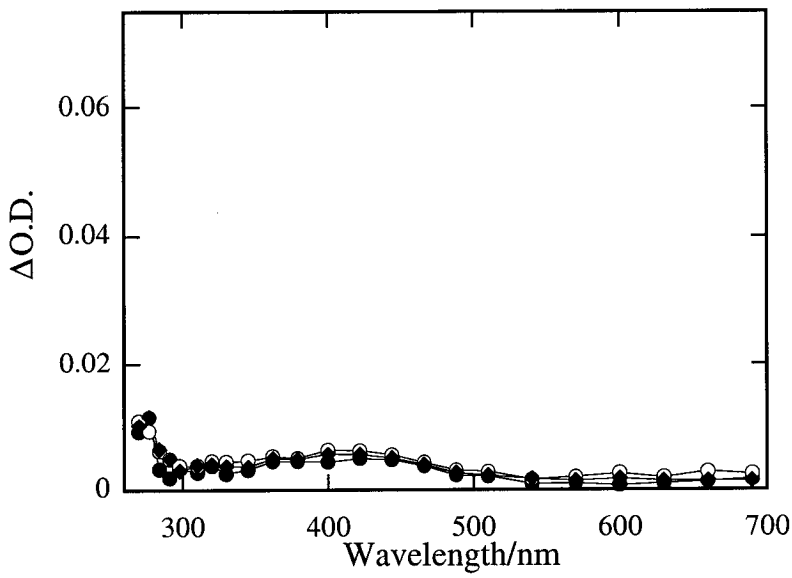

Figure 3-8. Transient absorption spectra generated after 266 nm laser photolysis of 2,4-bis(4-chlorophenyl)-1,5-dihydroxy-3-pentanone **6(Cl)** in oxygen-saturated HFIP containing 0.021 M perchloric acid. Spectra were recorded (◆) 0.24 μs, (○) 0.47 μs, (●) 0.83 μs, and (Δ) 1.6 μs after the laser pulse.

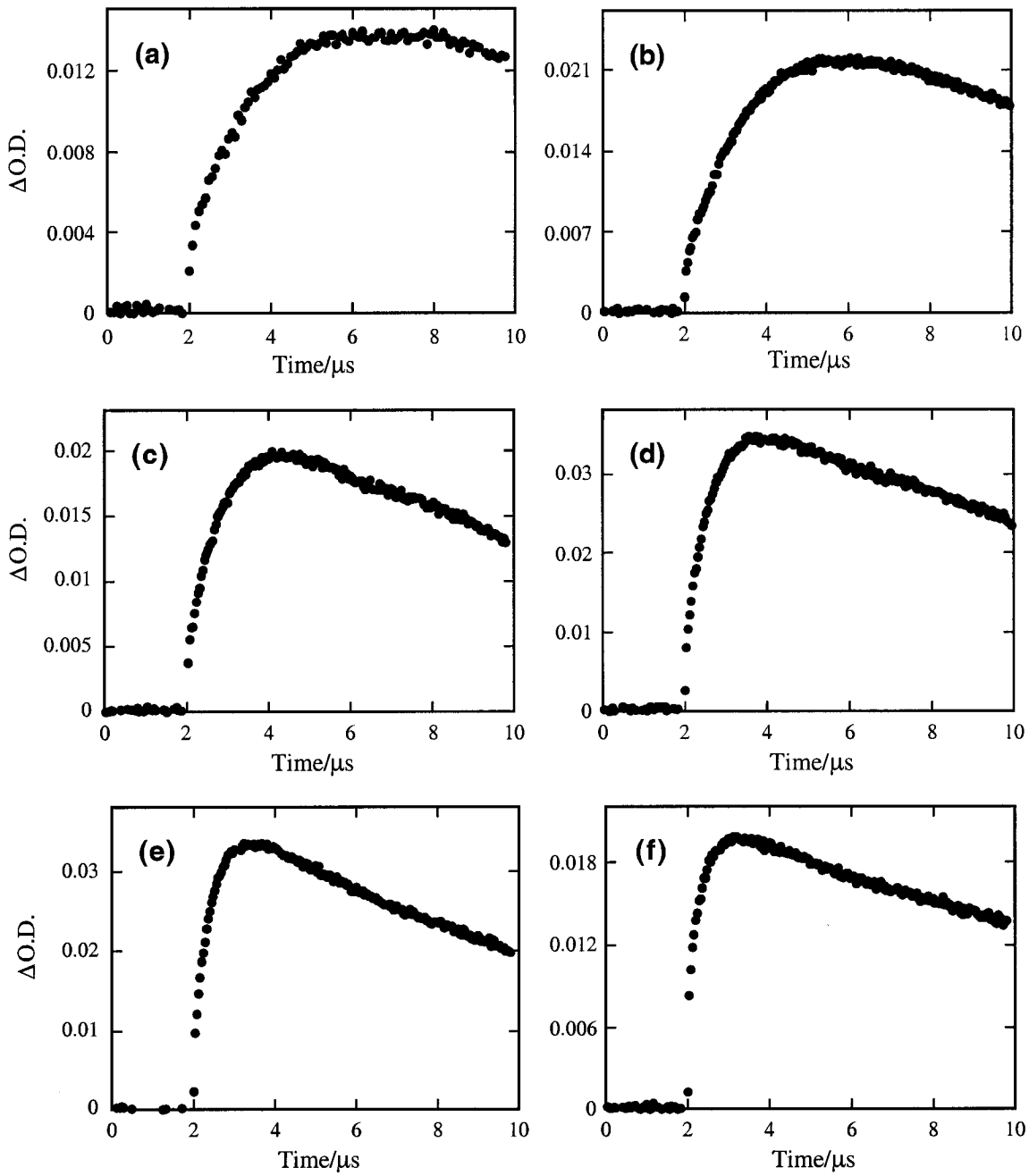

Figure 3-9. Time-resolved kinetic traces monitored at 630 nm upon 266 nm laser flash photolysis of 2,4-bis(4-chlorophenyl)-1,5-dihydroxy-3-pentanone **6(Cl)** in nitrogen-saturated HFIP containing (a) 0.0026 M, (b) 0.0052 M, (c) 0.016 M, (d) 0.031 M, (e) 0.052 M, and (f) 0.21 M of perchloric acid.

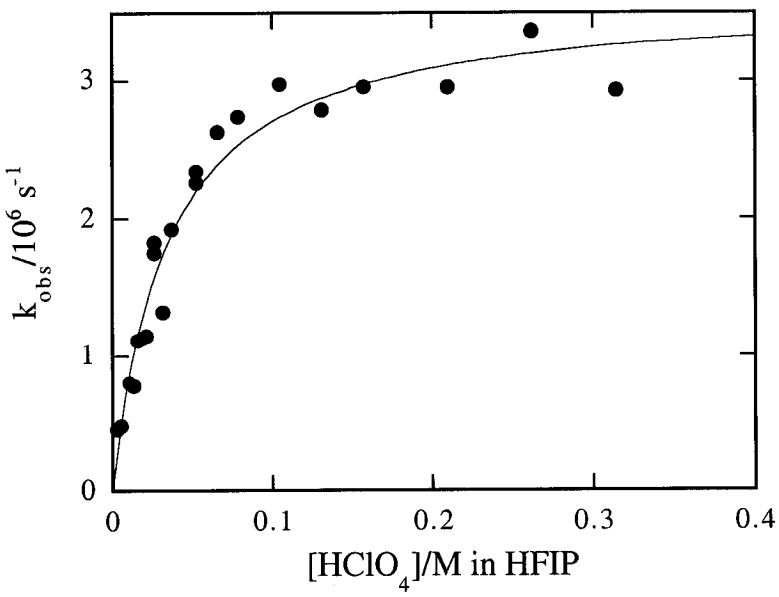

Figure 3-10. Observed rate constant for the growth of the 4-chlorostyrene radical cation **8(Cl)** as a function of perchloric acid concentration in nitrogen-saturated HFIP. k_{obs} was calculated from time-resolved kinetic traces monitored at 630 nm after 266 nm irradiation of 2,4-bis(4-chlorophenyl)-1,5-dihydroxy-3-pentanone **6(Cl)**.

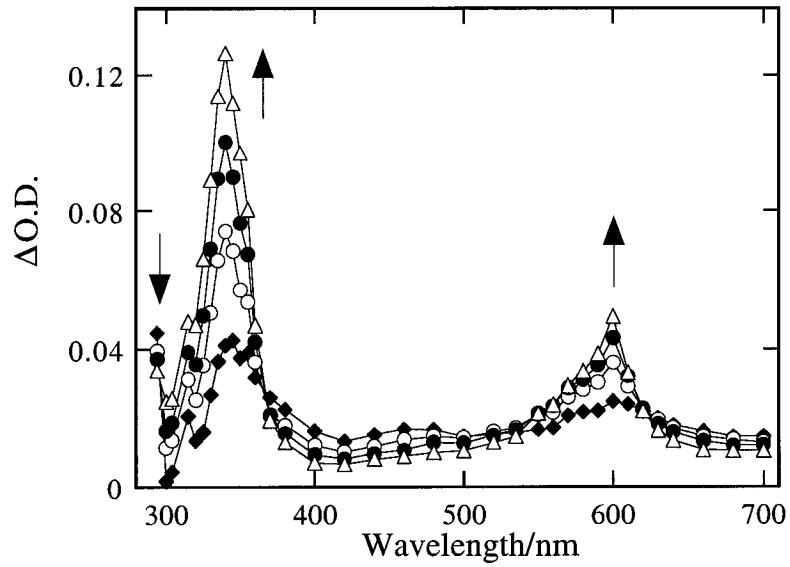

Figure 3-11. Transient absorption spectra acquired after 308 nm laser irradiation of 2,4-diphenyl-1,5-dihydroxy-3-pentanone **6(H)** in nitrogen-saturated HFIP containing 0.0078 M perchloric acid. Spectra were recorded (●) 0.16 μs, (◆) 0.42 μs, (○) 0.71 μs, and (Δ) 1.6 μs after the laser pulse.

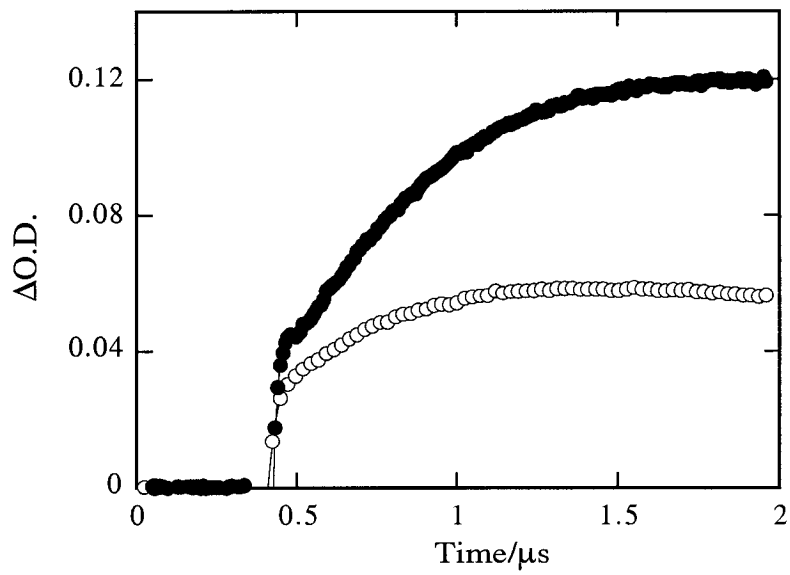

Figure 3-12. Time-resolved kinetic traces monitored at (●) 350 nm and (○) 600 nm after 308 nm laser irradiation of 2,4-diphenyl-1,5-dihydroxy-3-pentanone **6(H)** in nitrogen-saturated HFIP containing 0.0078 M perchloric acid.

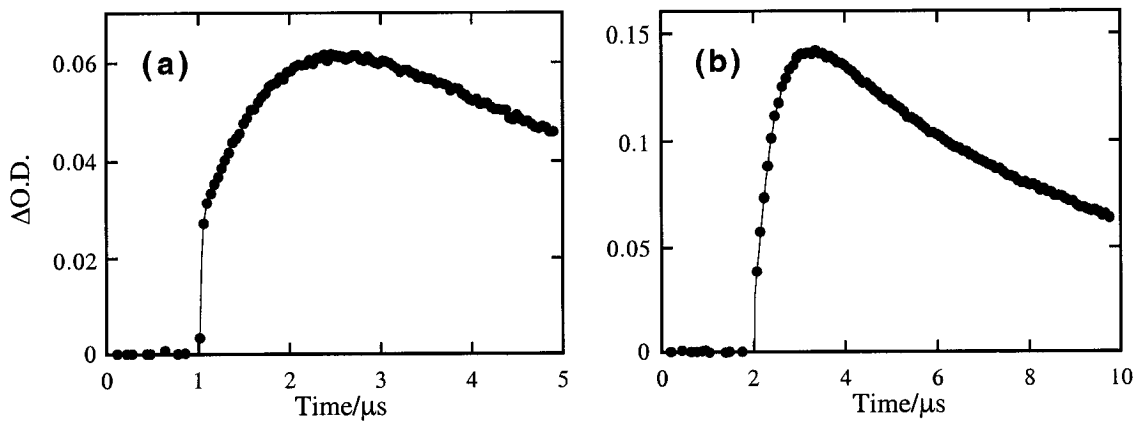

Figure 3-13. Time-resolved kinetic traces monitored at 600 nm following 308 nm laser flash photolysis of 2,4-diphenyl-1,5-dihydroxy-3-pentanone **6(H)** nitrogen-saturated HFIP containing (a) 0.0046 M and (b) 0.017 M perchloric acid.

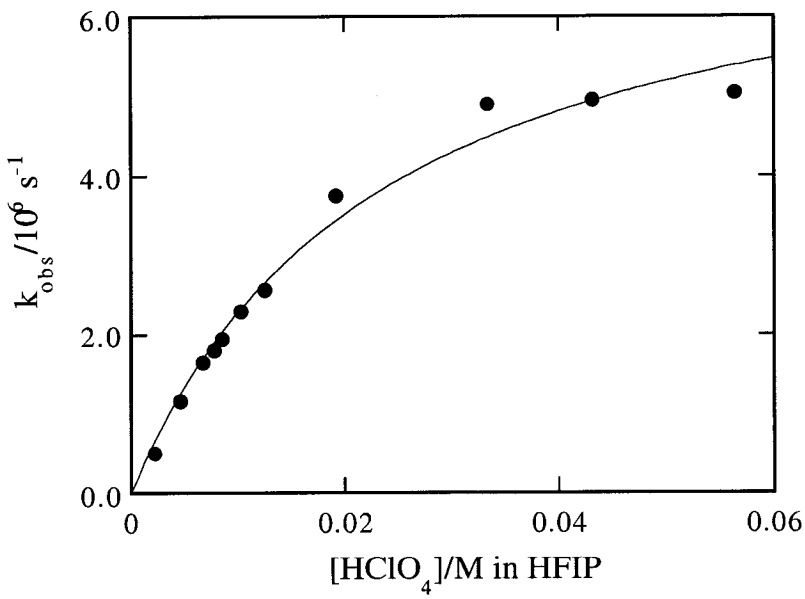

Figure 3-14. Observed rate constant for the growth of the styrene radical cation **8(H)** as a function of perchloric acid concentration in nitrogen-saturated HFIP. k_{obs} was calculated from time-resolved kinetic traces monitored at 600 nm after 308 nm irradiation of 2,4-diphenyl-1,5-dihydroxy-3-pentanone **6(H)**.

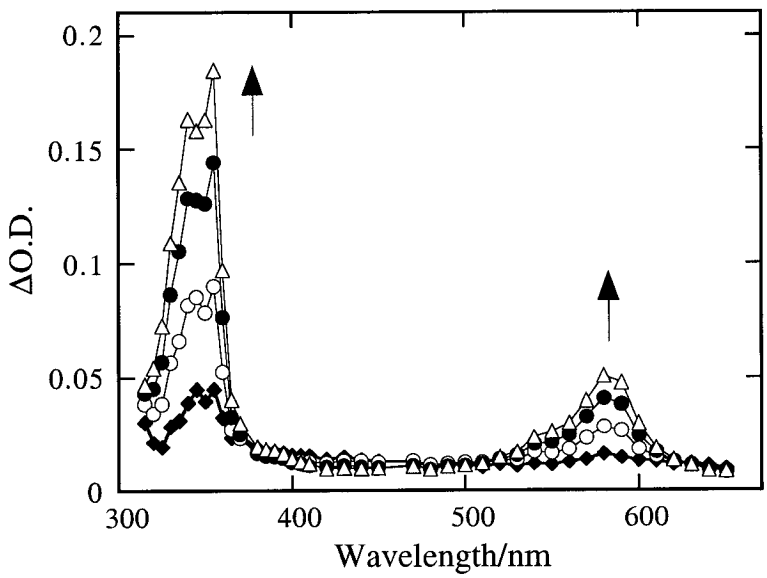

Figure 3-15. Transient absorption spectra acquired after 308 nm laser irradiation of 3-(4-fluorophenyl)-4-hydroxy-2-butanone **6(F)** in nitrogen-saturated HFIP containing 0.0049 M perchloric acid. Spectra were recorded (◆) 0.18 μs, (○) 0.51 μs, (●) 1.0 μs, and (Δ) 2.5 μs after the laser pulse.

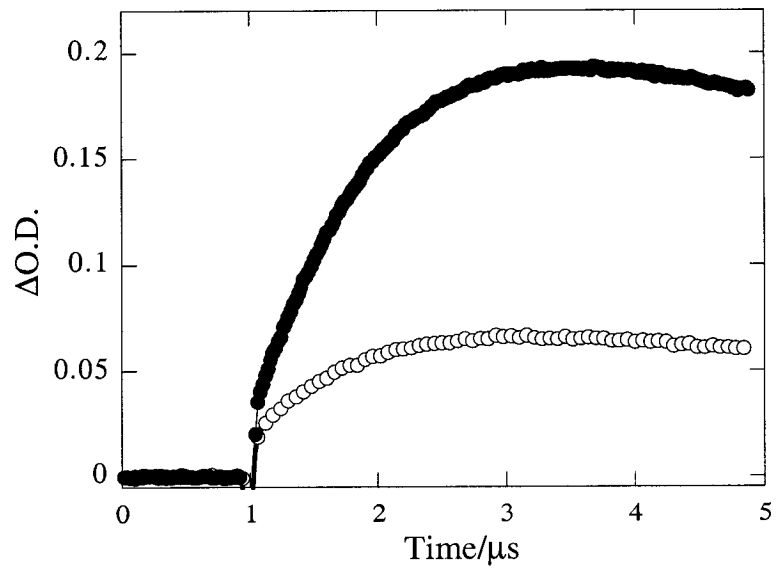

Figure 3-16. Time-resolved kinetic traces monitored at (●) 355 nm and (○) 585 nm following 308 nm laser irradiation of 3-(4-fluorophenyl)-4-hydroxy-2-butanone **6(F)** in nitrogen-saturated HFIP containing 0.0049 M.

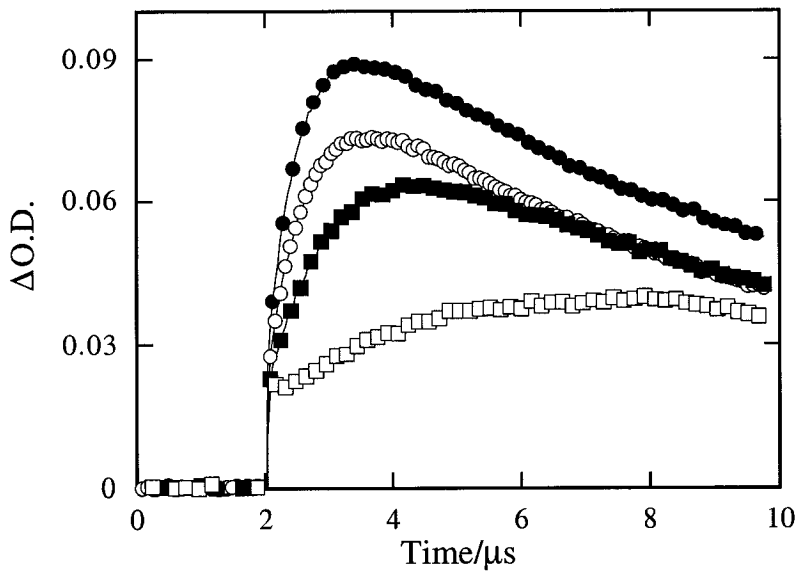

Figure 3-17. (a) Time-resolved growths at 585 nm recorded upon 308 nm laser flash photolysis of 3-(4-fluorophenyl)-4-hydroxy-2-butanone **6(F)** in nitrogen-saturated HFIP containing (□) 0.0022 M, (■) 0.0046 M, (○) 0.010 M, and (●) 0.013 M perchloric acid.

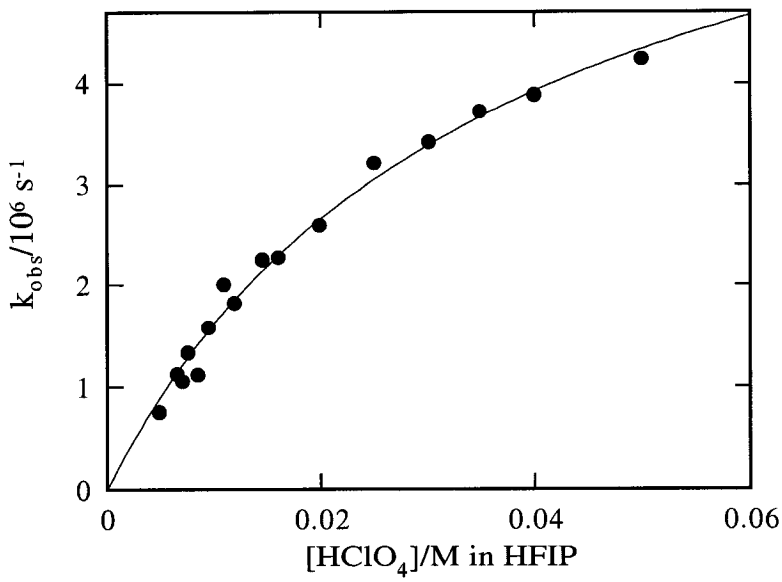

Figure 3-18. Observed rate constant for the growth of the 4-fluorostyrene radical cation **8(F)** as a function of perchloric acid concentration in nitrogen-saturated HFIP. k_{obs} was calculated from time-resolved kinetic traces monitored at 585 nm after 308 nm irradiation of 3-(4-fluorophenyl)-4-hydroxy-2-butanone **6(F)**.

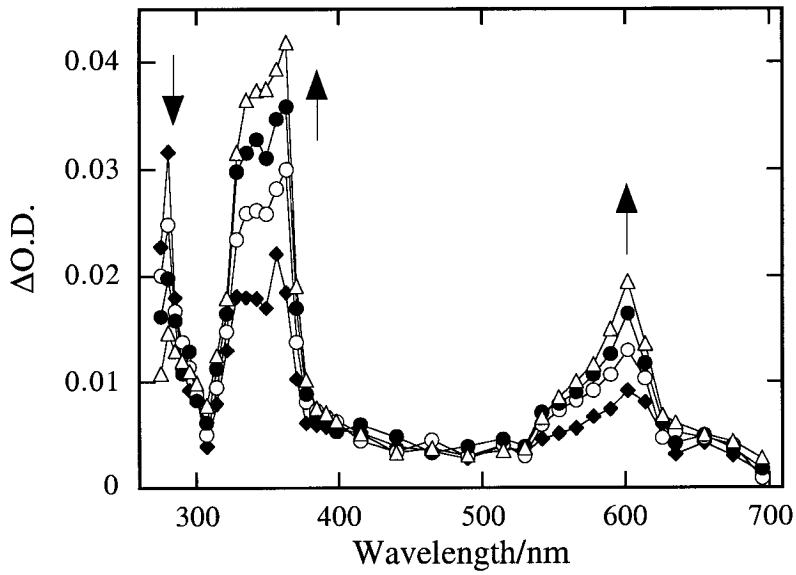

Figure 3-19. Transient absorption spectra obtained in nitrogen-saturated HFIP containing 0.010 M perchloric acid following 266 nm laser irradiation of 2,4-bis(4-methylphenyl)-1,5-dihydroxy-3-pentanone **6(Me)**. Spectra were recorded (◆) 0.12 μs, (○) 0.22 μs, (●) 0.38 μs, and (Δ) 1.0 μs after the laser pulse.

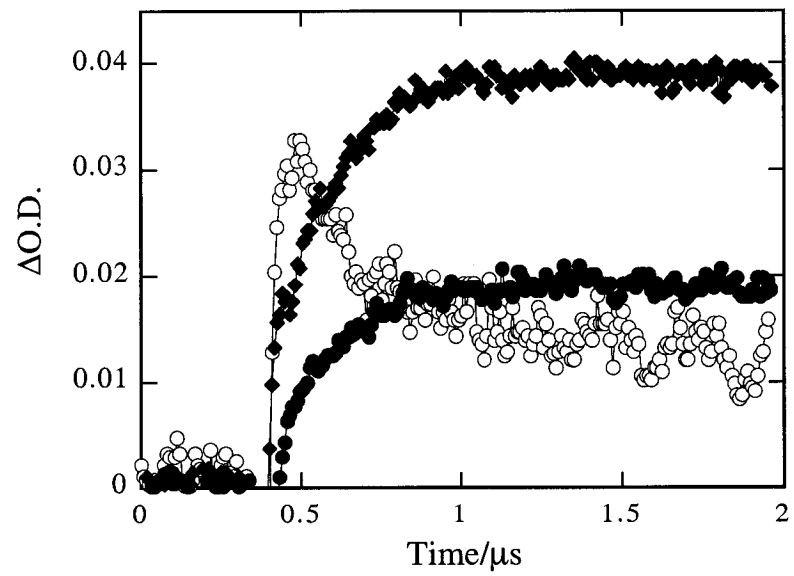

Figure 3-20. Time-resolved kinetics traces collected at (○) 280 nm, (●) 360 nm, and (◆) 600 nm and after 266 nm laser irradiation of 2,4-bis(4-methylphenyl)-1,5-dihydroxy-3-pentanone **6(Me)** in nitrogen-saturated HFIP containing 0.010 M perchloric acid.

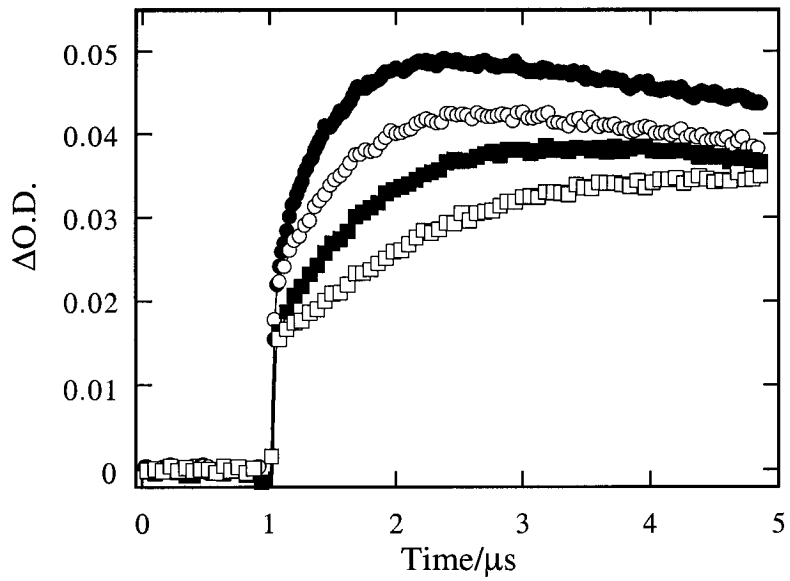

Figure 3-21. Time-resolved kinetic traces at 600 nm obtained upon 308 nm laser photolysis of 2,4-bis(4-methylphenyl)-1,5-dihydroxy-3-pentanone **6(Me)** in nitrogen-saturated HFIP containing (□) 0.0013 M, (■) 0.0021 M, (○) 0.0033 M, and (●) 0.0044 M perchloric acid.

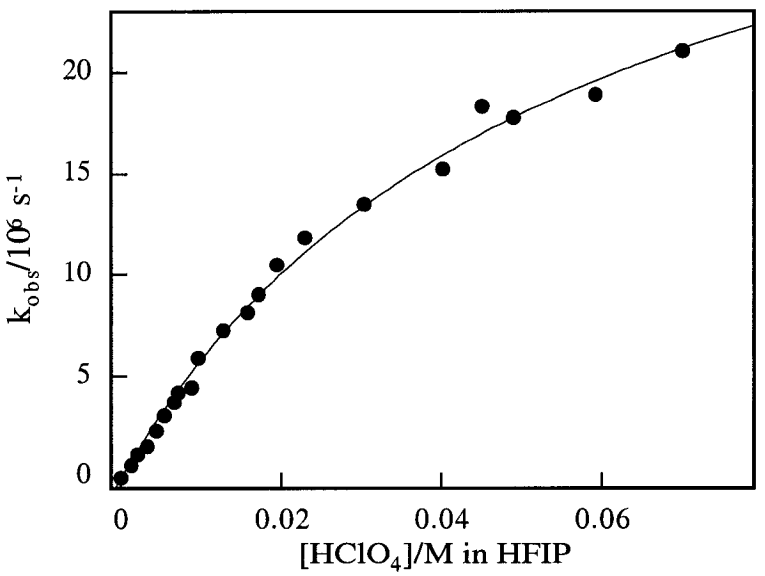

Figure 3-22. Observed rate constants for the growth of the 4-methylstyrene radical cation **8(Me)** measured at 600 nm following 308 nm laser irradiation of 2,4-bis(4-methylphenyl)-1,5-dihydroxy-3-pentanone **6(Me)** in nitrogen-saturated HFIP plotted as a function of perchloric acid concentration.

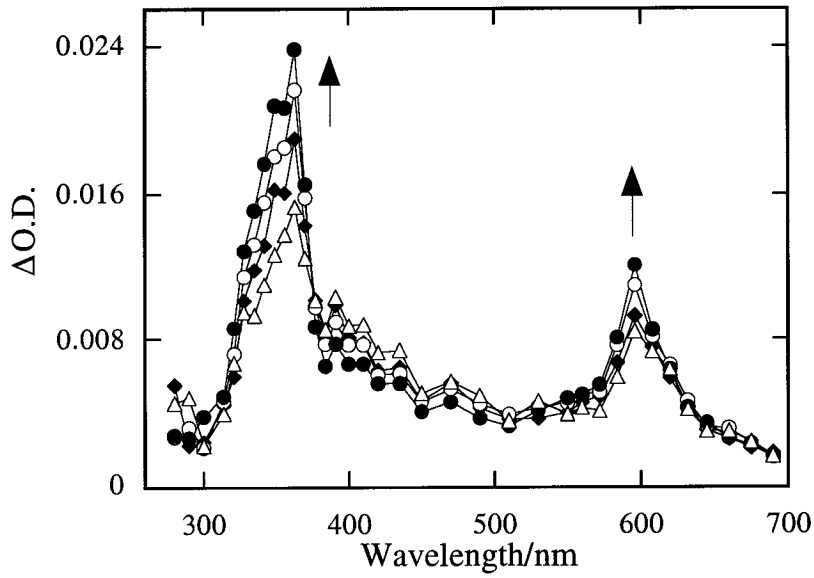

Figure 3-23. Transient absorption spectra obtained in nitrogen-saturated HFIP containing 0.0028 M perchloric acid following 266 nm laser irradiation of 3-(4-methoxyphenyl)-4-hydroxy-2-butanone **6(OMe)**. Spectra were recorded (◆) 0.42 μs, (○) 0.74 μs, (●) 1.2 μs, and (Δ) 2.9 μs after the laser pulse.

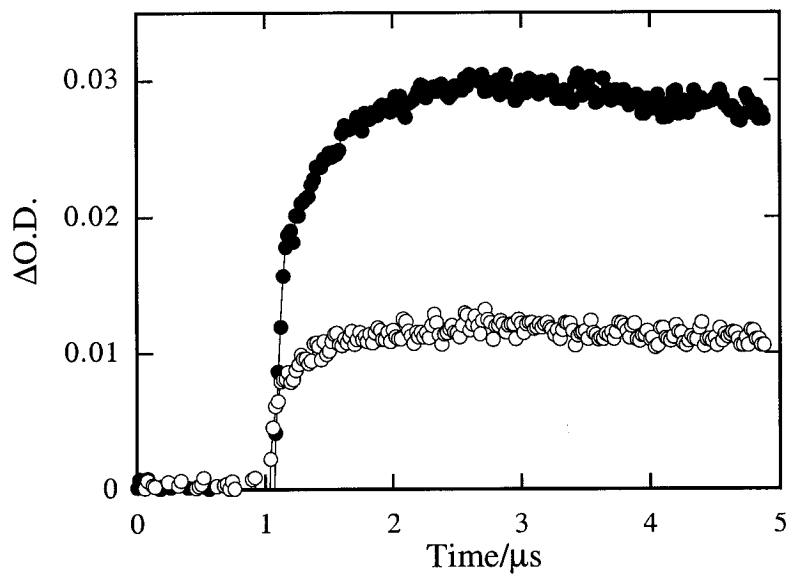

Figure 3-24. Time-resolved kinetic traces collected at (●) 350 nm and (○) 590 nm following 266 nm laser irradiation of 3-(4-methoxyphenyl)-4-hydroxy-2-butanone **6(OMe)** in nitrogen-saturated HFIP containing 0.0028 M perchloric acid.

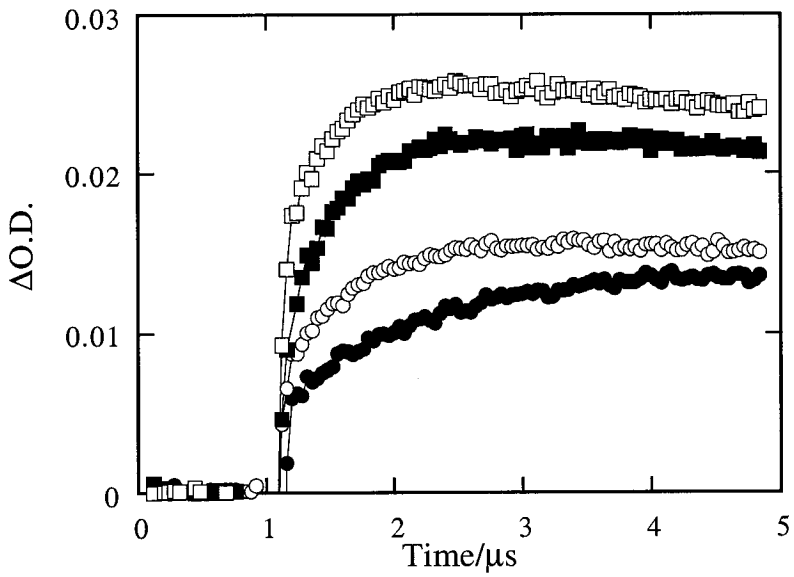

Figure 3-25. Time-resolved kinetic traces at 350 nm obtained upon 266 nm laser photolysis of 3-(4-methoxyphenyl)-4-hydroxy-2-butanone **6(OMe)** in nitrogen-saturated HFIP containing (●) 0.76 mM, (○) 3.2 mM, and (■) 2.8 mM and (□) 3.4 mM perchloric acid.

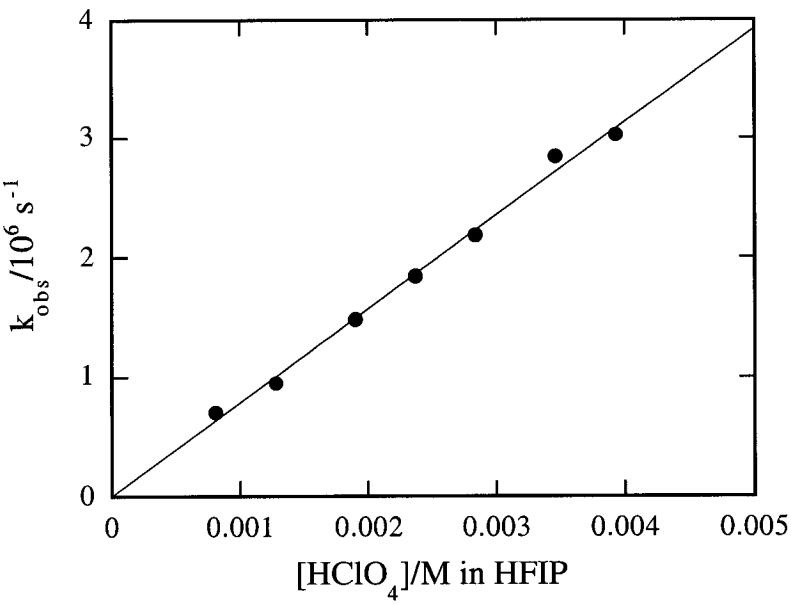

Figure 3-26. Observed rate constants for the growth of the 4-methoxystyrene radical cation **8(OMe)** monitored at 350 nm following 266 nm laser irradiation of 3-(4-methoxyphenyl)-4-hydroxy-2-butanone **6(OMe)** in nitrogen-saturated HFIP and plotted as a function of perchloric acid concentration. From the slope of the plot, $k_{cat} = 7.8 \times 10^8$ M^{-1} s^{-1}.

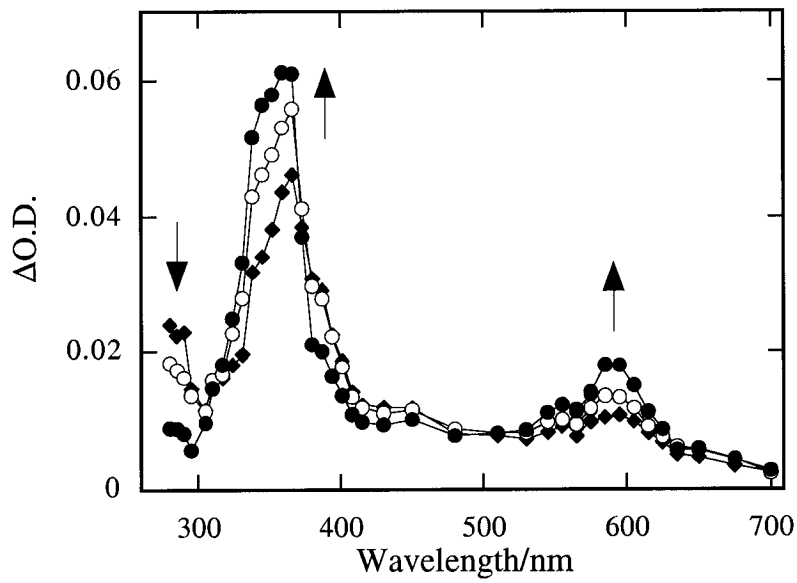

Figure 3-27. Transient absorption spectra obtained in nitrogen-saturated TFE containing 0.022 M perchloric acid following 266 nm laser irradiation 3-(4-methoxyphenyl)-4-hydroxy-2-butanone **6(OMe)**. Spectra were recorded (◆) 0.19 μs, (○) 0.34 μs, and (●) 1.2 μs after the laser pulse.

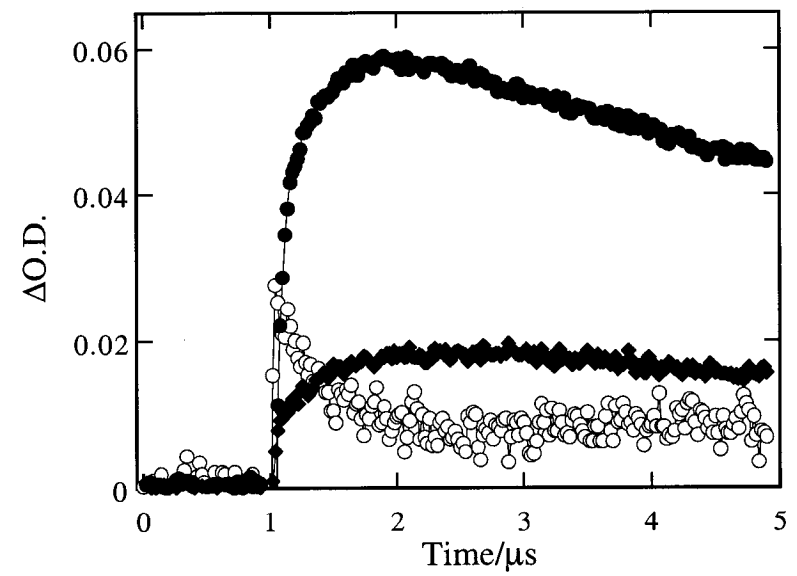

Figure 3-28. Time-resolved kinetic traces monitored at (○) 290 nm, (●) 350 nm, and (◆) 590 nm after 266 nm laser irradiation of 3-(4-methoxyphenyl)-4-hydroxy-2-butanone **6(OMe)** in nitrogen-saturated TFE containing 0.022 M perchloric acid.

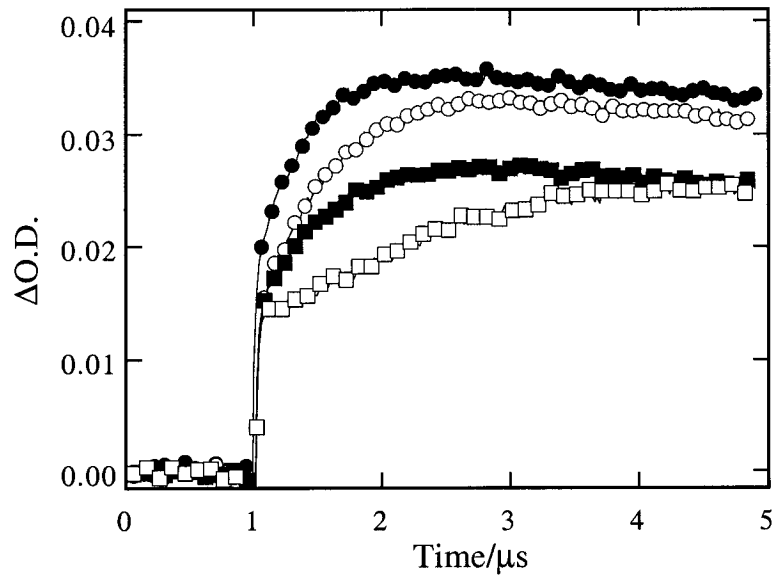

Figure 3-29. Time-resolved kinetic traces showing the rise in absorption at 590 nm of the 4-methoxystyrene radical cation **8(OMe)** following 266 nm laser irradiation of 3-(4-methoxyphenyl)-4-hydroxy-2-butanone **6(OMe)** in nitrogen-saturated TFE containing (□) 0.0041 M, (■) 0.012 M, (○) 0.020 M, and (●) 0.031 M perchloric acid.

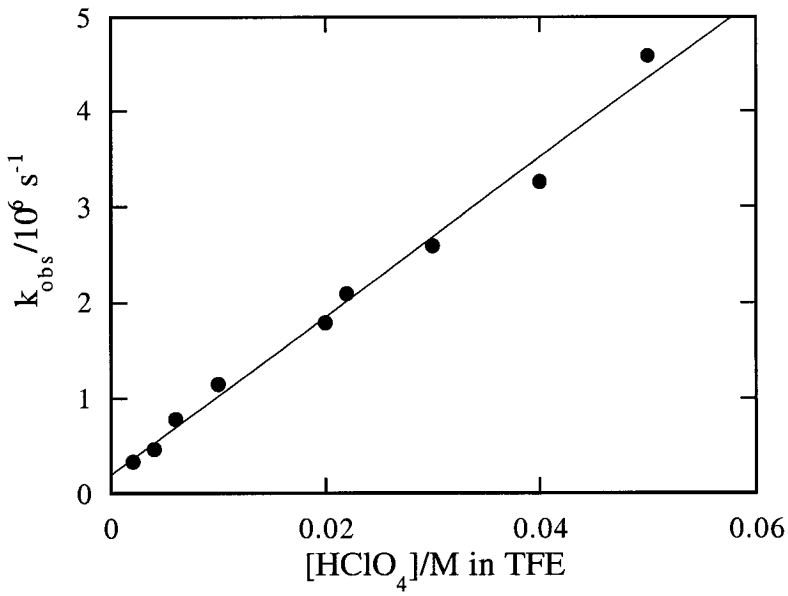

Figure 3-30. Observed rate constant for the growth of the 4-methoxystyrene radical cation **8(OMe)** calculated from the time-resolved kinetic traces acquired at 590 nm after 266 nm laser irradiation of 3-(4-methoxyphenyl)-4-hydroxy-2-butanone **6(OMe)** in TFE and plotted as a function of perchloric acid. From the slope of the plot, $k_{cat} = 8.3 \times 10^7$ M^{-1} s^{-1}.

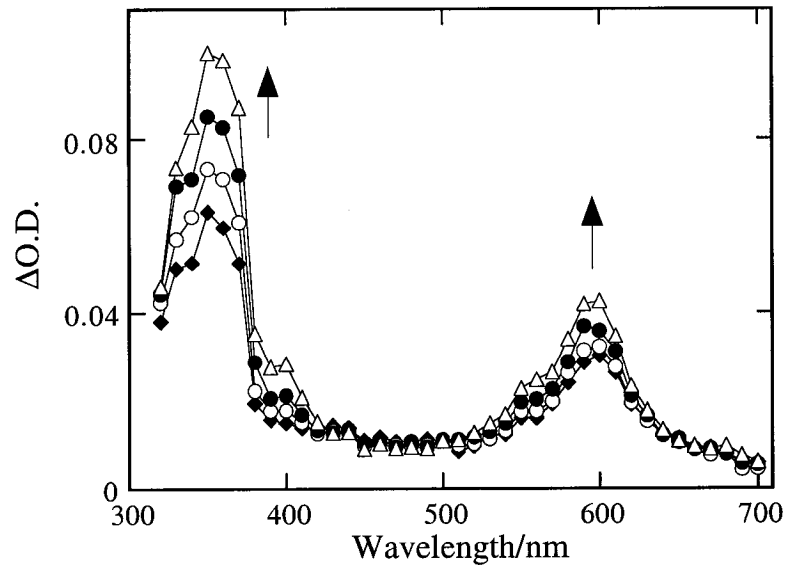

Figure 3-31. Transient absorption spectra obtained after 308 nm laser irradiation of 3-(4-methoxyphenyl)-4-hydroxy-2-butanone **6(OMe)** in nitrogen-saturated acetonitrile containing 0.0040 M perchloric acid. Spectra were recorded (◆) 0.27 μs, (○) 0.39 μs, (●) 0.54 μs, and (Δ) 1.2 μs following the laser pulse.

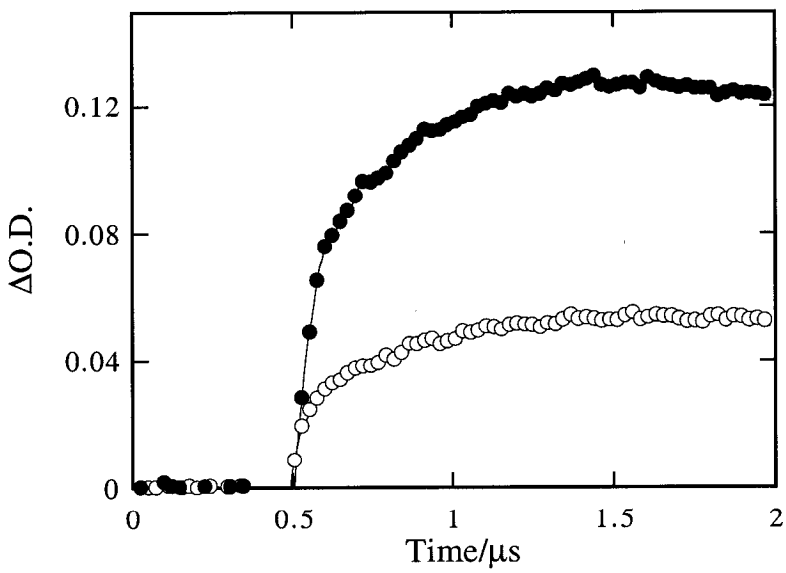

Figure 3-32. Time-resolved kinetic traces monitored at (●) 350 nm and (○) 590 nm after 308 nm laser irradiation of 3-(4-methoxyphenyl)-4-hydroxy-2-butanone **6(OMe)** in nitrogen-saturated acetonitrile containing 0.0040 M perchloric acid.

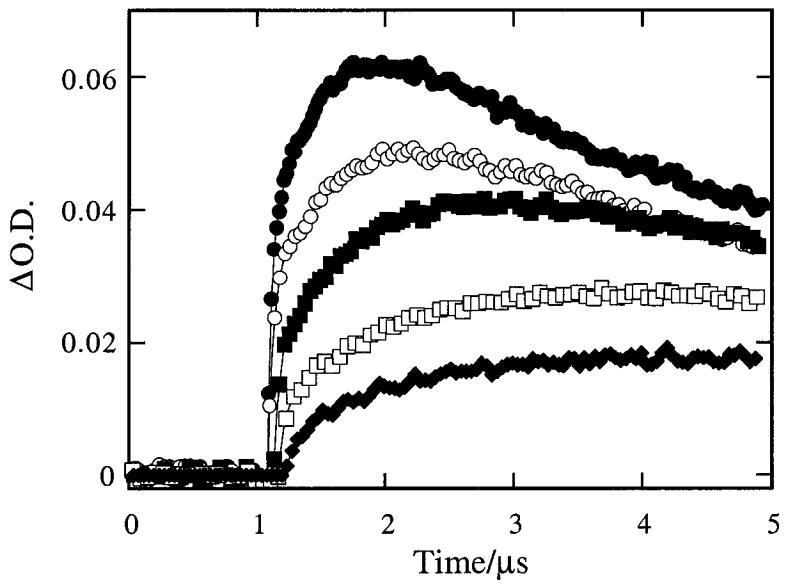

Figure 3-33. Time-resolved kinetic traces at 590 nm obtained upon 308 nm laser irradiation of 3-(4-methoxyphenyl)-4-hydroxy-2-butanone **6(OMe)** in nitrogen-saturated acetonitrile containing (◆) 0.6 mM, (□) 0.8 mM, (■) 2 mM, (○) 4 mM, and (●) 10 mM perchloric acid.

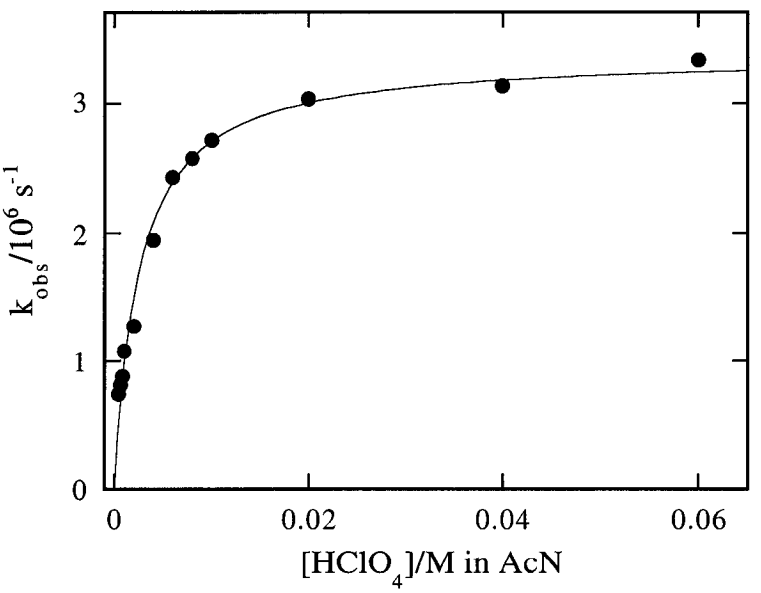

Figure 3-34. Observed rate constants for the growth of the 4-methoxystyrene radical cation **8(OMe)** measured at 590 nm following 308 nm laser irradiation of 3-(4-methoxyphenyl)-4-hydroxy-2-butanone **6(OMe)** in nitrogen-saturated acetonitrile plotted as a function of perchloric acid concentration.

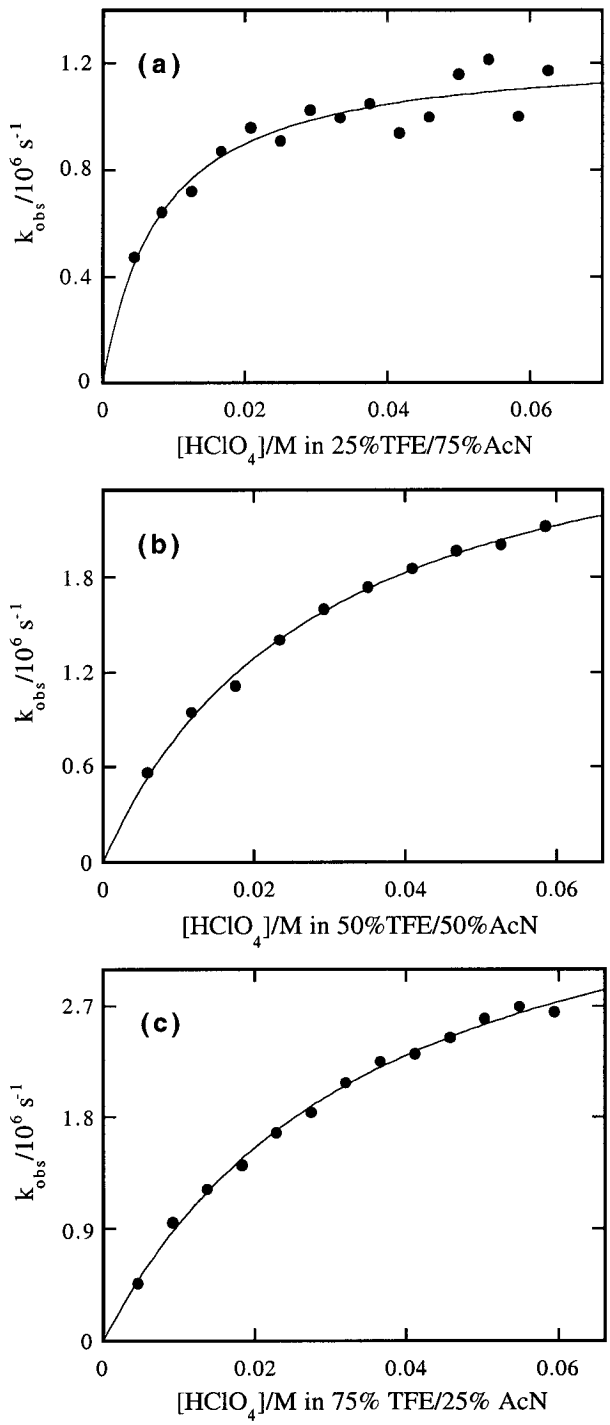

Figure 3-35. Observed rate constant for the growth of the 4-methoxystyrene radical cation **8(OMe)** as a function of perchloric acid concentration in nitrogen-saturated (a) 25% TFE/75% AcN, (b) 50% TFE/50% AcN, and (c) 75% TFE/25% AcN mixtures. Rate constants were measured from kinetic traces monitored at 590 nm after 266 nm laser irradiation of 3-(4-methoxyphenyl)-4-hydroxy-2-butanone **6(OMe)**.

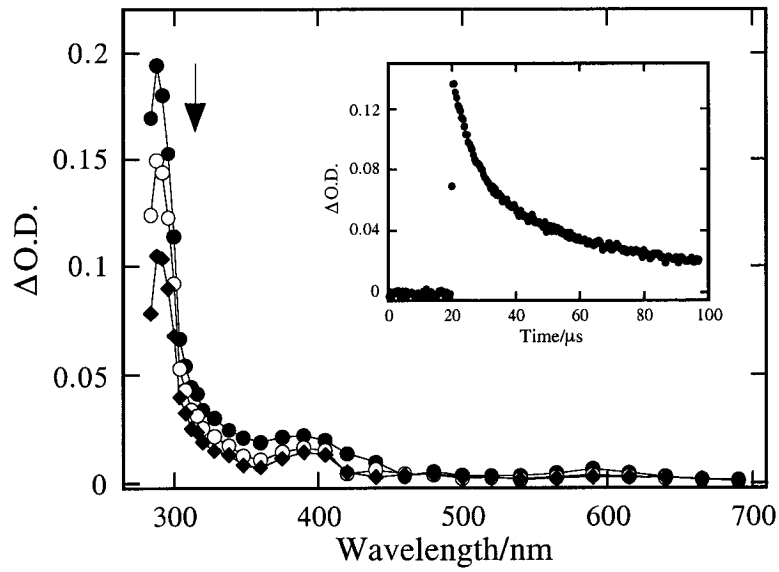

Figure 3-36. Transient absorption spectrum generated at (●) 2.5 μs, (○) 6.1 μs, and (◆) 14.1 μs after 266 nm laser irradiation of 2-(4-methoxyphenyl)-3-oxobutyl-diethylphosphate **9(OMe)** in nitrogen-saturated acetonitrile. Inset shows the time-resolved second-order kinetic trace monitored at 290 nm under the same conditions.

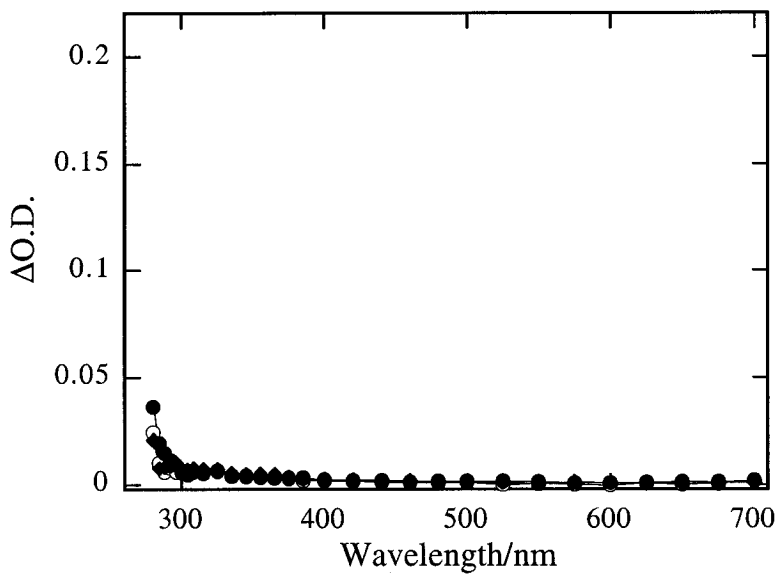

Figure 3-37. Transient absorption spectrum generated at (●) 2.5 μs, (○) 6.1 μs, and (◆) 14 μs after 266 nm laser irradiation of 2-(4-methoxyphenyl)-3-oxobutyl-diethylphosphate **9(OMe)** in oxygen-saturated acetonitrile.

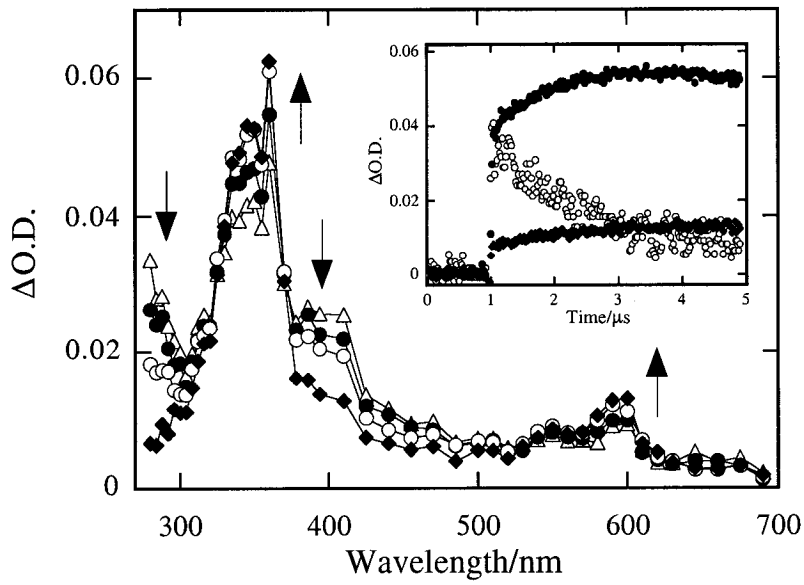

Figure 3-38. Transient absorption spectrum generated at (◆) 0.23 μs, (○) 0.67 μs, (●) 1.46 μs, and (Δ) 3.80 μs after 266 nm laser irradiation of 2-(4-methoxyphenyl)-3-oxobutyldiethylphosphate **9(OMe)** in nitrogen-saturated HFIP. Inset shows the transient kinetic traces generated at (○) 290 nm, (●) 350 nm, and (◆) 590 nm under the same conditions.

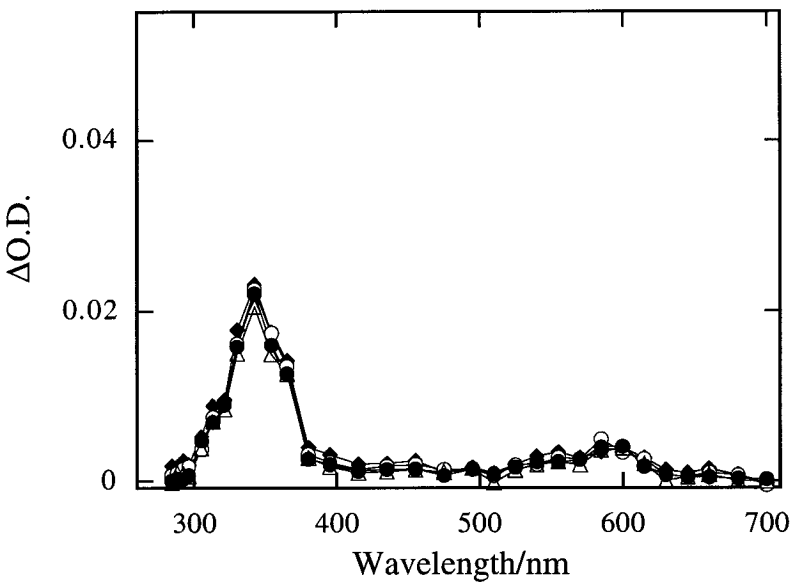

Figure 3-39. Transient absorption spectrum generated at (◆) 0.23 μs, (○) 0.67 μs, (●) 1.46 μs, and (Δ) 3.80 μs after 266 nm laser irradiation of 2-(4-methoxyphenyl)-3-oxobutyldiethylphosphate **9(OMe)** in oxygen-saturated HFIP.

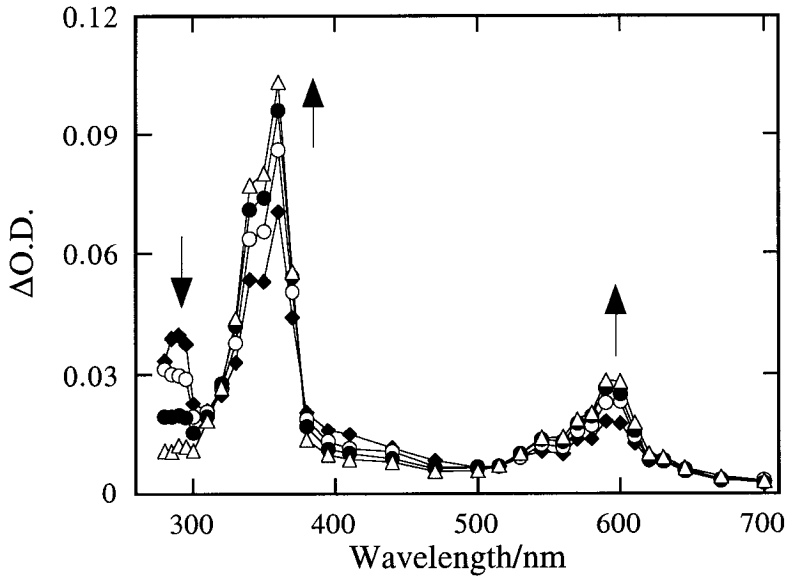

Figure 3-40. Transient absorption spectrum generated at (◆) 0.33 μs, (○) 0.72 μs, (●) 1.22 μs, and (Δ) 2.39 μs after 266 nm laser irradiation of 2-(4-methoxyphenyl)-3-oxobutyldiethylphosphate **9(OMe)** in nitrogen-saturated TFE containing 0.0039 M perchloric acid.

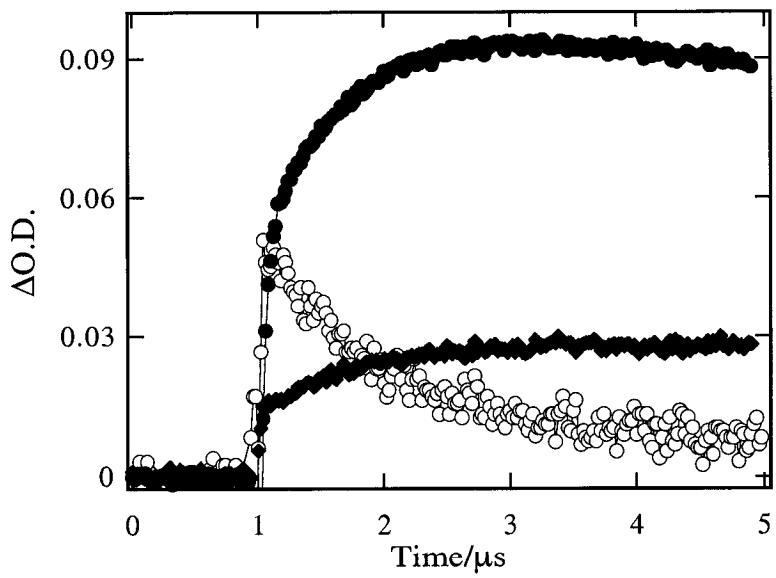

Figure 3-41. Time-resolved kinetic traces monitored at (○) 290 nm, (●) 350 nm, and (◆) 590 nm after 266 nm laser irradiation of 2-(4-methoxyphenyl)-3-oxobutyl-diethylphosphate **9(OMe)** in nitrogen-saturated TFE containing 0.0039 M perchloric acid.

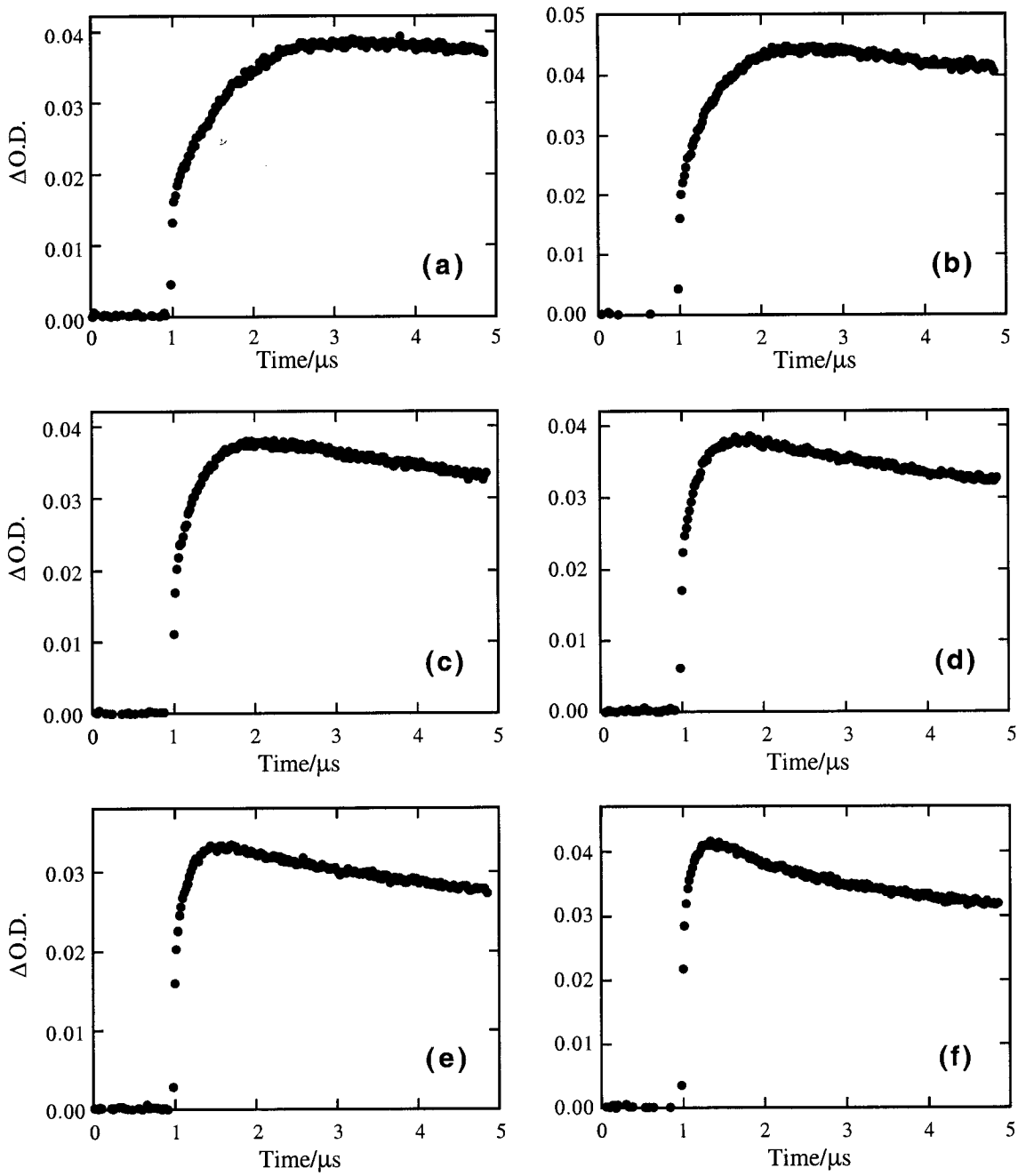

Figure 3-42. Time-resolved kinetic traces monitored at 590 nm showing the growth of the 4-methoxystyrene radical cation **11(OMe)** in nitrogen-saturated TFE containing (a) 0.0048 M, (b) 0.0096 M, (c) 0.014 M, (d) 0.024 M, (e) 0.034 M and (f) 0.048 M perchloric acid. Traces were obtained following 266 nm laser irradiation of 2-(4-methoxyphenyl)-3-oxobutyldiethylphosphate **9(OMe)**.

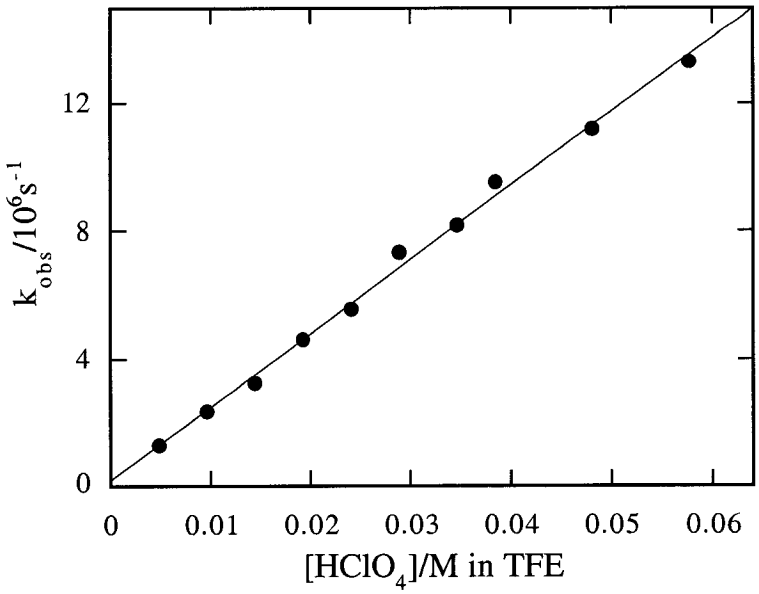

Figure 3-43. Observed rate constant for the growth of the 4-methoxystyrene radical cation **11(OMe)** as a function of perchloric acid concentration in nitrogen-saturated TFE. From the slope of the plot, $k_{cat} = 2.3 \times 10^8\ M^{-1}\ s^{-1}$. Rate constants were measured from kinetic traces monitored at 590 nm after 266 nm laser irradiation of 2-(4-methoxyphenyl)-3-oxobutyldiethylphosphate **9(OMe)** in various nitrogen-saturated TFE/perchloric acid mixtures.

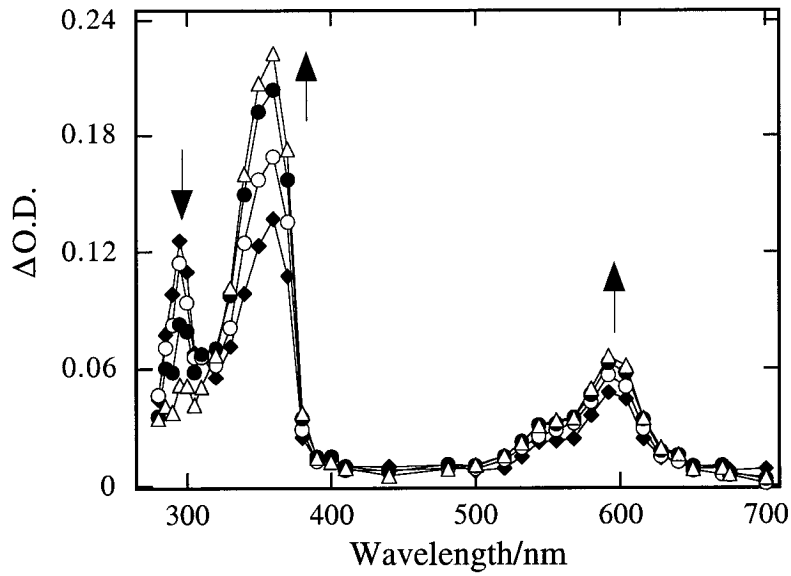

Figure 3-44. Transient absorption spectrum generated at (◆) 0.15 μs, (○) 0.25 μs, (●) 0.39 μs, and (Δ) 0.80 μs after 266 nm laser irradiation of 2-(4-methoxyphenyl)-3-oxobutyldiethylphosphate **9(OMe)** in nitrogen-saturated acetonitrile containing 0.008 M perchloric acid.

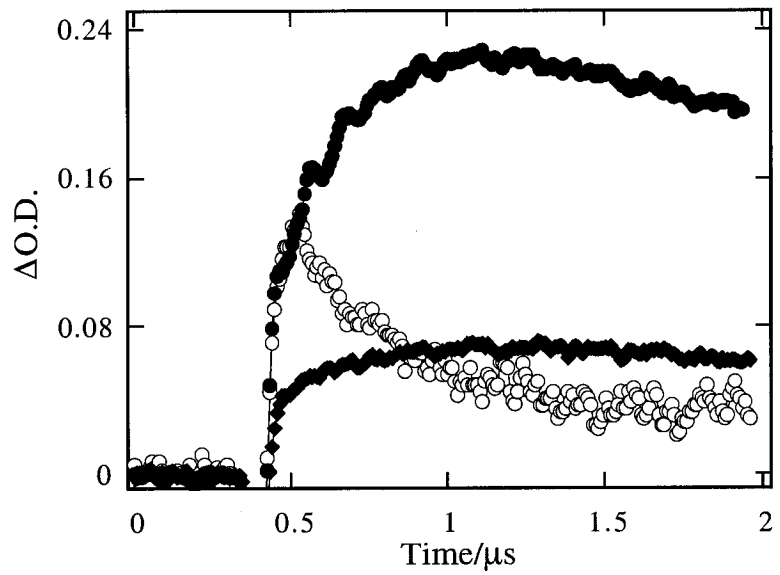

Figure 3-45. Time-resolved kinetic traces monitored at (○) 290 nm, (●) 350 nm, and (◆) 590 nm after 266 nm laser irradiation of 2-(4-methoxyphenyl)-3-oxobutyl-diethylphosphate **9(OMe)** in nitrogen-saturated acetonitrile containing 0.008 M perchloric acid.

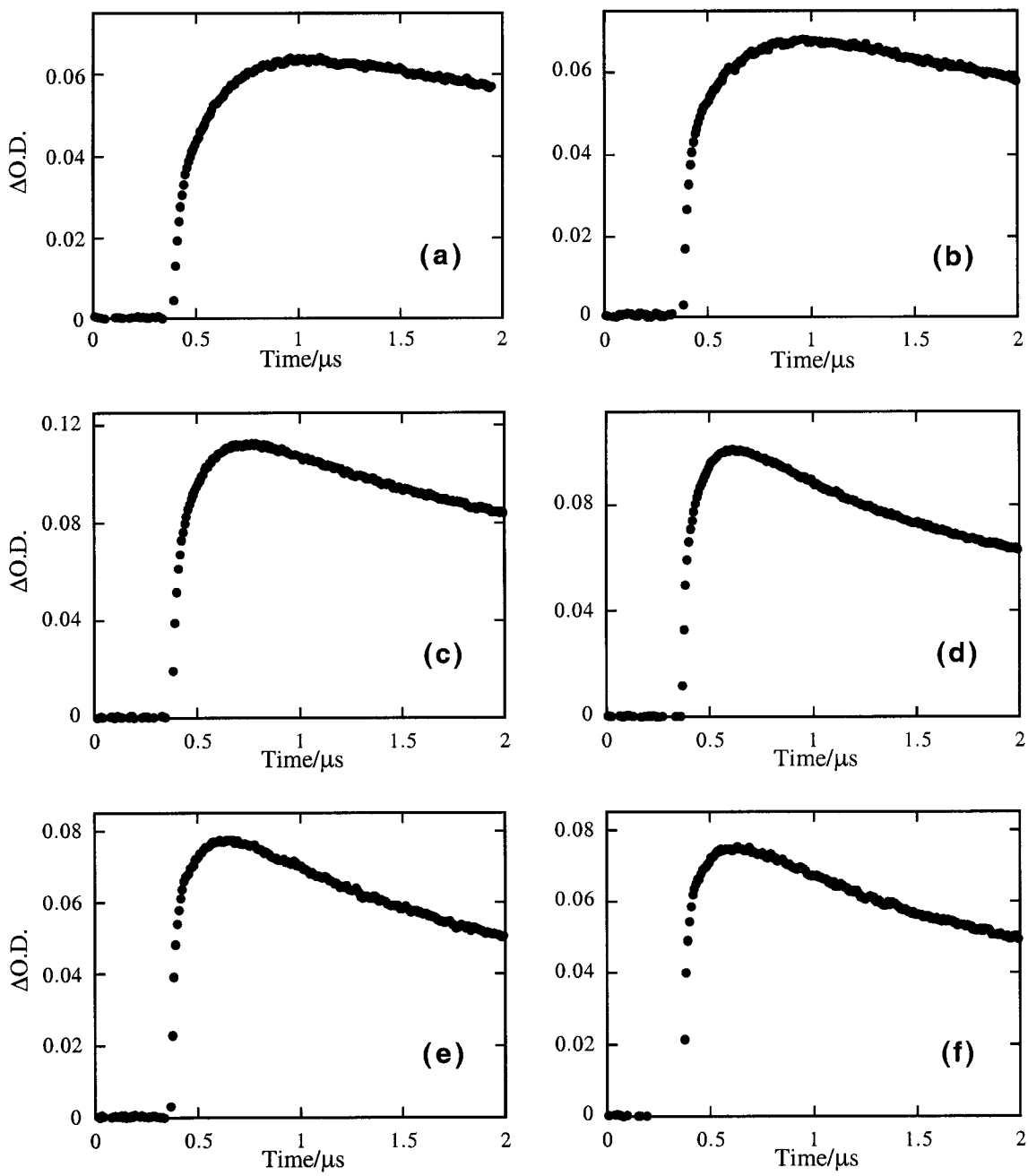

Figure 3-46. Time-resolved kinetic traces monitored at 590 nm showing the growth of the 4-methoxystyrene radical cation **11(OMe)** in nitrogen-saturated acetonitrile containing (a) 0.0044 M, (b) 0.0088 M, (c) 0.013 M, (d) 0.031 M, (e) 0.035 M and (f) 0.044 M perchloric acid. Traces were obtained following 266 nm laser irradiation of 2-(4-methoxyphenyl)-3-oxobutyldiethylphosphate **9(OMe)**.

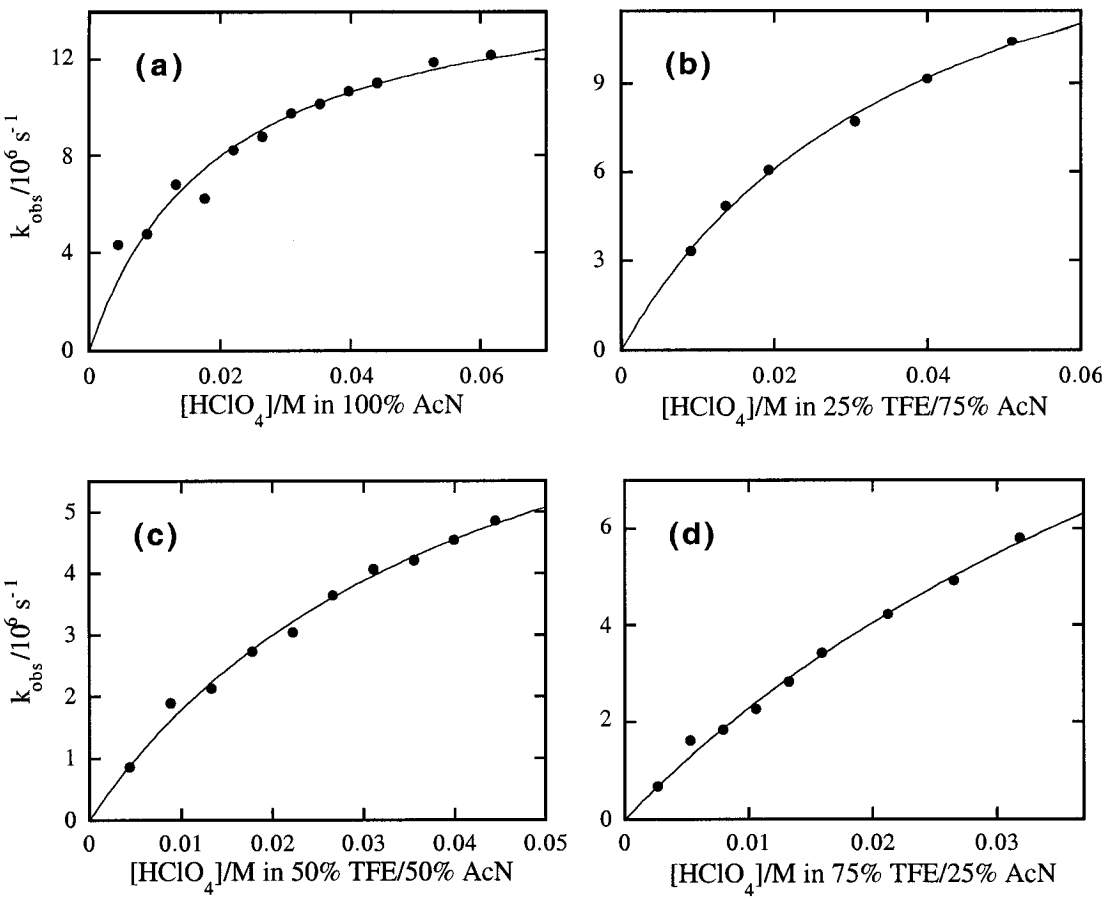

Figure 3-47. Observed rate constant for the growth of the 4-methoxystyrene radical cation **11(OMe)** as a function of perchloric acid concentration in nitrogen-saturated (a) neat AcN, (b) 25% TFE/75% AcN, (c) 50% TFE/50% AcN, and (d) 75% TFE/25% AcN mixtures. Rate constants were measured from kinetic traces monitored at 590 nm after 266 nm laser irradiation of 2-(4-methoxyphenyl)-3-oxobutyl diethylphosphate **9(OMe)**.

3.3 Discussion

3.3.1 Ionization of the β-Hydroxy Phenethyl Radicals

The spectral data acquired for each of the β-hydroxy phenethyl radicals **7(X)** generated upon laser irradiation in AcN, TFE and HFIP, provided no evidence to suggest that in polar solvents, the radicals undergo heterolytic cleavage of the β-OH group. More specifically, none of the transient absorption spectra shown in Figures 3-3, 3-4, and 3-5 have the characteristic absorption maxima near 350 and 600 nm associated with styrene-type radical cations that are the direct, detectable products of the β-heterolysis reaction. Moreover, an observed second-order rate constant is calculated from the kinetic decay traces of these radicals, indicating that their principal mode of reaction is bimolecular, thereby excluding the unimolecular ionization process. It is expected that the main reaction pathway under these solvent conditions is radical-radical recombination or disproportionation to form closed-shell products **12(X)**, as illustrated in Scheme 3-7.

Scheme 3-7

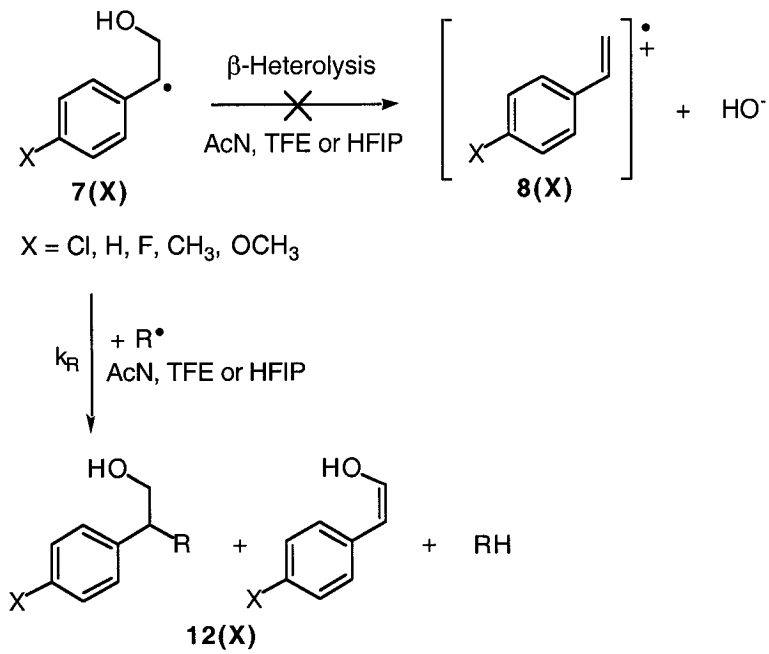

In these solutions, the absence of radical cations generated from radicals **7(X)** *via* the β-heterolysis reaction was anticipated due to the poor nucleofugality of the β-OH group. The hydroxide anion that would be produced is a small ion with the negative charge localized on an atom, making it an unfavorable candidate for heterolysis. However, the results provide unambiguous evidence that in the presence of an acid catalyst, perchloric acid, β-OH radicals **7(X)** undergo rapid ionization in polar solvents to yield the corresponding radical cations. In acidic HFIP, radicals **7(Cl)**, **7(H)**, **7(F)**, **7(Me)** and **7(OMe)** all undergo the β-heterolysis reaction. Similarly, the real-time detection of the growth curve of the 4-methoxystyrene radical cation demonstrated that radical **7(OMe)** also ionizes in acidic AcN and acidic TFE.

As described earlier, a simple two step mechanism readily explains these results. The first step is rapid protonation of the radical at the β-OH group. In the second step, the protonated radical undergoes heterolytic loss of water to yield the styrene radical cation, Scheme 3-5. Derivation of rate laws based on this Scheme is given in the following section.

3.3.2 Kinetics

The β-heterolysis reaction is a unimolecular process in which the reactant, a β-substituted radical $R^{\bullet}$, undergoes heterolytic bond dissociation and results in the loss of the β-group to form a radical cation. This reaction is simplistically represented in eq. 3.6.

$$R\bullet \xrightarrow{k_{het}} \underbrace{\text{Radical cation} + \text{Leaving group}}_{\text{Products (P)}} \qquad (3.6)$$

When the β-leaving group of the radical requires no catalytic assistance to depart, as seen for β-mesylate radical **2(X)**, the rate law for the β-heterolysis reaction is given by eq. 3.7.

The rate of formation of the radical cation is determined by the first-order rate constant k_{het} for the uncatalyzed ionization process and the concentration of the β-substituted radical.

$$\text{Rate of Heterolysis} = \frac{d[P]}{dt} = k_{het}[R^{\bullet}] \tag{3.7}$$

For radicals **7(X)** which possess a poor leaving group, ionization is facilitated by the presence of acid which can protonate the β-OH group and in doing so, assist its departure as a neutral water molecule. However, not all protonated radicals will ionize and a portion will deprotonate to regenerate $R^{\bullet}$ before heterolysis has the chance to occur. The mechanism of this acid-catalyzed β-heterolysis reaction may therefore be represented as the generalized two-step process depicted in Scheme 3-8. AH and A^- are used to represent the acid and its conjugate base, $R^{\bullet}$ designates the β-substituted radical, and $RH^{\bullet+}$ is the oxygen protonated radical.

Scheme 3-8

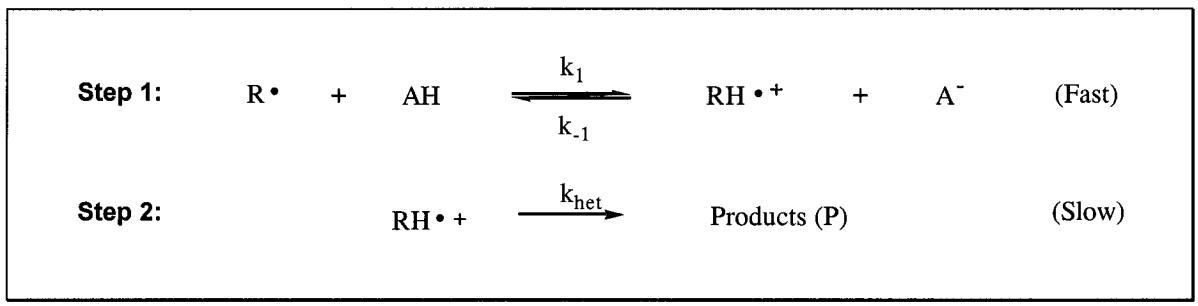

The kinetics for the above mechanism can be derived by assuming that the deprotonation process, k_{-1}, is significantly faster than the ionization reaction, k_{het}. By establishing *a priori* that $k_{-1} >> k_{het}$,, it is implied that step 1 in Scheme 3-8 involves a rapidly established pre-equilibrium between the protonated and unprotonated radical.

The rate of protonation and deprotonation is expressed as $k_1[R^\bullet][AH]$ and $k_{-1}[RH^{\bullet+}][A^-]$ respectively. The equilibrium constant K_1 in the first step can therefore be defined as:

$$K_1 = \frac{k_1}{k_{-1}} = \frac{[RH^{\bullet+}][A^-]}{[R^\bullet][AH]} \tag{3.8}$$

An acidity constant K_{AH} can also be established for the acidic catalyst AH that exists in rapid equilibrium with its conjugate base A^-, as shown in eq. 3.9.

$$AH \overset{K_{AH}}{\rightleftharpoons} A^- + H^+ \tag{3.9}$$

The dissociation constant K_{AH} for this equilibrium can be written as

$$K_{AH} = \frac{[A^-][H^+]}{[AH]} \tag{3.10}$$

Similarly, it is practical to introduce the dissociation constant, $K_{RH^{\bullet+}}$ for the protonated and deprotonated radical, eq. 3.11, that is defined as shown in eq. 3.12:

$$RH^{\bullet+} \overset{K_{RH^{\bullet+}}}{\rightleftharpoons} R^\bullet + H^+ \tag{3.11}$$

$$K_{RH^{\bullet+}} = \frac{[R^\bullet][H^+]}{[RH^{\bullet+}]} \tag{3.12}$$

It follows therefore that $K_{RH^{\bullet+}}$ can also be expressed as

$$K_{RH^{\bullet+}} = \frac{K_{AH}}{K_1} \tag{3.13}$$

Relative to the rapid pre-equilibrium in step 1, the β-heterolysis reaction in step 2 is slow and consequently rate-determining. Equation 3.14 establishes the elementary rate

law for product formation in which k_{het} is the first-order rate constant for the ionization reaction.

$$\frac{d[P]}{dt} = k_{het}[RH^{\bullet+}] \tag{3.14}$$

The total radical concentration $[R^{\bullet}]_T$ can be defined as the sum of the neutral radical concentration $[R^{\bullet}]$ and the concentration of its protonated form, $[RH^{\bullet+}]$, eq. 3.15.

$$[R^{\bullet}]_T = [R^{\bullet}] + [RH^{\bullet+}] \tag{3.15}$$

Rearranging eq. 3.15 to $[R^{\bullet}] = [R^{\bullet}]_T - [RH^{\bullet+}]$ and incorporating it in eq. 3.8 generates the following equation

$$K_1 = \frac{[RH^{\bullet+}][A^-]}{([R^{\bullet}]_T - [RH^{\bullet+}])[AH]} \tag{3.16}$$

Manipulation of eq. 3.16 eventually leads to

$$[RH^{\bullet+}] = \frac{K_1[AH][R^{\bullet}]_T}{K_1[AH] + [A^-]} \tag{3.17}$$

With use of eq. 3.10, eq. 3.17 rearranges to

$$[RH^{\bullet+}] = \frac{K_1[H^+][R^{\bullet}]_T}{K_1[H^+] + K_{AH}} \tag{3.18}$$

Introducing eq. 3.18 into eq. 3.14 generates the following rate law

$$\text{Rate} = \frac{d[P]}{dt} = \frac{k_{het}K_1[H^+][R^{\bullet}]_T}{K_1[H^+] + K_{AH}} \tag{3.19}$$

The total radical concentration $[R^{\bullet}]_T^0$ at the beginning of the reaction can be related to the concentrations of total radicals and products as shown in eq. 3.20.

$$[R^{\bullet}]_T^0 = [R^{\bullet}]_T + [P] \tag{3.20}$$

Rearranging and substituting for $[R^{\bullet}]_T$ in eq. 3.19 gives the following rate expression

$$\text{Rate} = \frac{d[P]}{dt} = \frac{k_{het}K_1[H^+]([R^{\bullet}]_T^0 - [P])}{K_1[H^+] + K_{AH}} \tag{3.21}$$

The observed rate constant that applies to the time resolved traces generated in the present work for the growth of the radical cation can be given as

$$k_{obs} = \frac{k_{het}K_1[H^+]}{K_1[H^+] + K_{AH}} \tag{3.22}$$

Finally, using eq. 3.13 allows eq. 3.22 to be reduced to

$$k_{obs} = \frac{k_{het}[H^+]}{[H^+] + K_{RH^{\bullet+}}} \tag{3.23}$$

The above rate expression quantifies the kinetics for the growth of the radical cation generated *via* acid-catalyzed β-heterolysis as outline in Scheme 3-8. Two extreme cases are now of special interest, according to whether $[H^+] << K_{RH^{\bullet+}}$ or $[H^+] >> K_{RH^{\bullet+}}$.

Case 1: Low Acid Concentration

At low acid concentrations, $K_{RH^{\bullet+}} >> [H^+]$ and the rate law in eq. 3.21 reduces to

$$\text{Rate} = \frac{d[P]}{dt} = \frac{k_{het}[H^+]\left([R^{\bullet}]_T^0 - [P]\right)}{K_{RH^{\bullet+}}} \tag{3.24}$$

The rate law therefore predicts that at low acid concentrations, the kinetics are dependent on radical and proton concentrations. Consequently, k_{obs} calculated for the growth of the radical cation is pseudo first-order due to excess acid concentration relative to the concentration of the radical generated within the laser pulse, eq. 3.25

$$k_{obs} = \frac{k_{het}[H^+]}{K_{RH^{\bullet+}}} \tag{3.25}$$

When k_{obs} is plotted as a function of acid concentration, the second-order rate constant k_{cat} for the acid-catalyzed β-heterolysis process can be calculated from the slope of the data measured at low acid concentrations and is defined as the following

$$k_{cat} = \frac{k_{het}}{K_{RH^{\bullet+}}} \tag{3.26}$$

The second-order rate constant k_{cat} measured for the acid-catalyzed β-heterolysis process is therefore proportional to the rate constant for the elementary ionization step 2, and inversely related to the dissociation constant of the protonated radical.

Case 2: High Acid Concentration

The mechanism described by eq. 3.21 predicts that k_{obs} does not increase indefinitely as the proton concentration increases but will attain a limiting value. Thus at high acid concentration, $[H^+] >> K_{RH^{\bullet+}}$ and the rate law in eq. 3.21 reduces to

$$\text{Rate} = \frac{d[P]}{dt} = k_{het}\left([R^{\bullet}]_T^0 - [P]\right) \tag{3.27}$$

This rate expression implies that under sufficiently acidic solvent conditions, the ionization of β-OH radicals **7(X)** is independent of proton concentration and the rate is

entirely controlled by the ionization step 2. The value of k_{obs} calculated at high acid concentration is first-order and therefore represents the unimolecular β-heterolysis reaction shown as the second step of the mechanism in Scheme 3-8.

$$k_{obs} = k_{het} \tag{3.28}$$

Rearranging eq. 3.26 and substituting for $K_{RH^{\bullet+}}$ in eq. 3.23 gives the following equation

$$k_{obs} = \frac{k_{het}k_{cat}[H^+]}{k_{het} + [H^+]k_{cat}} \tag{3.29}$$

This equation was used to determine the rate constants described in the results section. Furthermore, $K_{RH^{\bullet+}}$ can be determined by using eq. 3.30 obtained by rearranging eq. 3.26.

$$K_{RH^{\bullet+}} = \frac{k_{het}}{k_{cat}} \tag{3.30}$$

Values for these rate constants are summarized in Tables 3-1, 3-2, and 3-3.

Errors calculated for the parameters k_{het} and $K_{RH^{\bullet+}}$ by the fitting routine were typically small, approximately 5-10%. However, it should be noted that both values may have significantly larger errors associated with them due to the absence of data in the plateau region observed at higher concentrations of acid. In many cases, rate constant measurements could only be made up to acid concentrations where pronounced curvature was observed. As a result, it is reasonable to estimate errors as large as 20% associated with the results.

3.3.3 Substituent Electronic Effects

3.3.3.1 The Acid-Independent β-Heterolysis Reaction

Despite the uncertainty in the values for the rate constants of k_{het} and k_{cat}, some observations about the effect of substituents on the uncatalyzed and catalyzed β-heterolysis reactions can be made. For example, as shown Table 3-1, the value determined for the first-order rate constant k_{het} associated with loss of water from the protonated chlorinated radical **7(Cl)**, $k_{het} = 3.6 \times 10^6\ s^{-1}$, is significantly smaller than the rate constants for the same reaction of the fluorinated **7(F)** and unsubstituted **7(H)** radicals, $k_{het} = 7.5 \times 10^6\ s^{-1}$ and $7.6 \times 10^6\ s^{-1}$, respectively. A much larger five fold increase in k_{het} then takes place upon going to the radical **7(Me)**, $3.8 \times 10^7\ s^{-1}$, Figure 3-48.

To quantify these electronic substituent effects, the kinetic data were subjected to linear free-energy correlation analysis using the Hammett σ and the Brown-Okamoto σ^+ substituent parameters.[128,130] Figures 3-49 (a) and (b) show the correlation obtained with each of these scales for the kinetic data obtained at high acid concentration, that is the first-order rate constant k_{het}. Based on the correlation coefficient R which has a value of 0.957 with the σ parameters, the best linear correlation is established with the σ^+ scale, R = 0.985. These results are in agreement with those presented in Chapter 2 for the ionization of β-mesylate-*para*-substituted phenethyl radicals **2(X)** for which the uncatalyzed rate constants also correlated linearly with the σ^+ scale.

It is useful to reiterate that k_{het} corresponds to the rate constant for the ionization reaction of the β-H_2O group from radicals **7(X)**, step 2 in Scheme 3-8. The kinetics at high acid concentration are therefore independent of the pre-equilibrium step in which the radical of interest is protonated. Thus, the β-heterolysis reaction in this

linear free energy analysis involves only the protonated radical as the reactant. This rate-determining step is illustrated in eq. 3.31.

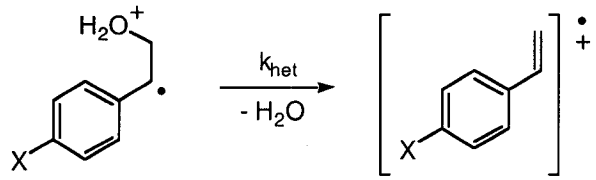

7(X) **8(X)** (3.31)

The observation of a good correlation between k_{het} and σ^+ suggests some degree of through resonance between the aromatic substituent and the reaction site during the β-heterolysis reaction in acidic HFIP. This can simply be explained by the existence of some overlap between the radical centre and the incipient positive charge developing at the adjacent carbon as heterolytic cleavage of the water group progresses, Scheme 3-9. This is similar to the mechanism described for the β-mesylate derivatives in Chapter 2.

The slope in Figure 3-49 (b) has a value of $\rho^+ = -2.40$ and implies that the rate constant for the ionization process is increased by electron donating substituents and decelerated as the aromatic group becomes increasingly electron withdrawing. A negative slope therefore also indicates a positive charge build-up as the reaction progresses from the starting material to the product. In principle, this analysis is somewhat simplistic since the reactant in this rate-determining, acid-independent step is the protonated form of radicals **7(X)** which already bears a full positive charge. Therefore, no charge is being created on the substrate as the reaction progresses from the

Scheme 3-9

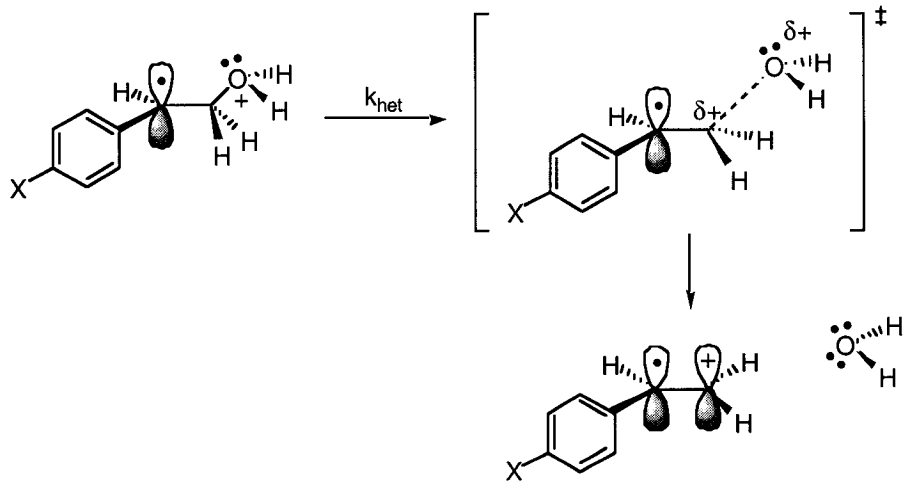

initial to the transition state. However, the positive charge in the starting structure is localized on the oxygen atom and not in direct resonance with the aromatic substituent. Thus, as the reaction proceeds and the carbon-oxygen atom bond breaks, a progressive redistribution of charge takes place. As the leaving group dissociates, the original positive charge on the oxygen atom lessens and is accompanied by a build-up of positive charge on the developing sp^2 hybridized orbital of the carbon atom. Due to the possible overlap between the incipient carbocationic centre and the singly occupied p-orbital, some degree of charge transmission to the aromatic substituent is now possible in the transition state. A negative slope on the Brown-Okamoto plot therefore highlights the fact that from the substituent's perspective, the reactant was not positively charged, while the transition state bears a positive charge that can, to some degree, be transmitted through the radical centre.

The ρ^+ value of -2.40 is less negative than the ρ^+ value of -3.02 determined for mesylate as the leaving group in Chapter 2. The lower sensitivity seems somewhat unusual, since the rate constant for heterolysis of water and heterolysis of mesylate for both sets of radicals having the same aromatic substituent are very similar. One possible

explanation for the reduced sensitivity to substituent effects deals with the differential energy of the reactant and the products that exists between the ionization reaction of radicals **2(X)** and **7(X)**. Since radicals **7(X)** are positively charged, it is reasonable to expect that the energies of these protonated radicals are higher (albeit to a small extent) than those of radicals **2(X)**. In addition, the ionization of β-OH_2 radicals **7(X)** produces radical cations and neutral water molecules, whereas the heterolysis of β-mesylate radicals **2(X)** results in the formation of radical cation/anion pairs. Since the product pair generated from the reaction of radicals **7(X)** bears only one charge, their overall energy is expected to be lower. Together, the higher energy of the reactant and the lower energy of the products for the ionization of radicals **7(X)** lead to an earlier transition state during the heterolysis of water relative to a β-mesylate group. An earlier transition state translates into a structure with less charge separation and reduced electronic requirements, resulting in a smaller value of ρ^+.

3.3.3.2 The Acid-*Dependent* β-Heterolysis Reaction

A similar trend to that observed for the unimolecular heterolysis of water is found with the second-order rate constant k_{cat} calculated for the acid-dependent ionization reaction of radicals **7(X)** in acidic HFIP, Table 3-1 and Figure 3-48. Once again, the slowest rate constant is associated with the ionization of the chlorinated radical **7(Cl)** which occurs with a k_{cat} value of $1.1 \times 10^8\ M^{-1}s^{-1}$, only slightly smaller than that calculated for **7(F)**, $k_{cat} = 2.1 \times 10^8\ M^{-1}s^{-1}$. The rate constant determined for the unsubstituted radical **7(H)** is again only slightly higher at $3.3 \times 10^8\ M^{-1}s^{-1}$, but this value then doubles to $6.8 \times 10^8\ M^{-1}s^{-1}$ for the ionization radical **7(Me)**. The largest rate constant was obtained with radical **7(OMe)** for which k_{cat} was calculated to be $7.8 \times 10^8\ M^{-1}s^{-1}$.

The relationship between these rate constants and the substituent parameters σ and σ^+ are shown in Figures 3-50 (a) and (b). In contrast with the k_{het} values calculated for the acid-independent ionization of radicals **7(X)** and the uncatalyzed ionization of β-mesylate radicals **2(X)** which both correlated with σ^+, the correlation between k_{cat} and the σ^+ scale was poor, R = 0.846. Instead a better linear relationship was observed using the Hammett σ scale, R = 0.989.

Since the rate-determining step for the k_{cat} reaction is the same as that for k_{het} reaction, one would expect that a better correlation would be obtained using σ^+ rather than σ parameters. One possible explanation for the poor fit using σ^+ lies in the fact that the value of k_{cat} is a composite of the rate constant for the ionization of water from the protonated radical, k_{het}, and the acid dissociation constant for the protonated radical $K_{RH^{\bullet+}}$. This situation could lead to a poor fit if the equilibrium constant shows a significant substituent effect that is different from the substituent effect on k_{het}. The values for $K_{RH^{\bullet+}}$ do change as a function of substituent, ranging from 0.023 for **7(H)** to 0.056 for **7(Me)**, but these changes are small and show no correlation with the σ and σ^+ substituent parameters, Table 3-4. Surprisingly, the most acidic protonated radical is **7(Me)**, $pK_{RH^{\bullet+}}$ = 1.25, followed by protonated radicals **7(F)**, **7(Cl)**, and **7(H)** with $pK_{RH^{\bullet+}}$ values of 1.44, 1.47 and 1.63 respectively. This is contrary to expectation based on the electron donating ability of the 4-methyl group that should stabilize the protonated form of the radical relative to the non-protonated form, and ultimately decrease the acidity. This expected behavior has been previously observed in the dissociation constants measured for radicals **3a**-**3e** protonated at the β-OH position in aqueous solution. As shown below, values of $K_{RH^{\bullet+}}$ were found to increase with an increasing number of electron donating methyl groups.[153]

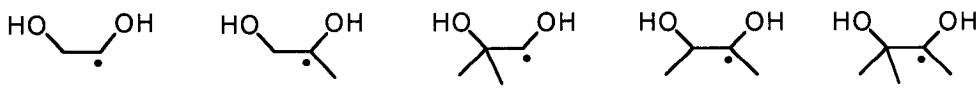

	3a	3b	3c	3d	3e
K_{RH}/ M	0.046	0.0056	0.0037	0.0026	0.00074
pK_{RH}	1.34	2.25	2.43	2.59	3.13

The small changes in the acidity constants calculated for radicals **7(X)** are likely due to the uncertainties in the calculated values. Nonetheless, since k_{cat} is in part determined by the $K_{RH^{\bullet+}}$, the poor fit of the data to σ^+ can to some extent be attributed to the variation of the value of $K_{RH^{\bullet+}}$ particularly for that part of the linear free energy relationship represented by the data points for **7(Me)**, **7(F)**, **7(Cl)**, and **7(H)**.

Table 3-4. Dissociation constants $K_{RH^{\bullet+}}$ and corresponding $pK_{RH^{\bullet+}}$ values calculated for β-hydroxy-*para*-substituted radicals **7(X)** in HFIP/perchloric acid mixtures.

Radical	$K_{RH^{\bullet+}}$/M	$pK_{RH^{\bullet+}}$
7(Cl)	0.0336±0.004	1.47
7(F)	0.0362±0.004	1.44
7(H)	0.0232±0.003	1.63
7(Me)	0.0560±0.005	1.25
7(OMe)	-	-

It should be noted that the low value of k_{cat} for the 4-methoxy derivative, for which no dissociation constant could be determined, is largely responsible for the poor fit of the data to σ^+, Figure 3-50 (b). In fact, if the data point for **7(OMe)** is removed, a reasonably good correlation is observed between the rate constants for the remaining four

radicals and σ^+, with a ρ^+ of -1.72 (R = 0.902), Figure 3-50 (c). The possibility that the large deviation of the methoxy substituent could represent a change in mechanism for the acid-catalyzed β-heterolysis reaction was considered. Thus, the assumption has been made that the mechanism involves a rapid pre-equilibrium followed by rate-determining loss of water. The observation of saturation kinetics for **7(Cl)**, **7(F)**, **7(H)** and **7(Me)** in acidic HFIP is consistent with that mechanism. However, for the methoxy derivative which showed no saturation kinetics, loss of the water from the protonated radical may be more rapid than deprotonation back to the neutral radical. Protonation of the β-OH group of the radical then becomes the rate-determining step and the value of k_{cat} would therefore represent the rate constant for protonation rather than the combined constants of k_{het} and $K_{RH^{\bullet+}}$. Unfortunately, proton transfer reactions to heteroatoms like oxygen typically occur at diffusion-controlled rate constants of *ca.* 10^{10} M^{-1} s^{-1}. This is considerably larger than the second-order rate constant of 7.8×10^8 M^{-1} s^{-1} determined in the present work.

An alternative explanation is that, unlike the other β-OH radicals studied, radical **7(OMe)** possesses two protonation sites, the oxygen atom on the β-OH and the methoxy group. It is possible that the HFIP/acid mixtures used in these experiments are sufficiently acidic to protonate the methoxy group rather than the oxygen on the β-OH which is required for the β-heterolysis reaction. Since the values of k_{cat} are dependent on the concentration of both the protonated radical and acid present, protonation at the methoxy site would significantly reduce the value of both of these terms and result in k_{cat} values that are lower than expected. This would explain why the value of k_{cat} for radical **7(OMe)** does not align itself with the rest of the data when presented as a function of σ^+, and why it is considerably lower than the value required for a linear correlation with this parameter scale.

3.3.4 Solvent Effects

3.3.4.1 The Acid-*Independent* β-Heterolysis Reaction

The ionization of radical **7(OMe)** was investigated in a number of solvent/acid mixtures, in which the solvent component was HFIP, TFE or AcN. The observed rate constants for the growth of the 4-methoxystyrene radical cation calculated from the time-resolved kinetic traces at 590 nm are overlapped in Figure 3-51. Over the range of acid concentration investigated, only the data acquired in neat AcN resulted in a leveling of k_{obs}. From this plateau, a value of k_{het} was calculated as $3.4 \times 10^6\ s^{-1}$ for the acid-independent heterolysis reaction of radical **7(OMe)**. In TFE and HFIP, k_{obs} may eventually level off, and if so, the values of k_{het} represented by the plateau region would be well above that measured in AcN. Thus, despite limited data, these results imply that the kinetics of the β-heterolysis reaction under acidic conditions are affected by the nature and extent of solvent interactions.

These solvent effects were investigated more thoroughly in a series of experiments in which rate constants for the β-heterolysis reaction of **7(OMe)** were measured in TFE/AcN mixtures, Figure 3-52. Over the range of acid concentration studied, a distinct plateau region was observed in neat AcN and in 25% TFE/75% AcN. In solutions containing 50% to 75% TFE, curvature was observed but a well-defined plateau region was not reached. The values of k_{het} were determined by fitting the data to eq. 3.2 and are presented in Table 3-2. However, the influence of solvent composition on the kinetics of the acid-independent heterolysis reaction is best appreciated with the graphical representation of the data, Figure 3-53.

Somewhat surprisingly, the data do not show significant variation in k_{het} with TFE content relative to AcN suggesting that changing the TFE/AcN ratio does not heavily influence the rate constant for the acid-independent β-heterolysis process. While

this finding is in sharp contrast with the results found for the ionization of the β-mesylate radicals **2(X)**, there are noteworthy differences between the heterolysis reaction of these two substrates. While radical **2(OMe)** is a neutral reactant whose stability is expected to be relatively insensitive to solvent effects, protonated radical **7(OMe)** is a distonic radical cation already carrying a full positive charge. Consequently, its energy is expected to vary according to the solvent's ability to stabilize the charge through solvation effects. Since a radical cation is the product of the reaction, solvation demands may be similar for the reactants and the products of this ionization reaction. Thus, as the ionizing ability of the medium increases with increasing TFE content, the protonated radical and the styrene-type radical cation will be stabilized to a similar extent. Since the energy level of the reactant and the products are influenced in the same manner, the position of the transition state will remain relatively unchanged.

Another important difference between the uncatalyzed ionization of the mesylate and the water group is that the former is negatively charged after departing while the latter is neutral. Solvation requirements of the transition state and the products are largely associated with stabilizing the nucleofuge. Therefore, when the leaving group is a mesylate anion, an ionizing solvent will provide needed stabilizing interactions and lower the activation barrier resulting in a strong solvent effect on the value of k_{het}. In the case of the water group, its neutrality substantially decreases the reaction's dependence on solvation both in the transition state and in the products and the effect of solvent on k_{het} is expected to be smaller. The difference in solvation requirement between the mesylate and water group is certainly one of the key reasons why the first-order rate constant for the β-heterolysis reaction of radical **7(OMe)** is less sensitive to solvent effects than **2(OMe)**.

As mentioned earlier, no plateau region was found in neat TFE or neat HFIP and, as a result, the values of k_{het} in these solvents are apparently significantly greater than the values measured in any of the mixed TFE/AcN solvents. Contrary to results described above, this strongly suggests that the polarity of the solvent does have a distinct influence on the rate constant for loss of water from the protonated radical. Currently, no reasonable explanation can be provided for this behavior in neat TFE or neat HFIP.

3.3.4.2 The Acid-*Dependent* β-Heterolysis Reaction

Solvent effects are found to play a particularly important role in the calculated value of k_{cat} for the ionization of radicals **7(X)**. This is apparent in Figure 3-51 in which k_{obs} for the growth of the 4-methoxystyrene radical cation is plotted as a function of acid concentration in three neat solvents that include AcN, TFE and HFIP. Measurements of k_{cat} were also made in TFE/AcN mixtures and the results are summarized in Table 3-2 and plotted in Figure 3-54. The rate constant k_{cat} for the acid catalyzed β-heterolysis process shows little variation between neat TFE and mixtures containing up to 75% AcN, but a sudden 9-fold increase is calculated for the value of k_{cat} in neat AcN.

The large increase upon going to neat AcN can be traced at least in part to the value of the dissociation constant for the protonated radical, $K_{RH^{\bullet+}}$. As shown in Figure 3-55, going from neat AcN to 75% TFE/25% AcN causes the value of $K_{RH^{\bullet+}}$ to increase by almost 15-fold, Table 3-5. In other words, the acidity of the protonated radical increases from $pK_{RH^{\bullet+}} = 2.6$ in neat AcN to $pK_{RH^{\bullet+}} = 1.4$ in the TFE rich mixture. Since k_{cat} is inversely proportional to the acidity of the radical, the value of k_{cat} is significantly greater in neat AcN than in the TFE/AcN mixtures.

Table 3-5. Dissociation constants $K_{RH^{\bullet+}}$ and corresponding $pK_{RH^{\bullet+}}$ values calculated for the β-hydroxy-4-methoxyphenethyl radical **7(OMe)** in various solvents acidified with perchloric acid.

Solvent	$K_{RH^{\bullet+}}$/M	$pK_{RH^{\bullet+}}$
AcN	0.0024±0.0003	2.62
25% TFE in AcN	0.0078±0.001	2.11
50% TFE in AcN	0.029±0.002	1.53
75% TFE in AcN	0.037±0.002	1.43
TFE	-	-
HFIP	-	-

The large difference in the $pK_{RH^{\bullet+}}$ value in neat AcN compared to those in the TFE/AcN mixtures is likely due to the different behavior of perchloric acid ($pK_a \sim -10$)[154] in AcN compared to alcohol solvents. While some authors claim that perchloric is extensively dissociated in AcN,[155-157] other state that it does not in fact fully ionize but instead forms a 1:1 complex with AcN and that the equilibrium lies almost entirely to the right, eq. 3.32.[158]

$$CH_3CN + HClO_4 \rightleftharpoons [CH_3CN{\bullet}HClO_4] \qquad (3.32)$$

Infrared measurements have confirmed that the complex is held together by hydrogen bonding and that there is no dissociation of the OH proton. Only after 50 hours did the authors observe the formation of ionic species as shown in eq. 3.33.[158]

$$CH_3CN + HClO_4 \rightleftharpoons CH_3C{\equiv}\overset{+}{N}H + ClO_4^- \qquad (3.33)$$

The perchloric acid used in the current experiments contained 30% w/w of water (which introduces 2.4 moles of water per mole of perchloric acid) and undoubtedly facilitates the dissociation of perchloric acid. Thus, the hydronium ion, H_3O^+, perchloric acid and possibly protonated AcN (pK_a = -4.4)[158,159] are likely the acids that ultimately provided the source of protons to generate the protonated radical. On the other hand, perchloric acid is likely to be completely ionized in TFE. The pK_a value for protonated TFE was not found but is estimated to be more acidic than $CH_3CH_2OH_2^+$ for which pK_a = -2.4.[160] However, it most likely remains the weaker acid relative to perchloric acid and thus the dominant acid in TFE rich mixtures should be $CF_3CH_2OH_2^+$ and a small percentage of hydronium ions. Based on the pK_a values presented, perchloric acid/TFE mixtures are expected to be less acidic than perchloric acid/AcN mixtures.

3.3.5 Ionization of the β-(Diethylphosphate)-4-methoxyphenethyl Radical

3.3.5.1 Solvent Effects in AcN/TFE Mixtures with Added Perchloric Acid

A summary of the rate and equilibrium constants for the loss of diethylphosphate from the β-(diethylphosphate)-4-methoxyphenethyl radical **10(OMe)** is given in Tables 3-3 and 3-6, and the data is plotted in Figure 3-56. These data share many similarities with the rate and equilibrium constants determined earlier for the loss of water from the corresponding β-OH radical **7(OMe)**. In both cases, there is very little variation in the value for the unimolecular loss of the leaving group, either diethylphosphoric acid or water, from the protonated radical upon going from neat AcN to TFE/AcN mixtures, Figure 3-57. In addition, the values of the acid-dependent rate constants of both radicals are fastest in neat AcN, and then decrease with increasing TFE content, Figure 3-58. For radical **7(OMe)**, the data indicate a factor of 3.6 decrease in k_{cat} as the TFE content increases from 0% to 50%. The values of k_{cat} do not appear to be

influenced by TFE content from 50% to 100%, and hover around an average value of $2.4 \times 10^6\ M^{-1}\ s^{-1}$.

Figure 3-59 presents the pre-equilibrium step, $K_{RH^{\bullet+}}$ calculated for the dissociation of the protonated radical **10(OMe)** as a function of %TFE in AcN. As previously observed for radicals **7(OMe)**, the value of $K_{RH^{\bullet+}}$ for **10(OMe)** increases with TFE content. This result implies that as the volume of TFE in AcN ratio increases, the concentration of protonated radical in solution decreases. These results are attributed to the differences in acidity of the two media, with AcN/perchloric acid solutions being more acidic than TFE/perchloric acid mixtures as discussed previously.

Insensitivity toward solvent composition for the reactivity of the protonated β-phosphate radical is presumably due to the same factors described earlier for the protonated β-OH radical. The starting material and the product, as well as the transition state, all carry a full positive charge. Using a more polar solvent like TFE instead of a less polar solvent like AcN affects all three states in a similar manner, and no change in the activation energy and ultimately the rate constant observed.

Table 3-6. Dissociation constants $K_{RH^{\bullet+}}$ and corresponding $pK_{RH^{\bullet+}}$ values calculated for the β-diethylphosphate-4-methoxyphenethyl radical **10(OMe)** in TFE/AcN mixtures acidified with perchloric acid.

Solvent	$K_{RH^{\bullet+}}$/M	$pK_{RH^{\bullet+}}$
AcN	0.0199±0.004	1.70
25% TFE in AcN	0.0416±0.004	1.38
50% TFE in AcN	0.0435±0.006	1.36
75% TFE in AcN	0.0708±0.015	1.15
TFE	-	-

3.3.5.2 Leaving Group Effect

Across the range of TFE/AcN mixtures investigated, the acidity of the protonated β-diethylphosphate-4-methoxyphenethyl radicals **10(OMe)** was found to be consistently greater than the protonated β-OH-4-methoxyphenethyl radical **7(OMe)**, Figure 3-59. For example, $pK_{RH^{\bullet+}}$ values calculated for radical **10(OMe)** and **7(OMe)** in neat AcN are 1.7 and 2.6, respectively (Tables 3-6 and 3-5). This finding is in agreement with the pk_a values calculated in water for related compounds. For instance, the pK_a of protonated triphenylphosphate **3(f)** has a value of -5.0[161] which is significantly more acidic that the protonated radical **3a** with a pK_a of 1.34.[153]

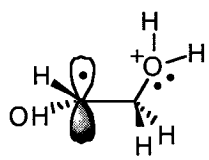

3a

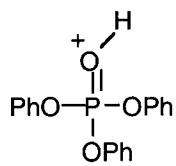

3f

This difference in acidity provides a possible explanation for the consistently greater k_{het} values measured for radicals **10(OMe)** relative to radical **7(OMe)**, as shown in Figures 3-57. The greater acidity, and hence greater destabilization of the protonated diethylphosphate group likely assists in the elimination of diethylphosphoric acid, resulting in a lower activation barrier for the reaction and increased values of k_{het}.

3.4 Conclusions

The results presented in this chapter have unambiguously demonstrated that β-heterolysis is the predominant reaction pathway of β-hydroxy and β-diethylphosphate phenethyl radicals when generated in acidic and polar media. Two limiting mechanisms are established. At low acid concentration, the observed rate constants for the heterolytic

loss of water or phosphoric acid are bimolecular and show a linear dependence with acid strength, k_{cat}. At high acid concentration, the k_{obs} levels off to a limiting, unimolecular and acid-independent rate constant, k_{het}.

Both k_{cat} and k_{het} for the ionization of **7(X)** in acidic HFIP show sensitivity to the electronic nature of the aromatic substituent. The values of k_{het} show an appreciable linear correlation with the σ^+ scale, with $\rho^+ = -2.40$. The reduced sensitivity of this reaction to electronic effects relative to the ionization of the β-mesylate radicals **2(X)** is partially attributed to an earlier transition state in the case of radicals **7(X)**. Substituent effects of the value of k_{cat} are not easily interpreted. A poor fit of k_{cat} to the σ^+ scale (R = 0.85) seems largely due to the unusually low value of k_{cat} calculated for the methoxy radical **7(OMe)**. Protonation at the methoxy oxygen has been put forward as a tentative explanation.

Unlike radicals **2(OMe)**, k_{het} values for radicals **7(OMe)** and **10(OMe)** showed no significant solvent dependence in TFE/AcN mixtures, a result that is partly explained by the neutrality of the nucleofuge (water and diethylphosphoric acid), compared to the mesylate anion which has greater solvation requirements due to its charge. Solvent effects on the values of k_{cat} showed similar trends for radicals **7(OMe)** and **10(OMe)**. In both cases, k_{cat} increases with decreasing TFE content in AcN. This has been explained by the greater acidity of the AcN/perchloric acid mixtures relative to the TFE/perchloric acid mixtures. This argument is also used to rationalize the greater acidity of the protonated radicals **7(OMe)** and **10(OMe)** in AcN than in 25% AcN/75% TFE.

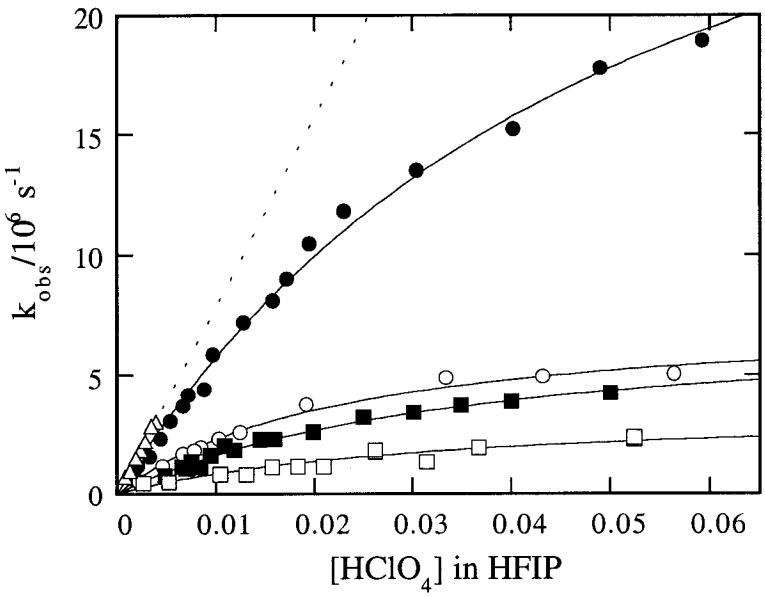

Figure 3-48. Observed rate constant for the growth of the (Δ) 4-methoxy, (●) 4-methylstyrene, (○) styrene, (■) 4-fluorostyrene and (□) 4-chlorostyrene radical cation plotted as a function of perchloric acid concentration in nitrogen-saturated HFIP. Rate constants were measured from kinetic traces acquired after 266 nm laser irradiation of (Δ) 3-(4-methoxyphenyl)-4-hydroxy-2-butanone **6(OMe)**, (●) 2,4-bis(4-methylphenyl)-1,5-dihydroxy-3-pentanone **6(Me)**, (○) 3-(4-fluorophenyl)-4-hydroxy-2-butanone **6(F)**, (■) 2,4-diphenyl-1,5-dihydroxy-3-pentanone **6(H)** and (□) 2,4-bis(4-chlorophenyl)-1,5-dihydroxy-3-pentanone **6(Cl)** in nitrogen-saturated TFE/perchloric acid mixtures.

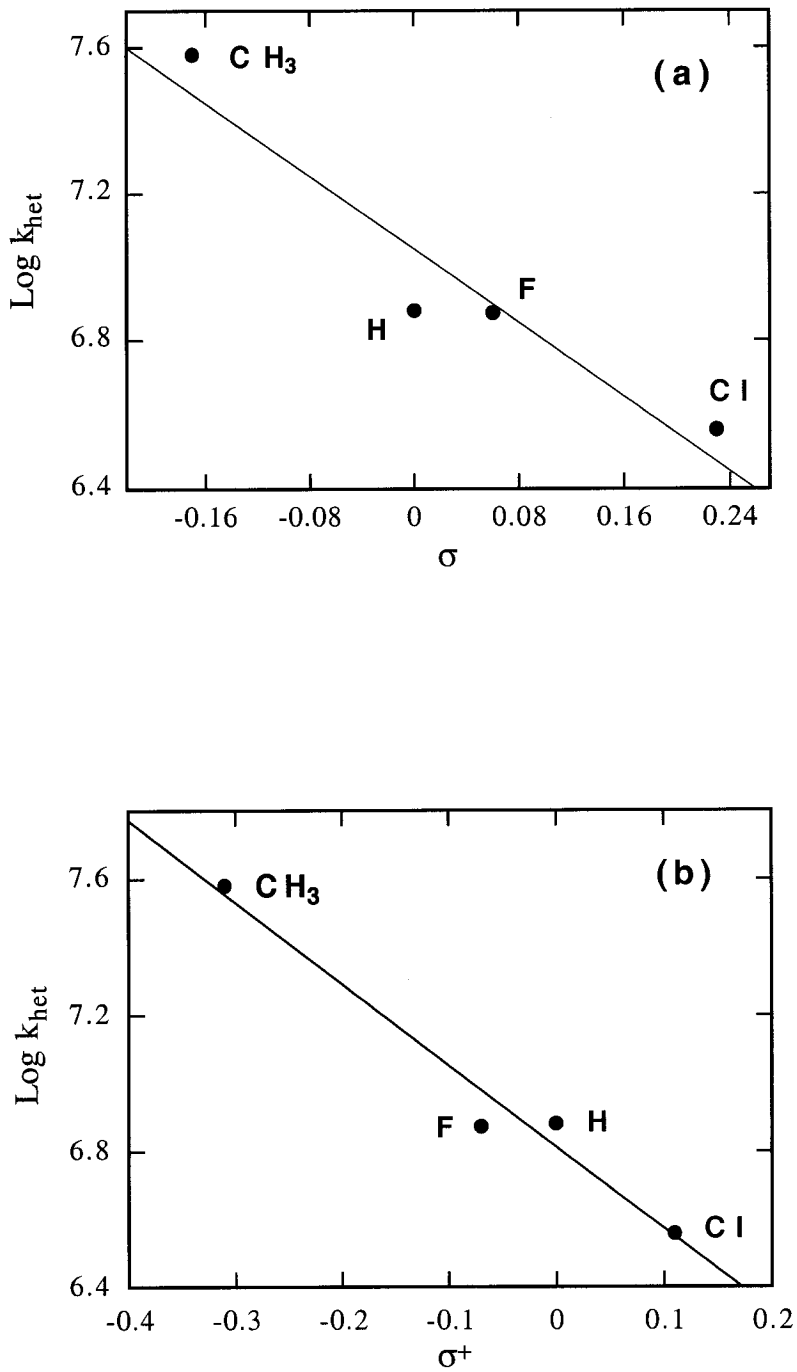

Figure 3-49. Correlation analysis of the acid-independent rate constant (k_{het}) in acidified HFIP, as a function of (a) the Hammett σ scale (ρ = -2.5) and (b) Brown-Okamoto σ^+ (ρ^+ = -2.4) substituent parameters for the ionization of β-hydroxy *para*-substituted phenethyl radicals **7(Cl)**, **7(H)**, **7(F)** and **7(Me)**.

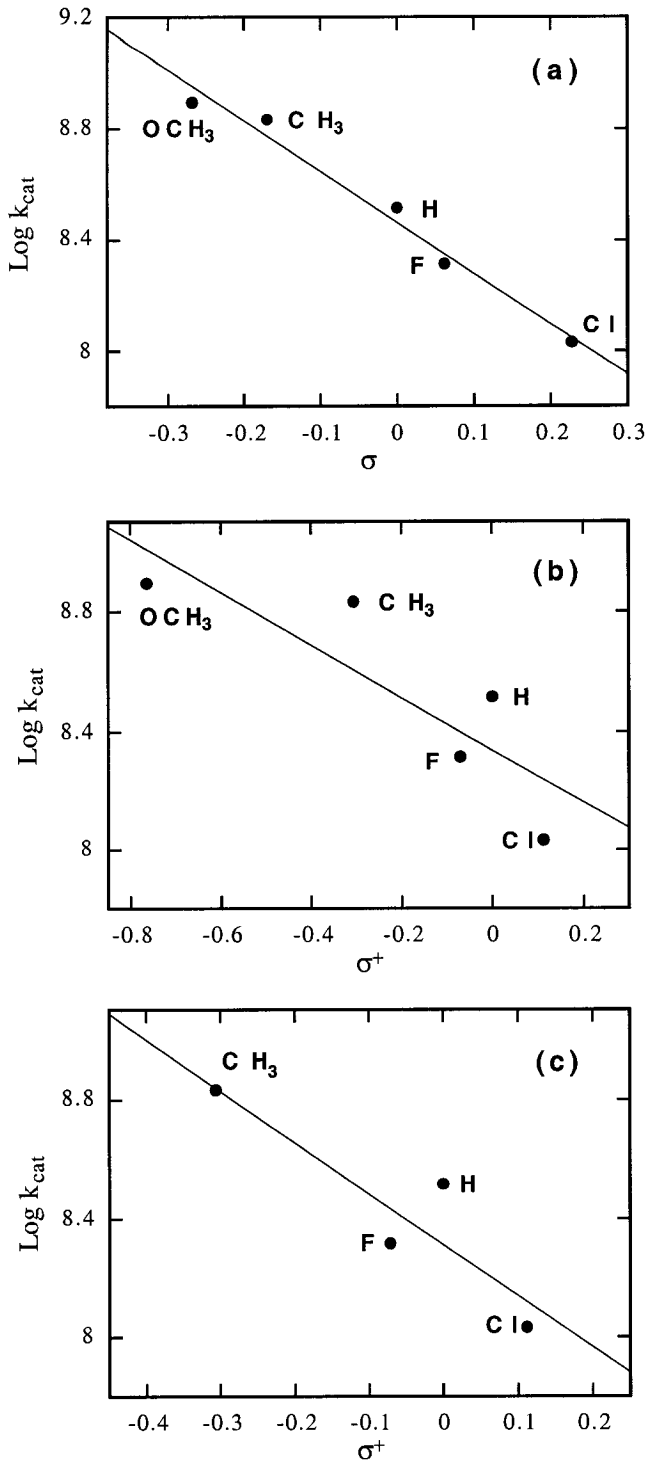

Figure 3-50. Correlation analysis of the acid-catalyzed rate constants k_{cat} in acidified HFIP as a function of the σ scale (a) ρ = -1.83 (R = 0.989), and the σ^+ scale (b) ρ^+ = -0.88 (R = 0.847), (c) ρ^+ = -1.72 (R = 0.902) for the ionization of β-hydroxy *para*-substituted phenethyl radicals **7(X)**.

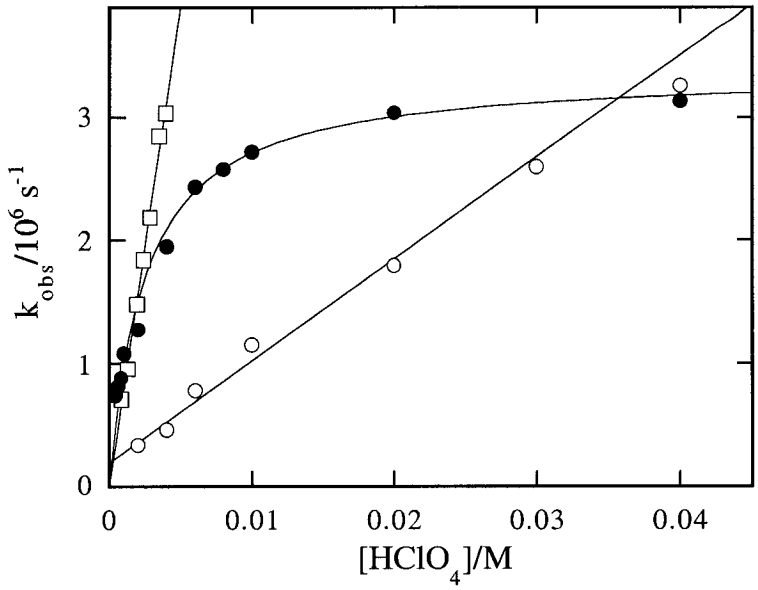

Figure 3-51. Observed rate constant measured in nitrogen-saturated (●) acetonitrile, (○) TFE, and (□) HFIP as a function of perchloric acid concentration. Rate constants were calculated from time-resolved kinetic traces at 350 and 590 nm obtained after 266 or 308 nm laser flash photolysis of 3-(4-methoxyphenyl)-4-hydroxy-2-butanone **6(OMe)**.

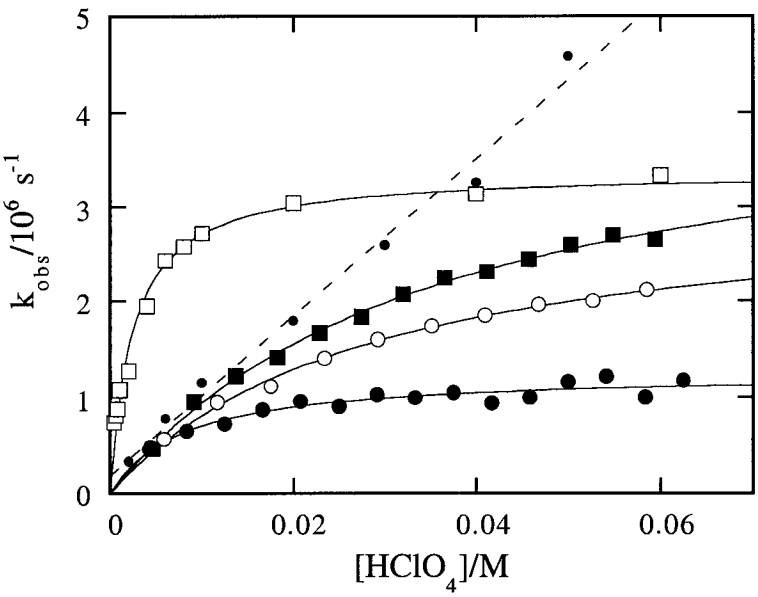

Figure 3-52. Observed rate constants measured in (□) neat AcN, (●) 25% TFE/75% AcN, (○) 50% TFE/50% AcN, (■) 75% TFE/25% AcN, and (•) neat TFE, plotted as a function of perchloric acid concentration. Rate constants were measured from kinetic traces monitored at 590 nm after 266 nm laser irradiation of 3-(4-methoxyphenyl)-4-hydroxy-2-butanone **6(OMe)**.

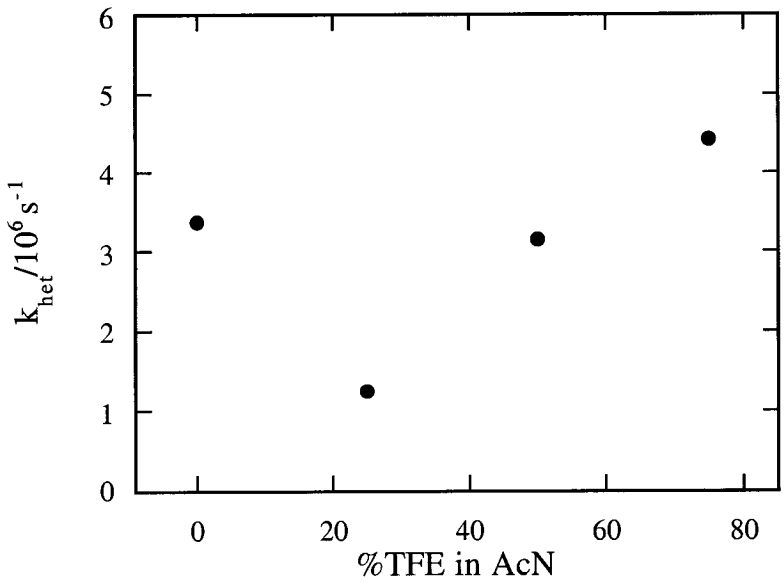

Figure 3-53. First-order rate constant k_{het} calculated for the growth of the 4-methoxystyrene radical cation **8(OMe)** and plotted against %TFE in nitrogen-purged acetonitrile mixtures acidified with perchloric acid. Rate constants were determined from kinetic traces acquired at 590 nm after 266 nm laser photolysis of 3-(4-methoxyphenyl)-4-hydroxy-2-butanone **6(OMe)**.

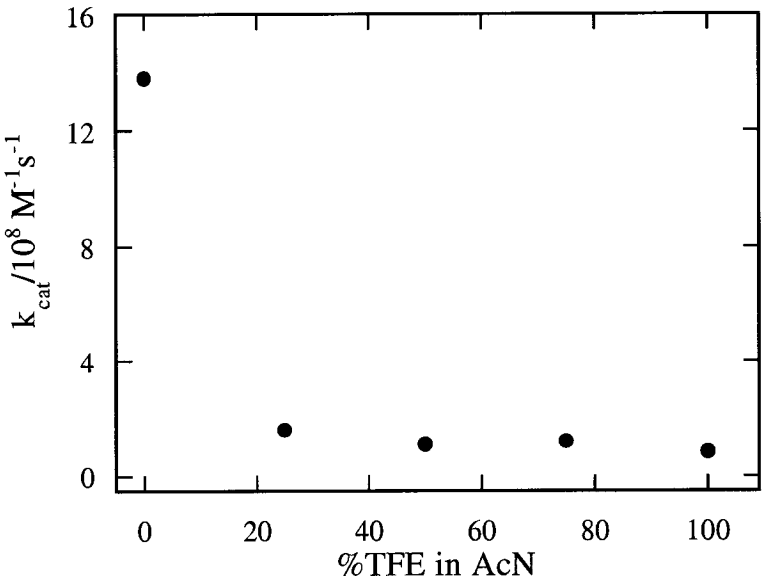

Figure 3-54. Second-order acid-catalyzed rate constant k_{cat} for the growth of the 4-methoxystyrene radical cation **8(OMe)** plotted as a function of %TFE in nitrogen-purged acetonitrile mixtures acidified with perchloric acid. Rate constants were determined from kinetic traces collected at 590 nm after 266 nm laser photolysis of 3-(4-methoxyphenyl)-4-hydroxy-2-butanone **6(OMe)**.

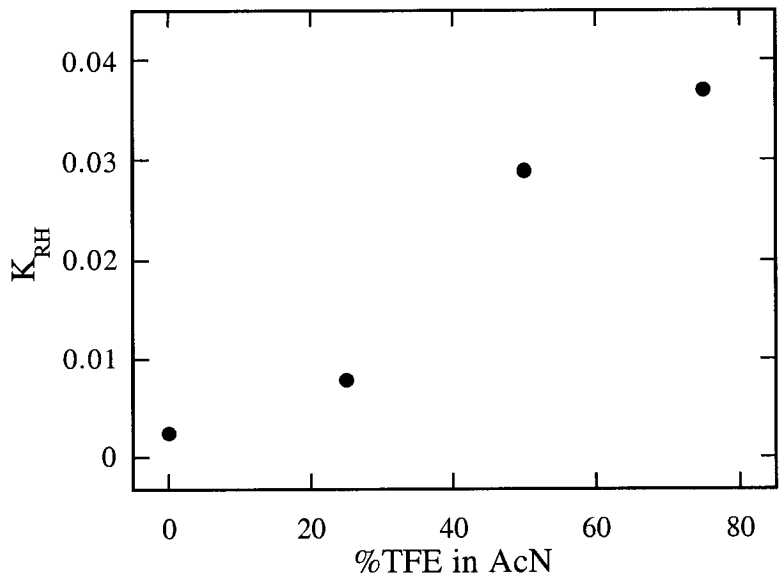

Figure 3-55. Acidity constant $K_{RH^{\bullet+}}$ calculated for the dissociation of the protonated β-hydroxy-4-methoxyphenethyl radical **7(OMe)** plotted as a function of %TFE in nitrogen-purged acetonitrile mixtures acidified with perchloric acid. Results were acquired from 266 nm laser photolysis of 3-(4-methoxyphenyl)-4-hydroxy-2-butanone **6(OMe)**.

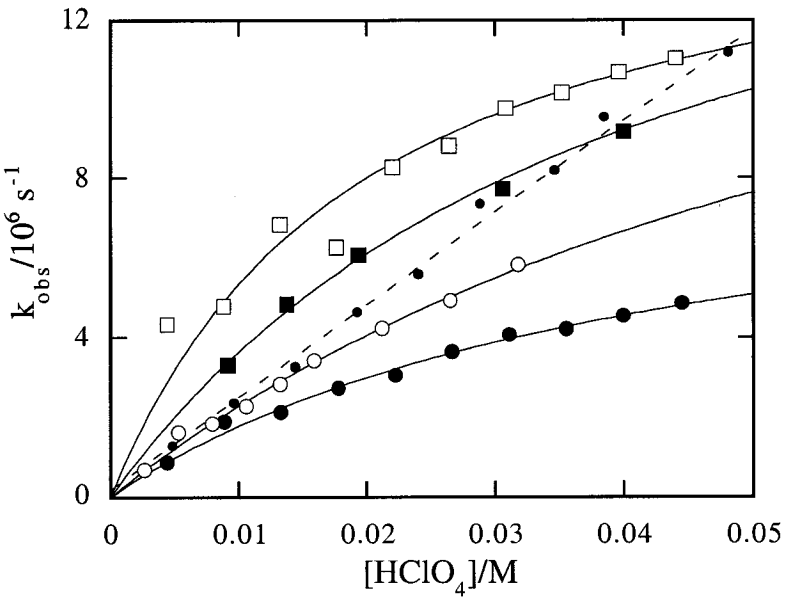

Figure 3-56. Observed rate constants calculated for the growth of the 4-methoxystyrene radical cation **11(OMe)** in (□) neat AcN, (■) 25% TFE/75% AcN, (●) 50% TFE/50% AcN, (○) 75% TFE/25% AcN, and (•) neat TFE, and plotted as a function of perchloric acid concentration. Rate constants were measured from kinetic traces monitored at 590 nm after 266 nm laser irradiation of 2-(4-methoxyphenyl)-3-oxobutyl-diethylphosphate **9(OMe)**.

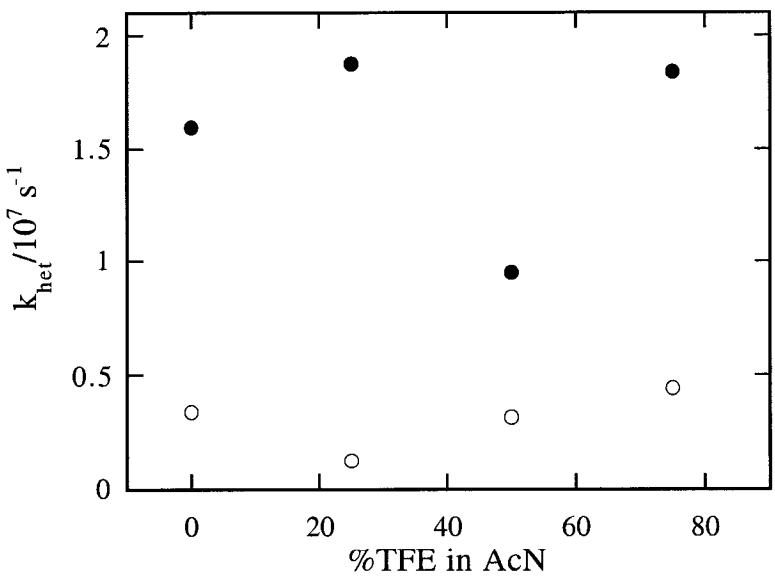

Figure 3-57. First-order rate constants versus %TFE in acetonitrile acidified with perchloric acid. Data was collected following 266 nm laser irradiation of (●) 2-(4-methoxyphenyl)-3-oxobutyldiethylphosphate **9(OMe)** and (○) 3-(4-methoxy-phenyl)-4-hydroxy-2-butanone **6(OMe)**.

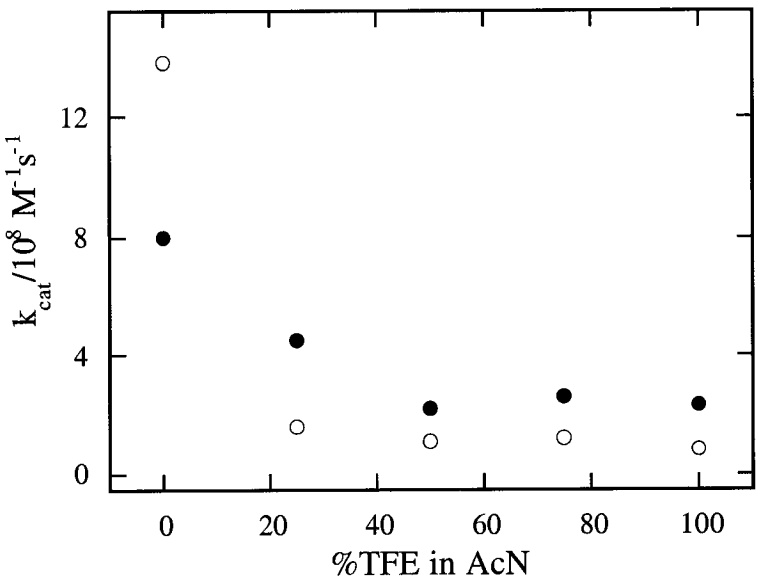

Figure 3-58. Second-order rate constants versus %TFE in acetonitrile acidified with perchloric acid. Data was collected following 266 nm laser irradiation of (●) 2-(4-methoxyphenyl)-3-oxobutyl diethylphosphate **9(OMe)** and (○) 3-(4-methoxyphenyl)-4-hydroxy-2-butanone **6(OMe)**.

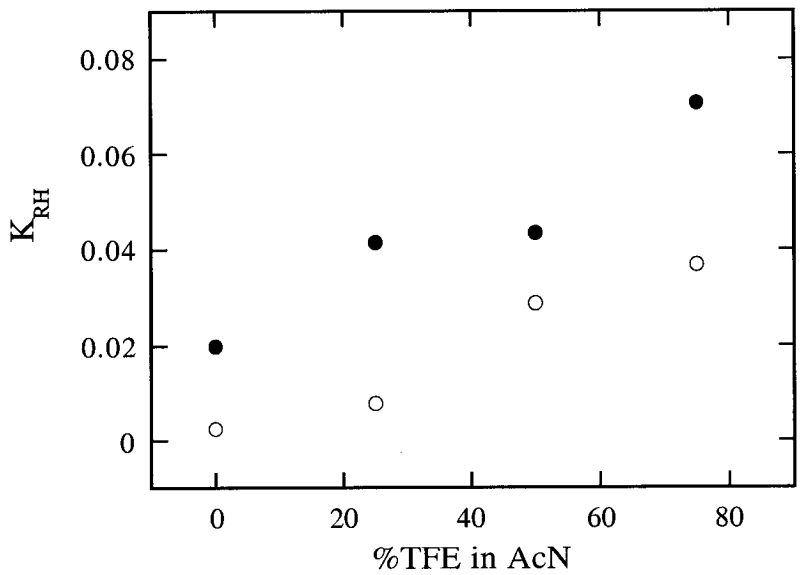

Figure 3-59. Acidity constant $K_{RH^{+\cdot}}$ calculated for the dissociation of the protonated (●) β-diethylphosphate-4-methoxyphenethyl radical **10(OMe)** and (○) β-hydroxy-4-methoxy phenethyl radical **7(OMe)** as a function of %TFE in acetonitrile acidified with perchloric acid.

CHAPTER 4
EXPERIMENTAL DETAILS

4.1 Nanosecond Laser Flash Photolysis

4.1.1 Sample Preparation and Experimental Technique

Samples were prepared in square 7 × 7 mm^2 laser cells manufactured from Suprasil quartz tubing. Each cell contained a 1 mL aliquot of solution and was capped with a rubber septum. Unless otherwise specified, samples were deaerated with ultra high purity (UHP) nitrogen or oxygen (all supplied by PraxAir) for 15 minutes prior to experimentation. Using a long needle, a regulated stream of gas was bubbled through the solution and the excess pressure released through a second needle. The flow rate was regulated and maintained low to minimize solvent evaporation and hence changes in precursor concentration. For each sample, the neat solvent or solvent mixture (% v/v) was systematically purged prior to injecting the precursor compound previously dissolved in AcN. The injection volumes ranged from 4-10 μl and generated precursor concentrations between 10-30 mM within the laser cell. These were adjusted such that the maximum absorbance of the solution was in the optimum range of 0.4-0.6 at the laser wavelength (266 or 308 nm). Within this optical density range, the solutions were

sufficiently dilute to maintain uniform concentration along the cell length and achieve homogeneous radical production upon laser irradiation. While not all experiments were carried out in CH_3CN, but the relatively small volume (approximately 1% of the total volume) introduced upon injection of the precursor solution was considered negligible and insufficient to affect the kinetics of the β-heterolysis reaction.

Following injection, the pierced septum was tightly wrapped with Parafilm and the freshly prepared sample mixed vigorously (by tapping the side of the cell) to ensure homogeneity. Lastly, the sample was wiped with a KimWipe to remove any traces of fingerprints, or other light-scattering materials. Sample cells were also checked for surface imperfections prior to use and care was taken to prevent dust from entering the solutions. Once the sample was placed in the holder ready to be photolyzed, the side of the sample facing the laser beam was marked. Every three laser shots, the sample was mixed using the same technique (3 taps) and replaced in the holder with the marked side having the same orientation to maintain consistency.

4.1.2 Additional Considerations for Samples Containing Acid

The thermal stability of the precursor compounds in acidic solutions was verified prior to experimentation. The precursor compound was injected into a solution of the strongest acid concentration studied and monitored every 5 minutes for a period of an hour using UV spectroscopy. Significant changes in absorption were anticipated upon decomposition of the precursor compounds and absorption changes were not observed under these experimental conditions. During laser experiments, a single sample was flashed for a maximum duration of thirty minutes. For all acid concentrations investigated, thermal decomposition was not observed by UV/Vis within this consequential half an hour time frame.

4.1.3 Experimental Set-Up for Transmission Laser Flash Photolysis

The rapid generation and detection of short-lived intermediates was made possible through the use of the fast reaction technique known as nanosecond laser flash photolysis (LFP).[162] A schematic of the experimental set-up employed for this fast reaction technique is presented in Figure 4-1. The transients of interest were generated with a pulsed excitation source originating from either a Lambda-Physik excimer laser filled with a Xe/HCl/He mixture (308 nm, ≤ 120 mJ, < 10 ns/pulse) or a Continuum Nd:YAG NY-61 laser (fourth harmonic, 266 nm, ≤ 10 mJ/pulse, < 8 ns/pulse).

Photogenerated transients were monitored with time-resolved absorption spectroscopy. The detection system consisted in part of a white light monitoring beam originated from a pulsed 150 Watt xenon arc lamp. As illustrated in Figure 4-1, a conventional right-angle arrangement was employed, with the monitoring and photolysis beams at a 90° angle relative to each other. The fraction of the monitoring beam absorbed by the transient, eventually expressed as ΔO.D., is monitored as a function of time at specific wavelengths using a grating monochromator coupled to a photomultiplier. The transmitted and filtered light subsequently reaches the photomultiplier tube where the light intensity is proportionally converted into a voltage and then amplified. The rapid changes in photomultiplier output (analog signals) are captured by a Tektronic-620A digitizing oscilloscope and then sent to an interfacing Macintosh PowerPC computer used for processing and storage. Triggering of the oscilloscope is synchronized by the laser light itself that is transmitted through a fiber optic connection. A customized operational program written in LabVIEW® (a programming language from National Instruments) allows precise control and manipulation of all experimental variables such as detection timescales and monitoring wavelengths.

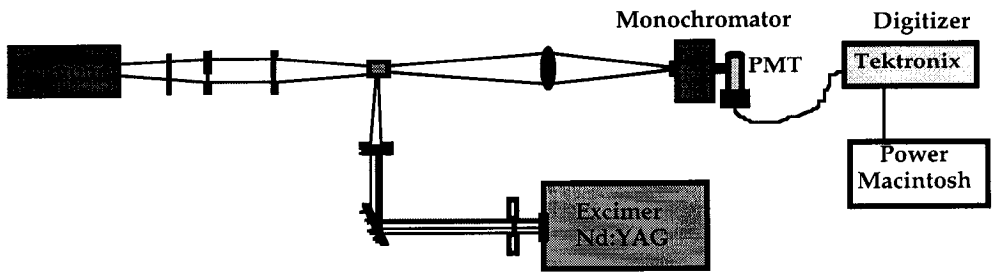

Figure 4-1. Schematic representation of the nanosecond laser flash photolysis apparatus used for transmission experiments.

4.2 Absorption Spectroscopy: Transient Detection

The nanosecond LFP system used for this research allows ΔO.D. to be measured both as a function of time and of wavelengths. These two types of experiments are described below.

4.2.1 Acquisition of Kinetic Data

The capacity to carry out real-time monitoring of changes in optical density permits a fundamental, kinetic insight into the reactivity of the transient of interest. The change in optical density is synonymous to absorbance at a specific wavelength and is linearly related to the signal intensity according to eq. 4.1.

$$\Delta O.D. = A = -\log\left(\frac{I_t}{I_0}\right) \tag{4.1}$$

In this expression, I_0 is the intensity of light transmitted in the absence of transient species (i.e. prior to the laser flash) and I_t represents intensity of light transmitted in the presence of transient species (after the laser flash).

The analysis of these kinetic traces was achieved with the assistance of KaleidaGraph software. More specifically, rate constants for the growth of the radical cation were calculated using kinetic traces acquired for the rise and decay of the

absorption signal observed near 600 nm (unless otherwise indicated). Each kinetic trace collected during LFP experiments has a total of 250 data points, and more often than not, the complete growth and decay of the signal could not be recorded on a single timescale. The analysis was therefore carried out in two separate steps.

First, the rate constant for the decay of the radical cation, k_{decay}, was determined using a kinetic trace ideally showing the maximum ΔO.D. and return of the signal back to zero or a constant residual value, as shown in Figure 4-2 (a). The pre-trigger points in trace (a) are subsequently removed in KaleidaGraph, Figure 4-2 (b), and the remaining data often analyzed using the first-order rate law given in eq. 4.2, where A_t is the absorbance at point t in time, A_{max} is the maximum transient absorbance, A_∞ is the residual absorption due to photoproducts, and t is the time. The relevant parameters are shown in Figure 4-2 (a).

$$Y=F(t; k_{decay}, A_{max}, A_\infty);\ A_t = A_\infty + (A_{max} - A_\infty)\exp(-k_{decay}t) \qquad (4.2)$$

Equation 4.2 represents a first-order monoexponential expression that is a function of time t with variables k_{decay}, A_{max} and A_∞. Initial estimates are provided for these variables and the program calculates the best fit for the data using an iterative method based on the Levenberg-Marquardt algorithm. In the example trace shown in Figure 4-2 (a), k_{decay} has a calculated value of $2.1 \times 10^5\ s^{-1}$ with less than 1% error.

In cases where the radical cation decays with second-order kinetics, eq. 4.3 is utilized to calculate k_{decay}. This expression is the second-order rate law and is a function of time t, with variables k_{decay}, A_{max}, A_∞ for which estimates must be provided prior to iteration by the KaleidaGraph program. Since the absorption coefficient of transient species is not easily obtained, k_{decay} calculated using eq. 4.3 for the reaction of two identical transient species, $2A \rightarrow B$, is defined as $k_{decay} = 2k/\varepsilon$ where ε is the absorption

coefficient of transient A and k is the true second-order rate constant.

$$Y = F(t; k_{decay}, A_{max}, A_{\infty});$$

$$A_t = A_{\infty} + 1/(k_{decay}t + \frac{1}{(A_{max} - A_{\infty})}) \quad (4.3)$$

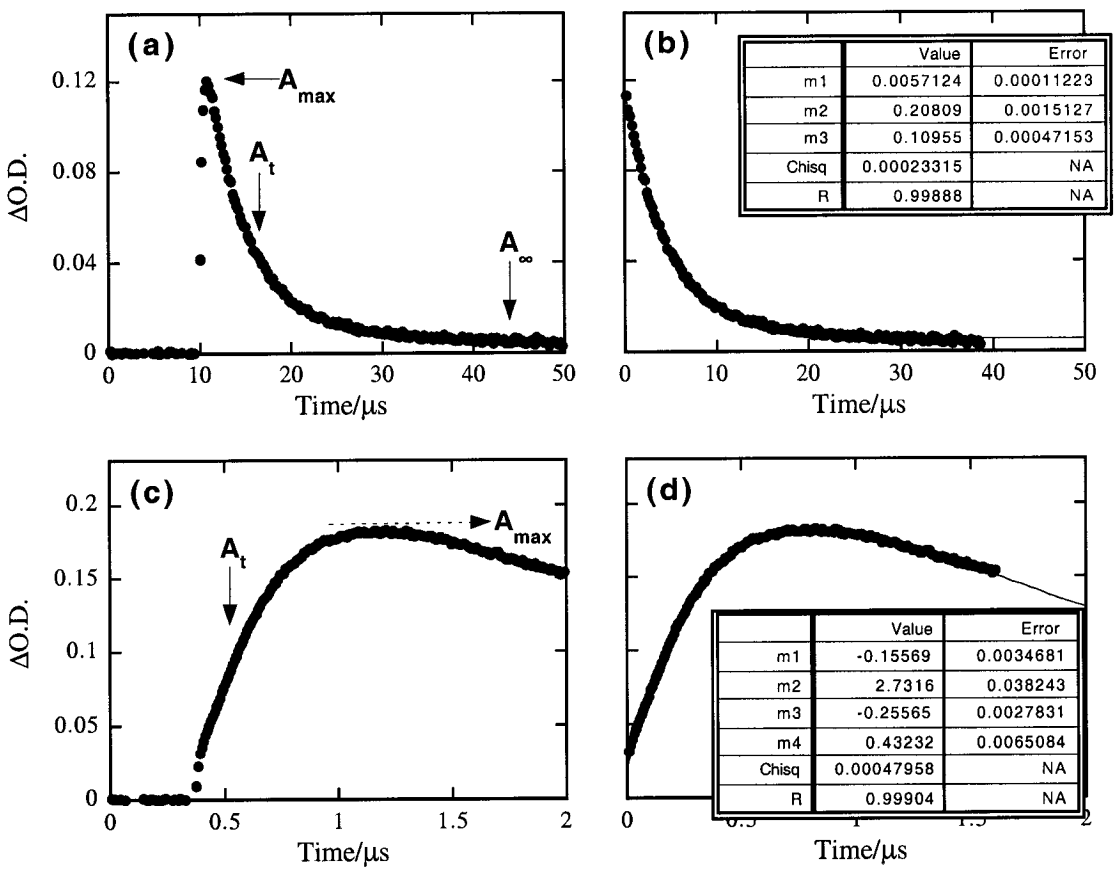

Figure 4-2. Exemplary time-resolved kinetic trace of (a) a decaying signal including the pre-trigger, (b) same decay trace without pre-trigger, analyzed with a monoexponential equation, $k_{decay} = 2.1 \times 10^5\ s^{-1}$, (c) growth trace with pre-trigger, (d) same growth signal with pre-trigger removed, analyzed with eq. 4.4 and fixing the value of k_{decay} as $2.1 \times 10^5\ s^{-1}$ as previously determined from trace (b), $k_{growth} = 2.7 \times 10^6\ s^{-1}$.

To determine the rate constant for radical cation formation, k_{growth}, a kinetic trace showing the rise of the signal is selected as exemplified in Figures 4-2 (c) and (d). As often found, very little of the decay is observed at the timescale best suited to observe the build-up of the radical cation. Consequently, the trace is fitted using eq. 4.4 which is a combination of two monoexponential expressions to analyze both the growth and the decay components with first-order kinetics. However, k_{decay}, which was previously calculated from the decay trace in Figure 2-4 (b), is now fixed at 2.1×10^5 s^{-1} in eq. 4.4. The remaining variables in this expression are k_{growth}, A_0, A_{max}, and A_∞, where A_0 is the absorbance at time zero and the other terms have previously been defined. In this specific example, the value of k_{growth} is determined to be 2.7×10^6 s^{-1}, Figure 4-2 (d).

$$Y = F\,(t;\, k_{growth},\, A_0,\, k_{decay},\, A_{max},\, A_\infty);$$

$$A_t = A_\infty + (A_0 - A_{max})\exp(-k_{growth}t) + (A_{max} - A_\infty)\exp(-k_{decay}t) \qquad (4.4)$$

Errors associated with the rate constants calculated from the KaleidaGraph fitting program are very small, on average less than 1%. However a more accurate representation of error is the experimental reproducibility which introduces an estimated 2-4% error in the calculated value of k_{obs}.

The time resolution of the detection system (< 10 ns) allowed kinetic measurements to be taken as early as 25 ns, and as late as 50 μs after the laser pulse. The timescale variable was selected as a time/division value for a total of 20 divisions. This therefore translates to a total detection time range of 0.5 μs to 1 ms respectively, following laser excitation. Each kinetic trace recorded was the average of a minimum of three traces (i.e. laser shots). The earlier timescales (25, 50 and 100 ns / division mainly) would commonly be used to measure the rate coefficients for the growth of the transitory species. Conversely, to measure the decay of the intermediate, the longer timescales

(500 ns and 1 to 50 μs/division) would be selected to follow the ΔO.D. signal back to zero (or until constant).

All experiments were carried out at room temperature (22 ± 1 °C) and under static conditions.

4.2.2 Acquisition of Spectral Data

It was often desirable to monitor changes in absorption over a wide spectral range (280-700 nm), particularly for exploratory work on a system that had not previously been studied. Within a chosen time frame, this kind of experiment could uncover wavelengths and approximate magnitude of transient absorptions for which the spectra were previously unknown or uncertain.

To acquire spectral data, a sample kinetic trace is first recorded at a wavelength of interest, showing either the rise or the decay of the signal. From this trace, a maximum of four time windows are selected, as shown in Figure 4-3 (a). These time windows establish the times following the laser pulse at which a spectrum is recorded. The range of wavelength is then specified, usually between 280 and 700 nm and the data points are recorded one wavelength at a time. Typical results are presented in Figure 4-3 (b), in which the spectra collected at times t_1, t_2, t_3 and t_4 together show an increase in absorption at 350 and 600 nm due to the build-up of styrene radical cation following the laser pulse.

Where only weak absorptions could be observed, scanning was carried out every 10-20 nm while in the specific spectral range of interest, monitoring was narrowed to every 5 nm. Whenever possible, these types of experiments were carried out at two timescales specifically chosen to show the growth and the decay of the radical cation at the two characteristic absorption maxima.

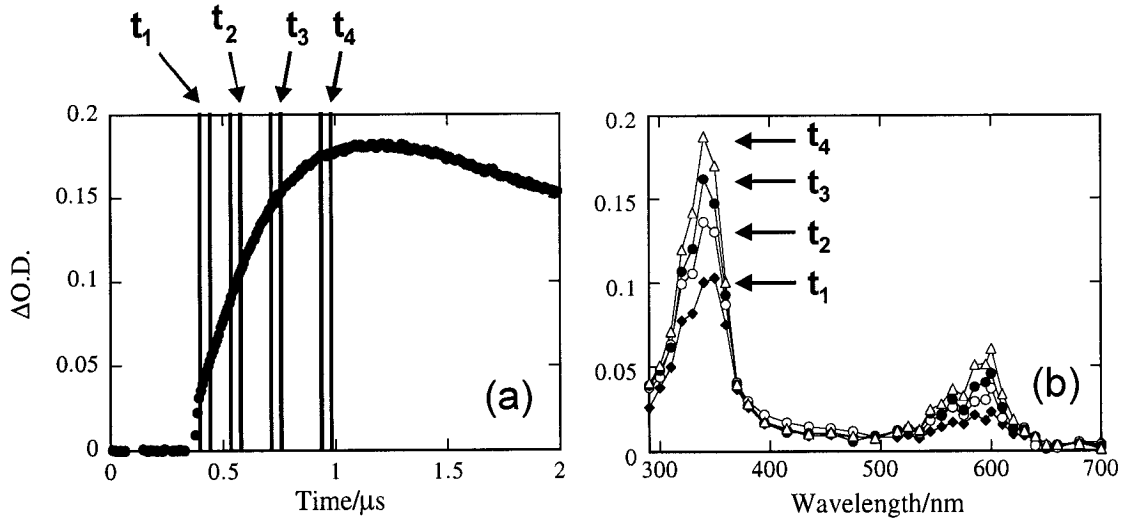

Figure 4-3. (a) Kinetic trace showing the rise of the signal at 350 nm with four time windows, t_1-t_4, selected for spectra acquisition. (b) Resulting spectra showing the increase in absorption at 350 nm at the four time windows selected from the kinetic trace. Spectra also reveals an additional rise in signal near 600 nm.

4.3 Synthesis of Precursor Compounds

4.3.1 General Techniques

^{1}H and ^{13}C NMR spectra were recorded in chloroform-*d* ($CDCl_3$, 0.05% TMS, Aldrich) on a Bruker AC-250 MHz NMR spectrometer operating at 250.13 and 62.9 MHz respectively. Chemical shifts are presented in parts per million (ppm) (±0.01 ppm) and are calculated relative to TMS (tetramethylsilane) given a reference value of δ 0.00 ppm in the case of ^{1}H NMR spectroscopy. Coupling constants (*J*) are reported in hertz (Hz). The reference point for ^{13}C NMR spectra was the central line of $CDCl_3$ (δ 77.23). When necessary, higher resolution spectra were acquired from a Bruker AMX-400 MHz operated by Mike Lumsden from the Atlantic Region Magnetic Resonance Centre at Dalhousie University. Low resolution mass spectroscopic data was attained from a Perkin Elmer Autosystem XL GC coupled to a TurboMass Spectrometer. Accurate mass measurements were performed by Bob Whitehead and Michael Potvin

(Dalhousie Mass Spectrometry Laboratory) using a CEC 21-110B mass spectrometer operated at a mass resolution of 8000 (10% valley) by computer controlled peak matching to appropriate PFK reference ions. Spectra were obtained using electron ionization at 70 volts and at a source temperature of 140 °C, with samples being introduced by means of a heatable quartz probe. Mass measurements were routinely within 3 ppm of the expected value. ESI/MS measurements were carried out by Michael Potvin using a Thermoquest LCQ ion trap instrument. Samples were infused in AcN at 40 µl/min (cap: voltage 4.5 kV at 200 °C) with trace levels of additives such as formic acid and sodium acetate. New compounds were subjected to additional characterization techniques. Melting points were determined with a Fisher-Johns melting point apparatus and are uncorrected. All UV/Vis absorption measurements were carried out on a Cary 100 Bio spectrophotometer (Varian).

Synthetic reactions were routinely monitored on a Perkin Elmer Autosystem Gas Chromatograph with a DB5 15-meter column. Parameter settings were as follows: injector temperature = 240 °C, T_1 = 60 °C (1 min.), T_2 = 240 °C (10 min.), ramp rate = 20 °C/min. Thin layer chromatography (TLC) was performed on 0.25 mm thick Whatman G/UV silica gel plates. Components were purified on silica gel 60 (70-230 mesh ASTM, 0.063-0.2 mm particle size) from Aldrich by flash column chromatography. Different ratios of crude hexanes and ethyl acetate were used as eluents. All organic extracts were dried with anhydrous $MgSO_4$.

4.3.2 Other Materials

4.3.2.1 Solvents

Solvents employed for LFP experiments included acetonitrile and methanol which were of spectroscopic grade supplied by OmniSolv, BDH. High grade 1,1,1,3,3,3-hexafluoro*iso*propanol and 2,2,2-trifluoroethanol were also used in LFP

experiments. Water used was singly distilled prior to use. Other solvents employed in synthetic procedures (diethylether, dichloromethane, hexanes, ethanol (95% and 98.5%), ethyl acetate and chloroform were commercially available and not subjected to additional purification prior to use unless otherwise specified.

4.3.2.2 Organic Reagents

Laboratory grade reagents required for synthesis were purchased from Aldrich and generally employed as received. These included sodium carbonate, sodium bicarbonate, magnesium sulfate, sodium chloride, formaldehyde, manganese chloride tetrahydrate, potassium carbonate, 4-chlorophenylacetic acid, 4-tolylacetic acid, *para*-substituted phenylacetones, tetrabutylammonium bromide (99%), diethylchlorophosphate, sulfuric acid (95-98% w/w). Exceptions include methanesulfonyl chloride that was distilled under reduced pressure. Pyridine was dried with calcium hydride by reflux for 24 hours and purified by distilling over 3 Å molecular sieves. 1,3-diphenyl-2-propanone was purified by multiple precipitations from dry ice-cooled diethylether, or recrystallized from ethanol/water. Hydrochloric acid (36.5-38% w/w) and perchloric acid (70% w/w) were acquired from Fisher Scientific Company. 4-Chlorophenyl acetone was purchased from Oakwood Products Incorporated.

4.3.3 Synthetic Procedures and Characterization Data

Depending on the commercial availability of the starting materials, precursors studied by LFP were synthesized in two to four steps as briefly outlined in Schemes 4-1 and 4-2. Substantial difficulties were encountered in both synthetic approaches as the alcohols (step A) and diols (step F) generated are prone to rapid dehydration to yield alkene products that are stabilized by extensive conjugation. This side reaction caused steps A and F to become the bottleneck for all of the syntheses carried out and in most

cases, limited the yield for alcohol and diol formation to less than 20%. This was despite numerous attempts to change the reaction conditions. Furthermore, upscaling the reaction proved unsuccessful and consequently, 1-1.5 g of starting material was reacted at any one time. As can be expected, the dibenzylketone derivatives were particularly difficult to isolate in good yield due to the double possibility of dehydration. Limiting the addition to only one benzylic site did not prove to be any more straightforward and in fact, the diols and dimesylate products were found to be more easily isolated and purified due to greater differences in polarity with the byproducts generated. Therefore, prior to carrying the laser work presented in this chapter, a substantial amount of time was invested in the synthesis of the mesylate precursors investigated. All compounds were purified such that all traces of alkene by-products were removed. Even small quantities of alkenes left in the sample could interfere with the laser flash experiments due to their strong absorption coefficients.

Scheme 4-1

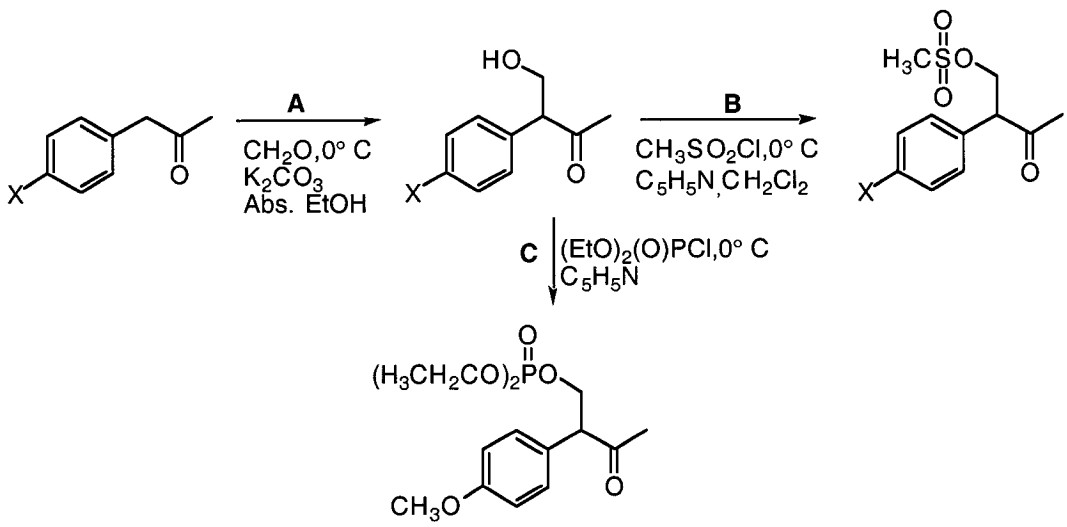

Scheme 4-2

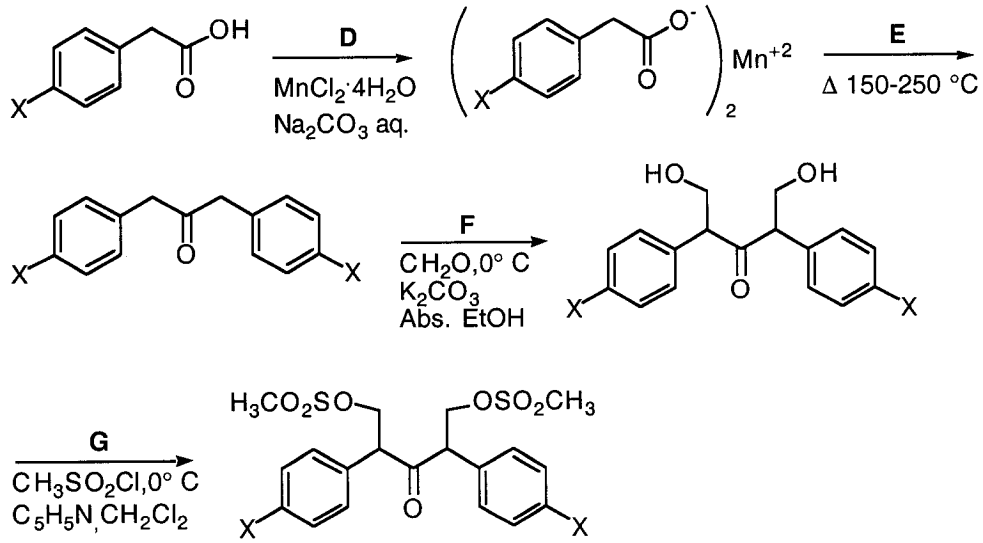

4.3.3.1 ^{1}H NMR Analysis

The precursor compounds synthesized have complex ^{1}H NMR spectra due to their chirality and consequently, the presence of diastereotopic hydrogen atoms. Figure 4-4 provides an exemplary ^{1}H NMR spectrum of 3-(4-fluorophenyl)-4-hydroxy-2-butanone **1(F)**, whose structure is shown below

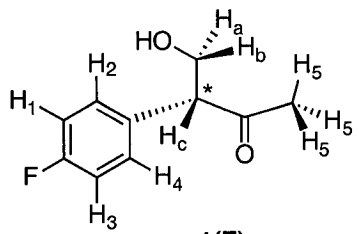

1(F)

* R or S enantiomer

Phenylacetone derivatives such as **1(F)** possess one chiral centre, leading to the possibility of (R) and (S) enantiomers. None of the enantiomeric mixtures produced during synthesis were resolved prior to experimentation since the results were not significantly influenced by the chirality of the precursor compounds. Enantiomers cannot

be discerned in NMR spectra due to the achiral medium, thus spectra such as the one shown in Figure 4-4 are not complicated by the mixture of (R) and (S) enantiomers. The AA'BB' pattern labeled as **1** on the spectrum corresponds of course to the four aromatic protons, H_1, H_2, H_3, and H_4 whose coupling pattern is further complicated by the presence of a fluorine atom on the ring. Singlet **2** at δ 2.07 is generated by the three hydrogens H_5 on the carbon atom that is adjacent to the carbonyl group. Less straightforward are the three multiplets **3** seen within the range of 3.62 and 4.13 that represent an ABC-type pattern generated by hydrogens H_a, H_b and H_c. Due to the influence of the chiral centre (identified by *), H_a and H_b are non-equivalent and the substitution test establishes that they are diastereotopic atoms, as shown in Scheme 4-3.

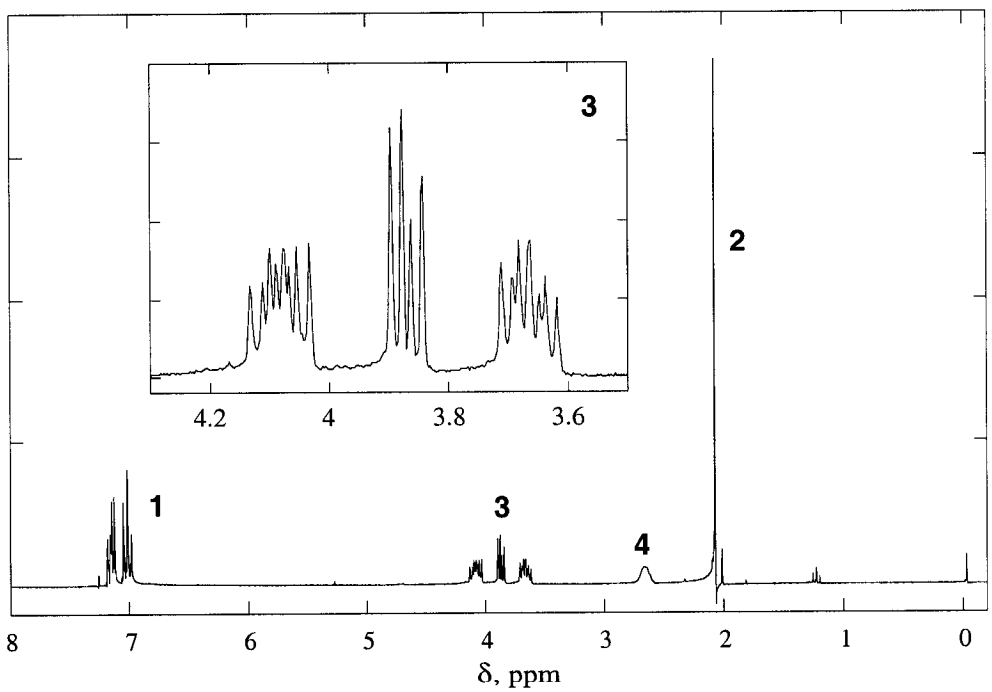

Figure 4-4. 250 MHz ^{1}H NMR spectrum of 3-(4-fluorophenyl)-4-hydroxy-2-butanone in $CDCl_3$. Inset shows close-up of ABCX splitting pattern.

Scheme 4-3

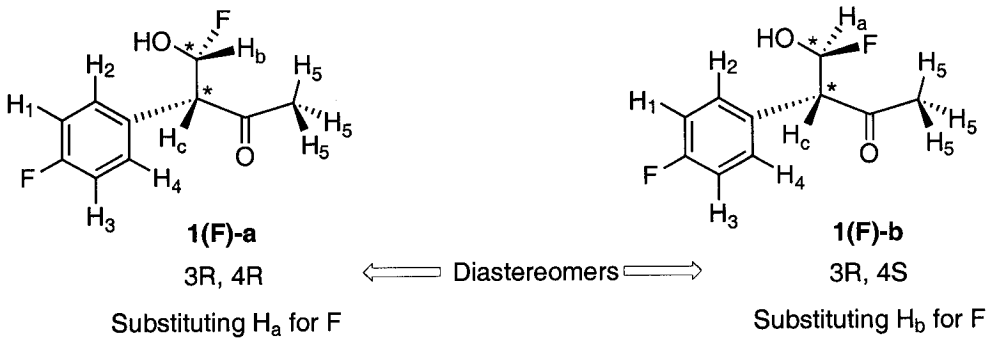

The chemical shifts of H_a and H_b will therefore differ significantly and the atoms, as expected, split each other into doublets. The spectrum becomes further complicated by the coupling of the adjacent proton H_c with H_a and H_b that should result in an ABC second order pattern. However, the spectrum shown in Figure 4-4 reveals a more complicated pattern that results from internal hydrogen bonding between the hydroxylic hydrogen and the carbonyl oxygen, as shown in **1(F)-c**. The restriction to rotation prevents an averaging of the different conformations and leads to an ABCX splitting pattern.

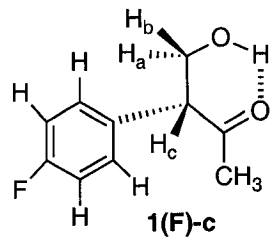

The broad peak labeled as **4** in the spectrum is assigned to the exchangeable proton of the hydroxyl group. Interestingly, spectra acquired for the other alcohols and diols show coupling of the OH group with H_a and H_b to clearly generate, in some cases, a double of doublets. This provides support for the notion that internal hydrogen bonding is taking place.

Precursor compounds synthesized from DBK and its derivatives showed more complicated spectra, as expected due to the presence of a second chiral centre on the molecule, Scheme 4-4. In cases where the diastereomers were not separated by the purification methods used, the resulting mixture complicates the NMR analysis due to differences in chemical shifts exhibited by each diastereomer. As in the case of 2,4-bis(4-methylphenyl)-3-oxopentyl-1,5-dimethylsulfonate, two separate sets of peaks were observed for each diastereomer. In light of the complexity of the ABC(X) patterns observed for the precursor compounds synthesized, in addition to the added interference of diastereomeric mixtures, the coupling constants for these multiplets were not calculated.

Scheme 4-4

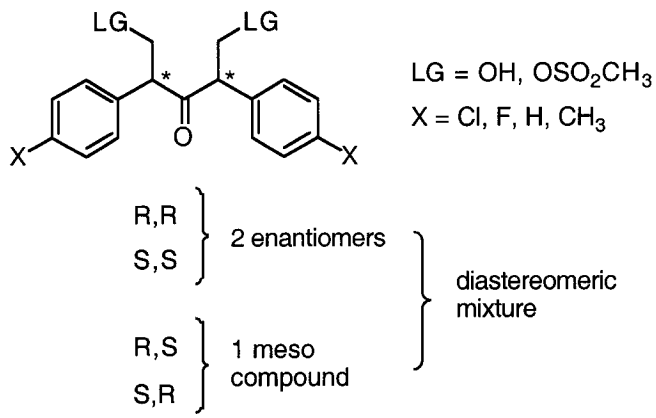

4.3.3.2 *Para*-Substituted Dibenzylketones

All *para*-substituted dibenzylketones were synthesized using the following general procedure and the steps correspond to Scheme 4-2. The appropriate *para*-substituted phenylethanoic acid (0.13 mol) was dissolved in aqueous Na_2CO_3 (0.18 mol) then slowly added to an aqueous solution of $MnCl_2 \cdot 4H_20$ (7.6 M), step D. The pale pink manganese salt, which immediately precipitated out of solution, was

isolated *via* suction filtration and left to dry *in vacuo* at 60 °C overnight. In step E, the dried product was pyrolyzed in a 100 mL round-bottom flask appropriately connected up for vacuum distillation. Using a heating mantle, the flask contents were heated to between 150-250 °C (depending on the starting ketone), along with the rest of the distillation apparatus with the use of a heating tape. The 1,3-bis(*para*-substituted phenyl)-2-propanone was distilled over but solidified rapidly as a yellow solid in the receiving flask left unheated. A heating gun was employed occasionally to prevent the distillate from crystallizing in the lower end of the distillation head. Purification was easily carried out by hot recrystallization with 95% ethanol to yield white crystals. Yields ranged from 60-70%.

1,3-Bis(4-methylphenyl)-2-propanone

CAN [70769-70-9]; mp 51-52 °C; colourless plates; ^{1}H NMR δ 2.31 (6H, s), 3.64 (4H, s), 7.00-7.12 (8H, AA'BB' system); ^{13}C NMR δ 21.08, 48.57, 129.40, 131.04, 136.60, 206.12; EIMS m/z (%) 238.1 ($M^{\bullet+}$, 45.39), 132.0 (11.84), 105.1 (100.0), 93.3 (4.85); HRMS: found 238.1360 (± 0.0008) u, calculated 238.1358 u for $C_{17}H_{18}O$. GC and GC/MS analysis revealed ≥ 99% purity. Melting point and NMR (^{1}H and ^{13}C) spectral data match those previously reported; 58% yield.[163]

1,3-Bis(4-chlorophenyl)-2-propanone

CAN [65622-34-6]; colorless plates; mp 94.5-95.5 °C; ^{1}H NMR δ 3.70 (4H, s), 7.04-7.30 (8H, AA'BB' system); ^{13}C NMR δ 48.4, 128.9, 130.8, 132.1, 133.2, 204.5; EIMS m/z (%) 282 ($M^{\bullet+}$ [^{37}Cl × 2], 0.63), 280 ($M^{\bullet+}$ [^{37}Cl + ^{35}Cl], 3.69), 278 ($M^{\bullet+}$[^{35}Cl × 2], 5.81), 153 (16), 127 (55), 125 (100), 90 (13), 89 (35); HRMS: found 278.0260 (± 0.0008) u, calculated 278.0265 u for $C_{15}H_{12}Cl_2O$. GC and GC/MS analysis revealed ≥ 99% purity. Melting point and NMR (^{1}H and ^{13}C) spectral data match those previously

reported; 70% yield.[164]

4.3.3.3 Alcohol and Diol Derivatives

The following synthetic procedure refers to steps A and F in Schemes 4-1 and 4-2 respectively. Potassium carbonate (0.1 g) was dissolved in 50 mL of absolute ethanol and the solution left to cool to 0 °C in an ice bath. The dibenzylketone (R = H, 4-CH_3, 4-Cl, or 4-F) or substituted phenylacetone (R = 4-OCH_3, 4-Cl or 4-F) was subsequently added (4.5 mmol) and the mixture left to stir for a further 30 minutes. Using a pressure equalized funnel, formaldehyde (3 molar equivalent per OH-group) further diluted in absolute ethanol (5 ml) was added dropwise with continuous stirring. The reaction progress was monitored by gas chromatography and TLC using ethyl acetate/hexanes solvent mixtures. Reaction times ranged between 1-4 hours. The reaction was quenched by adding cold brine (20 ml) which was extracted three to four times with diethyl ether (30 ml). The organic fractions were collected, combined and dried with magnesium sulfate and the ether removed under reduced pressure. The crude product mixture was purified by flash column chromatography using ethyl acetate/hexanes mixtures, or by several cold recrystallizations again in ethyl acetate/hexanes mixtures at 0 °C. Oily products were stored in the dark at ~ 0 °C.

3-(4-Fluorophenyl)-4-hydroxy-2-butanone

Pale yellow oil, enantiomeric mixture; ^{1}H NMR δ 2.07 (1H, s), 2.66 (1H, broad peak), 3.62-3.71 (1H, m), 3.84-3.96 (1H, m), 4.03-4.13 (1H, m), 7.01-7.19 (4H, AA'BB' pattern); ^{13}C NMR δ 29.61, 60.68, 63.94, 116.01, 116.36, 130.14, 130.28, 131.41, 131.47, 162.46 (d, J = 248.0 Hz), 209.00; UV (CH_3CN) λ_{max} (nm) 264 (1.80), 270 (1.61); EIMS m/z (%) 182 ($M^{\bullet+}$, 0.6), 139 (3), 123 (6), 122 (100), 121 (4), 109 (7), 42 (20); HRMS: found 182.0742 (± 0.0008) u, calculated 182.0743 u for $C_{10}H_{11}FO_2$.

3-(4-Methoxyphenyl)-4-hydroxy-2-butanone

Fine white powder, enantiomeric mixture; mp 50-51 °C; ^{1}H NMR δ 2.08 (3H, s), 2.32 (1H, dd, J = 5.50, 7.93 Hz), 3.62-3.72 (1H, m), 3.79 (3H, s), 3.80-3.86 (1H, m), 4.05-4.15 (1H, m), 6.86-7.13 (4H, AA'BB' system); ^{13}C NMR δ 29.53, 55.42, 60.83, 64.18, 114.75, 127.62, 129.74, 159.40, 209.67; UV (CH_3CN) λ_{max} (nm) 277 (1.53), shoulder at 283 (1.33); EIMS m/z (%) 194 ($M^{\bullet+}$, 16), 151 (86), 134 (79), 133 (72), 121 (100), 119 (36), 91 (91), 77 (45); HRMS: found 194.0945 (± 0.0008) u, calculated 194.0943 u for $C_{11}H_{14}O_3$.

2,4-Bis(4-chlorophenyl)-1,5-dihydroxy-3-pentanone

White solid; mp 148-150 °C; ^{1}H NMR δ 2.01-2.06 (2H, m), 3.62-3.71 (2H, m), 3.80-3.85 (2H, m), 4.02-4.16 (2H, m), 7.04-7.36 (8H, AA'BB' system); ^{13}C NMR δ 58.6, 63.8, 129.7, 130.2, 133.4, 134.3, 209.8; UV (CH_3CN) λ_{max} (nm) 267 (0.45), 296 (0.28), shoulder at 275 (0.37); EIMS m/z (%) 338 ($M^{\bullet+}$ [^{35}Cl × 2], 0.6), 155 (43), 140 (18), 138 (100), 125 (17), 35 (16); HRMS: found 338.0482 (± 0.0008) u, calculated 338.0476 u for $C_{17}H_{16}O_3Cl_2$.

2,4-Bis(4-methylphenyl)-1,5-dihydroxy-3-pentanone

Fine colorless needles, diastereomeric mixture; mp 92-93 °C; ^{1}H NMR δ 1.99 (1H, dd, J = 6.10, 7.63 Hz), 2.11 (1H, dd, J_1= 6.1 Hz, J_2 = not resolved), 2.28 and 2.35 (6H, s), 3.59-4.20 (6H, m), 6.82-7.19 (8H, two sets of AA'BB' patterns); ^{13}C NMR δ 21.10, 58.56, 60.99, 63.86, 64.97, 128.72, 129.33, 130.11, 131.89, 137.29, 211.11, 211.78; UV (CH_3CN) λ_{max} (nm) 264 (0.76), 272 (0.66), 292 (0.40); EIMS m/z (%) 298 ($M^{\bullet+}$, 52), 268 (100), 135 (39), 118 (62), 117 (17); HRMS: found 298.1561 (± 0.0008) u, calculated 298.1569 u for $C_{19}H_{22}O_3$.

2,4-Diphenyl-1,5-dihydroxy-3-pentanone

Colorless needles, diastereomeric mixture; mp 85-86 °C; ^{1}H NMR δ 3.66-3.75 (4H, m), 4.09-4.31 (4H, m), 6.91-7.13 (10H, m); ^{13}C NMR δ 61.70, 64.73, 127.48, 128.57, 128.76, 129.33, 129.60, 134.94, 211.28; UV (CH_3CN) λ_{max} (nm) 259 (0.13), 297 (0.10); EIMS m/z (%) 270.1 ($M^{\bullet+}$, 0.20), 240 (10), 121 (52), 105 (5), 104 (100), 103 (27), 91 (10); HRMS: found 270.1264 (± 0.0008) u, calculated 270.1256 u for $C_{17}H_{18}O_3$.

4.3.3.4 Mesylate Derivatives

While the alcohols themselves were difficult to synthesize in good yields, the alkylsulfonates were prepared from the corresponding alcohols in a relatively straightforward synthesis. However, the reactive nature of these primary sulfonate esters requires special precautions to prevent thermal and chemical decomposition through elimination to generate the alkene. The following general procedure refers to step B and G in Schemes 4-1 and 4-2, respectively.

The alcohol (2.5 mmol) was dissolved in a mixture of pyridine (25 mmol) and CH_2Cl_2 (3.5 mL). When cooled to 0 °C, methanesulfonyl chloride (10 mmol) diluted in CH_2Cl_2 (2 ml) was added dropwise to the reaction mixture with continuous stirring. Progress was monitored by NMR and reaction times ranged between 2.5-6.5 hours. The reaction was quenched with ice water and the mesylate product extracted with CH_2Cl_2. The organic layer was washed twice with 5% aqueous H_2SO_4, twice with saturated aqueous $NaHCO_3$, and twice with ice water. The organic fractions were combined and dried with $MgSO_4$, and the solvent evaporated under vacuum. The crude product was purified using flash column chromatography on silica gel and eluted with ethyl acetate/hexanes solvent mixtures. Alternatively, repetitive cold recrystallizations in ethyl acetate/hexanes mixtures were carried out to purify crystalline mesylate products. Dimesylates were synthesized similarly using the corresponding diols in a

1:8:20 molar ratio of diol/methanesulfonylchloride/pyridine. All compounds were stored in the dark at 0 °C.

2,4-Bis(4-methylphenyl)-3-oxopentyl-1,5-dimethylsulfonate

White powder, diastereomeric mixture; mp 91-92 °C; ^{1}H NMR δ 2.25 and 2.36 (6H, two singlets with ratio 4:21), 2.82 and 2.99 (6H, two singlets, 4:21), 4.00-4.29 (4H, m), 4.64-4.80 (2H, m), 6.76-6.95 and 7.03-7.22 (8H, two AA'BB' patterns with ratio 4:21); ^{13}C NMR δ 21.28, 37.24, 55.09, 68.81, 128.58, 128.74, 129.44, 129.66, 130.53, 139.11, 203.15; UV (CH_3CN) λ_{max} (nm) 264 (0.31), 293 (0.19); EIMS m/z (%) $M^{\bullet+}$ not observed, 270 (13), 262 (100), 233 (27), 219 (54), 118 (34), 117 (42), 115 (50), 105 (27), 91 (34), 77 (26); ESI$^+$/MS $(M+Na)^+$ m/z 477.1018 calculated, 476.9 measured with added Na^+.

2,4-Diphenyl-3-oxopentyl-1,5-dimethylsulfonate

Fine white crystals, diastereomeric mixture; mp 114-116 °C; ^{1}H NMR δ 2.99 (6H, s), 4.23-4.33 (4H, m), 4.73-4.82 (2H, m), 6.88-7.14 (10H, m); ^{13}C NMR δ 37.42, 57.91, 69.58, 128.42, 128.65, 128.98, 132.40, 205.13; UV (CH_3CN) λ_{max} (nm) 253 (0.38), 293 (0.19); EIMS m/z (%) $M^{\bullet+}$ not observed, 234 (29), 105 (10), 104 (100), 103 (75), 91 (13), 77 (30), 50 (15); ESI$^+$/MS $(M+K)^+$ m/z 465.0444 calculated, 464.9 measured with added K^+.

2-(4-Chlorophenyl)-3-oxobutylmethanesulfonate

Clear oil, enantiomeric mixture; ^{1}H NMR δ 2.14 (3H, s), 2.98 (3H, s), 4.10-4.16 (1H, m), 4.24-4.76 (1H, m), 4.69-4.76 (1H, m), 7.15-7.38 (4H, AA'BB' pattern); ^{13}C NMR δ 29.48, 37.24, 57.25, 69.17, 129.77, 129.86, 132.02, 134.82, 204.55; UV (CH_3CN) λ_{max} (nm) 267; EIMS m/z (%)$M^{\bullet+}$ not observed, 169 (6), 90 (42), 89 (99), 63 (100);

ESI+/MS (M+H with loss of $^{35}Cl)^+$ m/z 242.0613 calculated, 242.3 measured.

2-(4-Methoxyphenyl)-3-oxobutylmethanesulfonate

Clear oil, enantiomeric mixture; ^1H NMR δ 2.12 (3H, s), 2.97 (3H, s), 3.80 (3H, s), 4.06-4.12 (1H, m), 4.21-4.28 (1H, m), 4.68-4.76 (1H, m), 6.88-7.15 (4H, AA'BB' pattern); ^{13}C NMR δ 29.30, 37.12, 55.39, 57.02, 69.63, 114.88, 125.30, 129.61, 159.80, 205.24; UV (CH_3CN) λ_{max} (nm) 276 (0.3), with shoulder at 282 (0.3); EIMS m/z (%) $M^{\bullet+}$ not observed, 150 (61), 135 (43), 134 (100), 133 (75), 121 (95), 119 (48), 79 (27), 77 (42); ESI^+/MS $(M+Na)^+$ m/z 295.0616 calculated, 295.3 measured with added Na^+; ESI+/MS/MS $(M+Na)^+$ m/z 295.0616 calculated, 294.9 measured with added Na^+, ($M^{\bullet+}$ with loss of OSO_2CH_3) m/z 178.0994 calculated, 177.7 measured with added Na^+.

2-(4-Fluorophenyl)-3-oxobutylmethanesulfonate

Clear yellow oil, enantiomeric mixture; ^1H NMR δ 2.14 (3H, s), 2.98 (3H, s), 4.12-4.31 (2H, m), 4.70-4.78 (1H, m), 7.03-7.26 (4H, AA'BB' pattern); ^{13}C NMR δ 29.27, 36.99, 56.86, 69.33, 116.23, 116.57, 129.36, 129.41, 130.14, 130.27, 162.65 (d, J = 248 Hz), 204.81; UV (CH_3CN) λ_{max} (nm) 263 (0.54), 269 (0.47); EIMS m/z (%) 165 (1), 123 (19), 122 (100), 121 (17), 109 (11), 101 (9), 42 (50); HRMS: found 165.0709 (± 0.0008) u, calculated 165.0716 u for $C_{10}H_{10}OF$; ESI^+/MS, $(M+H)^+$ m/z 261.0597 calculated, 260.8 measured.

2,4-Bis(4-fluorophenyl)-3-oxobutylmethanesulfonate

Yellow oil, enantiomeric mixture; ^1H NMR δ 2.92 (3H, s), 3.67 (2H, s), 4.21-4.69 (3H, m), 6.98-7.15 (8H, AA'BB' pattern); ^{13}C NMR δ 37.10, 47.96, 52.54, 69.28, 115.43, 115.77, 116.37, 131.17, 160.83, 164.00, 164.77, 204.32.

4.3.3.5 Phosphate Derivative

Synthesis of 2-(4-Methoxyphenyl)-3-oxobutyldiethylphosphate: In a 3-necked 50 ml round bottom flask, 6.72 mmol (1.3 g) of the alcohol was added to 13.45 mmol of dried and distilled pyridine (1.10 ml). With constant stirring, the mixture was allowed to equilibrate to 0° C by placing the flask in an ice bath. Using a pressure equalized funnel, 6.72 mmol (~ 1 ml) of diethylchlorophosphate was added dropwise to the mixture. The reaction is exothermic hence slow addition is desired so as to maintain the reaction temperature < 5 °C. The reaction's progress was monitored using GC and NMR. The reaction mixture was stirred continuously for 1.5 hours, then quenched by extracting the product first with ice water and then twice with diethyl ether. The organic fraction was washed twice with 10% HCl_{aq}, 5% aqueous $NaHCO_3$, brine and ice water successively. The organic layer was dried with magnesium sulfate and the solvent evaporated under *vacuo*. The product was a light, yellow oil that was isolated in 50% yield. Note: the compound must be stored under cold conditions and seems to be less susceptible to decomposition if diluted in CH_2Cl_2. The product decomposes during column chromatography and hence was purified with repetitive cold recrystallizations in ethyl acetate/hexanes mixtures at 0 °C.

2-(4-Methoxyphenyl)-3-oxobutyl diethylphosphate

Pale yellow clear oil, enantiomeric mixture; ^{1}H NMR δ 1.27-1.32 (6H, m), 2.11 (3H, s), 3.78 (3H, s), 4.03-4.10 (6H, m), 4.55-5.31 (1H, m), 6.87-7.17 (4H, AA'BB' pattern); ^{13}C NMR δ 15.75 and 15.86 (d), 29.06, 54.97, 57.81 and 57.93 (d), 63.45 and 63.54 (d), 66.97 and 67.05 (d), 114.31, 126.12, 129.30, 159.24, 205.36; UV (CH_3CN) λ_{max} (nm) 276 (1.3), shoulder at 282 (1.15); EIMS m/z (%) $M^{\bullet+}$ not observed, 176 (29), 134 (9), 133 (100), 90 (13), 89 (17), 77 (9), 63 (10); ESI^+/MS, $(M+H)^+$ m/z 331.1310 calculated,

330.9 measured, ($M^{\bullet+}$ with loss of -OP(O)(OCH_2CH_3)$_2$) m/z 177.0916 calculated, 177.2 measured, $(M+Na)^+$ m/z 353.1130 calculated, 353.4 measured with added Na^+.

APPENDIX

Table A1. Physical properties, ionizing power and nucleophilicity of solvents used in this study.

Solvent	μ/D	ε	pK_a in water	Y_{Oms} [c]	Y_{Ots} [e]	N_{Ots} [e]
HFIP Dipolar protic	2.05[a]	16.7[a]	9.30[a]	3.72[d]	3.82	-
TFE Dipolar protic	2.03[a]	26.7[a]	12.37[a]	1.90	1.77	-3.07
Acetonitrile Dipolar aprotic	3.44[b]	37.5[b]	28.9[g]	-	-3.21	-
Water Dipolar protic	1.84[b]	78.5[b]	15.7[b]	-	4.1	-0.44
Methanol Dipolar protic	2.87[b]	32.7[b]	15.5[f]	-1.17	-0.92	-0.04

[a]ref.165, and references 6 and 42 therein.

[b]ref. 131 and references therein

[c]ref. Y_{OMs} values based on solvolysis of 2-adamantyl mesylate; data from ref. 136 and references therein.

[d]97% HFIP (%w/w water)

[e]ref. 166 and reference (23) therein.

[f] ref. 160

g ref. 167

Table A2. Observed rate constants for the ionization of the β-methanesulfonate-4-R-phenethyl radical in various nitrogen-saturated HFIP/TFE mixtures.

%HFIP in TFE	R = 4-Me $k_{het}/10^7$ s^{-1}	R = 4-F $k_{het}/10^7$ s^{-1}	R = H $k_{het}/10^7$ s^{-1}	R = 4-Cl $k_{het}/10^7$ s^{-1}
100	5.7	1.0	0.75	0.30
90	4.9	0.81	0.53	0.22
80	4.2	0.55	0.37	0.17
70	3.6	0.40	0.30	0.13
60	3.1	0.32	0.27	0.10
50	2.4	0.29	0.26	0.09
40	1.6	0.25	-	-
30	1.1	-	-	-
20	0.74	-	-	-
10	0.57	-	-	-
0	0.41	-	-	-

Table A3. Slopes (ρ^+) of the Hammett plots established with the ionization rate constants of β-methane-sulfonate-4-R-phenethyl radicals (R = Me, F, H, Cl) as a function of the σ^+ parameter in various HFIP/TFE mixtures.

%HFIP in Co-Solvent	ρ^+
100% in TFE	-3.02±0.04
90% in TFE	-3.19±0.07
80% in TFE	-3.32±0.16
70% in TFE	-3.41±0.27
60% in TFE	-3.49±0.29
95% AcN	-3.13±0.15
90% AcN	-3.68±0.12

Table A4. Observed rate constants for the ionization of the β-methanesulfonate-4-R-phenethyl radical in various nitrogen-saturated HFIP/AcN mixtures.

%HFIP in AcN	R = 4-OMe $k_{het}/10^7\ s^{-1}$	R = 4-Me $k_{het}/10^7\ s^{-1}$	R = 4-F $k_{het}/10^7\ s^{-1}$	R = H $k_{het}/10^7\ s^{-1}$	R = 4-Cl $k_{het}/10^7\ s^{-1}$
100	too fast	5.5	1.1	0.63	-
99.0	-	-	-	-	0.32
98.3	-	-	-	-	0.31
98.0	-	-	-	0.58	-
97.7	-	-	-	-	0.29
97.5	-	-	0.91	-	-
97.0	-	-	-	-	0.28
96.3	-	-	-	-	0.26
95.7	-	-	-	-	0.26
95.1	-	-	-	-	0.24
95.0	-	4.8	0.74	0.49	-
94.4	-	-	-	-	0.23
93.0	-	-	-	0.39	-
92.5	-	-	0.68	-	-
90.0	-	3.9	0.56	0.28	-
88.0	-	-	0.44	-	-
85.0	-	2.2	0.34	-	-
82.5	-	-	0.30	-	-
80.0	-	1.0	-	-	-
70.0	5.7	0.22	-	-	-
67.5	4.6	-	-	-	-
65.0	3.3	-	-	-	-
60.0	2.3	-	-	-	-
55.0	1.4	-	-	-	-
50.0	0.91	-	-	-	-
40.0	0.44	-	-	-	-
30.0	0.28	-	-	-	-
20.0	0.15	-	-	-	-
10.0	0.090	-	-	-	-

Table A5. Observed rate constants for the growth of the 4-methoxystyrene radical cation by heterolysis of the β-methanesulfonate-4-methoxyphenethyl radical in various solvent mixtures.

% Co-Solvent A in Solvent B	A: Water B: Methanol $k_{het}/10^7$ s^{-1}	A: TFE B: AcN $k_{het}/10^7$ s^{-1}	A: Water B: AcN $k_{het}/10^7$ s^{-1}
100	-	6.7	-
90.0	-	4.4	-
80.0	-	2.7	6.5
70.0	-	1.2	4.6
67.5	-	-	-
65.0	-	-	-
60.0	-	0.80	2.7
55.0	-	-	-
50.0	5.1	0.45	1.6
40.0	3.7	0.27	0.88
30.0	2.3	0.19	0.57
20.0	1.4	0.11	0.34
10.0	0.89	0.076	0.19

Table A6. Observed rate constants for the growth of the 4-methoxystyrene radical cation upon ionization of the β-X-4-methoxyphenethyl radical in methanol/water mixtures.

% Water in Methanol	Y_{Cl} values[a]	Y_{Br} values[a]	Y_{OMs} values[a]	X = Cl[b] $k_{het}/10^7$ s^{-1}	X = Br[b] $k_{het}/10^7$ s^{-1}	X = OSO_2CH_3 $k_{het}/10^7$ s^{-1}
10	-0.200	-0.140	-0.300	-	0.21	0.89
20	0.670	0.700	0.390	-	0.41	1.4
30	1.460	1.420	0.980	0.13	1.1	2.3
40	2.070	2.040	1.540	0.22	2.0	3.7
50	2.700	2.610	2.050	0.57	3.2	5.1
60	3.250	3.140	2.500	1.2	-	-
70	3.730	3.610	2.950	2.3	-	-

a Y-values taken from ref. 136

b Rate constant taken from ref. 83

REFERENCES

1) Stubbe, J. *Biochemistry* 1988, *27*, 3893-3900.

2) Stubbe, J. *Annu. Rev. Biochem.* 1989, *58*, 257-285.

3) Frey, P. A. *Chem. Rev.* 1990, *90*, 1343-1357.

4) Stubbe, J.; van der Donk, W. A. *Chem. Rev.* 1998, *98*, 705-762.

5) Fontecave, M. *CMLS Cell. Mol. Life Sci.* 1998, *54*, 684-695.

6) Retey, J. *Stereochemistry*; Elsevier: Amsterday, 1982; Vol. 3.

7) Golding, B. T.; Dolphin, D., Ed.; Wiley Interscience: New York, 1982; Vol. 1, pp Chap. 15.

8) Finke, R. G.; Schiraldi, D. A.; Mayer, B. J. *Coord. Chem. Rev.* 1984, *54*, 1-22.

9) Halpern, H. *Science* 1985, *227*, 869.

10) George, P.; Siegbahn, P. E. M.; Glusker, J. P.; Bock, C. W. *J. Phys. Chem. B* 1999, *103*, 7531-7541.

11) Smith, D. M.; Golding, B. T.; Radom, L. *J. Am. Chem. Soc.* 2001, *123*, 1664-1675.

12) Warncke, K.; Schmidt, J. C.; Ke, S.-C. *J. Am. Chem. Soc.* 1999, *121*, 10522-10528.

13) Stubbe, J. *J. Biol. Chem.* 1990, *265*, 5329-5332.

14) Stubbe, J.; van der Donk, W. A. *Chem. Biol.* 1995, *2*, 793-801.

15) Sjöberg, B.-M. *Nucleic Acids and Molecular Biology*; Springer: Berlin, 1995; Vol. 9.

16) Siegbahn, P. E. M. *J. Am. Chem. Soc.* 1998, *120*, 8417-8429.

17) Lenz, R.; Giese, B. *J. Am. Chem. Soc.* 1997, *119*, 2784-2794.

18) Buckel, W.; Golding, B. T. *FEMS Microb. Rev.* 1998, *22*, 523-541.

19) Retey, J.; Suckling, C. J.; Arigoni, D.; Babior, B. M. *J. Biol. Chem. Soc.* 1974, *249*, 6359-6360.

20) Foster, T.; West, P. R. *Can. J. Chem.* 1974, *52*, 3589-3598.

21) Gerfen, G. J.; van der Donk, W. A.; Yu, G.; McCarthy, J. R.; Jarvi, E. T.; Matthews, D. P.; Farrar, C.; Griffin, R. G.; Stubbe, J. *J. Am. Chem. Soc.* 1998, *120*, 3823-3835.

22) Steenken, S. *Chem. Rev.* 1989, *89*, 503-520.

23) von Sonntag, C. *The Chemical Basis of Radiation Biology*; Taylor & Francis: New York, 1987.

24) Hecht, S. M. *Bionconjugate Chem.* 1994, *5*, 513-526.

25) Newcomb, M. *Book of Abstracts, 215th ACS National Meeting* 1998.

26) Mo, X.-S.; Crich, D. *Book of Abstracts, 216th ACS National Meeting* 1998.

27) Pogozelski, W. K.; Tullius, T. D. *Chem. Rev.* 1998, *98*, 1089-1107.

28) Crich, D.; Mo, X.-S. *Tetrehedron Lett.* 1997, *38*, 8169-8172.

29) Crich, D.; Mo, X.-S. *J. Am. Chem. Soc.* 1997, *119*, 249-250.

30) Glatthar, R.; Spichty, M.; Gugger, A.; Batra, R.; Damm, W.; Mohr, M.; Zipse, H.; Giese, B. *Tetrahedron* 2000, *56*, 4117-4128.

31) Hader, D.-P.; Tevini, M. *General Photobiology*; Pergamon Press: Toronto, 1987.

32) Kohen, E.; Santus, R.; Hirschberg, J. G. *Photobiology*; Academic Press: New York, 1995.

33) Stubbe, J.; Kozarich, J. W.; Wu, W.; Vanderwall, D. E. *Acc. Chem. Res.* 1996, *29*, 322-330.

34) Lazo, J. S.; Sebti, S. M. *Bleomycins*; Pinedo, H. M., Longo, D. L. and Chabner, B. A., Ed.; Elsevier Science Publishers, 1993; Vol. Annual 14, pp 37-44.

35) Hughes, E. D.; Ingold, D. K.; Patel, C. S. *J. Chem. Soc* 1933, 526-530.

36) Stang, P. J.; Hanack, M.; Subramanian, L. R. *Synthesis* 1982, *pt.1*, 85-126.

37) Noyce, D. S.; Virgilio, J. A. *J. Org. Chem.* 1972, *37*, 2643-2647.

38) Hughes, E. D.; Juliusburger, F.; Masterman, S.; Topley, B.; Weiss, J. *J. Chem. Soc.* 1935, 1525-1529.

39) Hughes, E. S.; Juliusburger, F.; Scott, A. D.; Topley, B.; Weiss, J. *J. Chem. Soc.* 1936, 1173-1175.

40) Cowdrey, W. A.; Hughes, E. D.; Nevell, T. P.; Wilson, C. L. *J. Chem. Soc.* 1938, 209-211.

41) Scaiano, J. C.; Barra, M.; Krzywinski, M.; Sinta, R.; Calabrese, G. *J. Am. Chem. Soc.* 1993, *115*, 8340-8344.

42) Zipse, H. *J. Am. Chem. Soc.* 1994, *116*, 10773-10774.

43) Zipse, H. *Acc. Chem. Res.* 1999, *32*, 571-578.

44) Zipse, H. *J. Chem. Soc., Perkin Trans. 2* 1997, *12*, 2691-2697.

45) Choi, S.-Y.; Crich, D.; Horner, J. H.; Huang, X.; Martinez, F. N.; Newcomb, M.; Wink, D. J.; Yao, Q. *J. Am. Chem. Soc.* 1998, *120*, 211-212.

46) Johnston, L. J.; Schepp, N. P. *J. Am. Chem. Soc.* 1993, *115*, 6564-6571.

47) Zipse, H. *Angew. Chem. Int. Ed. Engl.* 1994, *33*, 1985-1988.

48) Kornblum, N.; Michel, R. E.; Kerber, R. C. *J. Am. Chem. Soc.* 1966, *88*, 5660-5662.

49) Russell, G. A.; Danen, W. C. *J. Am. Chem. Soc.* 1966, *88*, 5663-5665.

50) Kornblum, N. *Angew. Chem. Int. Ed. Eng.* 1975, *14*, 734-745.
51) Bunnett, J. F. *Acc. Chem. Res.* 1978, *11*, 413-420.

52) Gilbert, B.; Norman, R. O. C.; Williams, P. S. *J. Chem. Soc., Perkin 2* 1980, 647-656.

53) Gilbert, B. C.; Norman, R. O. C.; Williams, P. S. *J. Chem. Soc. Perkin 2* 1981, 1401-1405.

54) Steenken, S.; Davies, M. J.; Gilbert, B. C. *J. Chem. Soc., Perkin Trans. 2* 1986, 1003-1010.

55) Gilbert, B. C.; Larkin, J. P.; Norman, R. O. C. *J. Chem. Soc., Perkin Trans. 2* 1972, 794-802.

56) Bansal, K. M.; Gratzel, M.; A., H.; Janata, E. *J. Phys. Chem.* 1973, *77*, 16-19.

57) von Sonntag, C. *Adv. Carbohydr. Chem. Biochem.* 1980, *37*, 7-77.

58) Gilbert, B. C.; King, D. M.; Thomas, C. B. *J. Chem. Soc., Perkin Trans. 2* 1983, 675-683.

59) Livingston, R.; Zeldes, H. *J. Am. Chem. Soc.* 1966, *88*, 4333-4336.

60) Buley, A. L.; Norman, R. O. C.; Pritchett, R. J. *J. Chem. Soc. (B)* 1966, 849-852.

61) von Sonntag, C.; Thoms, E. *Z. Naturforsch. B* 1970, *25*, 1405-1407.

62) Dobbs, A. J.; Gilbert, B. C.; Norman, R. O. C. *J. Chem. Soc., Perkin Trans. 2* 1972, 786-794.

63) Gilbert, B. C.; Norman, R. O. C.; Dobbs, A. J. *J. Mag. Resonance* 1973, *11*, 100-102.

64) Behrens, G.; Bothe, E.; Eibenberger, J.; Koltzenburg, G.; Schulte-Frohlinde, D. *Angew. Chem. Int. Ed. Engl.* 1978, *17*, 604-605.

65) Behrens, G.; Bothe, E.; Koltzenburg, G.; Schulte-Frohlinde, D. *J. Chem. Soc., Perkin Trans. 2* 1980, 883-889.

66) Behrens, G.; Koltzenberg, G.; Schulte-Frohlinde, D. *Z. Naturforsch. C* 1982, *37c*, 1205-1227.

67) Wilkinson, R. W.; Williams, T. F. *J. Chim. Phys.* 1955, *52*, 600-614.

68) von Sonntag, C.; Ansorge, G.; Sugimori, A.; Omori, T.; Koltzenburg, G.; Schulte-Frohlinde, D. *Z. Naturforsch. B* 1972, *27*, 471-472.

69) Scholes, G.; Taylor, W.; Weiss, J. *J. Chem. Soc.* 1957, 235-246.

70) Samuni, A.; Neta, P. *J. Phys. Chem.* 1973, *77*, 2425-2429.

71) Steenken, S.; Behrens, G.; Schulte-Frohlinde, D. *Int. J. Radiat. Biol.* 1974, *25*, 205-210.

72) Kochetkov, N. K.; Kudryashov, L. I.; Chlenov, M. A.; Grineva, L. P. *Zh. Obshch. Khim.* 1971, *41*, 2071-2076.

73) Stelter, L.; von Sonntag, C.; Schulte-Frohlinde, D. *Z. Naturforsch. B* 1975, *30*, 656-657.

74) Stelter, L.; von Sonntag, C.; Schulte-Frohlinde, D. *Int. J. Radiat. Biol.* 1976, *29*, 255-269.

75) Stelter, L.; von Sonntag, C.; Schulte-Frohlinde, D. *Int. J. Radiat. Biol.* 1974, *25*, 515-519.

76) Ward, J. F. *Israel J. Chem.* 1972, *10*, 1123-1138.

77) Ward, J. F.; Kuo, I. *Int. J. Radiat. Biol.* 1973, *23*, 543-557.

78) Dizdaroglu, M.; von Sonntag, C.; Schulte-Frohlinde, D. *J. Am. Chem. Soc.* 1975, *97*, 2277-2278.

79) Behrens, G.; Koltzenburg, G.; Ritter, A.; Schulte-Frohlinde, D. *Int. J. Radiat. Biol.* 1978, *33*, 163-171.

80) Koltzenburg, G.; Behrens, G.; Schulte-Frohlinde, D. *J. Am. Chem. Soc.* 1982, *104*, 7311-7312.

81) Laughton, P. M.; Robertson, R. E. *Can. J. Chem.* 1956, *34*, 1714-1718.

82) Koltzenburg, G.; Bastian, E.; Steenken, S. *Angew. Chem. Int. Ed. Engl.* 1988, *27*, 1066-1067.

83) Cozens, F. L.; O'Neill, M.; Bogdanova, R.; Schepp, N. *J. Am. Chem. Soc.* 1997, *119*, 10652-10659.

84) Horner, J. H.; Newcomb, M. *J. Am. Chem. Soc.* 2001, *123*, 4364-4365.

85) Horner, J. H.; Taxil, E.; Newcomb, M. *J. Am. Chem. Soc.* 2002, *124*, 5402-5410.

86) Peppard, P. F.; Mason, G. W.; Andrejasich, C. M. *Inorg. Nucl. Chem.* 1965, *27*, 697-709.

87) Newcomb, M.; Miranda, N.; Huang, X.; Crich, D. *J. Am. Chem. Soc.* 2000, *122*, 6128-6129.

88) Beckwith, A. L. J.; Duggan, P. J. *J. Chem. Soc., Perkin Trans. 2* 1993, *9*, 1673-1679.

89) Surzur, J.-M.; Teissier, P. *C. R. Acad. Sci., Ser. C.* 1967, *264*, 1981-1984.

90) Surzur, J.-M.; Teissier, P. *Bull. Soc. Chim. Fr.* 1970, *8-9*, 3060-3070.

91) Beckwith, A. L. J.; Thomas, C. B. *J. Chem. Soc., Perkin Trans. 2* 1973, *6*, 861-872.

92) Barclay, L. R. C.; Griller, D.; Ingold, K. U. *J. Am. Chem. Soc.* 1982, *104*, 4399-4403.

93) Crich, D.; Yao, Q. *J. Am. Chem. Soc.* 1993, *115*, 1165-1166.

94) Koch, A.; Lamberth, C.; Wetterich, F.; Giese, B. *J. Org. Chem.* 1993, *58*, 1083-1089.

95) Crich, D.; Yao, Q.; Filzen, G. F. *J. Am. Chem. Soc.* 1995, *117*, 11455-11470.

96) Crich, D.; Jiao, X.-Y. *J. Am. Chem. Soc.* 1996, *118*, 6666-6670.

97) Crich, D.; Filzen, G. F. *Tetrahedron Lett.* 1993, *34*, 3225-3226.

98) Beckwith, A. L. J.; Duggan, P. J. *J. Am. Chem. Soc.* 1996, *118*, 12838-12839.

99) Beckwith, A. L. J.; Crich, D.; Duggan, P. J.; Yao, Q. *Chem. Rev.* 1997, *97*, 3273-3312.

100) Ogata, Y.; Takagi, K.; Izawa, Y. *Tetrahedron* 1968, *24*, 1617-1621.

101) Yang, N. C.; Feit, E. D.; Hui, M. H.; Turro, N. J.; Dalton, J. C. *J. Am. Chem. Soc.* 1970, *92*, 6974-6976.

102) Robbins, W. K.; Eastman, R. H. *J. Am. Chem. Soc.* 1970, *92*, 6076-6077.

103) Robbins, W. K.; Eastman, R. H. *J. Am. Chem. Soc.* 1970, *92*, 6077-6079.

104) Engel, P. S. *J. Am. Chem. Soc.* 1970, *92*, 6074-6076.

105) Felder, B.; Schumacher, R.; Sitek, F. *Helv. Chim. Acta* 1980, *63*, 132-147.

106) Turro, N. J.; Gould, I. R.; Baretz, B. H. *J. Phys. Chem.* 1983, *87*, 531-532.

107) Lunazzi, L.; Ingold, K. U.; Scaiano, J. C. *J. Phys. Chem.* 1983, *87*, 529-530.

108) Gould, I. R.; Baretz, B. H.; Turro, N. J. *J. Phys. Chem.* 1987, *91*, 925-929.

109) Arbour, C.; Atkinson, G. H. *Chem. Phys. Lett.* 1989, *159*, 520-525.

110) Noh, T.; Step, E.; Turro, N. J. *J. Photochem. Photobiol. A: Chem.* 1993, *72*, 133-145.

111) Tsentalovich, Y. P.; Fischer, H. *J. Chem. Soc., Perkin Trans. 2* 1994, 729-733.

112) Zhang, X.; Nau, W. M. *J. Phys. Org. Chem.* 2000, *13*, 634-639.

113) Kurnysheva, O. A.; Gritsan, N. P.; Tsentalovich, Y. P. *Phys. Chem. Chem. Phys.* 2001, *3*, 3677-3682.

114) Adachi, H.; Basco, N.; James, D. G. L. *Chem. Phys. Lett.* 1978, *59*, 502-505.

115) Adachi, H.; Basco, N.; James, D. G. L. *Int. J. Chem. Kinet.* 1981, *13*, 1251-1276.

116) Parkes, D. A. *Chem. Phys. Lett.* 1981, *77*, 527-532.

117) Basco, N.; Parmar, S. S. *Int. J. Chem. Kinet.* 1985, *17*, 891-900.

118) Claridge, R. F. C.; Fischer, H. *J. Phys. Chem.* 1983, *87*, 1960-1967.

119) Tokumura, K.; Ozaki, T.; Nosaka, H.; Saigusa, Y.; Itoh, M. *J. Am. Chem. Soc.* 1991, *113*, 4974-4980.

120) Nakamura, M.; Ito, O.; Matsuda, M. *J. Am. Chem. Soc.* 1980, *102*, 698-701.

121) Cozens, F. L.; Scaiano, J. C. *J. Am. Chem. Soc.* 1993, *115*, 5204-5211.

122) Marchaj, A.; Kelley, D. G.; Bakac, A.; Espenson, J. H. *J. Phys. Chem.* 1991, *95*, 4440-4441.

123) Steenken, S.; Warren, C. J.; Gilbert, B. C. *J. Chem. Soc., Perkin. Trans. 2* 1990, 335-342.

124) Hubig, S. M.; Bockman, T. M.; Kochi, J. K. *J. Am. Chem. Soc.* 1997, *119*, 2926-2935.

125) Phillips, D. *Helv. Chim. Acta* 1985, *68*, 912-918.

126) Maillard, B.; Ingold, K. U.; Scaiano, J. C. *J. Am. Chem. Soc.* 1983, *105*, 5095-5099.

127) Shorter, J. *Correlation Analysis in Organic Chemistry: An Introduction to Linear Free-Energy Relationships*; Clarendon Press: Oxford, 1973.

128) Hammett, L. P. *J. Am. Chem. Soc.* 1937, *59*, 96-103.

129) Jaffé, H. H. *Chem. Rev.* 1953, *53*, 191-261.

130) Brown, H. C.; Okamoto, Y. *J. Am. Chem. Soc.* 1958, *80*, 4979-4987.

131) Lowry, T. H.; Richardson, K. S. *Mechanism and Theory in Organic Chemistry*; 3rd ed.; Harper & Row: New York.

132) Swain, C. G.; Thornton, E. R. *J. Am. Chem. Soc.* 1962, *84*, 817-821.

133) Hammond, G. S. *J. Am. Chem. Soc.* 1955, *77*, 334-338.

134) Lomas, J. S. *Tetrahedron Lett.* 1978, *20*, 1783-1786.

135) Okamoto, Y.; Inukai, T.; Brown, H. C. *J. Am. Chem. Soc.* 1958, *80*, 4972-4976.

136) Bentley, T. W.; Llewellyn, G. *Prog. Phys. Org. Chem.* 1990, *17*, 121-158.

137) Grunwald, E.; Berkowitz, B. J. *J. Am. Chem. Soc.* 1951, *73*, 4939-4944.

138) Gutbezahl, B.; Grunwald, E. *J. Am. Chem. Soc.* 1953, *75*, 559-565.

139) Reichardt, R. *Chem. Rev.* 1994, *94*, 2319-2358.

140) Streitwieser, A.; Heathcock, C. H.; Kosower, E. M. *Introduction to Organic Chemistry*; 5th ed.; McMillan: New York, 1992.

141) Muller, P. *Pure Appl. Chem.* 1994, *66*, 1077-1184.

142) Grunwald, E.; Winstein, S. *J. Am. Chem. Soc.* 1948, *70*, 846-854.

143) Winstein, S.; Fainberg, A. H.; Grunwald, E. *J. Am. Chem. Soc.* 1957, *79*, 4146-4155.

144) Fainberg, A. H.; Winstein, S. *J. Am. Chem. Soc.* 1957, *79*, 1608-1612.

145) Streitwieser, A., Jr. *Solvolytic Displacement Reactions*; McGraw-Hill Book Co.: New York, 1962.

146) Takeuchi, K.; Ikai, K.; Shibata, T.; Tsugeno, A. *J. Org. Chem.* 1988, *53*, 2852-2855.

147) Richard, J. P.; Jencks, W. P. *J. Am. Chem. Soc.* 1984, *106*, 1383-1396.

148) Bentley, T. W.; Manfred, C.; Kemmer, R.; Llewellyn, G.; Oakley, J. E. *J. Chem. Soc., Perkin Trans. 2* 1994, *12*, 2531-2538.

149) Warncke, S.-C. K. a. K. *J. Am. Chem. Soc.* 1999, *121*, 9922-9927.

150) Chatgilialoglu, C. ; Scaiano, J. C., Ed.; CRC Press: Boca Raton: Florida, 1989; Vol. 2, pp 3-11.

151) Schepp, N. P.; Johnston, L. J. *J. Am. Chem. Soc.* 1994, *116*, 6895-6903.

152) Cozens, F. *Unpublished results.*

153) Davies, M. J.; Gilbert, B. C. *Free Radical Reactions; Table 1*; Coxon, J. M., Ed.; Jai Press Inc.: London, 1991; Vol. 1, pp 35-81.

154) Loudon, G. M. *Organic Chemistry*; The Benjamin/Cummings Publishing Company, Inc.: New York, 1995.

155) Coetzee, J. F.; McGuire, D. K. *J. Phys. Chem.* 1963, *67*, 1810-1814.

156) Kolthoff, I. M.; Bruckenstein, S.; Chantooni, M. K. Jr. *J. Am. Chem. Soc.* 1961, *83*, 3927-3935.

157) Coetzee, J. F.; Padmanabhan, G. R. *J. Phys. Chem.* 1962, *66*, 1708-1713.

158) Kinugasa, M.; Kishi, K.; Ikeda, S. *J. Phys. Chem.* 1973, *77*, 1914-1918.

159) Charlot, G.; Tremillon, B. *Chemical Reactions in Solvents and Melts*; Pergamon Press: Elmsford, N. Y., 1969.

160) Ege, S. *Organic Chemistry*; 3rd ed.; D.C. Heath and Company: Toronto, 1994.

161) Bunton, C. A.; Farber, S. J. *J. Org. Chem.* 1969, *34*, 3396-3403.

162) Hadel, L. M. *Laser Flash Photolysis*; Scaiano, J. C., Ed.; CRC Press: Boca Raton, 1989; Vol. I, pp 279-292.

163) Turro, N. J.; Weed, G. C. *J. Am. Chem. Soc.* 1983, *105*, 1861-1868.

164) Yang, H.; Hay, A. S. *Synthesis* 1992, 467-472.

165) Eberson, L.; Hartshorn, M. P.; Persson, O.; Radner, F. *Chem. Commun.* 1996, 2105-2112.

166) Fleming, S. A.; Pincock, J. A. *Photochemical Cleavage Reactions of Benzyl-Heteroatom Sigma Bonds*; Ramamurthy, V. and Schanze, K. S., Ed.; Marcel Dekker, Inc.: New York, 1999; Vol. 3.

167) Richard, J. P.; Williams, G.; Gao, J. *J. Am. Chem. Soc.* 1999, *121*, 715-726.